HAL
open science

Low-dose electron diffraction tomography (LD-EDT) for highly sensitive materials

Emre Yoruk

To cite this version:

Emre Yoruk. Low-dose electron diffraction tomography (LD-EDT) for highly sensitive materials. Materials Science [cond-mat.mtrl-sci]. Université Grenoble Alpes [2020-..], 2022. English. NNT : 2022GRALI076 . tel-04021415

HAL Id: tel-04021415

https://theses.hal.science/tel-04021415v1

Submitted on 9 Mar 2023

HAL is a multi-disciplinary open access archive for the deposit and dissemination of scientific research documents, whether they are published or not. The documents may come from teaching and research institutions in France or abroad, or from public or private research centers.

L'archive ouverte pluridisciplinaire **HAL**, est destinée au dépôt et à la diffusion de documents scientifiques de niveau recherche, publiés ou non, émanant des établissements d'enseignement et de recherche français ou étrangers, des laboratoires publics ou privés.

THÈSE

Pour obtenir le grade de

DOCTEUR DE L'UNIVERSITÉ GRENOBLE ALPES

École doctorale : I-MEP2 - Ingénierie - Matériaux, Mécanique, Environnement, Energétique, Procédés, Production
Spécialité : 2MGE : Matériaux, Mécanique, Génie civil, Electrochimie
Unité de recherche : Institut Néel

La diffraction des électrons en tomographie à faible dose appliquée à des matériaux très sensibles

Low-dose electron diffraction tomography (LD-EDT) for highly sensitive materials

Présentée par : **Emre Yörük**

Direction de thèse :

Stéphanie KODJIKIAN — Directrice de thèse
Ingénieure de Recherche, Institut Néel, CNRS/UGA

Holger KLEIN — Co-directeur de thèse
Maître de Conférences, Institut Néel, CNRS/UGA

Rapporteurs :

Philippe BOULLAY
Directeur de Recherche CNRS, CRISMAT - ENSICAEN - UNICAEN

François GOUTENOIRE
Professeur des Universités, IMMM, Le Mans Université

Thèse soutenue publiquement le **29 novembre 2022**, devant le jury composé de :

Muriel VERON — Présidente
Professeur des Universités, SIMaP, Grenoble INP/UGA

Philippe BOULLAY — Rapporteur
Directeur de Recherche CNRS, CRISMAT - ENSICAEN - UNICAEN

François GOUTENOIRE — Rapporteur
Professeur des Universités, IMMM, Le Mans Université

Marie COLMONT — Examinatrice
Maître de Conférences, Institut Centrale Lille, UCCS

Stéphanie KODJIKIAN — Directrice de thèse
Ingénieure de Recherche, Institut Néel, CNRS/UGA

Dominique LUNEAU — Invité
Professeur des Universités, LMI, Université Claude Bernard Lyon 1

Acknowledgements

This manuscript concludes three insightful years of work at Néel Institute, Grenoble. The work presented here is a result of contributions and support of many colleagues and friends and family, to whom I would like to thank for their valuable assistance and insight.

I thank my PhD supervisors Stéphanie Kodjikian and Holger Klein, for welcoming me to Néel Institute and giving me the opportunity to work on this very fascinating topic. I have especially appreciated their willingness to very quickly trust me early on to work independently on my research. During these 3 years, I could always count on them for valuable feedback whenever I needed it, it has been a pleasure to work with them.

I also thank the members of the jury, who were willing to read my manuscript and to provide a critical outlook; Philippe Boullay and François Goutenoire for accepting to be rapporteurs, Marie Colmont and Muriel Veron for accepting to be examiners and Dominique Luneau for accepting to participate as an invited member. I feel honoured to be able to defend my thesis under their supervision.

A significant portion of the work presented here would not have been possible without precious collaborations with numerous colleagues.

In addition to being an invited jury member, I offer my thanks to Dominique Luneau for providing me with quite interesting and well-crystallised samples, as well as for making himself available for discussion during data processing. I would also like to thank the MRS team at Néel Institute for providing me with samples and for inviting me to share and discuss over my results during their team meetings.

I would like to thank Wai-Li Ling and Dominique Housset for welcoming me to IBS Grenoble for data collection and their collaboration in data processing. They have been delightful to work with and were essential in overcoming key issues I encountered during data processing.

I am very grateful to Catherine Bougerol and Jean-Luc Puteaux for having accepted to be the members of my CSI jury. During the first two years of my thesis, they provided the most valuable outside input to my work. Their input led me to focus my literature work on beam damage in a more systematic manner and their encouragement reassured me to keep my motivation high.

In parallel to my research work, I am very thankful to Elise Ghibaudo and Frédérique Loiseau for providing me with the opportunity to give lectures at the University of Grenoble-Alpes. This was a very enriching experience which would not have been possible without their continued guidance and support.

Almost all experimental work was done on the Philips CM300 ST TEM in Néel Institute. Despite its old age, it did not let me down during my thesis, for which I am thankful. I would also like to thank Stéphanie again for teaching me how to use it and appreciate it.

I thank everyone who kept me company in the warm atmosphere of Néel Institute. Especially Jérémy Cathalan, Alexandra Cantarano, Pierre Gaffuri and Smail Amari, who made me feel welcome already on my first day. I appreciate the memories and their valuable friendship. I also am glad to have met Kylia Marcus and Maiia Botova, with whom I had the opportunity to organise the 2021 edition of RJP Grenoble, despite the difficult pandemic conditions. I feel lucky to have shared my office with Andea Montero, Italia Vallerini Barbosa, Zahra Sadre Momtaz and Ricardo Alvarado, whose company I will always profoundly

remember. I would also like to thank Mads Hansen, Valentina Guerrero-Florez, Julius Nunez, Nathan Bassot and Julia Gallenberger for their company, and for the good memories.

Outside of the scientific community, I would like to thank my dear friends that I have met in Grenoble; Florentin, Valentin, François, Marine, Sarah, Ni Li and my roommate Anastasia for the afterworks, nightouts, hiking and ski trips, movie nights, board game nights, and all the other things we have done together. I truly appreciated and will miss their company.

A big thanks to my mother, who has supported me all my life.

I would like to finish by thanking my dear cat, Meşhur. Even though he passed away shortly before the beginning of my PhD, he has supported me through many tough times to make it to this point, and I am sure would be proud of my achievements now.

Table of Contents

Introduction 10
Chapter I: Investigating Electron Beam Damage by Diffraction Fading 13
1) Introduction 14
2) Electron Beam Damage Mechanism 14
2.1 Origins of Electron Beam Damage 15
2.1.a Primary Damage 15
2.1.b Secondary Damage 16
2.1.c Tertiary Damage 18
3) Measuring Electron Beam Damage 19
3.1 Techniques to Monitor Beam Damage 20
3.2 Characteristics of Crystallinity Loss 22
3.2.1 The Exponential Model 22
3.2.2 Environmental Factors influencing Measurements 24
3.2.3 Internal Factors influencing Measurements 25
3.2.4 Site-Specific Damage 26
3.2.5 Latent Doses & Initial Increases 26
3.2.6 Non-Exponential Fading 27
3.2.7 Reflection Broadening 27
4) Diffraction Fading Results from Literature 28
4.1 Small-Molecules 28
4.1.1 Mechanisms of crystallinity loss 28
4.1.1.a Long-Chain Aliphatics 28
4.1.1.b Aromatics 31
4.1.1.c Amino Acids 36
4.1.2 Effect of Temperature 37
4.1.2.a Long-Chain Aliphatics 37
4.1.2.b Aromatics 38
4.1.2.c Amino Acids 39
4.1.3 Effect of Accelerating Voltage 40
4.1.3.a Long-Chain Aliphatics 40
4.1.3.b Aromatics 41
4.1.3.c Amino Acids 41
4.1.4 Effect of Encapsulation 41

4.2 Macromolecules 44
4.2.1 Mechanism of crystallinity loss 44
4.2.2 Effect of Temperature 46
4.2.3 Effect of Accelerating Voltage 48
4.2.3 Effect of Dose Rate 49
4.3 Polymers 50
4.3.1 Mechanism of crystallinity loss 50
4.3.2 Effect of Temperature 53
4.3.3 Effect of Accelerating Voltage 53
4.3.4 Effect of Dose Rate 53
4.3.5 Effect of Sample Preparation 54
4.3 Inorganics and Hybrids 56
4.4.1 Mechanism of crystallinity loss 56
4.4.2 Effect of Temperature 60
4.4.3 Effect of Accelerating Voltage 61
4.4.4 Effect of Dose Rate 61
5) Discussion 62
6) Conclusion 70
Chapter II: Electron Diffraction for Crystal Structures 73
1) Radiation-Matter Interaction – Advantages of Electrons 74
2) Features of Electron Diffraction in a Transmission Electron Microscope (TEM) 76
3) Precession Electron Diffraction 83
4) 3D Electron Diffraction (3D ED) 85
4.1 Concept 85
4.2 Step-wise 3D Electron Diffraction 87
4.3 Continuous Rotation 3D Electron Diffraction 89
4.4 3D ED Applications and Beam Damage 90
5) Low-Dose Electron Diffraction Tomography 91
5.1 Concept 91
5.2 LD-EDT Data Acquisition 93
5.2.a Specimen Preparation 93
5.2.b Experimental Setup 93
5.2.c Data acquisition 95
5.3 LD-EDT Data Reduction & Integration 96
5.4 Structure Determination 97
6) Conclusion 101
Chapter III: Structure Determination using LD-EDT 103

1) Bulachite 104
1.1 Background 104
1.2 Data Acquisition 106
1.3 Data Processing 107
1.4 Structure Solution 110
1.5 Structure Refinement 112
1.6 Discussion 117
2) $\{[Mn^{II}_2[NIT(H, H)Im]_3(CF_3SO_3)\}_n$ (reference YI_OTf03) 119
2.1 Background 119
2.2 Specimen Preparation 120
2.3 Data Acquisition 122
2.4 Data Processing 123
2.5 Alternative Data Collection to Break Preferential Orientation 126
2.6 Structure Determination 128
2.7 Discussion 139
Chapter IV: Implementation of a Dose-Symmetric Tomography Scheme in 3D Electron Diffraction 142
1) Introduction 143
1.1 Effect of Apparent Crystal Thickness 143
1.2 Dose-Symmetric Tomography & Sub-Tomogram Averaging 145
2) Implementation in 3D Electron Diffraction 147
2.1 Proof of Concept with $Sr_5CuGe_9O_{24}$ 148
2.1.a $Sr_5CuGe_9O_{24}$ 148
2.1.b Data Acquisition 150
2.1.c Data Processing 150
2.1.d Results 154
2.2 Application to Manganese Formiate 161
2.2.a Manganese Formiate 161
2.2.b Data Acquisition 161
2.2.c Data Processing 164
2.2.d Results 165
3) Analysis of Raw Data in case of Unknown Compounds 173
4) Discussion 175
Conclusion and Perspectives 180
Appendix 186
References 190

Introduction

Knowledge of the crystal structure of a material, in addition to its chemical composition, is crucial to rationalize its physicochemical and biological properties. For a given chemical composition, these properties depend essentially on the crystal structure. For instance, whether a material has piezoelectric properties, or its dielectric properties can be rationalized by in which space group it crystallizes. In chemical sciences, the chirality or conformation of molecules can influence how they react with other species, or their optical properties. Depending on their bonding scheme, carbon atoms can form graphite or diamond phases which showcase significant differences in thermal and electrical properties. Rationalizing properties with crystal structures also helps to guide synthesis of new materials with target properties. As an example, the tolerance factor for Perovskite structures can predict in which symmetry a compound can crystallize [1], which can influence its ferroelectric behavior. Characterization of the crystal structure of a material is therefore an essential step in rationalizing its properties, which can be done via diffraction methods.

Atomic structure determination in materials science has traditionally been associated with X-ray diffraction. For a long time, electron diffraction remained far behind, penalized by the strong interaction between electrons and matter and the associated dynamical effects. Its main ambition concerned the determination of the crystal system and the unit cell. The determination of the space group was accessible only at the cost of significant efforts, for example by means of convergent beam experiments. A structural model could eventually be confirmed by comparing high-resolution images with simulated images, but structural determination was not routine.

In recent decades, major technical developments have transformed the scope of electron diffraction: electron beam precession [2], tomographic experiments [3], along with fast and sensitive detectors. The former two developments have made it possible to limit the dynamical effects making the electron diffraction data compatible with traditional data processing techniques based on the kinematical approximation. An alternative to X-ray diffraction, referred to as 3D Electron Diffraction (3D ED) had emerged, capable to elucidate atomic structures of nano-sized crystals. This was the “nanocrystallography revolution” [4].

Moreover, the strong electron-matter interaction, which was initially a disadvantage in electron diffraction, has become its advantage instead. High scattering cross sections of electrons allow for

diffraction data collection, although at much smaller crystal sizes compared to synchrotron X-rays and using more accessible TEM equipment. Compared to X-rays, electrons also have a higher ratio of elastic events per inelastic event [5], meaning that more diffraction data can be recorded before energy deposition via inelastic events causes structure damage. However, this does not preclude beam damage during electron diffraction experiments, and crystal structures may be modified or destroyed during data acquisition. Beam damage is a well-recognized issue in the 3D ED field [6].

This doctoral work is focused on novel applications of the Low-Dose Electron Diffraction Tomography (LD-EDT) method [7], developed recently in Néel Institute for conducting *ab initio* atomic structure determination on beam-sensitive materials, whose atomic structure is otherwise inaccessible by traditional X-ray or electron crystallography methods. This method, based on low dose electron diffraction in tomography mode essentially has potential to be successfully applied to all radiation sensitive compounds, difficult to obtain in sufficiently large crystals for single crystal X-ray diffraction, and whose structure is too complex to be solved by powder X-ray diffraction.

In order to better understand how beam damage affects electron diffraction data, a literature review was conducted on the kinetics of crystallinity loss under electron exposure. This is presented in Chapter 1 "**Investigating Electron Beam Damage by Diffraction Fading**".

Chapter 2 "**Electron Diffraction for Crystal Structures**" presents a description of modern electron diffraction methods with a focus on LD-EDT.

Chapter 3 "**Structure determination using LD EDT**" contains results obtained on the application of the low-dose method on two unknown compounds, whose structure remained inaccessible despite diffraction experiments in synchrotron radiation. The first compound of interest was the hydrated mineral called Bulachite $[Al_6(AsO_4)_3(OH)_9(H_2O)_4]\cdot 2H_2O$. This work was conducted in collaboration with Ian Grey (CSIRO, Melbourne, Australia). The second compound was a 2D manganese-radical layered metal organic framework $\{[Mn^{II}_2[NIT(H, H)Im]_3(CF_3SO_3)\}_n$. This work was conducted in collaboration with Dominique Luneau (LMI Lyon France), Dominique Housset (IBS Grenoble France) and Wai-Li Ling (IBS Grenoble France).

A further improvement on the low-dose method was conceived during this thesis, which included modifications to both data acquisition and data processing. This is presented in Chapter 4 "**Implementation of a Dose Symmetric Tomography Scheme in 3D Electron Diffraction**".

Conclusion and perspectives are presented at the end of this manuscript.

Chapter I: Investigating Electron Beam Damage by Diffraction Fading

1) Introduction

Transmission electron microscopy (TEM) is an essential technique to obtain high-resolution information from specimens in both life and materials sciences. In addition to 3D ED, sub-nanometer resolution can be routinely achieved by imaging via techniques of high-resolution transmission electron microscopy (HRTEM) in materials science [8], and cryo-electron tomography (cryoET) and single particle analysis (SPA) in life sciences [9]. Despite the vast amount of potentially available information using these methods, electron beam damage to some specimens often limits what is practically available. Exposure of specimens to the electron beam inside a TEM can cause considerable energy deposition from the beam into the specimen, beam damage can therefore have a significant impact on measured data.

This chapter gives an overview on the physical background of beam damage to crystalline specimens. The physical background of beam damage is presented in section 2, followed by a description of how beam damage can be monitored using diffraction (section 3). The literature contains a vast amount of information on crystallinity loss measured through electron diffraction. These are presented in section 4, which is organized into sub-sections for different types of specimens. This section contains all the data collected in the literature, in an extensive way, so that it could be used in the future by any microscopist crystallographer seeking information on diffraction fading due to beam damage for a given type of material. Nevertheless, to facilitate the assimilation of the large amount of sometimes technical information contained in this chapter, the general trends observed are finally discussed in section 5, then summarized in the conclusion. This section involves discussions on properties of crystal structures. For an overview on fundamentals of electron crystallography, see Chapter 2.

2) Electron Beam Damage Mechanism

A phenomenological understanding of electron beam damage is essential to rationalize how crystals are affected by the beam. This section provides the driving mechanisms behind beam damage, which occurs through multiple timescales. Even though a complete description of damage events at the molecular scale is not available, common trends discussed in literature are presented here.

2.1 Origins of Electron Beam Damage

2.1.a Primary Damage

Beam damage refers to any unintended modification to a specimen as it is probed by a beam. The driving force behind these modifications can be the displacement of atoms from their original positions, and the breakage of chemical bonds. This is fueled by energy deposition into the specimen by the beam particles. In the case of an electron beam, electrons travelling close to atomic nuclei can deposit high amounts of energy to specimen atoms, sufficient to knock them out of their original positions if this energy is above a certain displacement threshold. This is referred to as knock-on damage [10]. These atoms will be knocked out into interstitial positions inside the specimen, and eventually can escape from the surface leading to vacancies, changes to chemical composition and mass loss. Knock-on damage can be thought of as elastic, in the sense that the total energy between the beam electrons and the specimen atom is conserved, while an energy transfer occurs between them.

Energy deposition may also occur in an inelastic manner between the beam electron and the specimen atom, with the energy deposited into the specimen atom being released in form of secondary electrons, photons or heat, upon relaxation. This can lead to ionization damage by excitation of molecules, as the energy transfer to atomic electrons can dislodge them from their orbits. Sharing of the deposited energy by many atomic electrons through collective excitations is possible, but dampens quite fast ($<10^{-15}$s) and does not contribute to the ionization process [11]. This usually concerns electrons in the valence and conduction bands. Inner-shell excitation is 20 times less probable but may deposit much larger amounts of energy into the crystal when it occurs [12], [13]. The amount of inelastic scattering is quantified by its cross-section, which is especially dependent on the chemical nature of specimen atoms and the energy of incident electrons [14].

The probability of inelastic events increases for decreasing atomic number [15], meaning that it is especially efficient on specimens containing light atoms, such as organic crystals and macromolecules. For organic specimens, ionization by inelastic scattering is the dominant damage process, even at high accelerating voltage [10], [14], [16]. These compounds can also suffer knock-on damage, but compared to the efficiency of ionization damage, this only makes a minor contribution [17]. It has been shown that even for inorganic specimens, the knock-on damage cross-section is smaller than the ionization damage,

and in cases where it is dominant such as metals and conductors, the doses required to inflict considerable damage is many orders of magnitude higher than the doses needed for ionization damage [18].

Excitation of single atomic electrons leads to a high energy state with vacancies. This process is fast, taking place in a sub-femtosecond scale [19]. If the vacancies can be rapidly filled within the same timeframe as they are generated, no permanent damage will occur. This is the case for conducting and metal specimens, whose high free electron density can fill in the vacancies in the order of femtoseconds, faster than the timescales associated with atom movement [17]. Aromatic organic compounds can also rapidly fill their vacancies as they are delocalized over many π type bonds [20]. For insulating and semiconducting specimens, relaxation can take as long as a few microseconds, bond breakage and atom movement can occur beforehand as deposited energy is transferred to nuclei through phonons or excitons in the order of sub-picoseconds. Bond breakage and radical/ion formation due to excitation is referred to as radiolysis. This is referred to as primary damage.

2.1.b Secondary Damage

Dissipation of the excess energy can result in light, x-ray as well as heat generation [11]. Heating is not prominent unless very high electron fluxes are used [12], [16], [21]. Most importantly, secondary and Auger electrons are generated following primary excitation, in femtoseconds. Since it takes only a few eV to break a chemical bond, most of the deposited potential energy goes into secondary electron production. These secondary electrons have kinetic energies in the order of a few dozens of eV and can diffuse inside the specimen in the order of 10^{-14} s [18] causing ionization damage to nearby molecules leading to a chain reaction [11]. It has been estimated that 80% of all damage is due to secondary electrons [18].

Radicals and ions formed by radiolysis are most often locally trapped near their initial positions. This can either be due to steric hindrance by contact with surrounding molecules, or reduction in diffusion at low temperature. This phenomenon is referred to as the cage effect. The cage effect can help maintain intermolecular bonds for a longer period and can lead to recombination of broken bonds. The duration of the cage is dependent on the temperature and the efficacy of the trap. The cage can be weakened if the local concentration of damaged molecules becomes too high. Free radicals can then diffuse and react with other molecules in the order of 10^{-9}s [22]. These reactions can form further unstable species which then degrade into smaller molecules in the order of microseconds [23], diffusing more easily and spreading

damage. Damage by secondary electrons and spread of damage by secondary reactions are referred to as secondary damage.

For organic compounds, weak intermolecular bonds are most often disrupted before intramolecular bonds, but it is not always the weakest energy bonds who break first. **Figure 1.1** illustrates possible mechanisms of bond breakage and potential outcomes, where X refers generally to any peripheral atom attached to a carbon, such as hydrogen and halogens. Even though C-C bonds have lower binding energy than C-X bonds, the latter possess more localized energy due to the electronegativity difference, which can lead to easier breakage. The tendency depends heavily on the molecular structure & conformation, in addition to the elemental composition [24]. In case of C-X bond breakage, positively charged ions and free radicals are formed with radicals often being the major product [25]. Secondary electrons (e_S^-) contribute significantly to bond breakage alongside beam electrons (e_B^-). Degradation produces smaller moieties which can diffuse more easily inside the crystal accelerating damage and eventually escaping from the crystal surface.

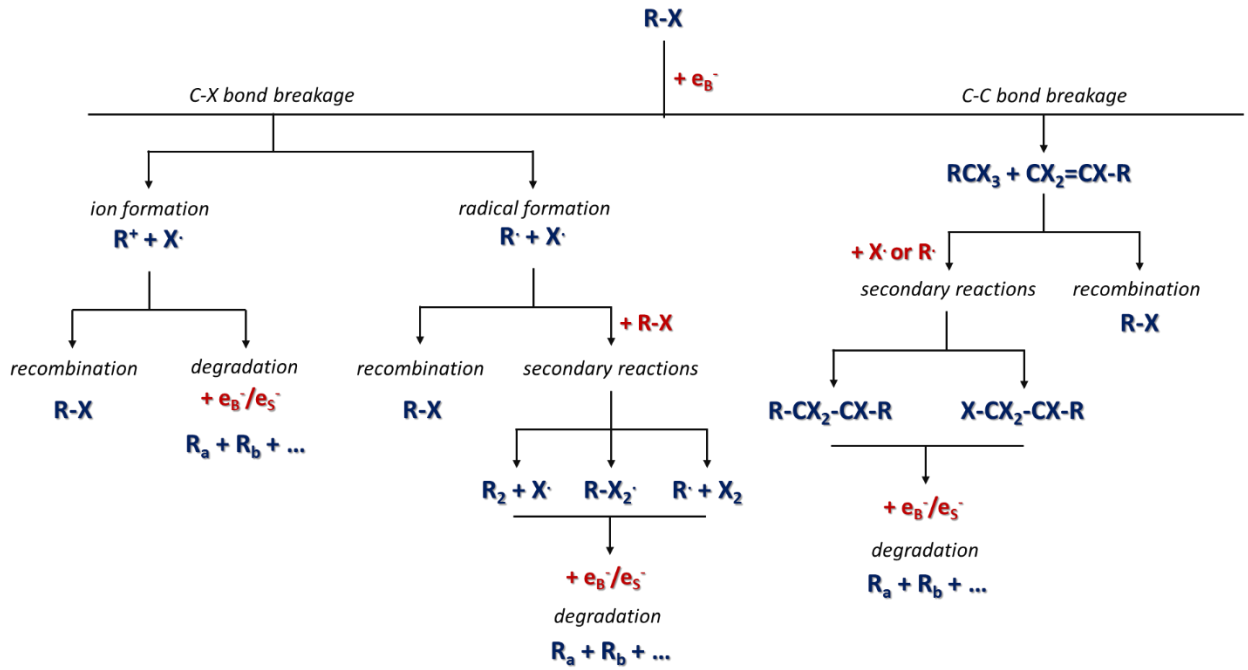

Figure 1.1: *Representation of possible outcomes following excitation of an organic molecule.*

Following C-X bond breakage, if the cage effect prevents peripheral X atoms from diffusing away, recombination may occur. If, however the bonds remain broken, the resulting radicals and ions will eventually degrade by either further excitation by secondary or beam electrons, or through secondary reactions with other damaged moieties. It is possible for energy absorbed by one molecule to be transferred to another by charge transfer, even though they are in limited contact [26]. However, transfer of energy to another part of the molecule is more effective than in-between molecules, so one specific type of radical can be formed regardless of where the primary excitation occurs [11].

Following bond breakage by radiolysis, it is possible that new bonds form between two sites left unbound by radiolysis upon C-C bond breakage, which is referred to as cross-linking [20, 21]. For instance, some polymers with large side groups on the main chain undergo bond breakage forming smaller molecules, while those without large side groups undergo cross-linking favored by a lack of steric hindrance [16]. For inorganic compounds, radiolysis can cause halogen loss for alkali halides or oxygen loss for metal oxides [29]. The rate of damage is heavily dependent on the lifetimes of the radicals, and how fast the degraded moieties can diffuse.

2.1.c Tertiary Damage

The primary damage events also cause electrostatic charging of crystals due to secondary electron generation, which can induce an internal electric field further accelerating diffusion of ionized molecules [29]. This can cause dielectric breakdown in poorly conducting specimens, or a drift of charged species in ionic compounds. Electrostatic charging of the specimen can deviate the incident beam resulting in signal loss and cause mechanical movement by attraction of ions [14]. This can cause bending of the specimen, changing its orientation with respect to the beam. Specimen movement can also occur due to pressure build-up as a result of radiolytic free radicals occupying larger volumes compared to their bound counterparts, and mechanical strains due to bond breakage. This drift is not uniform throughout an exposure and is seen to be greater at the beginning than at the end [30].

Movement of molecules due to intermolecular bond breakage causes short-range crystallinity loss. Cross-linking between vacant sites can lead to shorter bond lengths, altering lattice spacing. As molecules eventually degrade and intramolecular bonds are broken, long-range periodicity is lost and a complete loss of crystallinity may occur. Radiolysis products can eventually diffuse out of the specimen surface leading to mass loss and structural collapse, contributing to specimen drift and bending by mechanical stress. Mass loss can be substantial, with proteins losing as much as 50% of their mass at high doses [31]

leading to specimen thinning. Since diffusion rates depend on the atom size, mass loss is often accompanied by changes in chemical composition. The outcome of beam damage phenomena can vary from changes to molecular and crystalline structure to complete amorphization, changes in chemical composition and mass loss, leading eventually to modifications of physicochemical properties of the specimen. These are referred to as the tertiary damage processes.

Figure 1.2 presents a summary of the above discussion by illustrating the relative timing of damage events due to inelastic scattering.

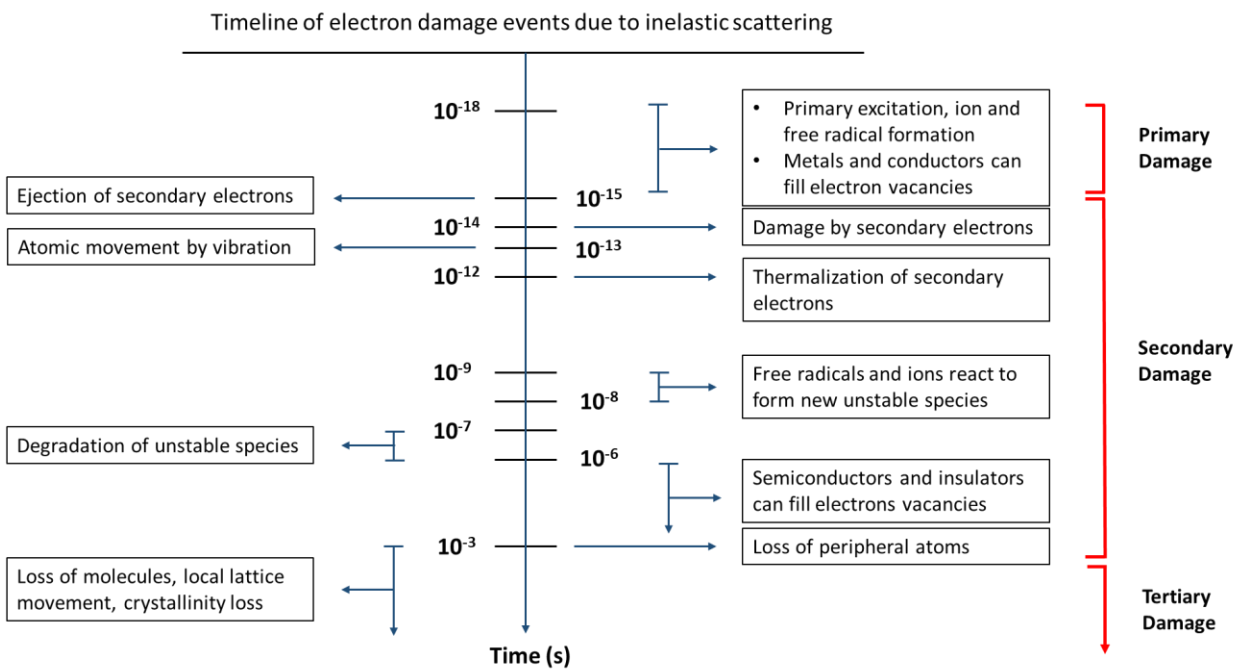

Figure 1.2: *Chronology of processes related to electron beam damage due to inelastic scattering.*

3) Measuring Electron Beam Damage

In order to characterize beam damage properly, some terms have to be clarified: the amount of energy deposited is proportional to the number of incident electrons per unit area of the specimen, expressed in $e^-/Å^2$. This quantity is referred to as the *fluence*, while the electron *dose* is defined as the charge density hitting the specimen [12]. This distinction is useful since the same number of electrons (i.e. *fluence*) with different incident energies can deposit different quantities of energy (i.e. *dose*) into the sample. However, in the majority of the electron microscopy literature, the term *dose* is used to refer to what is technically the *fluence*. For simplicity, the same terminology is used throughout this thesis, where the term *dose*

refers to the number of electrons received per unit specimen area. The *dose rate* then refers to the dose per unit of time.

Measuring the extent of damage to a specimen at a given dose is essential for adjusting illumination parameters for extracting the most amount of relevant information. Exposures necessary to achieve high-resolution data might damage beam-sensitive crystals, while reducing the incident beam intensity results in a low signal to noise ratio (SNR). Sensitivity of a specimen as a function of the dose provides valuable insight in order to optimize illumination settings to achieve the optimal SNR. This can be expressed in terms of a critical dose, which can be defined as the electron dose above which valuable information is lost. Some specimens may be sensitive to the dose rate instead of the dose [10], [12], [22], but most studies show limited dose rate dependence in typical dose rate ranges. The term critical dose intrinsically implies a criterion for its measurement, which could be the loss of diffraction intensity at a certain resolution, complete amorphization or certain changes to the chemical composition. Measurements can also affected by the irradiation conditions and crystal properties, such as crystal thickness.

3.1 Techniques to Monitor Beam Damage

The primary and secondary damage processes are too fast to be analyzed for most conventional analysis, however the tertiary processes can be probed by adapted techniques. If the specimen is crystalline, the most sensitive technique is to monitor changes to Bragg reflection intensities under illumination, referred here as simply diffraction fading. The intensities are normalized to the initial intensity in order to measure relative changes due to beam damage. The first tertiary symptom is usually the loss of short-range crystalline order. Loss of periodic order caused by bond breakage, displacement of atoms from their initial positions, and disintegration/repacking of molecules results in a decrease of Bragg intensities that characterize the lattice symmetry.

Figure 1.3 illustrates how tertiary damage processes manifest in different forms of data: reflections containing high-resolution information are sensitive to the breakage of intermolecular bonds before molecular damage, and therefore fade the fastest [32], [33] as short-range order is lost due to molecular repacking. As the electron dose accumulates, intramolecular bonds are broken which leads to a loss of short-range order and fading in Electron Energy Loss Spectroscopy (EELS) spectra. Loss of specific elements and destruction of molecular order can be monitored by EELS intensity loss, as the absorption peaks corresponding to different atoms and molecules will fade due to mass loss and intramolecular bond breakage, respectively [32], [34]. EELS can also be used to monitor the degree of electron excitations and

breakage of specific bonds. Intramolecular bond breakage eventually leads to complete amorphization and complete fading of Bragg intensities, while small atoms and molecules generated by bond breakage can diffuse out of the specimen, leading to a detectable mass loss.

2D representation of modifications to a crystal under electron irradiation	Phenomenological description of damage mechanism	Measurement of Beam Damage
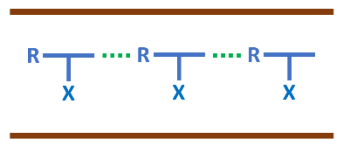	• Initially crystalline state composed of long-range ordered molecules • Packing governed by intermolecular bonds	
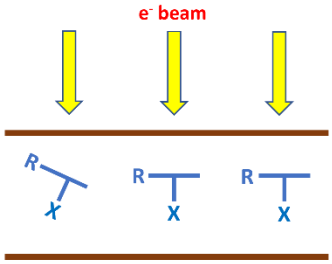	• Under electron exposure, intermolecular bonds are preferentially broken. • Molecules stay intact but may repack inside the crystal • Long-range crystallinity is lost	• Fading of high-resolution Bragg reflections • No change to EELS spectra
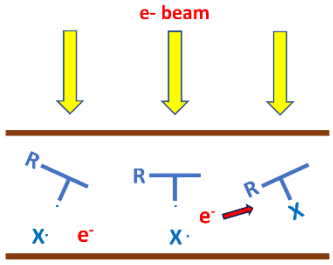	• Intramolecular bonds are broken, generating secondary electrons, free radicals or ions • Preferential loss of peripheral atoms (X) • Molecules may continue to repack • Secondary electrons diffuse and react with nearby molecules causing a cascade	• Low-resolution Bragg reflections fade until eventual complete amorphization due to loss of both short and long-range order. • Fade of EELS spectra due to intramolecular bond breakage
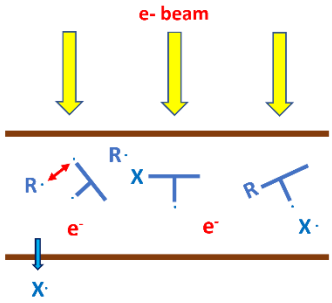	• Unstable radicals may degrade into smaller moieties • Non-bound small moieties may diffuse out of the crystal leading to mass loss • Molecules may stabilize by cross-linking with nearby diffusing species	• Further fade of EELS spectra • Mass loss detectable by thickness contrast

Figure 1.3: *Simplified illustration of crystallinity loss due to radiolysis, with corresponding probing techniques at different stages. In the crystal illustration, R represents any organic molecular group while X represents peripheral atoms such as hydrogens and halogens*

This can be monitored by the increase in electron transmission intensity [35], or by the decrease in x-ray emission intensity [36]. The loss of crystallinity is not always accompanied by a change in chemical composition [37], which may later occur at higher doses by mass loss. Critical doses measured from different methods can vary significantly, since they correspond to probing different phases of tertiary processes. For most compounds, the fading of the diffraction pattern is followed by mass loss and fading of EELS spectra due to compositional change [32], [35], [37]. This makes diffraction fading the most sensitive technique to measure beam damage for a crystalline compound, in addition to requiring the fewest amount of electron dose for recording.

3.2 Characteristics of Crystallinity Loss

The fading of diffraction intensities reflects the decrease in crystalline order, caused by radiolytic bond breakage and subsequent movement of atoms. Both inter- and intramolecular bond breakage contribute to fading [38] as the contents of individual unit cells become more and more dissimilar. In many cases, rapid breakage of intermolecular bonds is evidenced by rapid fading of diffraction patterns, while EELS intensities, which are only sensitive to intramolecular bond breakage, fade relatively slower [32]. The opposite case is also possible [39]. In most cases, both processes occur simultaneously at different rates. The fading rate can vary significantly among different compounds, but most of the time it is exponential [12].

3.2.1 The Exponential Model

If the structure factors from different unit cells are modified without any strain on the lattice, the Bragg reflections will remain at their initial positions but lose intensity over time, due to reduced contributions from unit cells containing damaged molecules who will instead contribute to diffuse scattering. Clark *et al.* [27] and Reimer & Spruth [40] proposed a model where a binary mixture of undamaged and damaged unit cells contribute to the intensity from a damaged crystal, with the fraction of undamaged cells decreasing as a function of the dose:

$$\boldsymbol{I_{hkl}(d) = e^{-2M_g} N^2 |F^u_{hkl}|^2 \left[n^2(d) + [1 - n(d)]^2 r^2_{hkl} + 2n(d)[1 - n(d)] r_{hkl}\right]}$$

with

$$\boldsymbol{n(q) = 1 - \left[1 - e^{-\sigma d}\right]^m}$$

$$r_{hkl} = \frac{F^d_{hkl}}{F^u_{hkl}}$$

In this model, e^{-Mg} is the Debye-Waller factor describing intensity attenuation due to thermal motion, N the number of unit cells in the crystal, F^u_{hkl} and F^d_{hkl} mean structure factors from undamaged and damaged unit cells respectively, $n(d)$ the fraction of undamaged unit cells at a given accumulated electron dose d, σ the damage cross section expressed in inversed electron dose units, and m the number of times a sensitive target must be hit with inelastic events before it is destroyed. This takes into account how some molecules can resist to beam damage at different rates, aromatic molecules for instance being able to take multiple hits before any significant bond breakage. This model makes the approximation that unit cells are damaged one by one after taking m hits each, with undamaged and damaged cells contributing to diffraction intensities at different amplitudes, represented by their mean structure factors. Propagation of damage can be thought of as a nucleation of growth process, starting at specific sites such as dislocations or edges, where the cage effect is initially weak.

As the electron dose accumulates, the fraction of undamaged cells $n(d)$ will decrease with the exact decrease rate being dependent on m and σ, which are specimen specific. Considering the intensity normalized to its undamaged value, the fading can be expressed as:

$$I_{hkl}(d = 0) = I_0 = e^{-2M_g} N^2 |F^u_{hkl}|^2$$

$$\frac{I_{hkl}(d)}{I_0} = \left[n^2(d) + [1 - n(d)]^2 r^2_{hkl} + 2n(d)[1 - n(d)] r_{hkl}\right]$$

$$\frac{I_{hkl}(d)}{I_0} = n^2(d)(1 - r_{hkl})^2 + n(d)(2r_{hkl} - 2{r_{hkl}}^2) + {r_{hkl}}^2$$

This model agrees with fading curves from organic compounds at low temperature. As discussed in Section 2.1, most of the potential energy deposited during primary damage events goes to secondary electron production, which in turn can cause further damage to the surrounding molecules leading to a cascade. This phenomenon might explain the exponential decay in the fraction of undamaged unit cells, as opposed to a linear profile as a function of the dose. In cases where knock-on damage is dominant, a zero-order linear fit may be used instead [12]. Instead of working in diffraction mode, loss of crystallinity can also be followed through Fourier amplitudes obtained from TEM images [30], [41]. Jeng & Chiu [42] proposed a

correction to fading diffraction intensities where damaged frames are scaled back to the first undamaged pattern, using a disordering factor proportional to the critical dose.

Determining a critical dose based on diffraction fading involves choosing a particular criterion when analyzing fading curves. Different criteria have been used in damage studies, such as the dose for complete fading D_c [43], the dose for initiating intensity loss D_i [44], or the dose necessary for fading to a specific level [45]. A very commonly used one is D_e [46], which is defined as the dose at which the intensity falls to 1/e of its pre-damage value. This criterion is argued to be more objective since the exact moment of fading initiation or complete fading may not always be very clear, due to noise effects. The dose for complete fading may be of use as a limit for observing diffraction contrast in images [47]. D_e is useful when comparing relative beam-sensitivity of different compounds under a given illumination, or for assessing protection factors gained from specific experimental settings for a same compound, such as the specimen temperature or incident beam energy [33], [48]. The following equation represents a typical fading curve of a Bragg reflection, where d represents the dose, $I(d)$ the reflection intensity after d, I_0 the initial intensity.

$$\boldsymbol{I(d) = I_0 e^{-d/D_e}}$$

3.2.2 Environmental Factors influencing Measurements

The rate of fading for a given compound varies depending on exposure conditions. Typically, fading slows down as the temperature is lowered [14], [15]. This is due to enhanced cage effects limiting diffusion of radiolysis products, favoring recombination. Critical doses increase when higher accelerating voltages are used due to less inelastic scattering, although elastic scattering is also reduced so the ratio of useful signal over damage events does not necessarily increase [33]. The dose is proportional to the square of the speed of the incident beam electrons, following the Bethe Law [49]–[51].

Apart from voluntary variations of environmental factors, diffraction fading measurements on the same type of crystals with the same supposed irradiation settings in different microscopes can also yield different results due to unavoidable differences in irradiation conditions. These include differences in dose measurement, underestimation of critical dose by pre-exposure prior to measurements, coarse sampling of fade data, differences in local specimen temperature depending on thermal conditions related to its contact with the support film, or unaccounted differences in crystal thickness [52]–[54].

3.2.3 Internal Factors influencing Measurements

Different Bragg reflections from the same crystal can fade at varying rates [38], meaning that the critical dose value depends on the choice of reflections to follow. Typically, reflections corresponding to similar lattice spacing or resolution will fade at similar rates.

Figure 1.4 shows an example of a diffraction fading measurement on a beam-sensitive crystal. Comparison of diffraction patterns before and after illumination clearly shows crystallinity loss. When the measurement is made on high-resolution reflections (red curve, "B"), exponential fade described by Eq. 1 is observed. Not all reflections behave in this way however, as evidenced by the reflection ''A'' (black curve) where the intensity increases briefly before starting to fade. Measurements based on the total intensity from all reflections (blue curve) shows an intermediary result influenced by various reflections behaving differently under the beam. Diffraction fading measurements therefore are sensitive to the choice of reflections, and the behavior of each reflection may depend on internal or external conditions. The rationalisation of this behaviour is discussed below and results obtained in literature are presented in section 4.

Calculating a critical dose by summing all reflections may lead to an overestimation, since the faster fading of high-resolution reflections may be blinded by more intense low-resolution reflections lasting longer. Different crystals from the same compound can also showcase different beam resistance depending on a variety of crystal properties such as thickness, degree of crystallinity and specimen preparation technique [28], [32], [55]. Taylor & Glaeser [21] observed different points of damage onset for crystals diffracting at different resolutions, with those reflections at initially lower resolution showing no damage during an initial period. Thicker crystals also resist longer, as more undamaged regions remain over time while the damage per unit volume remains constant [56]. Smaller particles tend to be less resistant due to a larger concentrations of ionization products being inside the crystal at a given time [57]. There could be however a critical size below which more ionization products are close to the crystal surface escaping without causing further damage [12]. The relationship of damage rate with crystal thickness is therefore complex.

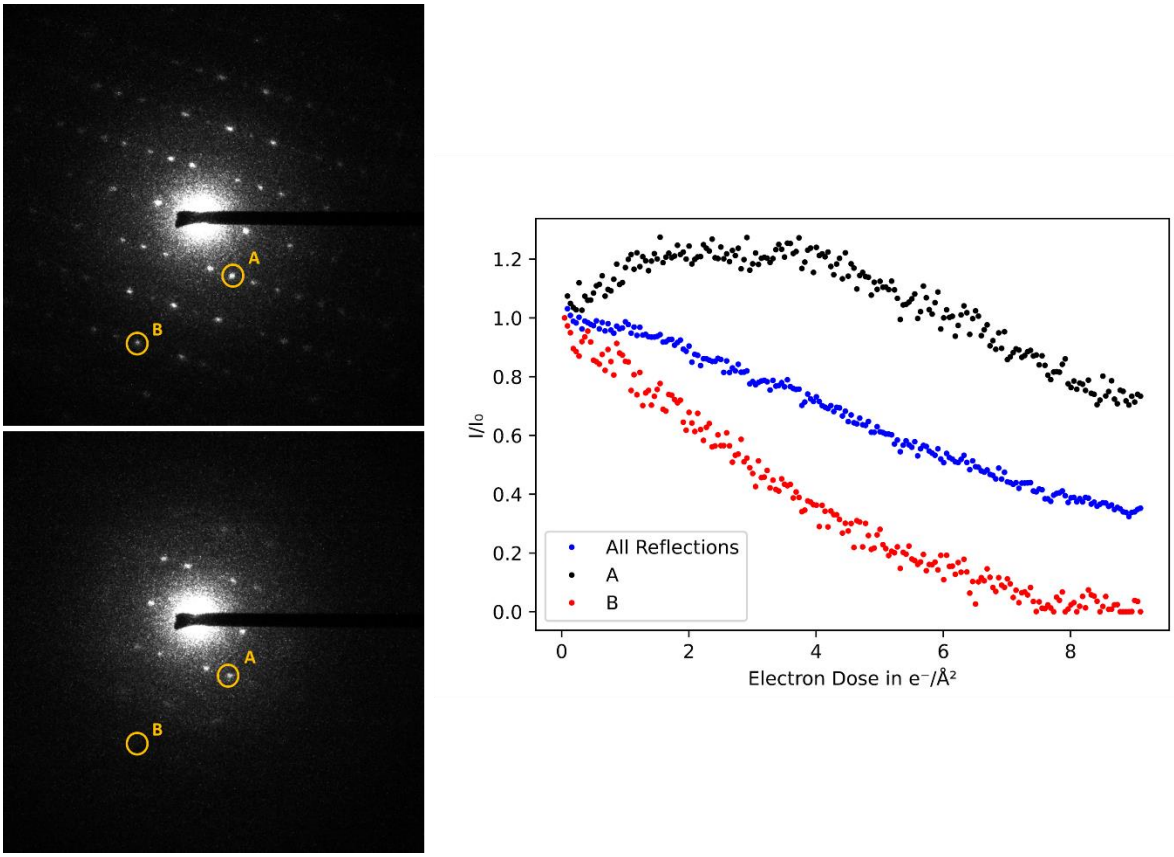

Figure 1.4: *Example of a diffraction fading measurement on manganese formiate. The diffraction pattern on top left shows the initial recorded intensities while on bottom left the same pattern is shown after a dose of 9.1 $e^-/Å^2$. Measurements are shown on the figure on the right-hand side, for reflections A and B and for all reflections (blue curve). Measured intensities are normalized to their initial values. For each measurement, background intensity measured near the reflection is subtracted from the total measured intensity.*

3.2.4 Site-Specific Damage

The rate of damage in reciprocal space may not always correlate with damage in real space, since site-specific damage is possible [58]. Site-specific damage describes the extent of beam damage in real space as damage selectively impacts certain moieties, as opposed to global damage interpretation by fading in reciprocal space. Site-specific damage has been well documented in the field of x-ray damage [59], but it is difficult to correlate critical doses from fading to site-specific damage thresholds.

3.2.5 Latent Doses & Initial Increases

The decay curves may not always be purely exponential, due to phenomena such as latent dose effects [60] and initial increases in intensity [61]. The latent dose effect refers to an initial period of exposure during which the intensity remains stable, before eventually starting to fade. This phenomenon is often

observed in low temperature conditions [43], [51], although it is not always the case [20], [57]. They might be related to strong cage effects by slow diffusion and steric hindrance of radiolytic products, or chemical bonds being strong enough to withstand multiple hits before breakage. Initial increases on the other hand refer to initial periods in exposure where the diffraction intensity is seen to increase, instead of fading. Although they are most often seen in early exposure, brief increases can also occur during later stages [51]. These might be related to crystal reorientations under the beam, or reductions in negative contributions to the structure factors by a displacement of atoms. These phenomena however remain poorly understood and render interpretation of diffraction fading data more difficult. In cases where latent doses or initial increases are observed, an exponential fit can still be made over the later fading region of the curve.

3.2.6 Non-Exponential Fading

In certain cases, even though fading is monotonous, it may not be exponential [55], [62], [63]. Bammes *et al.* [62] and Hattne *et al.* [58] observed that for weak reflections at low temperature, an exponential fit overestimated data at low dose and underestimated the data at high doses. Adding a square root dose term inside the exponential might improve the fit. Leijten *et al.* [55] showed that intensities could be fit with a linear decay for organic thin films at low temperature. Some reflections can also fade faster than an exponential fit can account for, showcasing high beam-sensitivity of the specimens [46], [64]. In some cases, reflections corresponding to large lattice spacing and low resolution may stabilize after a certain period and may not completely fade [27], [46].

3.2.7 Reflection Broadening

In addition to fading in intensity, the reflections may also broaden [14], [62], [65], due to lattice distortion or a decrease in the coherent scattering volume. Generation of dislocations may also contribute to broadening [66]. Unlike fading, the rate of broadening of the reflections does not depend on the crystal size [67]. This might imply that the actual damage rate does not depend on thickness, but thicker crystals last longer as there are more undamaged regions remaining over time. It has also been seen that spot width can initially decrease before broadening, in sync to initial increases in intensity [65].

4) Diffraction Fading Results from Literature

Diffraction fading has been used to measure beam damage inflicted upon beam-sensitive samples in TEM. These studies focus either on determining optimal irradiation conditions for a given specimen, or on measuring relative stability of different specimens to gain insight on underlying damage mechanisms. Most studies have focused on organic samples, which are divided here into 3 subcategories of small molecules, macromolecules (molecules with more than 1000 atoms in the asymmetrical unit) and polymers. Results from inorganic compounds are presented in a separate section. Critical doses measured for different compounds are presented at the end of each section.

4.1 Small-Molecules

This section regroups all organic compounds who are not considered polymers or macromolecules. Given the abundance of diffraction fading studies done on organic materials, this section is further divided into long-chain aliphatics, aromatics and amino acids. Most often, compounds with similar chemical characteristics behave similarly under the beam, as discussed below. The characteristics of crystallinity loss investigated by diffraction fading are presented first, followed by effects of specific factors including temperature, accelerating voltage, and specimen encapsulation.

4.1.1 Mechanisms of crystallinity loss

4.1.1.a Long-Chain Aliphatics

The 3 compounds who have most often been subject of diffraction fading studies are the paraffins hexatriacontane (orthorhombic $Pca2_1$, **a** = 7.42 Å, **b** = 4.96 Å and **c** = 95.14 Å) [68] and tetratetracontane (orthorhombic *Pbca*, **a** = 4.982(1) Å, **b** = 7.427(2) Å and **c** = 102.74(3) Å) [69], and behenic acid, (monoclinic $P2_1/m$, **a** = 5.62 Å, **b** = 7.40 Å, **c** = 52.93 Å, β = 52.93°) [70] a carboxylic saturated fatty acid.

Paraffins (or alkanes) are non-cyclic saturated hydrocarbons made of C-H and C-C bonds. **Figure 1.5a and 1.5b** contains 2 examples of paraffins commonly studied with diffraction fading. Due to the homogeneity of chemical bonds in different types of paraffins, they often behave similarly under the beam, although sensitivity may depend on the chain length in some cases [71]. Damage mechanism is dominated by C-H bond breakage, which results in hydrogen diffusion and double C=C bond formation leading to chain defects. C-H bond breakage can push carbon chains apart and the change in bond angles due to double

bond formation can lead to structural stress and rearrangement. Critical dose measurements on some long-chain aliphatics are regrouped at the end of the section 4.1, in **Table 1.1**.

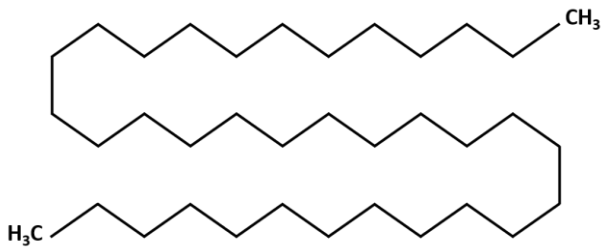

a)

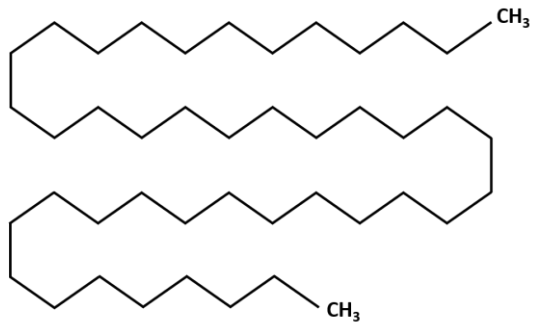

b)

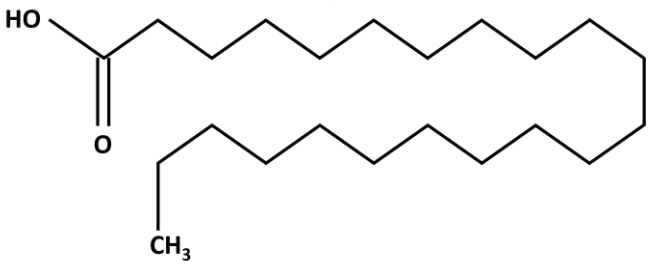

c)

Figure 1.5: *Molecular structures of 3 long-chain aliphatics;*

a) hexatriacontane
b) tetratetracontane
c) behenic acid.

For hexatriacontane (**Figure 1.5a**) crystals, the lattice spacing does not change under exposure. However, the inner 00l reflections fade much faster compared to other reflections. This strongly resembles patterns obtained from specimens heated to a hexagonal pre-melt phase [72]. W. Chiu *et al.* [48] observed a transition to a disordered phase shown by an initial blurring of 110 and 200 reflections, which then fade slower than higher order reflections.

Similarly to hexatriacontane, when paraffin n-tetratetracontane (**Figure 1.5b**) is irradiated at room temperature, a transition to a hexagonal phase similar to a pre-melt phase is seen [73]. Alternatively, irradiation below 15 K shows a transition to an intermediate rotationally disordered orthorhombic chain packing, evidenced by phasing of the measured intensities. This manifests as a change in the observed systematic extinctions following an initial loss of resolution, while the ratio of the unit cell parameters remains constant [74].

Importantly, it was seen that details necessary to locate hydrogen atoms in the chain cross-sections are lost beyond 2.0 $e^-/Å^2$ under a 100 kV beam, while the chain cross-section shape changes possibly due to chain defects similar to n-hexatriacontane. Initial increases in intensity are also seen for n-tetratetracontane, which concern not only certain specific reflections but the total diffraction intensity

[73, 75]. **Figure 1.6** shows how reflections from a sensitive crystal can behave differently under the beam. Non-monotonous fading behavior at low doses is clearly visible for multiple reflections. Some reflections fade eventually while others retain a similar intensity to their original intensity, up until the dose limit of the measurement. **Figure 1.6** therefore shows how reflections can behave drastically different from the standard monotonous fading model. It was seen that the timing of the relative intensity changes, which could be attributed to molecular disordering, do not correlate with specimen drift.

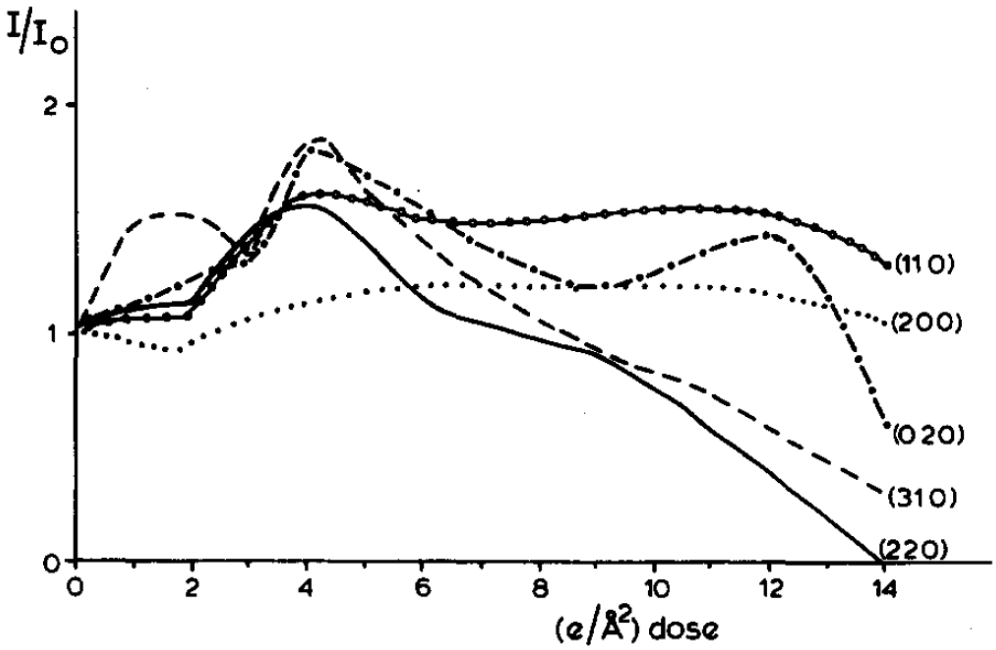

Figure 1.6: *Fading curves measured from specific reflections of paraffin n-tetratetracontane*. *Reproduced from* [74]. *Copyright: Journal of Ultramicroscopy, Elsevier.*

As with the paraffins, the behaviour of behenic acid under the electron beam shows parallelisms with its thermal behaviour. Relative changes to reflection intensities induced by the beam to behenic acid (**Figure 1.5c**), resemble a high-temperature subcell packing from similar long—chain molecules [76]. A study over multiple fatty acid compounds reveals a dependence of beam resistence to chain length and melting temperature [71]. For instance, cardiolipid crystals containing multiple fatty acid chains with few unsaturated bonds are exremely sensitive to the beam, their D_c at 100 kV measured to be less than 1.0 $e^-/Å^2$ [77]. Beam damage to behenic acid is driven by C-H bond breakage and the movement of consequent radical sites along and between the chains, which can be slowed down at low temperature. D_e for the first-order 4.2 Å reflections from a monolayer behenic acid crystal is measured between 0.6-2.0 $e^-/Å^2$ [67], [71], [78]. The critical dose also increases linearly with crystal thickness, as shown in **Figure 1.7**.

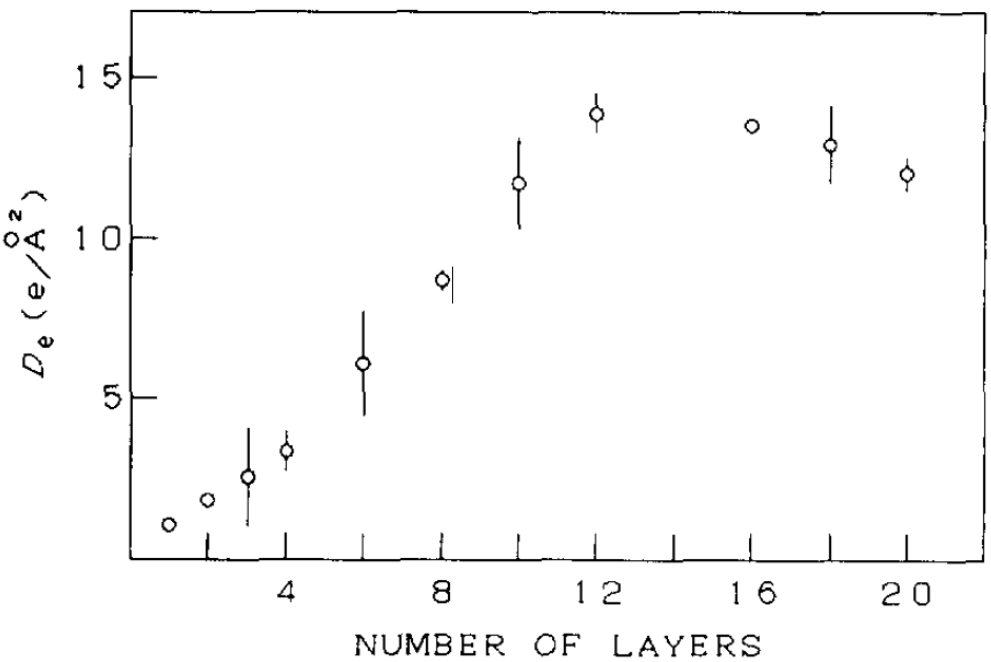

Figure 1.7: *Critical dose of behenic acid films as a function of number of layers. Reproduced from* [67]. *Copyright: Journal of Ultramicroscopy, Elsevier.*

The 1/e critical dose reaches up to 13.9 $e^-/Å^2$ for a 12-layer crystal, followed by a small decrease at higher thickness [67]. This is due to a reduced latent dose and initial increase effects at higher thickness, such as the 8-layered crystals showing no change in intensity until 2.0 $e^-/Å^2$. The initial increases are accompanied by decreases in reflection spot width, which then subsequently increase while the intensity fades. In contast to the intensity, reflection broadening is independent of crystal thickness.

4.1.1.b Aromatics

A considerable amount of diffraction fading data has been collected from aromatic compounds due to their high stability under the beam. Holes in the valence band left by ionization can be rapidly filled by delocalized π-electrons without any atom movement can take place, preserving chemical bonds. Damage is inflicted instead by inner-shell ionization, which although being less probable than valence band ionization can deposit higher amount of energy into the crystal [17]. In **Table 1.1** at the end of the section, a comparison of critical dose measurements on aromatics with other types of organic compounds indeed reveals their much-improved stability.

Phthalocyanine (Pc) (monoclinic $P2_1/a$, **a** = 19.407 Å, **b** = 4.790 Å, **c** = 14.628 Å and β = 120°*)* [79] is one of the most stable organic compounds to be examined for beam damage in the TEM. It is a polycyclic compound possessing four isoindole units connected by nitrogen atoms (**Figure 1.8a**). The four aromatic

isoindole units making up its periphery significantly reduces damage by valence band excitation. **Figure 1.9** shows a comparison of how diffraction intensities and EELS peaks fade. The stability of the molecules is evidenced by the fact that the critical electron dose for molecular damage measured by EELS is considerably higher than the dose for crystalline damage [46].

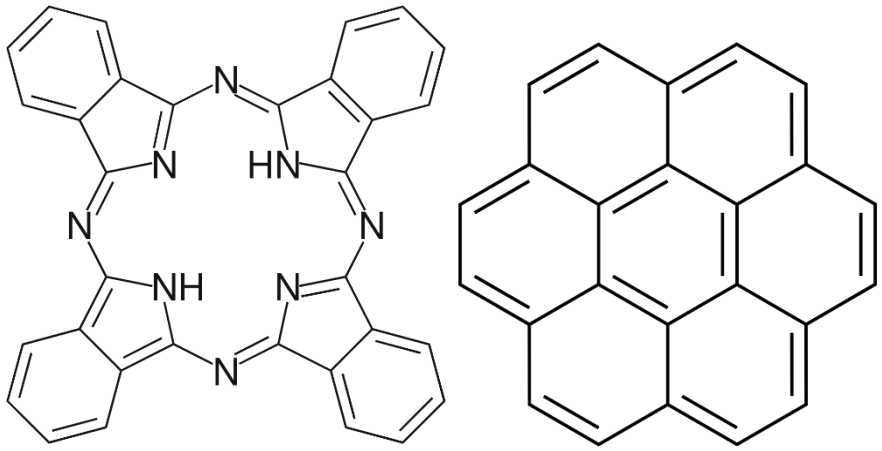

Figure 1.8: *Molecular structures of two polycyclic aromatics; a) Phthalocyanine (Pc) and b) Coronene.*

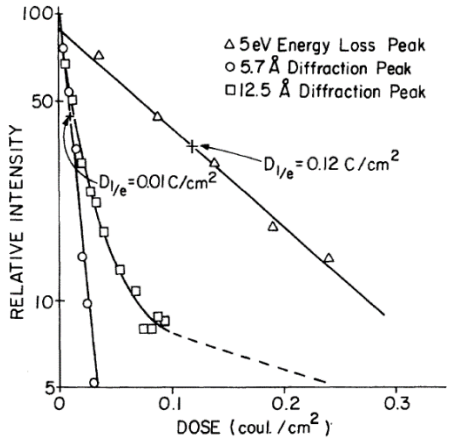

Figure 1.9: *Diffraction fading and EELS intensity loss measurements on Cu-Pc. The intensity is plotted on a log scale, while the electron dose is given in Coulombs per cm^2(1 C/cm^2 = 625 e$^-$/Å^2). Reproduced from* [46]. *Copyright: Radiation Research, Radiation Research Society.*

Results from Isaacson *et al.* [46] and Stevens *et al.* [13] show that for copper phthalocyanine (Cu-Pc), reflections at 12.5-13 Å resolution resist considerably longer than other reflections. This resolution corresponds to the spacing between the Cu-Pc molecules, and it is possible that Cu atoms stabilise inside

a repacked organic matrix with the same long range spacing as the initial state. Similar results are obtained for hexabromobenzene and tetrabromoquinone, where for the latter the reflections with a spacing approximately equal to the intermolecular Br-Br distance last much longer than other reflections [80].

Changes in diffraction pattern spacing of Cu-Pc are seen in form of expansions along [100], which is the direction in which the molecules are stacked with the shortest intermolecular distance, in addition to contractions along [001] [81]. Imaging also shows slight lattice contractions in the vicinity of damaged areas [82]. A detailed analysis by Clark *et al.* [27] found that there is a brief inital increase phase for the lowest order spots until 12.0 $e^-/Å^2$. This is visible in **Figure 1.10**, which is a measurement on the 002 reflection. This increase and further brief increases seen throughtout the illumination are attributed to the modifications to the structure factors by the cross-linking peripheral atoms, due to the progressive shrinkage of the average structure.

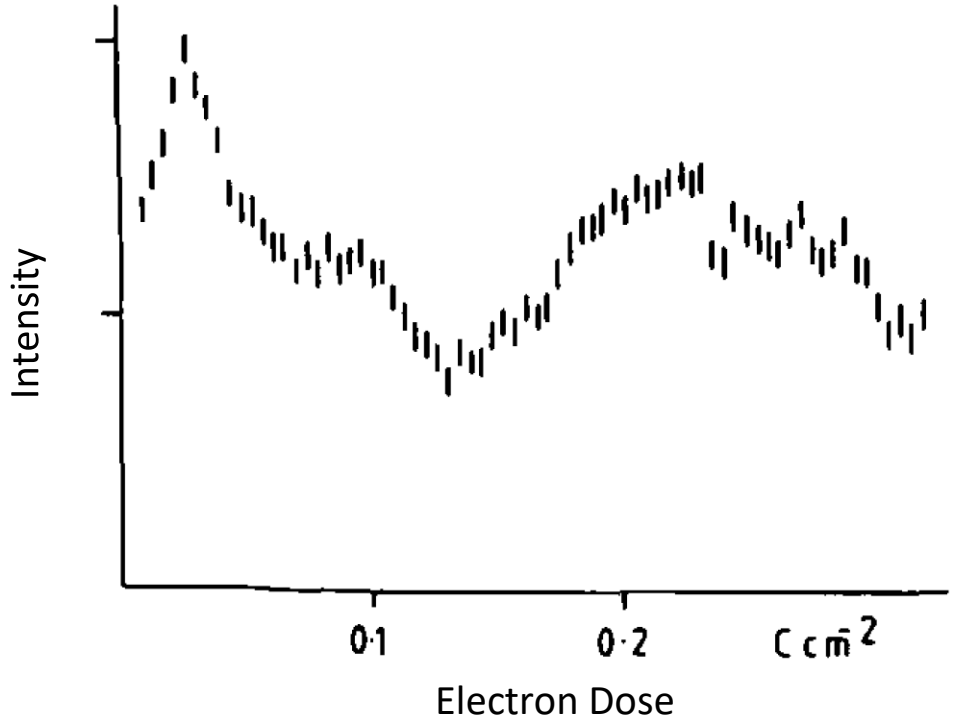

Figure 1.10: *Fading behavior of the 002 reflection from Cu-Pc. The intensity is plotted on an arbitrary scale, while the electron dose is given in Coulombs per cm²(1 C/cm² = 625 $e^-/Å^2$). Reproduced from* [27]*. Copyright: Journal of Ultramicroscopy, Elsevier.*

At higher dose, a rapid fade of higher resolution peaks occurs until 60 $e^-/Å^2$ as intermolecular bonds are disrupted and the metastable matrix is formed. A slow fading phase then takes place until the pattern completely fades at 600-1200 $e^-/Å^2$ as the molecules get damaged eventually. For cytosine, adenine,

thymine and uracil, which are aromatic nucleobases containing nitrogen and oxygen atoms at peripheral positions, beam damage is indeed initiated by peripheral atom loss as the EELS critical doses for nitrogen and oxygen loss correspond to the dose for fading of high-resolution reflections [83]. **Figure 1.11** shows how nitrogen loss measured by EELS correlates to the fading of a high-resolution reflection from cytosine.

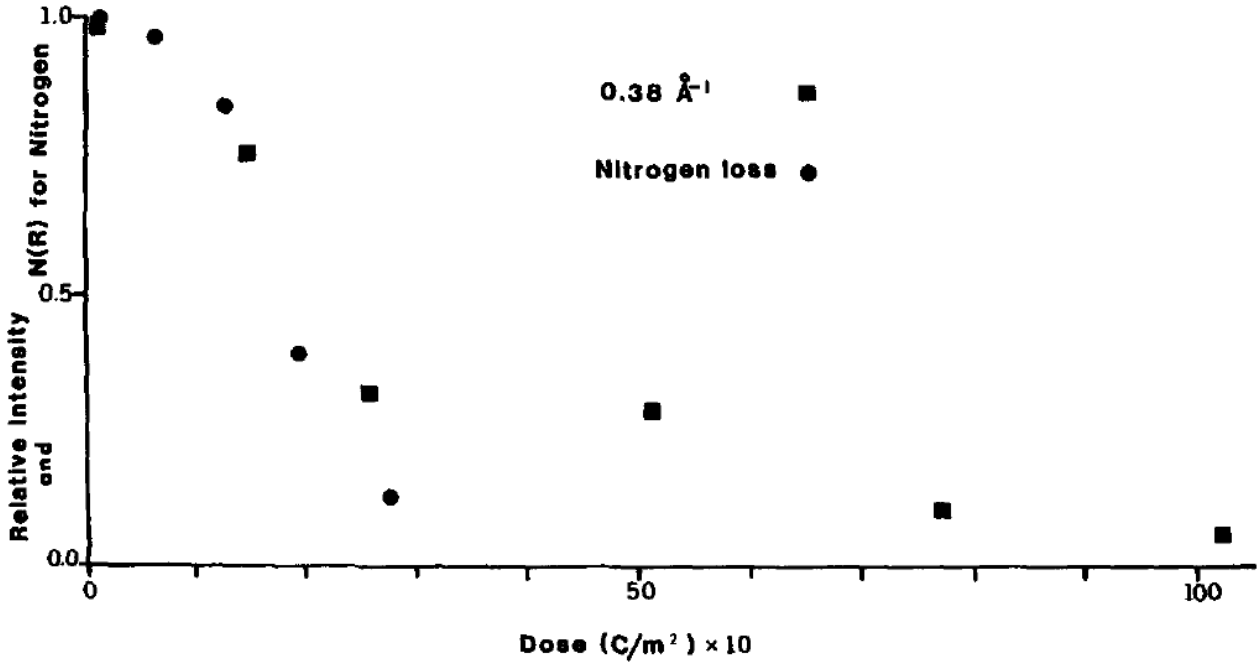

Figure 1.11: *Superposition of diffraction fading of a 2.6 Å reflection and nitrogen loss measured by EELS. The electron dose is given in Coulombs per cm²(1 C/cm² = 625 e⁻/Å²). Copyright: Journal of Ultramicroscopy, Elsevier.*

Similarly, EELS data on TCNQ shows that nitrogen loss occurs just after D_e [84]. Following peripheral atom loss, EELS data on aromatic nucleobase guanine shows that inner-shell excitation of carbon atoms contributes to bond breakage [46].

The stability of Pc can be further improved by replacing the peripheral hydrogens with Cl or Br [85]. Under a 100 kV beam, reflections from chlorinated hexadecachloro copper phthalocyanine (Cu-Pc-Cl) can last up to 25-30k $e^-/Å^2$ [27], [80]. Compared to Cu-Pc, there is relatively less difference in fading rates of different reflections Cu-Pc-Cl, and shift or broadening of reflections is seen. This could be due to the reduced contribution of the cross-linked molecules to the structure factor since damage propagates slower as a result of limited Cl diffusion. Halogenation with F atoms however is an exception to this trend, as fluorinated Cu-Pc does not showcase any major beam resistance improvement compared to its hydrogenated counterpart. This is related to the differences in crystalline structures. Cu-Pc halogenated with Cl and Br leads to a tightly packed structure, whereas fluorinated Cu-Pc has a lower molecular

occupancy which allows for an easier diffusion of atoms from broken bonds, preventing recombination [85]. The same result was also obtained for fluorinated cyanocarbon TCNQ, whose structure is less tighly packed than TCNQ [84].

Cu-Pc crystals are also sensitive to the dose rate, with increased critical doses obtained at lower dose rates [86]. **Figure 1.12** shows how the critical dose evolves as a function of the dose rate, where a clear decrease at higher dose rates is seen.

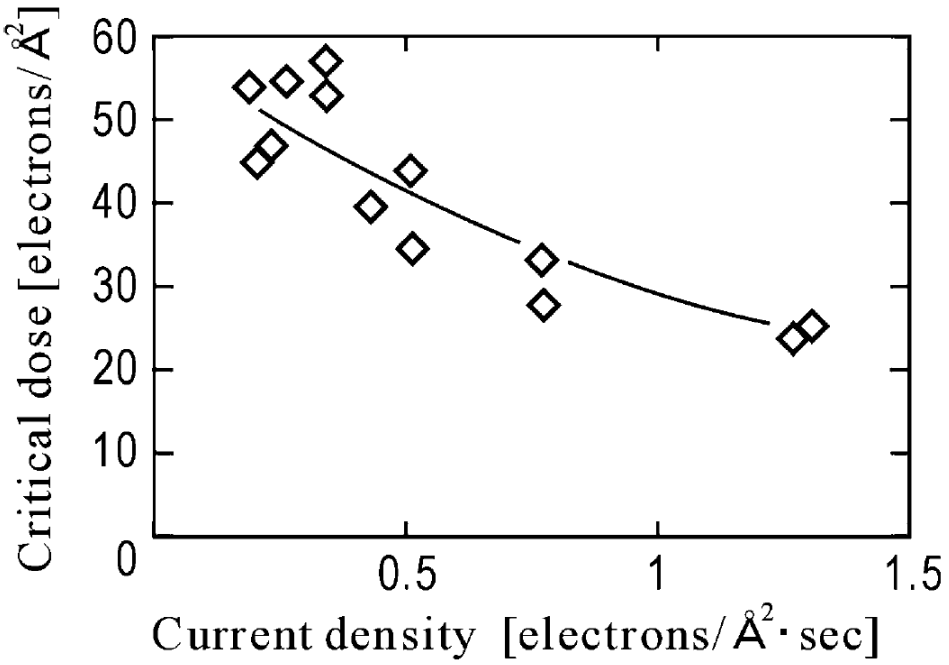

Figure 1.12: *Critical dose measured on Cu-Pc as a function of dose rate (current density). Copyright: Nuclear Instruments and Methods in Physics Research, Elsevier.*

Irradiation using a smaller beam diameter also increases beam resistance. TEM imaging shows that damage is initiated at random positions inside the crystal and its edge, and expands in a circular manner at a rate of one lattice repeat per 2.5ke$^-$/Å^2 [27], [87], [88]. Illuminating a smaller area of the crystal might therefore slow down the expansion of damage improving crystal lifetime. Critical doses also depend significantly on crystal thickness, with the critical dose for Pc improving from 104.0 e$^-$/Å^2 for a 80 Å thick crystal to 1200.0 e$^-$/Å^2 for a 200 Å thick crystal.

Coronene, a polycyclic aromatic compound with 7 benzene rings (**Figure 1.8b**), is less resistant to the beam compared to Pc. This could be due to weaker intermolecular bonds between coronene molecules [43]. Dominance of damage by inner-shell excitation is evidenced by fading slowing down significantly below 800 eV, with a 3.8 factor improvement between 300 eV and 250 eV [6, 36]. IR spectroscopy shows that

only 3% undergoing K-shell excitation leads to 10% of all C-H bonds being destroyed. For perylene, another polycyclic aromatic compound with a comparable molecular structure, a more significant reduction of fading is seen from 400 eV to 200 eV. Damage below 284 eV is only due to valence band excitation. Aliphatic compounds such as tetracontane show much smaller changes in sensitivity across the carbon K-edge, since valence band excitation contributes significantly to damage.

Individual fading profiles of reflections are dissimilar, but the reflections are seen to fade approximately at the same time [13], [89]. Measurements on 500 Å thick crystals show that the high-resolution reflections fade to ¾ of their initial intensity at 31.0 $e^-/Å^2$ for a 100 kV beam, which is doubled at 200 kV [89]. This dose corresponds to 3 inelastic events for every 4 carbon atoms, considering the thickness and scattering cross-sections. At 200 kV, measurements on the most intense reflections show a D_e of 106.0 $e^-/Å^2$, and a complete fading dose of 231.0 $e^-/Å^2$ [43]. For perylene, 5 inelastic events are necessary to destroy the contents of one unit cell at room temperature, which is also the case for adenine and pentacene [40]. For tetracene who contains 4 aromatic rings, 4 hits are necessary while 2 hits are sufficient to destroy the unit cell contents of amino acid tyrosine containing one aromatic ring.

4.1.1.c Amino Acids

Under the electron beam, amino acids degrade to products of low molecular weight by deamination and decarboxylation [83]. EELS data from glycine points out to possible loss of COOH groups, while even the aromatic parts of phenylalanine molecules can be lost at high doses [35]. Degradation does not necessarily result in mass loss, amino acids such as tyrosine and histidine can cross-link instead [35]. This is evidenced by low mass loss in parallel to the fading of the diffraction pattern. Comparing diffraction fading measurements with elemental loss and radiolytic yield calculations reveals that crystallinity loss of valine, cysteine and methionine crystals is initially governed by side-chain rotations or breakage of intermolecular H-bonds disrupting molecular packing, before eventual molecular fragmentations by bond breakage and mass loss take place [83]. The larger dose necessary for mass loss compared to diffraction fading could be due to local trapping of radicals and ions.

Aliphatic amino acids are usually very sensitive to the beam. For leucine, D_e for a 4.7 Å reflection is 1.3 $e^-/Å^2$ for a 100 kV beam [40], while site-specific damage is observed already at 0.2 $e^-/Å^2$ for prion hepta-peptide [58]. **Table 1.1** regroups results obtained on some amino acids, and comparison with other small-molecules reveals a similar or even weaker beam resistance compared to long-chain molecules, significantly inferior than aromatics.

Valine (monoclinic $P2_1$, **a** = 9.71(1) Å, **b** = 5.27(2) Å, **c** = 12.06(2) Å β = 90.8(2)°) [90] is an amino acid containing an amino group a carboxylic acid group along with an isopropyl group on its side-chain (**Figure 1.13**). Under a 80 kV beam, D_e of 1.6 Å and 2.3 Å spots from valine are measured to be only 0.1 $e^-/Å^2$ and 0.3 $e^-/Å^2$ respectively, while D_c of all spots is at 1.9 $e^-/Å^2$ for a 100kV beam [81], [91]. Contraction along the [001] direction is seen under irradiation, which is consistent with the removal of functional groups [81].

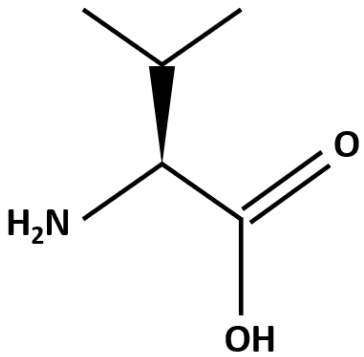

Figure 1.13: *Molecular of structure of amino acid valine*

A similar observation is made on the nucleobase cytosine, which shows contractions along [100] and [010] before complete fading. For both compounds, D_c is approximately 10 times higher than the dose to initiate damage, which corresponds to the breakage of C-H bonds [46]. Changes to 3.4 Å reflection lattice spacing were also observed for histidine crystals, which were attributed to cross-linking [35].

4.1.2 Effect of Temperature

How temperature affects the mechanism of crystallinity loss on small molecules has been investigated via diffraction fading. The results are presented here for each sub-category.

4.1.2.a Long-Chain Aliphatics

For paraffin, there is a 4-fold improvement to D_e at 4 K compared to room temperature, using a 1 MeV beam [51]. If reflections up to the third order are measured with a 100 kV beam at 4 K, a lower D_e is obtained due to faster fading of higher order spots despite the lower beam energy. Irradiation at 4 K showcases non-monotonous fading behavior in form of latent doses and initial increases. The initial increase behavior is especially dominant for first order reflections from thin crystals. Thicker crystals show abnormal behavior with intensity fluctuations under the beam, possibly due to specimen reorientation.

No latent dose effect is seen at room temperature, meaning that it could indeed be caused by an amplified cage effect in cryogenic conditions. D_c of paraffin tetratetracontane, which is 2.5-3.0 $e^-/Å^2$ at room temperature with a 100 kV beam, increases by a factor of 3-4 at 4 K [48], with most of the protection already achieved by 100 K.

For behenic acid at low temperature, the migration of radical sites along or between the chains slows down, as a result of which a latent dose effect is observed. D_e increases as the temperature is lowered, reaching 8.0 $e^-/Å^2$ at 150 K and 22.0 $e^-/Å^2$ at 6 K. **Figure 1.14** shows how critical doses evolve for different long-chain fatty acids. It can be seen that the gains in critical dose as a function of temperature follow similar curves for different fatty acids.

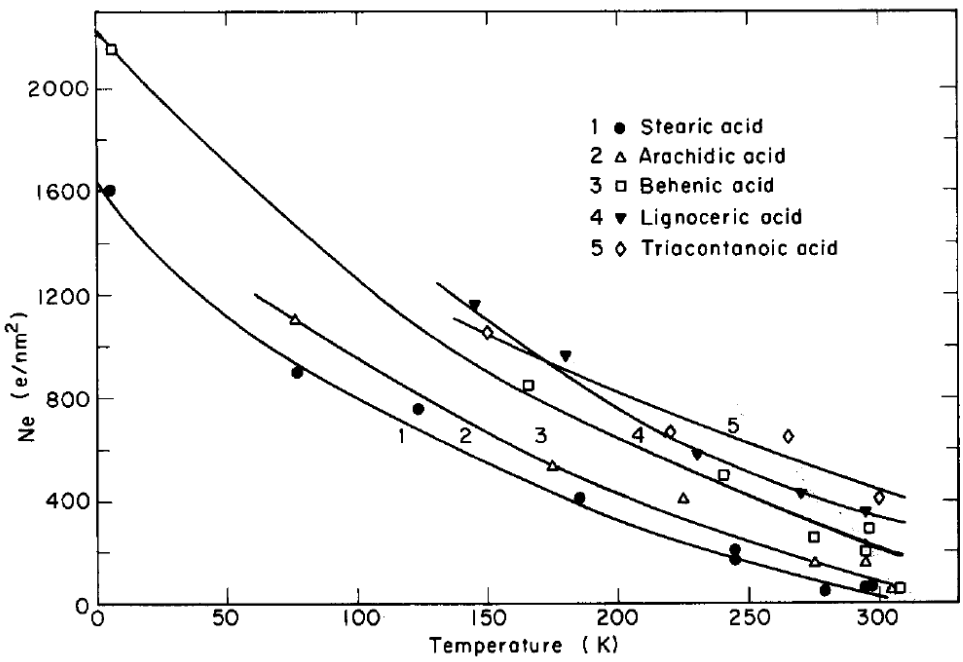

Figure 1.14: *Evolution of critical dose as a function of temperature for five long-chain fatty acids. D_e (N_e) is given in e^-/nm^2 units. Reproduced from* [71]. *Copyright: Ultramicroscopy Elsevier.*

4.1.2.b Aromatics

For coronene, the temperature dependence of the critical dose for complete fading of the diffraction pattern shows an improvement factor of 4-5 at 10 K compared to room temperature [92]. In contrast to other small molecules where most of the cryo-protection is achieved by 100 K, a factor of 1.5 is achieved at 150 K with a further factor of 4.0 between 150 K and 10 K. A similar 1.7 factor improvement at 90 K was found by Li and Egerton [43]. Salih and Cosslett [93] found a protection factor of 3-4 at 20 K compared to room temperature, for the most intense 7.66 Å reflection. Ovalene, whose polycyclic molecular structure

is very similar to coronene, also gains the most cryo-protection below 150 K, with a 12-factor improvement at 10 K [92]. The cryo-protection factor and fading profile of anthracene is identical to coronene, which is also due to molecular similarity. The fading profile at 20 K is seen to be non-exponential, which could be due to damage being dominated by intramolecular bond breakage which requires multiple hits, since intermolecular bond breakage is reduced by the amplified cage effect. This might also be the cause for the latent dose effect observed at 90 K, also observed on EELS data [43]. A latent dose effect at room temperature was also observed for low resolution reflections from CNBA, along with a redistribution of intensities of reflections in the 2-4 Å range possibly due to molecular rearrangement [57]. It is however not the case for coronene at room temperature, where the dose for molecular destruction is 9 times higher than the dose to destroy crystallinity [43]. Compared to ovalene, a much smaller protection factor is obtained for adenine (**Table 1.1**), which might be due the the latter containing more peripheral hydrogen atoms who can escape the cage effect more easily.

4.1.2.c Amino Acids

Measurements on valine at 4 K show that D_e for reflections up to the third order increases to 12.0 $e^-/Å^2$ for a 200 kV beam [94]. Lamvik *et al.*[63] found a cryo-protection factor between 4-6 at 4 K compared to room temperature, considering fading of all reflections. A latent dose effect is observed until 1.0 $e^-/Å^2$. Although no dose rate effects have been observed at room temperature [91], [95], using high dose rates at 4 K seems to increase the damage rate, leading to a beam resistance even worse than at room temperature [94]. This could be related to the reduced thermal conductivity at low temperature, which induces local heating inside the crystal when a high dose rate is used. Furthermore, irradiating a crystal with a low dose rate, shifting the beam then coming back on the same crystal shows a reversal of fading. This behaviour is only observed when the beam is shifted to a Cu bar of the grid, meaning that it could be related to an electrical discharge reversing specimen reorientation originally induced by charging due to low electric conducitivity. The electron dose for the disappearance of extinction contours increases on a gold-coated holey carbon grid, compared to a carbon film due to better charge dissipation. Using a graphene support instead of a continous carbon film was also seen to increase the critical dose for aromatic theophylline [52]. This phenomenon is not observed for thick crystals, for which the amplitude of conductivity loss might be less significant. [93] also observed inconsistent fading at low temperature, which was attributed to differences in crystal thickness.

4.1.3 Effect of Accelerating Voltage

The impact of TEM accelerating voltage on the rate of crystallinity loss on small molecules has been investigated via diffraction fading. The results are presented here for each sub-category.

4.1.3.a Long-Chain Aliphatics

Irradiating paraffin at 400 kV and 100 K gives an equivalent improvement factor compared to a 100 kV beam at 4 K [96] for reflections in the 4-3 Å range, while for reflections in the 3-2 Å range the critical dose is smaller at 400 kV and 100 K. Comparing fading data from 100 kV and 300 kV, Peet *et al.* [33] however showed that despite higher critical doses obtained at 300 kV vs. 100 kV (12.5 $e^-/Å^2$ vs. ^2.2 $e^-/Å^2$ at 80 K), the elastic scattering cross-section decreases further than the critical dose improvement, meaning that it is more efficient to gather data at 100 kV. For behenic acid, the evolution of fading curves against accelerating voltage is plotted on **Figure 1.15**. It can be seen that fading is slower at a given dose at higher voltage. D_e reaches 1.8 $e^-/Å^2$ at 500 kV and 2.2 $e^-/Å^2$ at 1000 kV for a monolayer crystal [97].

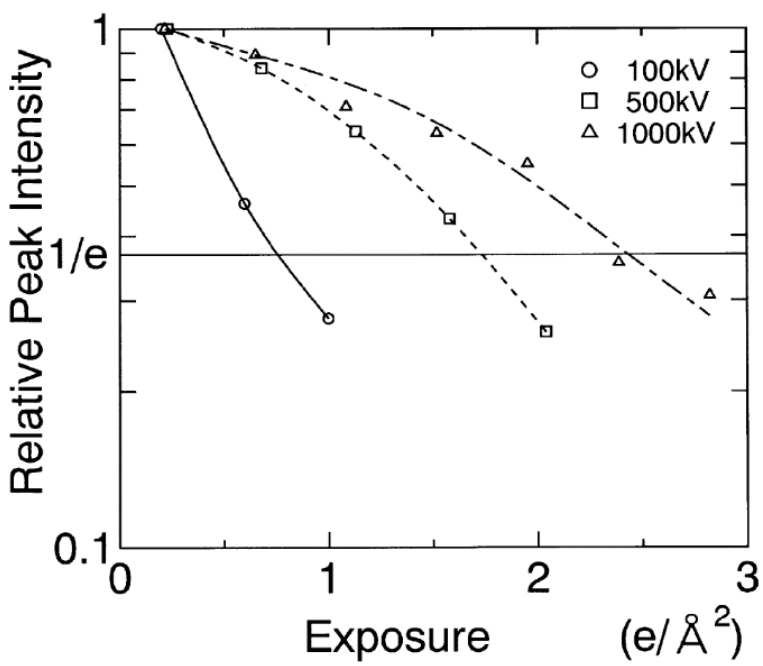

Figure 1.15: *Different fading curves obtained by changing TEM accelerating voltage, from behenic acid crystals. The 1/e limit is drawn as an horizontal line. Reproduced from* [97]*. Copyright: Micron, Elsevier.*

4.1.3.b Aromatics

Working with very low beam voltages reduces damage by reducing inner-shell excitation [13]. Plotting the inverse of the dose for complete fading of 6 Å reflections against the beam energy reveals a threshold around 600 eV, higher than the carbon K-edge of 284 eV, which is attributed to dynamical diffraction effects and competition from valence band excitation. Damage is also not completely prevented below 284 eV, since valence and Cu inner-shell excitations may still occur.

4.1.3.c Amino Acids

For valine, D_c increases almost 5 times at 2 MeV compared to 100 kV (**Table 1.1**) [91]. The energy dependence of the critical dose shows correlation with the Bethe formula, but with a cubic dependence on the electron velocity.

4.1.4 Effect of Encapsulation

The same rate of protection obtained at low temperature on paraffin can be obtained at room temperature by encapsulation of n-hexatriacontane with a carbon film, with the D_c of first order reflections increasing from 8.0 $e^-/Å^2$ to 25.0 $e^-/Å^2$ under a 100 keV beam [88]. This protection factor is independent of the carbon film thickness [87], and the 3-fold increase is similar to factors obtained from metal-free phthalocyanine, perylene and catalase. At room temperature with a 100 kV beam, D_e for all reflections also increases by a factor of 3, to 4.6 $e^-/Å^2$ (**Table 1.1**). Using a pulsed electron beam also reduces damage [23], [98]. Irradiating with single electron packets with 100 µs between each hit shows an improvement factor of 2 on the 110 spot fading rate.

In the case of Pc, the dominance of peripheral atom diffusion on the damage rate is further evidenced by differing protection factors obtained by encapsulation [87], [88]. Encapsulating Pc crystals with carbon increases the critial dose by a factor of 3, while for halogenated Cu-Pc, factors ranging from 6-10 are obtained. These correlate with the inverse diffusion rates of hydrogen and different halogens, as encapsulation helps keep hydrogens and halogens inside the crystal to favor recombination. It is possible to increase protection factors by encapsulation if halogenated layers are used, as halogens released from the layers react with radicals and ions in the crystyal to stabilise them [99]. Crystal thickness also plays a role, as smaller protection factors are obtained for thicker crystals due to increased space for diffusion despite encapsulation [82]. A thickness dependence of the critical dose has been well documented for Pc crystals. **Figure 1.16** shows the effect of crystal thickness for both encapsulated and non-encapsulated

cases. D_c of first order reflections from Pc with a 100 kV beam increases from 116.0 $e^-/Å^2$ for a 60 Å thick crystal to 200.0 $e^-/Å^2$ for a 140 Å thick crystal [92]. A much higher dose of 1200.0 $e^-/Å^2$ is measured for a 200 Å crystal [87]. Crystal thickness has less effect on protection as the temperature gets lower, and cryo-protection factors are thickness-dependent [92].

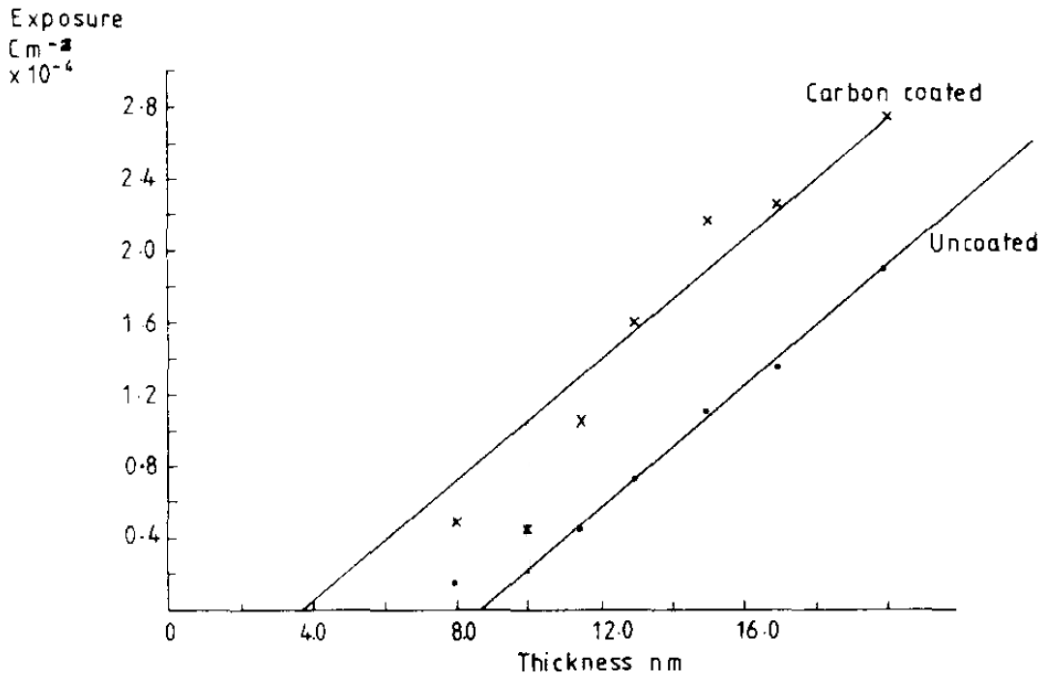

Figure 1.16: *Evolution of critical dose as a function of crystal thickness, measured on Pc crystals. Two linear fits are made in cases of encapsulated and non-encapsulated crystals. The electron dose is given in Coulombs per cm²(1 C/cm² = 625 e⁻/Å²). Reproduced from* [87]. *Copyright: Ultramicroscopy, Elsevier.*

Similar to improvements in beam resistance for Pc, encapsulation of coronene by aluminium and gold coating reduces fading by 5x and 3x respectively, by enhanced protection against charging and scavenging of radiolytic products by metals [100]. The lower protection obtained for Al coating is attributed to the partial oxidation of Al atoms. For perylene, protection factors between 2.6-3.0 were obtained by carbon coating depending on specimen thickness [88]. Although no dose rate effects were observed up to 6 $e^-/Å^2.s$ [43], a better resistance is possible at very high dose rates, since Fryer [22] showed that it is possible to take a lattice image from a hexabenzocoronene with a 93 $e^-/Å^2$ dose administered with at a rate of 4000.0 $e^-/Å^2.s$. This is also the case for anthracene and acetyl pyrene.

Table 1.1 summerizes critical dose measurements made on small-molecules compounds. Since the measurements depend on various parameters, only measurements that are inter-comparable are presented. The much higher resistence of aromatic compounds can be seen in comparison to long-chain molecules and amino acids.

Table 1.1: *Critical doses of small-molecule compounds measured by diffraction fading in $e^-/Å^2$. Unless otherwise specified, results presented here correspond to measurements made on all reflections, at room temperature and using the 1/e criterion. For the column showcasing higher voltage measurements, data from the highest available voltage was chosen. If a specific reflection was used, the corresponding lattice spacing is given in parenthesis with the smallest available lattice spacing chosen.* D_c *refers to the use of complete fading instead. Measurements at low temperature are given in a separate column where the accelerating voltage is specified if it is different than 100 kV, with the lowest available temperature being chosen. Intervals given for some compounds are due to differences in dose rate, specimen preparation and thickness.*

Compound	100 kV	at 200 kV	300 kV or above	Low Temperature	Ref.
Long-Chain Aliphatics					
Paraffin	1.5-4.6		8.0 (4.5Å) (1000kV)	9.6 (8 K)	[48], [51], [87]
Behenic acid	1.0-13.9 (4.2Å)		2.2(1000kV) (4.2Å)	22.0 (6 K) (4.2Å)	[67], [71], [78], [97]
Cardiolipin	0.6 (D_c)				[77]
Aromatics					
Phthalocyanine	104.0-1706.0 (D_c)				[87]
Cu-Phthalocyanine		343.0 (5.1Å)			[85]
coronene			600.0 (500kV) (7.7Å) (D_c)		[93]
Perylene	87.5 (3.5Å)				[40]
Adenine	187.5 (3.8Å)			112.5 (3.8Å) (45 K)	[40]
Hexabromobenzene	937.5 (1.9Å)				[93]
Pentacene	100.0 (3.2Å)				[40]
Anthracene			600.0 (500kV) (3.7Å) (D_c)		[93]
TCNQ	62.5 (2.7Å)				[40]
Ovalene	217.0 (D_c)			2652.0 (10 K) (D_c)	[92]
Tetrabromoquinone	125.0 (D_c)				[80]
Tetracene	81.0 (3.2 Å)				[40]
Amino Acids					
valine	1.9 (D_c)	3.1 (D_c)	9.4 (2000kV) (D_c)	13.75 (500kV) (20 K) (D_c)	[91], [93], [95]
Tyrosine	9.4 (2.8Å)				[40]
Leucine	0.6 (2.7Å)				[40]
Prion hepta peptide				2.1-2.3 (100 K) (200kV)	[58]

4.2 Macromolecules

In this section, macromolecules are defined as organic compounds containing more than 1000 atoms inside their unit cell. These compounds are extremely beam-sensitive and can rapidly lose their crystallinity. Their sensitivity is comparable to long-chain aliphatic small molecules, but their crystallinity loss mechanism differs significantly, as discussed below. Macromolecules have been subject to extensive studies concerning the effect of low temperatures and specimen preparation, due to the emergence of the cryo-electron microscopy field. Crystallinity loss mechanisms are presented first, followed by effects of temperature, accelerating voltage, and dose rate.

4.2.1 Mechanism of crystallinity loss

Macromolecules irradiated inside the TEM undergo rapid beam damage as their structure is perturbed by intermolecular bond breakage followed by ionization of large molecules, and the subsequent secondary reactions. Compared to other types of specimens, damage is amplified due to the hydrated nature of these specimens, which can dehydrate due to the TEM vacuum and radiolysis of H_2O can produce many small, reactive radicals and ions which heavily contribute to secondary damage processes [14]. Most biological specimens will undergo major modifications to their structure by 5.0 $e^-/Å^2$, and high-resolution information can be lost even at 0.1 $e^-/Å^2$ [31], [101]. Even though the inelastic cross-section for ionization is similar to that of small-molecule materials, larger unit cells in macromolecular structures with more complex molecular interactions are more prone to beam damage through intermolecular bond breakage, which results in a faster loss of high-resolution information [38]. This phenomenon can be so severe that in some cases, a complete loss of crystallinity can occur prior to any bond breakage measured by EELS [53]. On the other hand, functional damage can be inflicted to some specimens before the onset of crystallinity loss, such as damage to specific amino acid residues in proteins [14]. Mass loss can be quite substantial and will lead to changes in chemical composition as O and H atoms are preferentially lost. The underlying secondary damage mechanisms are often difficult to rationalize due to the complexity of their structure. There is some evidence from the X-ray diffraction community of an inverse dose-rate effect [102] on proteins, since the damage is dominated by slower secondary processes which can be outrun. Specimen drift and bubbling can however be reduced at lower dose rates [103].

In macromolecules, quantifying structural damage by diffraction fading can be difficult due to a very small number of unit cells inside the crystals, showing weak diffraction. This can be overcome by measurements

on many overlapping crystals resulting in circularly averaged reflections [104]. Soft-matter specimens can also suffer from buckling and bending under the beam due to internal strains induced by bond disruption and void formation, resulting in an unreliable evolution of the intensities [14], [47]. In these cases, measuring the end-point critical dose is usually more reliable. Results obtained on some macromolecules are presented in **Table 1.2**. Overall comparison to doses measured on small molecules reveals a similar or lower beam resistance to long-chain aliphatics and amino acids.

Catalase has been one of the most frequently used protein crystals for assessing electron beam damage. It is a tetramer enzyme composed of four polypeptide chains. When irradiated at 200 kV without any fixation procedure, most high-order reflections vanish after a dose of 1.2 $e^-/Å^2$, with complete vanishing at 2.0 $e^-/Å^2$ [105]. Crystals can be embedded in glucose at room temperature to preserve their natural structure. In this case, D_e is 0.5 $e^-/Å^2$ at 100 kV, measured for the reflection with the highest decay rate [106]. While the high-resolution reflections fade exponentially, fading profile of lower resolution reflections is more variable, with initial increases in some cases. Complete fading is observed after 4.0 $e^-/Å^2$ at room temperature (**Table 1.2**).

When uranyl acetate-stained catalase is irradiated, a significant protection is achieved for the low-resolution reflections [95]. Crystals initially diffracting until 15 Å retain all their reflections until a dose of 10.0 $e^-/Å^2$ at 80 kV, after which higher order reflections start to fade. Most spots above 25 Å disappear by 300.0 $e^-/Å^2$. Further exposure leads only to minor changes, and low-resolution reflections remain sharp at very high doses. Importantly, while higher resolution reflections fade, relative intensities of the remaining spots are modified considerably, with visible changes starting at 100.0 $e^-/Å^2$. These are possibly related to molecular repacking. The same phenomenon was also noted for the polycyclic aromatic small-molecule 9,9-bianthracene-10-carbonitrile (CNBA), attributed to rearrangement of molecules [57]. Encapsulating one side of a catalase crystal with a carbon layer improves the critical dose by a factor of 3 [88].

Site-specific damage has been observed on Proteinase-K crystals [58] by measuring multiple electron diffraction datasets from the same wedge of the reciprocal space and phasing each dataset to observe changes in the real space density map. It is seen that the disulfide bonds break at 0.9 $e^-/Å^2$, while the total diffraction intensity has only fallen to 75% of its initial value. Weakening of their real space map density can already be observed as low as 0.1 $e^-/Å^2$. The real space map density representing acidic sidechains around glutamate and aspartate starts to at weaken at 2.0 $e^-/Å^2$, which corresponds to D_e for the 2 Å resolution reflections and 50% fade of the total diffraction intensity. It then disappears completely at 5.0 $e^-/Å^2$, which is slightly higher than D_e of low-resolution reflections of 5 Å and above.

4.2.2 Effect of Temperature

The dose for complete fading of glucose-embedded catalase increases to 12.0 $e^-/Å^2$ at 153 K, with a higher value of 27.0 $e^-/Å^2$ obtained for frozen-hydrated catalase [21] (**Table 1.2**). Initial increases from low-resolution peaks are also observed for frozen hydrated crystals at 4 K [62], thought to be due to modifications to structure factors under the cage effect. Interestingly, frozen hydrated crystals initially diffracting at low resolution were insensitive to any fading until high accumulated exposures [21]. How the critical dose changes for reflections at different resolutions is given in **Figure 1.17**. It can be seen that there is a roughly 10-fold increase going from 3 Å to 10 Å. A frozen hydrated catalase crystal initially diffracting at a resolution of 2.8 Å fades to 3.6 Å after a dose of 2.5 $e^-/Å^2$, and still diffracts at 8.5 Å after 11 $e^-/Å^2$ [21].

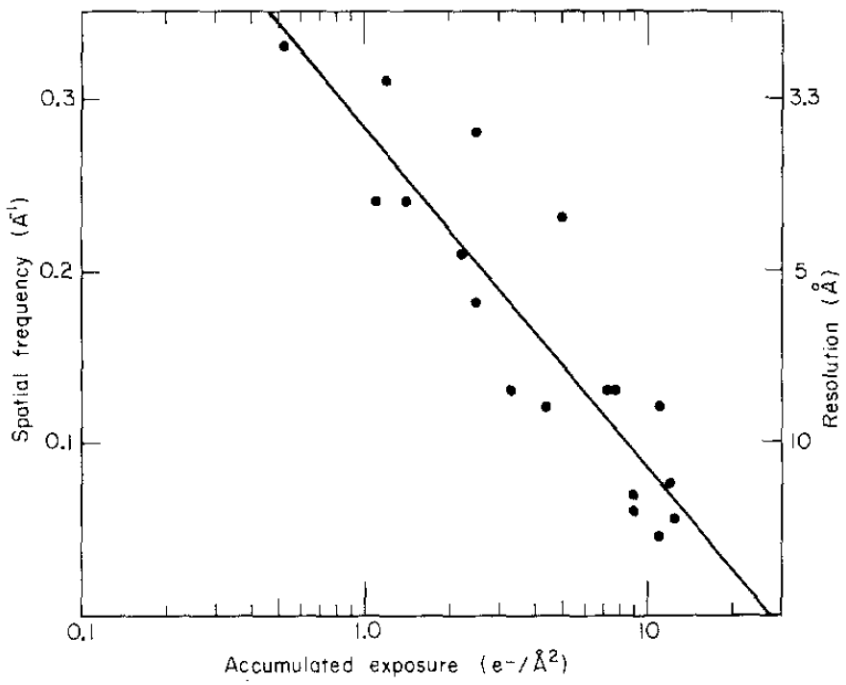

Figure 1.17: *Critical dose as a function of resolution, measured on frozen hydrated catalase. The left vertical axis gives resolution in $Å^{-1}$ while Å units are given on the right-hand side. A log-scale is used for the electron dose. Reproduced from* [21]*. Copyright: Journal of Structural Biology, Elsevier.*

Initial increases seen for hydrated bi-layered phosphatidylcholines near their transition temperature are attributed to the formation of gel state domains by free acyl chains from severed ester bonds, which are more organized than the original phospholipids domains [107]. Jeng & Chiu [42] found that for crotoxin crystals at low temperature, the amount of total diffraction intensity difference from the initial structure remains constant at high exposure while the details of the structure continue to change.

For catalase, differences in fading curves from different crystals are attributed to differences in crystal dimensions and crystallinity, those with initially higher initial intensity requiring higher doses for fading. Although small differences in fading kinetics are seen at high-resolution, similar critical doses are measured as a function of temperature for reflections with resolutions above 10 Å. This is also true for crotoxin crystals [108], while tRNA crystals resist 2 times better when embedded in glucose compared to embedding in Au-thioglucose [109], the latter possibly inducing more disorder inside the crystals. For catalase, the optimal temperature for preserving crystallinity is measured to be an intermediate range between liquid nitrogen and helium temperatures (25-42 K), although there is no considerable difference in protection factors below 100 K if the total exposure is kept low [62]. Using amplitudes from Fourier transforms of images for fading analysis, it is seen that an exponential function containing a square root term fits the fading data better compared to a pure exponential. This is due to high-resolution reflections showcasing steep initial decays, compared to more gradual fading from low resolution spots.

Surprisingly, fading is amplified when irradiating stained catalase in low temperature [110]. When the crystals are continuously cooled under irradiation, a sudden irreversible loss of crystallinity occurs at 35 K, reducing the resolution down to 25 Å. If a crystal is pre-damaged to lower the resolution to 25 Å at room temperature, no sudden loss is seen upon cooling down. Furthermore, crystals cooled down to 35 K and subsequently reheated without any exposure do not undergo a sudden loss. One explanation is that 35 K is a critical point in terms of radiolytic product diffusion, below which the cage effect is very strong, possibly aided by the uranyl acetate stain. The high concentration of trapped radiolytic products reaches a critical threshold where a chain reaction occurs, suddenly damaging the structure. In some cases, complete fading of diffraction is observed at low temperature, possibly as a result of stronger mechanical strains in the stained structure due to thermal contraction. A similar high protection is observed for uranyl acetate-stained yeast tRNA crystals, who are more resistant to beam damage compared to proteins thanks to the presence of aromatic bases in their molecules, and the presence of phosphate groups with a higher elastic to inelastic scattering ratio [109]. Another example of better damage resistance at higher temperature are hydrated phosphatidylcholine bilayers, where the bilayer structure ruptures at a higher dose when the temperature approaches and passes their structural transition temperature [107]. This could be due to the bilayer structure getting more fluid and allowing for an easier diffusion of structure defects generated by beam damage.

Purple membrane, a two-dimensional crystalline patch containing bacteriorhodopsin membrane proteins of halobacterium salinarum, has been studied to assess cryo-protection factors against electron beam

damage. Although fading is always exponential, the slopes are seen to be temperature dependent. D_e of all reflections increases by 13.5 times at 110 K (**Table 1.2**). Fading rate of high-resolution peaks from glucose embedded purple membrane is found to be similar to catalase [106], the fastest decaying reflection showing a D_e of 0.5 $e^-/Å^2$ at 100 kV and room temperature. At 80 K, there is an initial slower phase of fading followed by an exponential loss [33]. The cryo-protection factors are not resolution dependent [104]. Improvement factors in critical dose for glucose embedded crystals at 153 K vary between 4.9 to 7.7. All diffraction intensity disappears by 3.5 $e^-/Å^2$ at room temperature, and by 8.5 $e^-/Å^2$ at 153 K. A bigger 9-factor improvement has been seen at 98 K for 7 Å reflections [111]. Critical dose measurements at low temperature are more divergent compared to room temperature, which might be related to specimen drift and reorientation. Specimen drift of purple membrane crystals has been noted to increase at low temperature [112]. Measurements show that for low-resolution peaks, most cryo-protection is achieved by 110 K, with little improvement below [48], [111]. At 100 kV, D_e measured from all reflections from a crystal initially diffracting at 7 Å is 13.5 $e^-/Å^2$, while at 4 K D_e measured from a 6 Å reflection is 14.0 $e^-/Å^2$ [112]. The improvement at 4 K is slightly better for higher resolution peaks, 3 Å reflections show a 2.5 factor improvement from 98 K to 4K [111]. Glucose embedded crotoxin crystals show a 2-factor improvement from 125 K to 4 K [42], [108].

4.2.3 Effect of Accelerating Voltage

Beam resistance of catalase can be improved by using higher voltages [64]. Considering reflections in the 4-6 Å range, D_e is seven times higher at 800 kV for glucose-embedded crystals, compared to 100 kV (**Table 1.2**). Some reflections show abnormal behavior where fast fading is followed by increases in intensity. This is shown in **Figure 1.18**. On **Figure 1.18**, the lines represent averaged fading data measured at different accelerating voltages.

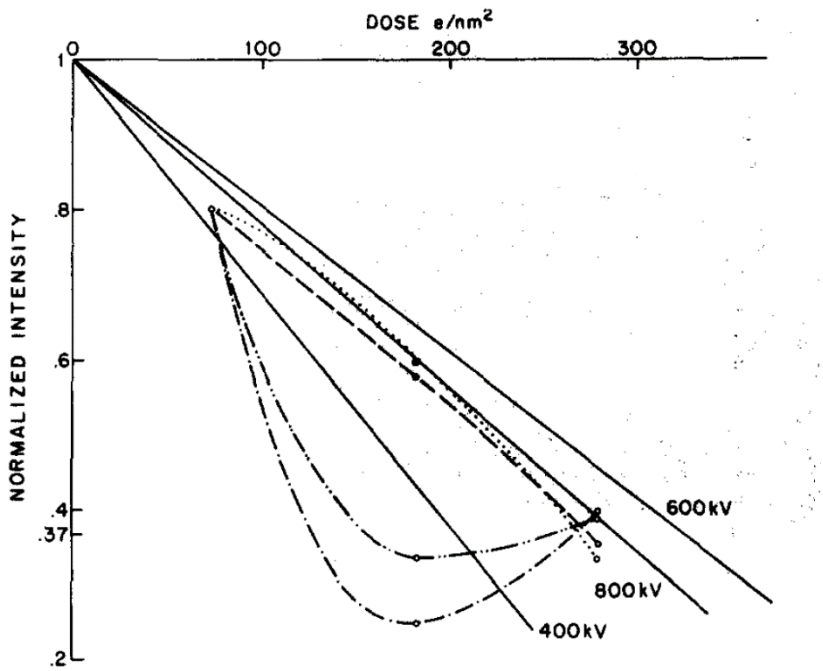

Figure 1.18: *Diffraction fading from glucose-embedded catalase at different accelerating voltages Solid lines represent averages from 24 reflections in the range of 16.0-25.0 Å. The dashed line represents abnormal behavior with intermediary increases in intensity, which were observed throughout all accelerating voltages. Reproduced from* [64]. *Copyright: Ultramicroscopy, Elsevier.*

A similar behavior is seen for reflections in the 16-22 Å range from hydrated actin bundles at 400 kV [41]. Higher critical doses for purple membrane are measured for higher beam voltage, but there are 25% more elastic scattering events per unit damage at 100 kV than at 300 kV [33].

4.2.3 Effect of Dose Rate

No dose rate effects have been observed on diffraction fading of macromolecules, except for pulsed beam experiments on purple membrane [98]. Analysis of fading from an 8.8 Å ring reflection shows a 2-factor improvement compared to a regular continuous beam. Another exception could be lysozyme. When vitrified lysozyme crystals are irradiated at 200 kV with short pauses between each diffraction pattern, reflections in the resolution zone 2.9 – 4.6 Å remain unchanged until 9.0 $e^-/Å^2$, after which they start to fade [113]. However, when they are continuously irradiated, 3-6 Å reflections fade to half of their initial intensity by 6.0 $e^-/Å^2$ [114]. This could be an example of a direct dose-rate effect, as excitation products diffuse out of the specimen during pauses without reaching a high concentration, which slows down beam damage. Buecker *et al.* [115] found the optimal dose for lysozyme at cryo temperatures to be 2.6 $e^-/Å^2$, by fractionating the dose over low exposure movie frames and determining the best half-set correlation coefficient over different frame sums.

Table 1.2 summerizes critical dose measurements made on macromolecules. Since the measurements depend on various parameters, only measurements that are inter-comparable are presented. The impact of low temperatures can be seen on catalase, purple membrane and crotoxin.

Table 1.2*: Critical doses of macromolecules measured by diffraction fading in $e^-/Å^2$. Unless otherwise specified, results presented here correspond to measurements made on all reflections, at room temperature and using the 1/e criterion. For the column showcasing higher voltage measurements, data from the highest available voltage was chosen. If a specific reflection was used, the corresponding lattice spacing is given in parenthesis with the smallest available lattice spacing chosen. D_c refers to the use of complete fading instead. Measurements at low temperature are given in a separate column where the accelerating voltage is specified if it is different than 100 kV, with the lowest available temperature being chosen. Intervals given for some compounds are due to differences in dose rate, specimen preparation and thickness.*

Compound	100 kV	200 kV	300 kV or above	Low Temperature	Ref.
Catalase	4.0 (D_c)		3.5 (800kV) (4.0-6.0Å)	12.0-27.0 (153 K) (D_c)	[91]
Purple Membrane	1.0		7.8 (300kV) (4.0Å)	13.5 (110 K)	[33], [48]
Crotoxin	0.5 (<6.0Å)			7.0 (4 K) (<6.0Å)	[108]
tRNA		8.0 (4.5Å)			[109]
Proteinase K				1.9 (100 K)(200kV) (2.0Å)	[58]

4.3 Polymers

Polymer beam resistivity is relatively more diverse compared to other types of organic compounds, with critical doses in different orders of magnitude on different compounds, depending on the chemical nature of the monomer motif. Characteristics of crystallinity loss are described followed by effects of temperature, accelerating voltage, dose rate and specimen preparation.

4.3.1 Mechanism of crystallinity loss

In terms of electron beam-sensitivity, polymers are often placed into two categories regarding the nature of the secondary damage processes. Upon radiolytic bond breakage, those who fragment into smaller moieties are called scission-type polymers, while those who favor formation of new bonds are called cross-linking polymers.

Cross-linking can cause modifications to the lattice parameters, while diffusion of broken radicals propagates damage, destroying crystallinity. Damage kinetics can be heavily dominated by the size and nature of the side chains, who can detach from the main chain forming radicals. Ionized parts of adjacent main chains can then cross-link to stabilize. This will lead to progressive amorphization without significant mass loss.

If, however cross-linking is sterically hindered by the presence of large side groups, or the newly formed radicals are small enough to escape the cage effect, parts of the chain will break instead forming smaller molecules, leading to scission. Scission can occur at random along the chains, reducing the average molecular weight. This can cause amorphization accelerated by secondary diffusion processes, leading eventually to mass loss.

Double bond formation inside the chain may also occur, so inter and intra-molecular cross-linking is possible. It has been observed that the Bragg reflections completely fade out as a result of damage for the scission type polymers, while the spots blur into rings for cross-linking polymers [116].

Measurements on polyethylene (PE) (**Figure 1.19a**) show that the spotty diffraction patterns fade into diffuse halo rings, meaning that damage is dominated by cross-linking, without detectable mass loss [116], [117]. While fading, the spots shift inward as lattice spacing gets larger. Enlargement of the unit cell under exposure is also observed for polyether ether ketone (PEEK) [118]. This is thought to be due to the directional nature of cross-linking along the main chain. No dose rate effects were observed between 0 and 0.09 $e^{-}/Å^{2}.s$.

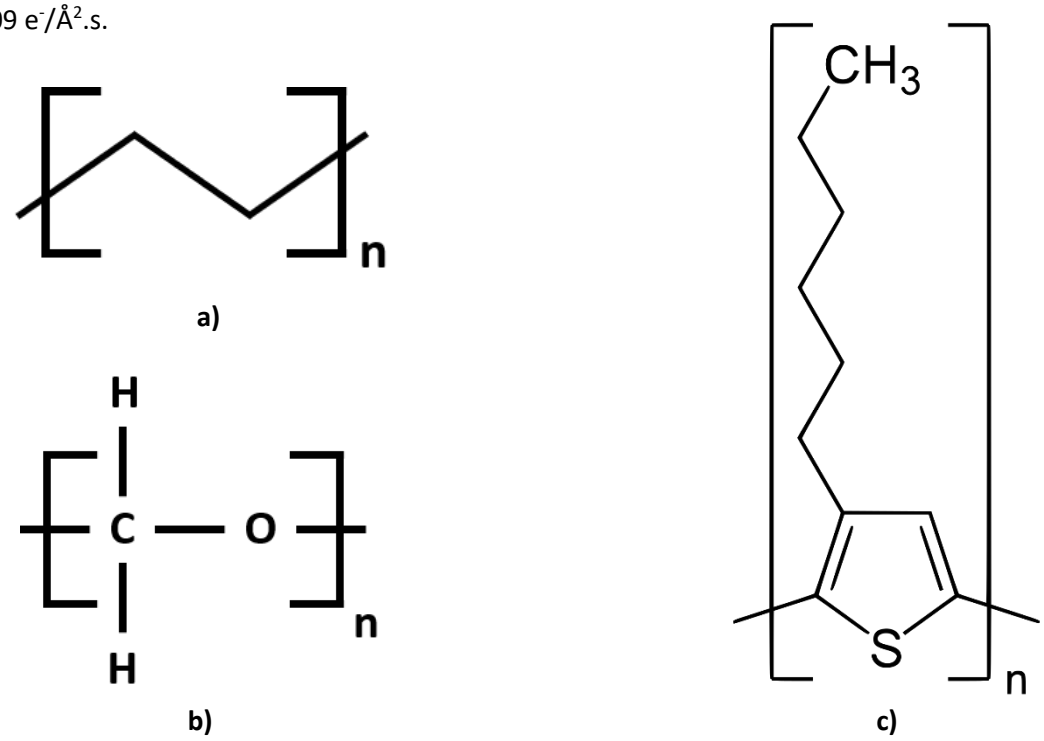

Figure 1.19: *Molecular structures of 3 polymers; a) polyethylene (PE), b) polyoxymethylene (POM) and c) poly(3-hexylthiophène) (P3HT)*

More examples of cross-linking compounds are diacetylene polymers polyTSHD and polyDCHD [119]. For both compounds, reflections fade without detectable mass loss. Fading is accompanied by a loss of

contrast and modifications to lattice spacing in TEM images. At room temperature, all spots fade at after a dose of 6.2 $e^-/Å^2$ for polyTSHD under a 100 kV beam. PolyDCHD side groups are more aromatic compared to polyTSHD, so its beam resistance is much higher as some reflections still remain even after 10000.0 $e^-/Å^2$. Similar to PE, positions of the reflections change as lattice spacing is altered, but without broadening. Some lattice spacings decrease as function of the electron dose for both compounds while others increase or remain stable. Changes in specific *d*-spacings are also observed for polymers poly(p-phenylene benzobisthiazole) (PBZT), poly(p-phenylene benzobisoxazole) (PBO) and poly(p-phenylene terephtalamide) (PPTA), the latter showcasing an increase in *d*-spacing along the main chain together with a decrease along the perpendicular direction, due to a perturbation of H-bonding among the adjacent chain molecules [118]. An interesting result is that for polyTSHD, different orientations of crystals give the same fading rates, while the damage rate is found to be orientation dependent for polyDCHD as much different D_c are measured for [110] and [122] zones, the latter containing some higher order reflections who persist under prolonged exposure even after the first-order reflections fade. This could be related to the stable carbazole groups from the aromatic side chain, who may cross-link with each other forming layers along this plane who remain stable under the beam.

Polyoxymethylene (POM) (**Figure 1.19b**), is a scission-type polymer where the Bragg spots remain sharp but fade out completely due to beam damage [116]. Damage is dominated by bond breakage in the main chain, and subsequent diffusion of radicals. An initial phase of slower fading at initial exposure exists [117], but is not well defined since departure from the subsequent exponential decay is small. POM lifetime is improved when using higher voltages [120]. Total diffraction intensity fades completely around 4.0 $e^-/Å^2$ at 300 kV and room temperature. Kobayashi & Sakaoku [116] give a higher value, but without a precise dose rate, the critical dose dependence upon which is not investigated. Scission leads to considerable mass loss, and from a thick crystal, only a thin residue remains after prolonged exposure [117], [120].
Poly(3-hexylthiophene) (P3HT) (**Figure 1.19c**), is a p-type semiconducting polymer which was studied for its beam-sensitivity [55]. The specimen was prepared as a heterojunction with phenyl-C61-butyric acid methyl ester (PCBM), an n-type semiconductor. The rings fade exponentially in a scission-like profile [121]. At room temperature with a dose rate of 1.0 $e^-/Å^2.s$, D_c is 10.0 $e^-/Å^2$ for a 200 kV beam. PffBT4T4-2OD has a lower critical dose under the same conditions. This is due to its branched side chains that undergo rapid rearrangement, disfavoring recombination over scission [122]. Rings from PCBM fade slower, this is attributed to PCBM particles being more amorphous to begin with. This contrasts with measurements on segmented poly ester urethanes (PESU), where better crystallized samples are seen to resist better [123].

4.3.2 Effect of Temperature

Lowering the temperature slows fading for PE, D_c being tripled at 77 K, with little further improvement below [117]. At low temperature, the increase to *a*-spacing in PE is seen to be smaller [73], while an initial decrease in *b*-spacing seen at high temperature is absent when the temperature is lowered. This might be related to rapid rotation and repacking of molecules due to intermolecular bond breakage, which is hindered at low temperature. Synchronous with fading, the evolution of the *a/b* ratio suggests a transition to a hexagonal phase, which however does not occur at low temperature. This could also explain initial intensity increases observed at room temperature [49], [117], which are otherwise attributed to specimen drift and reorientation. Broadening of the spots due to lattice distortion might also give the apparent impression of an initial increase [66].

Radical diffusion from the sidechains is reduced significantly at low temperature. Slower diffusion of ionized chain molecules at low temperature might disfavor the probability for cross-linking, preserving crystallinity. This is evidenced by measurements on poly-yne, a conjugated polymer containing transition metals As and Pt in its main chain, and butyl molecules in its side chains [124]. At 120 kV, D_c from all reflections is measured at 2.0 $e^-/Å^2$, while cooling with liquid nitrogen increases it to 30.0 $e^-/Å^2$. For P3HT, fading slows significantly at 80 K where a linear fit can be made. Both P3DT and PffBT4T4-2OD also show significant lifetime improvement at cryogenic temperature, and the relative lifetime differences are reduced.

4.3.3 Effect of Accelerating Voltage

For PE, D_c measured from all reflections increases from 5.6 – 6.1 $e^-/Å^2$ for 100 kV to 11.3 – 13.8 at 300 kV. Thomas et al. [120] found a higher critical dose at higher voltage for POM, but measurements conflict with other studies [116], [117].

4.3.4 Effect of Dose Rate

Radical diffusion from long P3HT sidechains can be outrun by using high dose rates [121], [122]. **Figure 1.20** shows how critical doses evolve as a function of the dose rate for 3 different polymers. Overall, critical doses increase for polymers with longer and more branched chains. This is due to a relatively slow diffusion of large side chain radicals broken from the main chain. Crystal lifetimes increase when the beam is blanked in-between exposures, showcasing the dominance of secondary reactions which go on without exposure. There exists however a certain dose rate threshold around 15.0 $e^-/Å^2.s$, above which local

heating speeds up diffusion, lowering the critical dose. At room temperature and 300 kV, D_e varies between 16.0-21.0 $e^-/Å^2$ for different dose rates (see **Table 1.3**). An even greater variation is seen at 80 K. For P3DDT, less improvement compared to P3HT is seen when increasing the dose rate. The higher ratio of alkanes over aromatics in the molecular structure leads to faster damage spread which is more difficult to overrun. For PffBT4T4-2O, dose rate effects are present at room temperature but are absent at low temperature, since the already slowed down damage process at low temperature may render dose rate effects obsolete. Dose rate effects are also observed for PCBM, with D_e varying between 265.0-412.0 $e^-/Å^2$ at 200 kV and room temperature as a function of the dose rate.

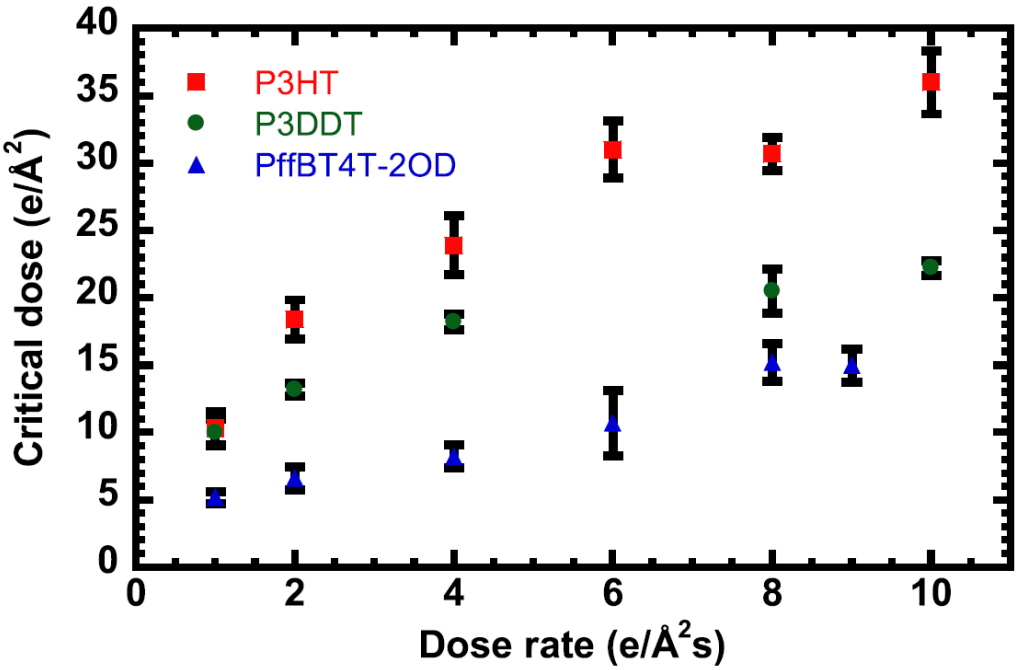

Figure 1.20: *Critical doses as a function of dose rate for P3HT, P3DDT, and PffBT4T-2OD at 200 kV and room temperature. Reproduced from* [122]*. Copyright: Macromolecules, American Chemical Society.*

4.3.5 Effect of Sample Preparation

Sample preparation of P3HT has an impact on the fading rate; dry samples prepared without water and oxygen contamination resist much better at 80 K compared to wet samples, while no difference is seen at room temperature. **Figure 1.21** shows diffraction fading measurements for two different sample preparation techniques at different temperatures. This is related to the trapped water and oxygen molecules in the wet specimen. At room temperature, these molecules will diffuse out of the sample due to the TEM vacuum, whereas they will be trapped at 80 K and will accelerate the damage, water molecules being especially prone to radiolysis producing various excitation products (see Section 2.1). The effect of

specimen preparation has less of an effect on PCBM, since it is more hydrophobic. The effect of sample preparation has also been evidenced on hard-segmented homopolymers (HSH), where specimen films crystallized at different temperatures fade at different rates [123].

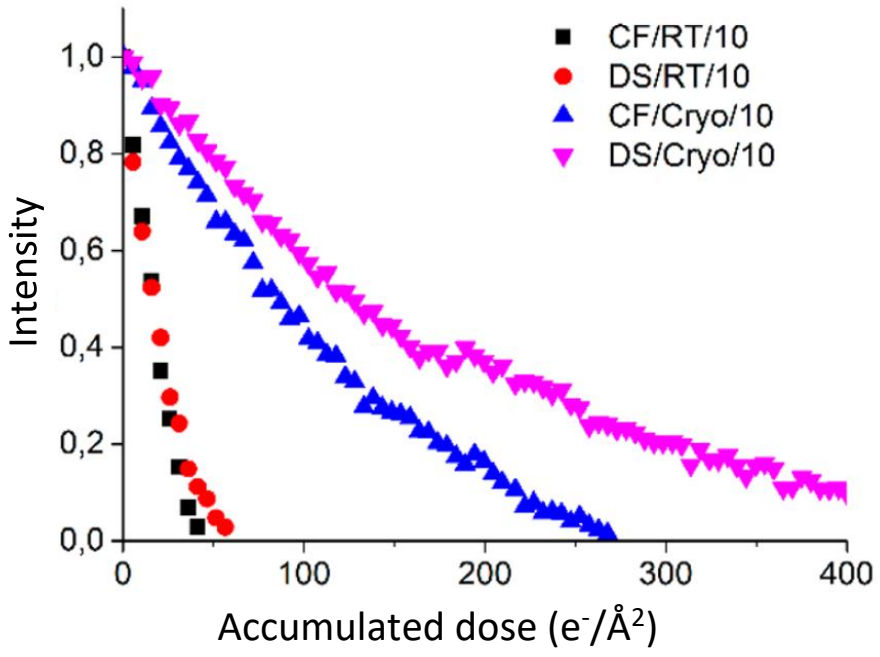

Figure 1.21: *Diffraction fading for P3HT showing the effect of sample preparation at room temperature and at 80 K (cryo). CF refers to conventional sample preparation while DS refers to direct spin-coating. The dose rate was 10 $e^-/Å^2s$ for all experiments. Reproduced from* [55]*. Copyright: Journal of Physical Chemistry A, American Chemical Society.*

Alternatively, the secondary reactions can be hindered at room temperature by adding antioxidant radical scavengers such as BHT and TEMPO [125]. This technique also applies to PffBT4T4-2OD and P3DDT, although the latter to a lesser extent since the higher fraction of side chains over the main chain generates too many reactive species to scavenge.

Table 1.3 summerizes critical dose measurements made on polymers. Since the measurements depend on various parameters, only measurements that are inter-comparable are presented. Compared to other types of organic compounds, an increased variety in terms of beam-sensitivity can be seen.

Table 1.3: *Critical doses of polymers measured by diffraction fading in $e^-/Å^2$. Unless otherwise specified, results presented here correspond to measurements made on all reflections, at room temperature and using the 1/e criterion. For the column showcasing higher voltage measurements, data from the highest available voltage was chosen. If a specific reflection was used, the corresponding lattice spacing is given in parenthesis with the smallest available lattice spacing chosen. D_c refers to the use of complete fading instead. Measurements at low temperature are given in a separate column where the accelerating voltage is specified if it is different than 100 kV, with the lowest available temperature being chosen. Intervals given for some compounds are due to differences in dose rate, specimen preparation and thickness.*

Compound	100 kV	200 kV	300 kV or above	Low Temperature	Ref.
PE	5.6-6.1 (D_c)		11.3-13.8 (300 kV) (D_c)		[66], [116], [117]
P3HT		10.0	16.0-21.0 (300 kV)	108.0-188.0 (80 K) (300kV)	[55], [122]
POM	4.5 (D_c)	4.0-15.0 (D_c)	7.0 (D_c) (900kV)		[116], [117]
P3DDT		10.0-22.0			[122]
PffBT4T4-2OD		5.0-10.0			[122]
PCBM		265.0-412.0		596.0 (200kV) (80 K)	[122]
PEEK	28.0 (4.7Å, 3.9Å)				[118]
PPTA	281.0 (4.3Å, 3.9Å, 2.2Å)				[118]
ABPBI	406.0 (3.5Å)				[118]
ABPBO	81.0 (3.4Å)				[118]
PBO	100.0 (3.5Å, 5.5Å)				[118]
PBZT	875.0 (3.5Å, 5.8 Å, 12.5 Å)				[118]
poly-yne				30.0 (77 K) (D_c)	[124]

4.3 Inorganics and Hybrids

Compared to organic compounds, there is significantly less literature available on the use of diffraction fading on inorganic compounds. This is due to their relative stability under the beam compared to organic compounds. However, some inorganic compounds can still be subject to beam damage leading to crystallinity loss, especially those containing organic moieties inside their structure, referred to as hybrid compounds. The mechanisms of crystallinity loss on inorganics is presented followed by the effects of temperature, accelerating voltage and the dose rate.

4.4.1 Mechanism of crystallinity loss

Inorganic compounds are generally less prone to beam damage compared to organic compounds. This is due to often better conducting (or semiconducting) properties of inorganic compounds inhibiting ionization damage by rapidly filling holes left by excitation, similar to aromatics. They may suffer from knock-on damage, but this process is so ineffective compared to radiolysis that if crystallinity loss occurs due to knock-on damage, the critical dose is orders of magnitude higher than what is necessary for

radiolysis [126]. Some inorganic hybrid compounds may suffer from radiolysis due to the presence of organic moieties, and porous materials such as zeolites are known to be beam-sensitive due to the pores inside the structure facilitating diffusion and structural collapse, metal organic frameworks (MOFs) meanwhile potentially suffer from both radiolysis due to organic linkers and knock-on damage due to atoms near pores having lower displacement energy thresholds [12].

$CaCO_3$ (calcite) is an example of a compound suffering knock-on damage only. Under 200 kV electron exposure, it remains stable until $3.9*10^4$ $e^-/Å^2$ where calcium oxide rings start to appear [126]. Loss of O and C is confirmed by EDX data. At doses above 10^8 $e^-/Å^2$, a complete transformation into calcium oxide occurs.

ZIF-8 (cubic *I-43m*, *a* = 16.9856(16) Å*)* [127] is a beam-sensitive MOF. At room temperature and 300 kV, crystallinity loss starts at 25 $e^-/Å^2$ leading to complete amorphization at 50.0-70.0 $e^-/Å^2$ [128], [129]. Diffraction fading data on MOF ZIF-L shows a pronounced loss of intensity at 25.0 $e^-/Å^2$ with a 200 kV beam [129]. The brightest 020 spot fades by 100.0 $e^-/Å^2$. Damage leads to structural rearrangement and pore collapse as shifts in reflection positions reveal 2.5% and 5% decreases to *b* and *c* axis lengths respectively. Broad, amorphous-like peaks appear under exposure, with spacings corresponding to Zn-Zn distances. Short-range order of the parent structure is therefore retained.

$CH_3NH_3PbI_3$ ($MAPbI_3$) (tetragonal *I4/mcm*, *a* = 8.8776(7) Å and *c* = 12.6702(8) Å*)* [130] is a hybrid perovskite known to be beam-sensitive. D_e at room temperature is measured at 12.0 $e^-/Å^2$ [128] with a 200 kV beam through Fourier amplitudes of TEM images. Irradiation at room temperature initially shows a phase transition into a superstructure by 35.0 $e^-/Å^2$ revealed by diffraction fading data collected on the [001] direction [131]. This could be governed by octahedral tilts and rotations as the organic molecule in the A site gets damaged [132]. This is also evidenced by decreases in 002 and 110 plane spacing as a function of the dose, triggered by the loss of organic moieties around the PbI_6 octahedra. The destruction of the structure is illustrated in **Figure 22**.

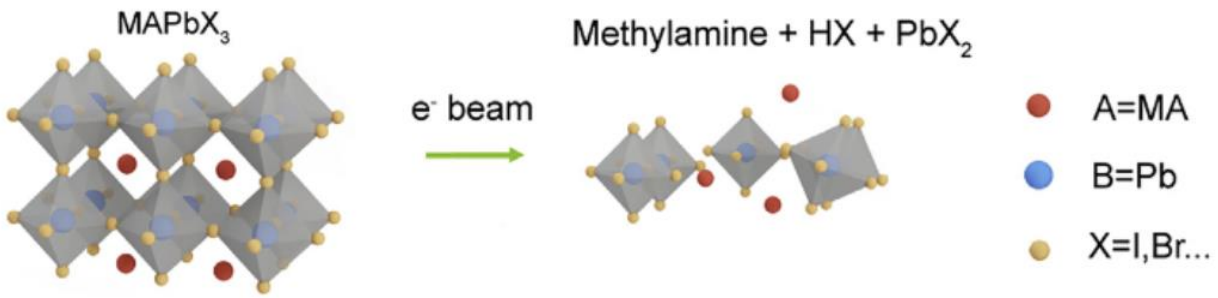

Figure 1.22: *Decomposition of hybrid perovskites under the electron beam. The PbX_6 octahedra stay intact while the organic molecules at the A-site are damaged* [128]*. Copyright: Joule, Cell Press.*

Eventually complete amorphization occurs at 475.0 $e^-/Å^2$ by transformation into PbI_2. The dose for superstructure generation is 10 times faster when the [001] direction is irradiated, compared to [100]. This is possibly due to a smaller migration barrier for I atoms on the [001] surface. Stability is improved when I is replaced by Br [131]. **Figure 1.23** shows the comparison of amplitude loss from both compounds. Rothmann *et al.* [132] observed that irradiation destroyed intrinsic twinning initially present in the specimen.

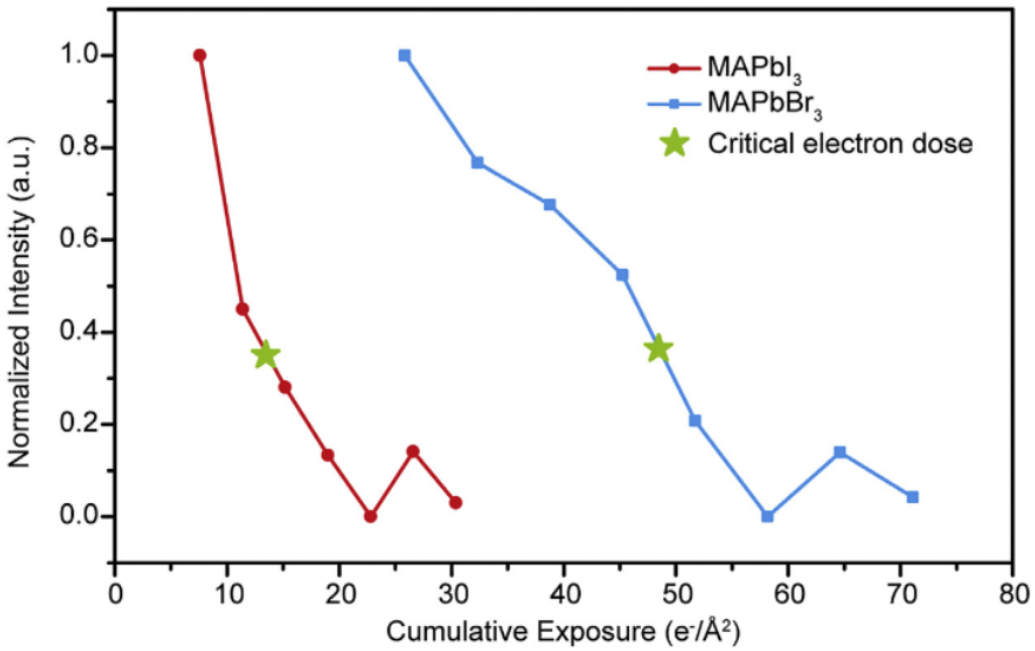

Figure 23: *Diffraction fading curves of two hybrid perovskites with different halogens on the X site. Amplitudes from Fourier transforms of TEM images are used to monitor beam damage, as opposed to diffraction fading. Reproduced from* [128]*. Copyright: Joule, Cell Press.*

The alloy $Al_{62}Cu_{20}Co_{15}Si_3$ also transforms from a quasi-crystal into a crystal under the beam [133]. This is due to the knock-on displacement of an atom being large enough to bring it into an equilibrium position.

Diffraction intensities from $Al_{62}Cu_{20}Co_{15}Si_3$ vary unpredictably under exposure, with latent doses, increases and broadening being observed depending on the reflection. A diffuse halo ring is eventually observed which gets more intense with accumulated dose.

The minerals albite $NaAlSi_3O_8$ and natrolite $Na_2(Al_2Si_3O_{10})\cdot 2H_2O$ are examples of pure inorganic compounds suffering radiolysis damage due to the presence of covalent bonds [134]. **Figure 1.24** shows diffraction fading from albite as an example. Loss of crystallinity visible on the figure is dominated by Si-O bond breakage which generates local defects. Generation of defects can either lead to diffusion or recombination, for instance through Si-O-O-Si peroxy cross-linkage.

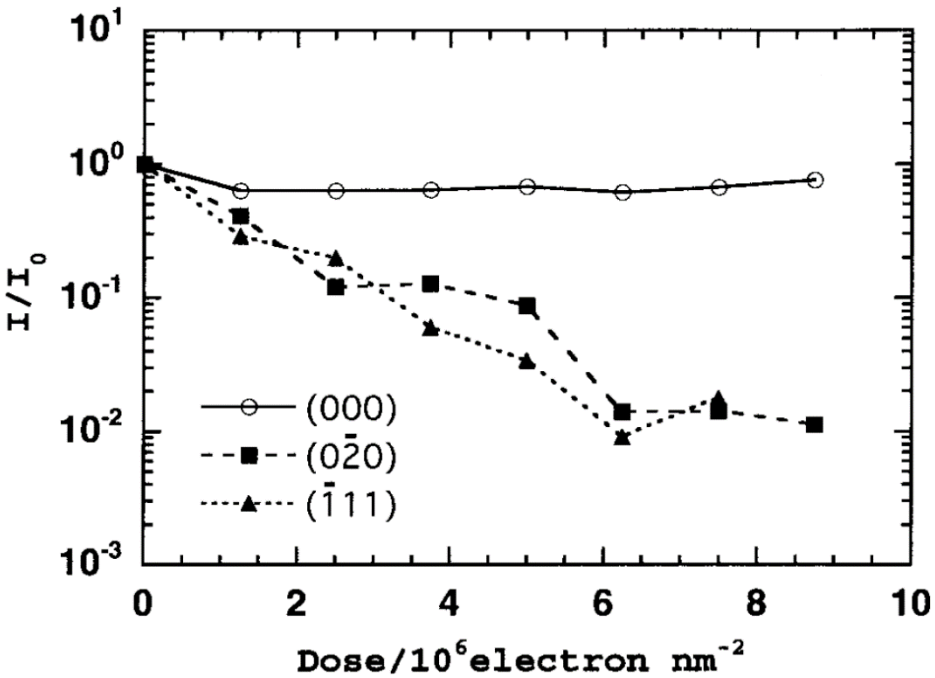

Figure 1.24: *Diffraction fading curves of 2 reflections from albite. The direct beam intensity is also drawn (000). The The electron dose is given in 10^6e-/ Å^2. Reproduced from* [134]. *Copyright: Microscopy, Oxford University Press.*

Fullerenes C60 and C70 also suffer molecular damage as evidenced by EELS data [135], with outer diffraction spots becoming more diffuse and inner-spots beginning to disappear due to changes to sizes of the molecules.

Hydrated minerals are known to be beam-sensitive due to the presence of water inside their structure. The mineral ettringrite $Ca_6Al_2(SO_4)_3(OH)_{12}\cdot 26H_2O$ (trigonal *P31c*, *a* = 11.234 Å, and *c* = 21.501 Å) dehydrates under exposure, which leads to diffraction fading [136] along with contractions of *a* and *c* axis lengths. Formation of domains with different water content leads to appearance of extra incommensurate spots along the ***a*** direction. Dehydration is observed to be step-wise, as isolated water molecules being lost first

followed by apical counterparts. In carbonate ettringrite where sulfate groups are replaced by carbonates, a slower fade is observed but the *c* axis length is reduced to half of its initial length, indicating that dehydration still occurs. Calcium silica hydrates on the other hand resist the beam much longer, with diffraction fade starting at $8.0*10^3$ $e^-/Å^2$ and $2.4*10^3$ $e^-/Å^2$ for ribbon-type and fibrous phases respectively [137].

In thaumasite $\underline{Ca}_3\underline{Si}(O\underline{H})_6(\underline{CO}_3)(\underline{S}O_4)\cdot 12\underline{H}_2\underline{O}$, which has a very similar crystal structure to ettringrite, fading occurs with no changes to crystal symmetry, indicating no dehydration occurs. This is possibly due to stronger H bonding compared to ettringrite.

4.4.2 Effect of Temperature

Measurements at low temperature on minerals albite and natrolite show that while damage is reduced at low temperature for albite, it is actually enhanced for natrolite [134]. Despite having a similar chemical composition to albite, natrolite contains water molecules in its structure. It is possible that natrolite breaks down more easily due to the water molecules, and enhancement of damage could be due to a prevention of recombination of defects at low temperature, due to reduced defect diffusion.

Another example of damage enhancement at low temperature is the hybrid perovskite $MAPbI_3$. Irradiation at 90 K reveals that the transition to a superstructure occurs below 30.0 $e^-/Å^2$ down from 35.0 $e^-/Å^2$ at room temperature, and the dose necessary for complete amorphization is more than 3 times smaller [131]. Similarly to natrolite, this is explained in terms of inability of defects and vacancies to move and recombine. Rothmann *et al.* [132] also observed no protection effects at low temperature on $MAPbI_3$. Similar results are observed on a natural zeolite thomsonite, who fades 16 times faster at 21 K compared to room temperature [138], due to the inability of broken bonds to recover, following water loss. This is plotted in **Figure 1.25**, where the clear decrease in critical dose at lower temperature is visible. This measurement was made at two different accelerating voltages, which has more impact on the critical voltage at room temperature compared to low temperature.

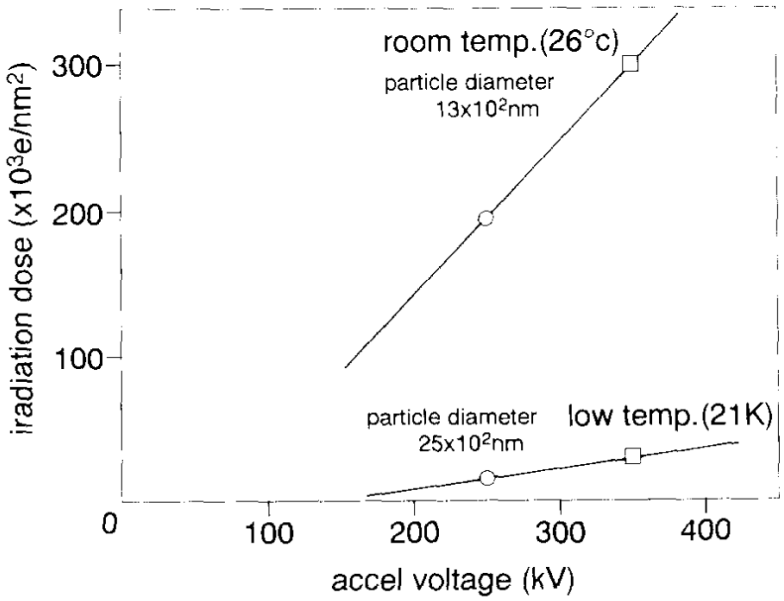

Figure 1.25: *Dependence of critical dose on temperature and accelerating voltage, measured on thomsonite. The electron dose is given in 10^3e-/ nm^2. The diameters of the spherical particles is given for each experiment. Reproduced from* [136].

Copyright: Ultramicroscopy, Elsevier.

Irradiation of silicon carbide (SiC) with a 2 MeV beam at different temperatures reveals that while the dose for amorphization is constant below 250 K, it decreases with temperature until 340 K, above which no amorphization occurs [139].

In contrast, calcium silica hydrates resist better at low temperature, the dose for initiation of fade improving up to 16 times at 100 K compared to room temperature [137]. An improvement is also observed for the MOF ZIF-8, who undergoes only partial crystallinity loss at 90.0 $e^-/Å^2$ [129] compared to complete amorphization below 70.0 $e^-/Å^2$ at room temperature [129].

4.4.3 Effect of Accelerating Voltage

Damage to both albite and natrolite is reduced at 400 kV compared to 300 kV, which proves that radiolysis is the dominant damage mechanism due to covalent bonding in these compounds [134]. Similar results are observed on calcite, where the dose for crystallinity loss initiation is 1.6 times higher at 300 kV compared to 80 kV [126], [140]. For $MAPbI_3$, the dose for superstructure generation is 2-3 times higher at 300 kV compared to 200 kV [131]. Stability is also improved at higher voltage for ZIF-L and thomsonite [138], [141].

4.4.4 Effect of Dose Rate

Although no dose rate effects have been observed in a majority of diffraction fading experiments to inorganics, there is some evidence of dose beam effects using pulsed beams. Damage to $MAPbI_3$ is

reduced when a pulsed beam is used [142]**.** Measurements on reflections with lattice spacing smaller than 6.3 Å with a 200 kV beam show that after an irradiation of 10 $e^-/Å^2$, there is a 19.2% loss of intensity when a pulsed beam is used, compared to 23.2% with a continous beam. Zhu *et al.* [132] also observed faster disappearance of reflections when a very high dose rate was used. Irradiation of double metal cyanides also reveals significant increases to critical doses using very low dose rates [143].

Table 1.4 contains critical doses measured on some inorganic compounds, with much less data available compared to organics. Comparison of available data shows comparable resistance to aromatic organic compounds.

Table 1.4*: Critical doses of macromolecules measured by diffraction fading in $e^-/Å^2$. Unless otherwise specified, results presented here correspond to measurements made on all reflections, at room temperature and using the 1/e criterion. For the column showcasing higher voltage measurements, data from the highest available voltage was chosen. If a specific reflection was used, the corresponding lattice spacing is given in parenthesis with the smallest available lattice spacing chosen.* D_c *refers to the use of complete fading instead. Measurements at low temperature are given in a separate column where the accelerating voltage is specified if it is different than 100 kV, with the lowest available temperature being chosen. Intervals given for some compounds are due to differences in dose rate, specimen preparation and thickness.*

Compound	100 kV	200 kV	300 kV or above	Low Temperature	Ref.
ZIF-8			70.0 (300kV) (D_c)		[129]
$MAPbI_3$		12.0-46.0 (<2 Å)			[128]
$MAPbBr_3$				81 (200kV) (90 K)	[131]

5) Discussion

Diffraction fading data sheds light on the effects of beam damage to crystal structures. Although data can be complex to interpret and without explicit information on structural modifications, crucial information such as the lifetime of crystallinity and how the lifetime evolves under different conditions can be obtained. In contrast to other beam damage assessment methods, diffraction fading is sensitive to the rapid initial loss of short-range crystalline order, represented by preferential fading of high-resolution reflections. While measurements lack reproducibility due to errors in dose measurement, differing vacuum conditions, temperature variations, and most of all differences in individual crystal sizes/thicknesses, trends do however appear in diffraction fading measurements.

Influence of the specimen nature. Considering the chemical nature of the specimens, macromolecules and amino acids are the most sensitive, followed by long-chain aliphatics while aromatic molecules and inorganic structures can stay intact under exposure for a longer time. The initial loss of crystallinity occurs due to intermolecular bond breakage and repacking, affecting mainly high-resolution/short-range information. Macromolecules can lose short-range order faster than other compounds due to easier molecular repacking in large unit cells. This shows that crucial information can be lost at doses much lower than the measured D_c and D_e values and short-range crystalline order can be significantly disrupted prior to any measurable molecular damage.

Influence of the crystal thickness. Morphology of the crystals play a role in their ability to resist the beam. Thicker crystals are seen to maintain their diffraction intensities over a longer period, as protection factors from encapsulation vary at different crystal thicknesses. This is not due to an improved ability to resist the beam at higher thickness, but due to more undamaged diffracting regions remaining over time. This is evidenced by the fact that the reflection broadening rates are independent of thickness (ex: behenic acid), which is a direct measurement of the rate of crystallinity loss. Thicker crystals, however, might be better at dissipating electrostatic charging due to secondary electron production.

Influence of specimen preparation. Specimen preparation also influences the rate of crystallinity loss. Crystals resist better at low temperature when prepared in dry conditions, compared to a wet preparation [77],[55]. This is due to the trapping of water molecules. Hydration also plays a role, initial increases seen for hydrated crystals are absent for dehydrated crystals [107]. Hydrophobic compounds show less difference between the two preparation techniques.

Specimen environment can also play a significant role. When crystals are encapsulated with a thin carbon layer which prevents diffusion of radiolytic products, recombination reactions are promoted, and crystallinity lifetime increases. This has been evidenced on paraffin, Pc, perylene, and catalase crystals, and on coronene crystals with gold and aluminum layers. Different protection factors obtained for each compound relate to the diffusion rate of their common radiolytic products, which are often their peripheral atoms. Better protection can be obtained if layers containing halogens are used, which can reinforce vacant peripheral positions on specimen molecules. Similarly, antioxidants have been used as radical scavengers to increase lifetimes of some polymers. Protection factors often decrease with increasing crystal thickness but are independent of coating thickness. Embedding media (uranyl acetate, glucose) may also have an impact but has been less thoroughly investigated. A brief overview of specimen preparation for electron diffraction is given in **Appendix A**.

Influence of experimental conditions: temperature. Irradiation conditions have significant influence on the fading rate. It has been widely demonstrated that irradiating crystals at low temperature reduces beam damage, by reducing diffusion rates and favoring recombination by amplified cage effects. Thermal vibrations necessary to convert the absorbed energy into momentum for electronic excitations are reduced at low temperature, limiting radiolytic damage [10]. The probability of secondary reactions who have a large activation energy may also be reduced at low temperature [31]. Delayed fading of reflections often manifests as a latent dose effect at initial exposure, followed by slower fading. Eventually local concentration of ionized sites may become too high, which weakens the cage effect. Although fading is most often exponential, the slopes are temperature dependent. Cryo-protection factors on fading are specimen specific. **Figure 2.26** compares cryo-protection factors for different specimens at different temperatures. For some compounds such as paraffin, most protection is often achieved at roughly 80-100 K with little improvement below [48], [61]. In contrast, ovalene and crotoxin show significant improvement below 5 K. For many compounds, critical dose improves by 1.5-6.0 times in the 80-150 K region, compared to room temperature.

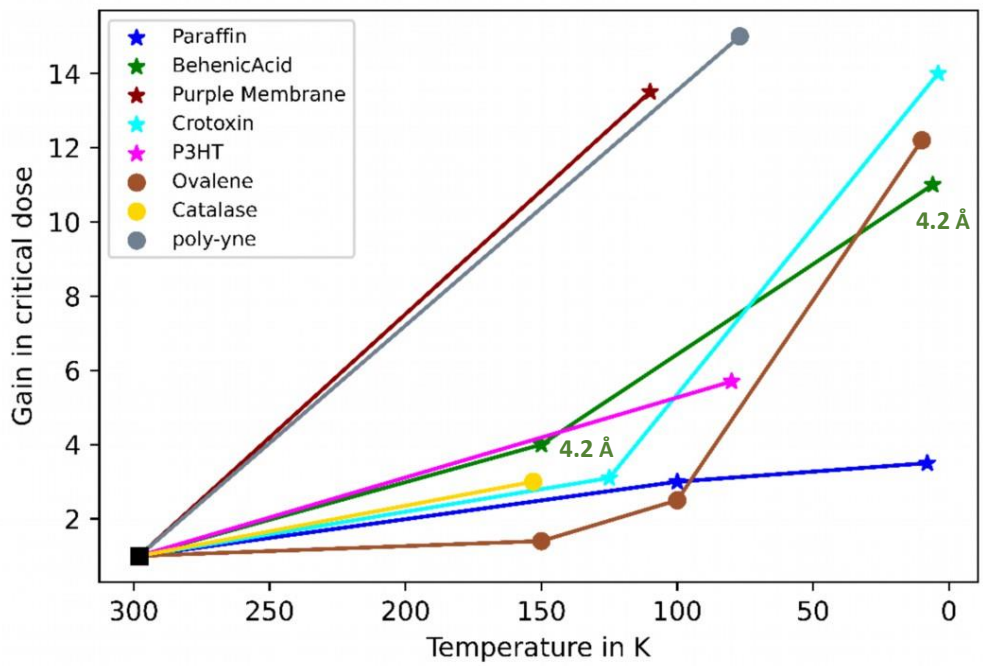

Figure 1.26: *Gains in critical dose for 8 different compounds as a function of temperature. The gain is defined as the critical dose measured at a given temperature divided by the dose at room temperature while all other parameters stay identical. Data points in shape of circles correspond to D_c values whereas those in shape of stars correspond to D_e. Unless otherwise specified, doses are measured on all reflections.*

Similarly, variation of protection factors among compounds might be related to the diffusion rates of radiolytic products, and how effective the trapping by the cage effect is. Overall, there are smaller differences among specimen lifetimes at lower temperature. This shows the dependence of damage kinetics on secondary diffusion processes, which are leveled out at low temperature. For scission type polymers, loss of crystallinity is dominated by secondary reactions caused by diffusing radicals from the long side chains, which is inhibited at low temperature.

However, even though crystal lifetimes are considerably improved, working at low temperature might not be optimal in some cases. Some specimens may transition into different phases when irradiated at low temperature, while specimen drift and reorientation can be amplified. This is helped by thermal contraction leading to stronger mechanical strains. Damage may also be amplified due to reduced conductivity of specimens at low temperature, especially if high dose rates are used. Trapping of radiolytic products via strong cage effects at low temperatures may also lead to a sudden chain reaction, damaging the structure.

Moreover, increased intensity fluctuations at low temperature were observed for thicker paraffin crystals, possibly due to increased specimen reorientation. The reduced surface to volume ratio at higher thickness might make encapsulation less effective, while reduced charging might already slow down radiolytic product diffusion, which in turn reduces the gain at low temperature. Latent dose effects are most often seen at low temperature, possibly due to an amplified cage effect favoring recombination reactions. The crystal structure can survive unchanged for a certain period before the concentration of broken bonds and radicals becomes high enough to bypass the cage effect.

Influence of experimental conditions: beam energy. If knock-on damage is dominant, adjusting the beam energy below the displacement threshold can reduce beam damage. If ionization however is the dominant damage mechanism, increasing the beam energy prolongs crystal lifetime, due to the decreased probability of inelastic scattering events at higher energies. This can be modelled with Bethe's formula for describing electron energy loss per unit length as a function of the incident, which agrees with diffraction fading data [49], [51], [91]. **Figure 1.27** shows gains in beam resistivity at different voltages normalized to a common reference, for different compounds.

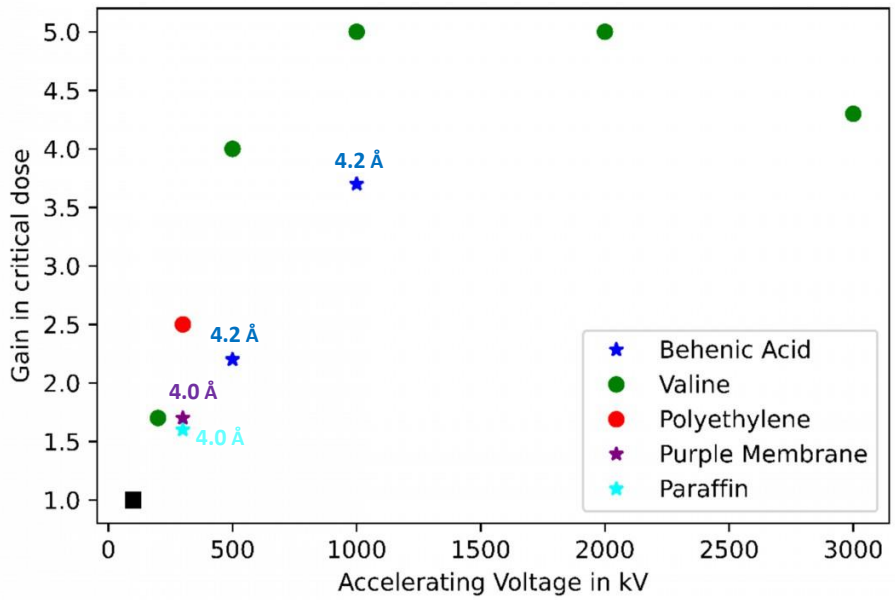

Figure 1.27: *Gains in critical dose for 5 organic compounds as a function of TEM accelerating voltage. The gain is defined as the critical dose measured at a given accelerating voltage divided by the dose at 100 kV while all other parameters stay the same. Data for behenic acid is normalised to 114 kV instead of 100 kV. Data points in shape of circles correspond to D_c. values whereas those in shape of stars correspond to D_e. Unless otherwise specified, doses are measured on all reflections.*

Working at high voltage might not always be benificial to maximise the SNR. Experiments on paraffin and purple membrane show that going from 100 kV to 300 kV, the inelastic scattering cross-section decreases by 1.57, while the elastic scattering cross-section decreases 2 times [33]. Higher loss of useful information at high voltage is masked in diffraction fading experiments since the intensities are always normalised to the initial intensity value. Working with very low beam energies reveals a threshold effect possibly related to the 285 eV carbon K-shell edge [13], [43], although this is not supported by X-ray absorption data [144].

Influence of dose rate. Rate of crystallinity loss can be dose rate dependent due to the specific timing of damage and healing events. Electrostatic charging, which is generated through release of secondary electrons, is dose-rate dependent [12]. Low dose rates can benefit charge and heat dissipation generated by poor electrical and thermal conductivity, and a lower density of broken bonds at a given time may increase chances of recombination. In other cases, high dose rates can be used to outrun slow propagation of secondary damage processes due to limited diffusion. It is therefore possible that compounds show different dose rate dependence at different beam energies.

For some small molecule compounds and many macromolecules, no dose rate effects have been observed [43], [116], [145], [146]. This could be due to a majority of studies not covering a sufficiently large spectrum of dose rates, most of them probing damage until 10 $e^-/Å^2s$ and it is possible that all compounds are in essence dose rate dependent, but at very different dose rate magnitudes. For measuring diffraction fading, it is important that the dose rate stays uniform throughout the fading experiment.

Influence of considered reflection(s) and resolution. Figure 1.28 compares the critical dose for different compounds depending on the data resolution. As it is evident by the fact that high-resolution reflections fade faster, critical dose measurements depend significantly on which reflections are being taken into account. For example in PE, although different reflection intensities fade irregularly, Friedel pairs follow the same curves, suggesting that differences among reflections are not random, but originate from specific rates of crystallinity loss at different spatial resolutions. However, the experimenter should be wary of artifacts related to dynamical scattering, specimen drift and reorientation (discussed below), molecular repacking modifying structure factors or simply errors in measurement (ex: hexabromobenzene, pentacene).

Most often, fading of reflections can be modelled as a monotonous exponential decay curve, from which specific thresholds of intensity or resolution loss can be measured. Fading of reflections corresponding to different resolutions can be separately analyzed in order to find the optimal dose to achieve a given data resolution. Instead of measuring curves from individual reflections, the diffraction pattern can be divided into resolution zones and fading of the sum of intensities inside each zone can be measured. It is often seen that the different fade curves from individual reflections eventually become similar at high dose. This could be the result of the initial short-range distribution of crystallinity loss being more anisotropic, which averages out as damage progresses. D_c is therefore more reproducible compared to D_e.

Figure 1.28 (next page): *Comparison of critical doses for different compounds and lattice spacings. For better comparison, only data measured at room temperature with a 100kV beam using the 1/e criterion are given. A log scale is used to compare dose values at different orders of magnitude on the same figure.*

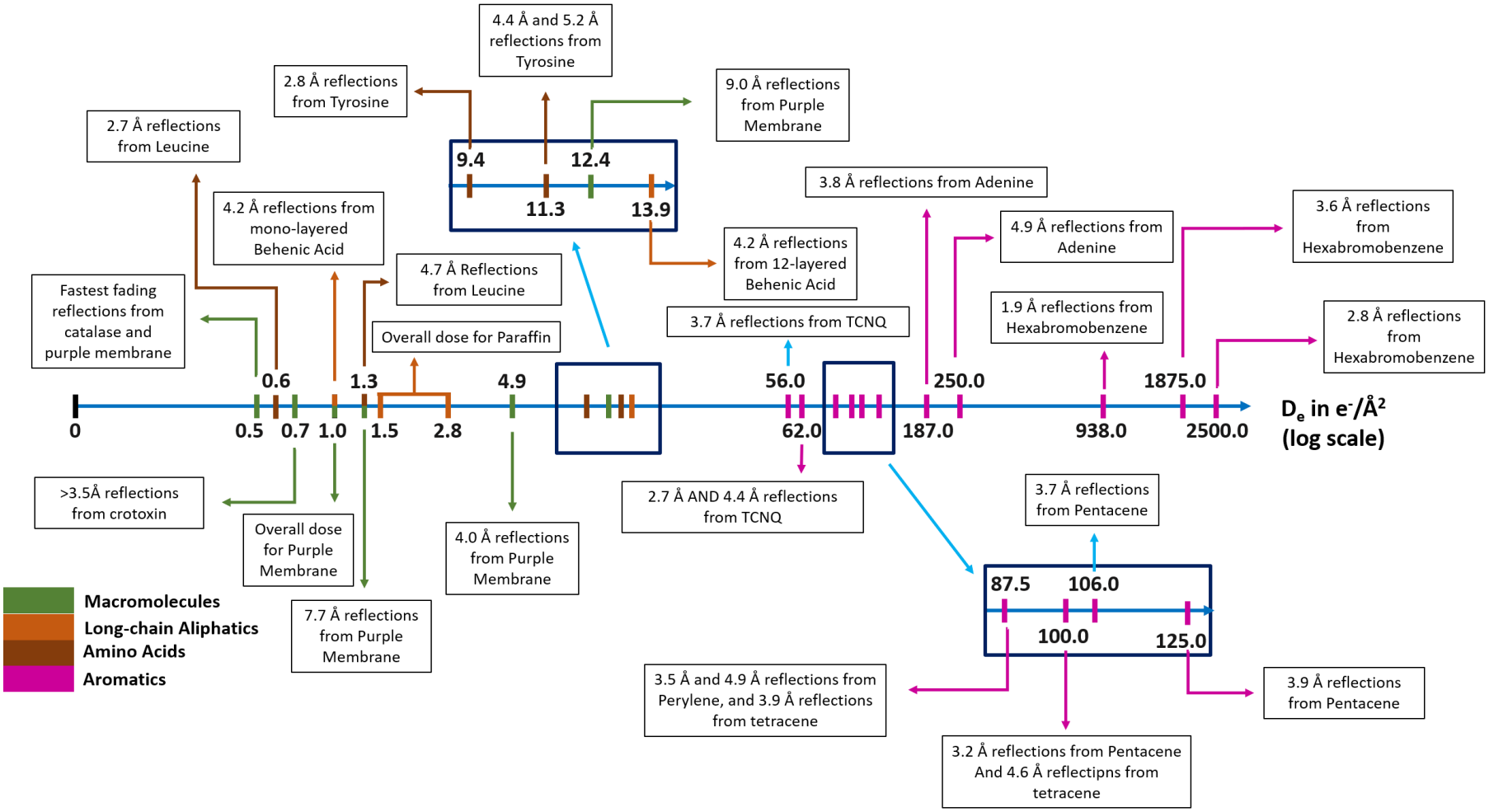
4.4 Å and 5.2 Å reflections from Tyrosine
2.8 Å reflections from Tyrosine
9.0 Å reflections from Purple Membrane
2.7 Å reflections from Leucine
9.4
12.4
11.3
13.9
3.8 Å reflections from Adenine
4.2 Å reflections from mono-layered Behenic Acid
4.9 Å reflections from Adenine
3.6 Å reflections from Hexabromobenzene
4.2 Å reflections from 12-layered Behenic Acid
4.7 Å Reflections from Leucine
Fastest fading reflections from catalase and purple membrane
1.9 Å reflections from Hexabromobenzene
3.7 Å reflections from TCNQ
2.8 Å reflections from Hexabromobenzene
Overall dose for Paraffin
0.6
1.3
4.9
56.0
250.0
1875.0
0
0.5
0.7
1.0
1.5
2.8
62.0
187.0
938.0
2500.0
D_e in $e^-/Å^2$ (log scale)
>3.5Å reflections from crotoxin
Overall dose for Purple Membrane
4.0 Å reflections from Purple Membrane
2.7 Å AND 4.4 Å reflections from TCNQ
3.7 Å reflections from Pentacene
87.5
106.0
100.0
125.0
Macromolecules
Long-chain Aliphatics
Amino Acids
Aromatics
7.7 Å reflections from Purple Membrane
3.5 Å and 4.9 Å reflections from Perylene, and 3.9 Å reflections from tetracene
3.9 Å reflections from Pentacene
3.2 Å reflections from Pentacene And 4.6 Å reflectipns from tetracene

Influence of initial effects (reorientation, flattening, repacking). Deviations from monotonous fading however make data interterpretation more difficult. Numerous measurements show evidence of initial increases in diffraction intensities, as well as latent dose effects where no change to diffraction intensity is observed for an initial period of exposure. For some specimens such as catalase and actin, brief increases in intensity of some specific reflections are also seen in later stages of illumination, as well as fluctuations.

In many cases, initial increases have been attributed to a reorientation of the specimen due to exposure, as bond breakage may result in a mechanical strain-induced movement of the particle. The reorientation can affect diffraction data and is known to occur predominantly during initial exposure [30], [147]. It can be amplified at low temperature where charge accumulation due to decreased electrical and thermal conductivity may induce movement on the grid. This can induce errors in damage measurement since the intensity evolution will not completely depend on beam damage. In this case, the dose for complete fading will be a more reliable indicator to characterize damage kinetics. Specimen flattening is also possible due to longitudinal motions along the chain directions provoked by the beam, which enables more areas of the crystal to become aligned to Bragg conditions [33], [75]. Using a thicker carbon film to mount the crystals reduces specimen movement by possibly providing a better structural support [148].

In some measurements (ex: paraffin n-tetratetracontane), the increase involves the total diffraction intensity as opposed to specific reflections, and the timing of the increase does not correlate with specimen drift. This behaviour could be due to molecular repacking: intermolecular bond breakage modifies the crystal plane occupancies and structure factors, possibly resulting in some crystal planes diffracting more intensely.

In order to explain initial intensity increases, Van Dyck &Wilkens [149] developed a fading model where damage within the unit cells was considered. Considering that atoms are displaced from their original positions due to the beam, a spatial distribution factor for individual atoms can be introduced to modulate their contribution to the structure factor, representing this displacement as a function of the dose. As atoms diffuse from their original positions, the destructive phase interference among some atoms may be removed, resulting in an initial increase before the atoms move so far away that the Bragg condition is lost and reflections fade. The spatial displacement can be considered as a one-hit collision, or a continuous Brownian displacement with each hit leading to a Gaussian around the initial position. This can affect the intensities as certain reflections might move farther or closer to the perfect Bragg condition

6) Conclusion

A significant amount of data on the rate of crystallinity loss is available in literature. Diffraction fading has been used for both assessment of beam-sensitivity of different compounds in a given irradiation setting, and for assessment of how beam-sensitivity evolves as certain irradiation conditions are altered. Critical doses have been defined for a more quantitative comparison of beam stability. However, evaluation of critical dose values can be quite complex, since for a given compound, the critical dose can depend on temperature, beam voltage, specimen preparation, dose rate, crystal size, lattice spacing of measured reflections, and the criterion chosen for the critical dose. In some cases, fading can be non-monotonous due to phenomena such as initial increases and latent dose effects.

Despite the complex dependency of critical dose values to various parameters, some clear trends have been established (sections 5):

- Beam stability is often improved at lower temperature, although the rate of improvement at a given temperature is specimen-specific.

- Beam stability also improves with increasing beam voltage, although the ratio of useful signal over damage might not actually improve.

- Preventing free radicals and ionised peripheral atoms from leaving the crystal also improves stability by favouring recombination, through encapsulation of crystals, vitrification or embedding in glucose. The gains in stability are also specimen-dependent.

- Thicker crystals tend to resist longer, as more unit cells in a given irradiation area require more electrons to destroy crystallinity.

- Bragg reflections representing smaller lattice spacing are more sensitive to short-range crystallinity loss, which occurs faster than long-range crystallinity loss due to fast repacking of molecules and peripheral atom loss.

- Fading rates of individual reflections can be affected by specimen reorientation, and modifications to structure factors.

- For a given measurement, the critical dose can be chosen as the dose necessary to initiate fading, to achieve complete amorphization or to reduce the intensity to 1/e of its initial value. The latter is arguably

the most objective choice, since detection of start of fading and complete amorphization can be less precise.

- The trends observed for dose rate effects are less clear, with some specimens resisting better at higher dose rate, some at lower dose rate and some showing no dose rate effects.

Ideally, the electron dose should be adjusted to a certain point where damage to data is avoided but a reasonable SNR is maintained to allow structure determination. This necessitates an understanding of how the impact of damage on the intensities affects structure determination. If, for instance, all reflections faded partially at the same rate with no changes to lattice spacing, structure determination would not be affected since relative intensities would be unchanged. If, however relative intensities are modified or high-resolution data completely fades, there would be consequences for structure determination.

For this thesis, interested in structure determination of sensitive materials using diffraction data, accurate intensity measurement is extremely important. Particularly, collection of data corresponding to small lattice spacings is necessary to reveal fine details in the structure. The criterion chosen for LD-EDT experiments was therefore the dose at which high-resolution reflections start to fade. Diffraction data collection in low dose conditions is described in the next chapter.

Chapter II: Electron Diffraction for Crystal Structures

The power of electron diffraction in the study of crystal structures resides on one hand in the strong electron-matter interactions within the sample, and on the other hand in the very small wavelength used for the incident radiation. The ratio of elastic to inelastic events is much higher compared to other techniques, which makes electrons suitable to investigate sensitive samples. This chapter first presents the advantages of these specific features in detail, then discusses the major technical developments of recent years, from the development of beam precession to data acquisition and processing methods.

1) Radiation-Matter Interaction – Advantages of Electrons

Crystal structures can be determined through diffraction experiments, where crystals elastically scatter probing beams. In order to determine atomic positions inside a crystal, a precision on the order of interatomic distances is required. This is in the order of 10^{-10} m. This can be achieved by X-rays, neutrons and electrons, whose wavelengths can be tuned to be in the same order or smaller than the interatomic distances. Neutrons react directly with atomic nuclei, being sensitive to isotopes and can be used to reveal magnetic structures since they possess a magnetic moment. Their high scattering cross section with lower atomic weight (Z) atoms also make them sensitive to hydrogen positions. However, neutron diffraction requires very large single crystals in the order of 0.1 mm^3 [150], and available neutron sources are limited compared to other types of radiation. X-rays and electrons are much more commonly used for structure determination due to their increased interaction with matter.

Instead of atomic nuclei, X-rays interact with atomic electrons surrounding them. The most commonly used Cu-K_α source produces X-rays with a wavelength of 1.54 Å. Since most atomic electrons are situated close to the nucleus, X-rays can give information on the positions of atoms as diffraction data can be used to map electron density inside which mean positions of atoms and molecules can be identified. X-ray diffraction can either be performed on a powder sample (PXRD) or on single crystals (SCXRD). SCXRD data can be used for accurate structure determination, but requires a certain minimal crystal size due to weak interaction of X-rays with matter [5]. Even with the latest generation synchrotron X-ray sources with high brilliance, the minimum crystal size necessary for SCXRD is still in the order of tens of µm [151], and much higher in typical laboratory X-ray diffractometers. PXRD can be performed on smaller crystals, down to tens of nm and can also allow reliable determination of unit cells as well as structure refinement. However, in cases of low symmetry and large unit cell parameters, PXRD suffers from peak overlaps, in addition to peak broadening as crystal sizes get smaller. Furthermore, if multiple crystal phases are present in a mixture, it becomes extremely difficult to discern which reflections are from which phase.

Unlike neutrons and X-rays, electrons are charged particles and interact with the electrostatic potential inside the crystal through Coulomb forces. The electrostatic potential is generated by positively charged nuclei and negatively charged atomic electrons. The negative charges partially shield the positive charges concentrated in the small nuclei since atomic electrons are in close proximity. The positive potential of the atoms therefore appear as sharp peaks over a low background in the electrostatic potential map [152].

For many specimens, such as porous metal organic frameworks (MOFs), covalent organic frameworks (COFs) or zeolites, it can be difficult to obtain crystals with sufficient size for SCXRD, and their often-complex structures are unsuitable for PXRD. For other compounds such as naturally occurring hydrated minerals, it might not be possible to separate multiple phases in a powder. In these cases, electron diffraction can be used for accurate structure determination.

Furthermore, gathering data from smaller crystals can be advantageous since smaller crystals show less mosaicity and twinning, and multiple crystal phases can clearly be distinguished, in contrast to PXRD. Electrons also have a higher elastic to inelastic scattering ratio compared to X-rays and neutrons [5]. For specimens sensitive to the electron beam who might get damaged due to inelastic scattering and absorption, more useful signal per damage event can therefore be acquired by electrons. Electron scattering cross-sections increase less steeply as a function of *Z* compared to X-rays, so light elements such as hydrogen next to heavier atoms can be detected more easily. Another advantage of electrons is that crystallographic phase information can be directly measured from electron micrographs, although this aspect is not often taken advantage of in modern electron diffraction methods.

With typical accelerating voltages of 100 to 400 kV in a transmission electron microscope (TEM), the electrons wavelength is between 0.016-0.037 Å, much smaller than typical X-rays. This allows to reveal atomic-scale details inside a crystal. The advantage of using electrons as probe is that structural information can be obtained from areas as small as few tens of nanometers. Moreover, scattering cross-sections of electrons with matter are much higher than X-rays and neutrons [5], leading to a mean-free path in the order of nanometers. This means that meaningful diffraction data can be gathered from crystals 2-3 order of magnitude smaller than those suitable for X-ray diffraction (**Figure 2.1**).

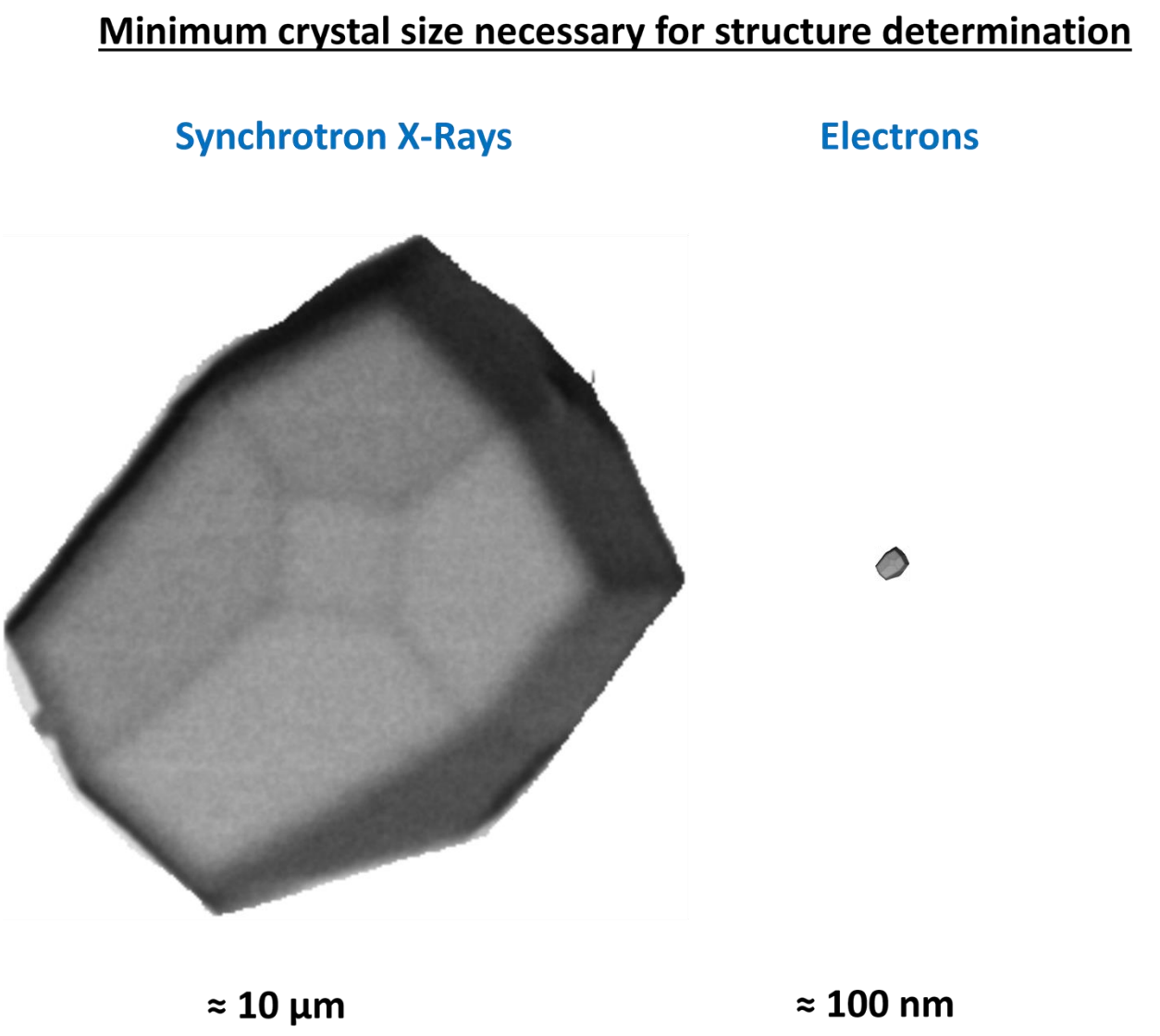

Figure 2.1: *Comparison of minimum typical crystal sizes necessary for crystal structure determination using synchrotron X-rays and electrons. Electrons can gather data from crystals 3 orders of magnitude smaller than X-rays, thanks to their larger elastic cross-section with matter.*

2) Features of Electron Diffraction in a Transmission Electron Microscope (TEM)

A typical TEM possesses an electron gun which generates an electron beam at a specific energy, a condensing system made of lenses and apertures to guide the beam in terms of beam size and coherency, and an image-forming system which focuses the beam onto the specimen stage, as well as intermediate

and projector lenses to refocus the beam after it goes through the specimen into either an image or a diffraction pattern. **Figure 2.2** shows a schematic view of imaging and diffraction modes in a TEM.

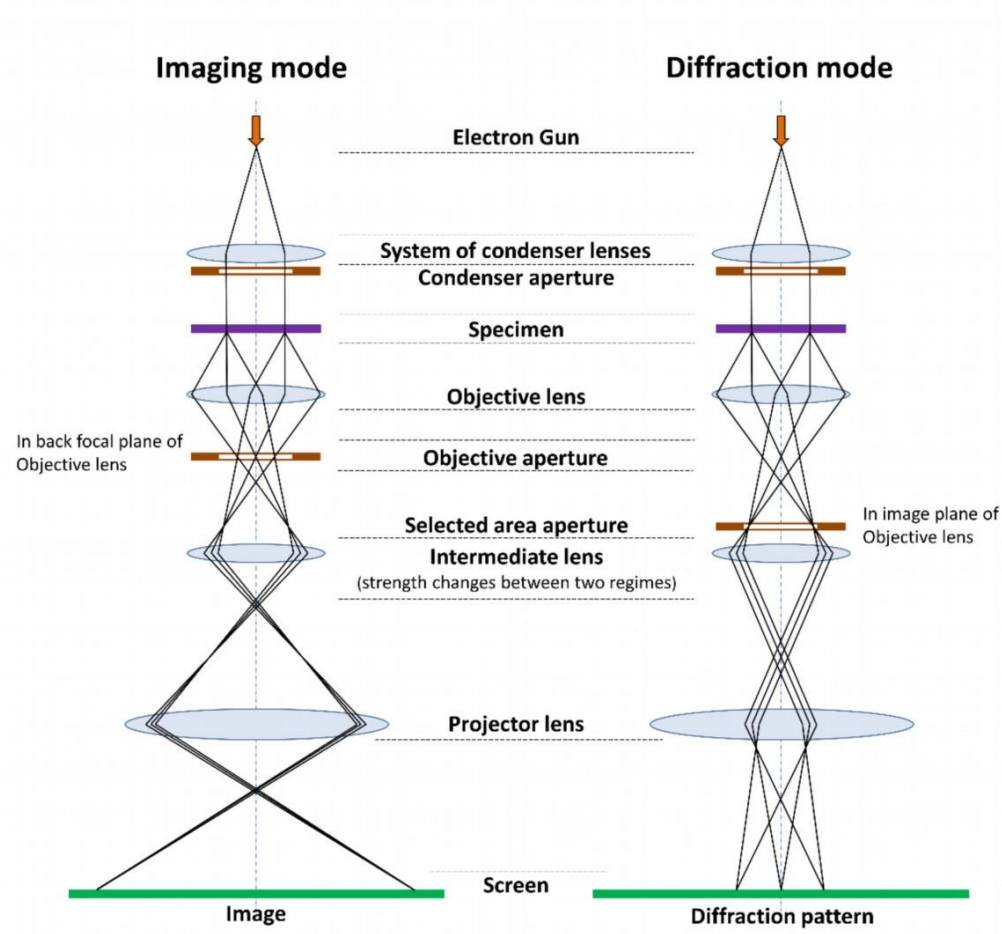

Figure 2.2: *Simplified illustration of TEM optics for image formation (left) and diffraction pattern formation (right). The lenses guiding the electrons consist of magnetic fields. Reproduced from Wikipedia.*

In the case of an image, all electrons diffracted from the same point in a crystal will be focused on the same position on the detector, while for a diffraction pattern all electrons diffracted at a same angle will be focused on the same point.

The structure of a crystalline material is characterized by the types and positions of atoms inside the crystal, which constitute an ordered pattern. This pattern can be characterized by a regular repetition of a motif in three dimensions. The unit cell of a crystal is characterized by the 3 basis vectors defining the lattice directions and periodicity, as well as the angles between them. On an electron diffraction pattern, the relative positions of diffracted beams are directly related to the crystal symmetry. How the angle of a reflection is related to the crystal structure can be described by Bragg's Law [153]. This law states that the

wavefronts of waves traveling through a crystal interfere with each other, leading to an anisotropic distribution of diffracted waves. The diffracted waves will only be observed in case of constructive interference, which is stated to occur when the difference in path travelled by two diffracted beams is equal to an integer number of wavelengths λ of the incident beam:

$$\boldsymbol{2d_k sin\theta = n\lambda}$$

Eq. 2.1

where d_k represents the distance in-between lattice planes diffracting the beam, θ is the angle between the incident beam and the crystal plane diffracting the beam, and *n* a positive integer representing multiple possible constructive interference conditions, referred to as the reflection order. In this model, the crystal is assimilated to a series of crystal planes containing atoms. The index **k** in d_k indicates a given crystal plane family containing planes with identical plane distances. On an electron diffraction pattern, each reflection corresponds to a beam diffracted by a crystal plane family, in specific directions determined by the crystal lattice. The value of d_k is the distance between the planes of the plane family. For a given λ, Bragg's Law for a crystal plane family will be satisfied for a specific θ, and a diffracted beam can be recorded. Since many different crystal plane families are present inside a crystal, each of them will satisfy Bragg's Law at different θs, for different orders of *n*. θ can be adjusted by tilting the crystal to record as many diffracted beams as possible, in form of diffraction patterns containing multiple diffracted beams at different orientations.

The diffraction geometry can also be described in reciprocal space by the Ewald sphere [154], which is a sphere drawn through the origin of the reciprocal lattice with a radius of 1/λ. In this case, the reciprocal lattice nodes that intersect with the sphere satisfy Bragg's condition for constructive interference. **Figure 2.3** illustrates how the Ewald's sphere is constructed for X-rays and for electrons. Due to the much smaller wavelength of the electrons, the radius of the sphere is considerably larger. The sphere can there be approximated as a flat plane.

In electron diffraction, due to the thin nature of the crystals, the reciprocal lattice nodes are not perfectly flat and are often elongated in shape of rods. This is also shown on **Figure 2.3**. It is therefore possible to record a reflection without being at the exact Bragg condition.

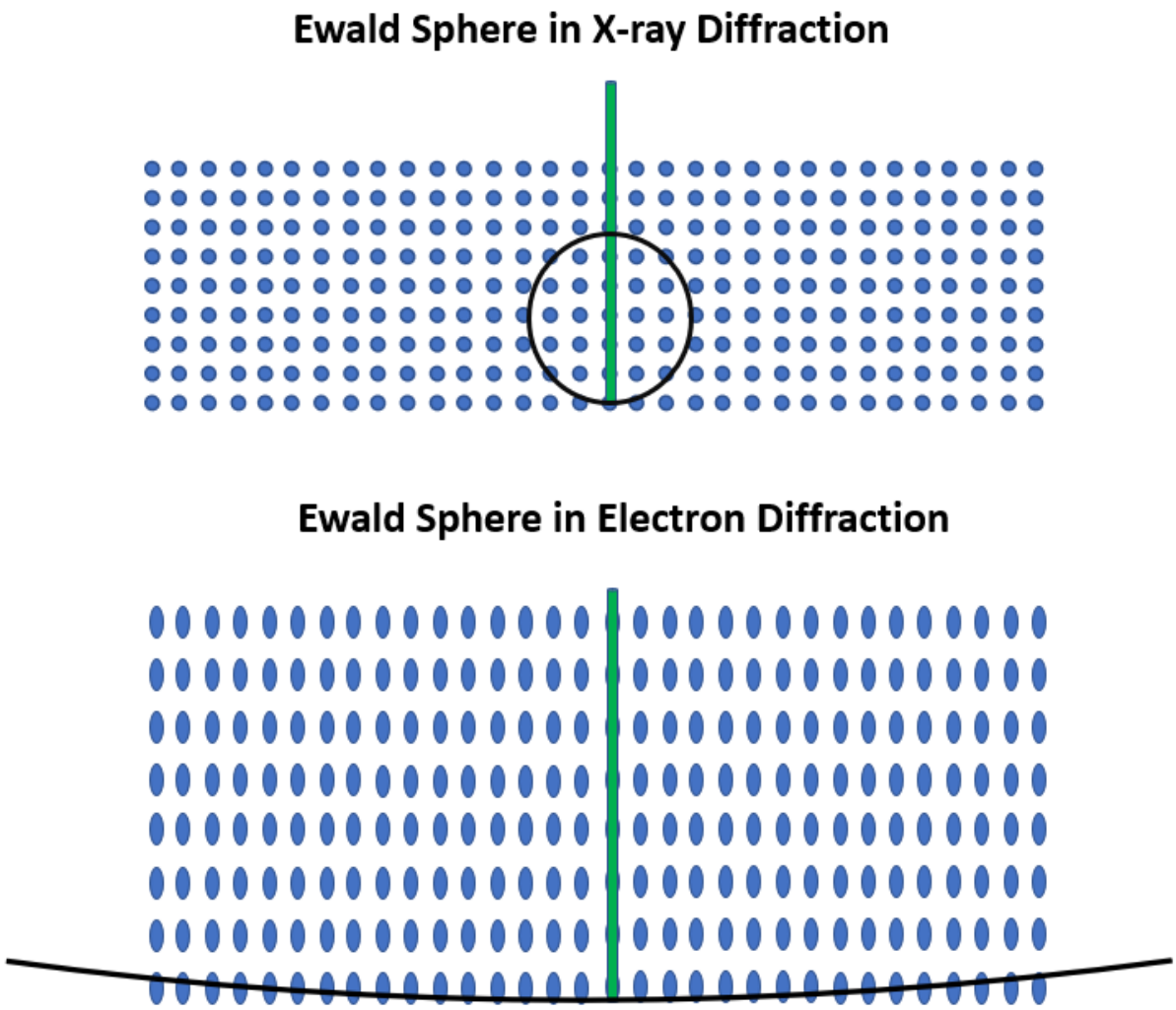

Figure 2.3: *Comparison of the Ewald sphere for X-rays and electrons. The blue dots and rods represent nodes in reciprocal space, while the X-rays and electron beams are represented in green. In the case of electrons, the Ewald sphere can be approximated into a flat line. The reflections are elongated in electron diffraction due to thin crystal thicknesses. As a result, it can be seen that more reflections satisfy the Bragg condition with electrons than with X-rays.*

On an electron diffraction pattern, the positions of the reflections can be measured to determine the unit cell since λ is known, and reflections can be indexed using unit cell. Knowledge of relative reflection positions is however not sufficient to determine where atoms are located inside the cell. This information lies within the relative intensities of the reflections.

When incident electrons pass through a crystalline specimen, they interact with the crystal potential generated by charged nuclei and electrons. If there are *N* atoms in the unit cell, the potential at a position **r** has the form:

$$\varphi(r) = \sum_{i=1}^{N} \varphi_i(\boldsymbol{r} - \boldsymbol{r}_i)$$

Eq. 2.2

In **Eq. 2.2**, φ_i represents the contribution of an atom located at $\mathbf{r}_i$, to the potential measured at **r**, with the potential expressed in Volts. The Fourier transform of $\varphi(\mathbf{r})$ gives the structure factor, defined as:

$$FT(\varphi(\boldsymbol{r})) \propto F(\boldsymbol{k}) = \sum_{i=1}^{N} f_i(\boldsymbol{k}) \mathrm{e}^{-2\pi \mathrm{j}(\mathbf{k}\boldsymbol{r}_i)}$$

Eq. 2.3

In **Eq. 2.3**, $f_i(\mathbf{k})$ is the atomic electron scattering vector of atom *i*, and **k** is a position vector in reciprocal space as a result of changing spaces through a Fourier transform. j is the imaginary unit. The right-hand side of **Eq. 2.3** therefore represents how atoms at different $\mathbf{r}_i$ contribute to a diffracted beam along **k** in reciprocal space. This contribution depends both on the chemical identity through $f_i(\mathbf{k})$ but also on the position $\mathbf{r}_i$ in relation to **k**. $F(\mathbf{k})$ is generally a complex number due to the exponential term, which can be expressed as:

$$F(\boldsymbol{k}) = |F(\boldsymbol{k})| e^{-j\phi(\boldsymbol{k})}$$

Eq. 2.4

$|F(\mathbf{k})|$ and $\phi(\boldsymbol{k})$ represent the amplitude and phase of $F(\mathbf{k})$, respectively. If each electron gets diffracted only once, each reflection on an electron diffraction pattern has a corresponding $F(\mathbf{k})$ where **k** defines the direction of the beam, and atoms on the crystal plane contribute to the signal depending on their identity and position. To determine the contents of the unit cell, the relative intensities of reflections should be analyzed. If $F(\mathbf{k})$ of all reflections from a crystal can be recorded, $\varphi(\mathbf{r})$ can be determined as its inverse Fourier transform. Since $\varphi(\mathbf{r})$ contains sharp peaks at atomic positions against a low background, atomic positions can be determined in form of a structure model.

However, $F(\mathbf{k})$ cannot be directly measured in a diffraction experiment. The intensities of the recorded reflections are related to the squares of the amplitudes of the structure factors. The phase however cannot be directly retrieved. If arbitrary phases are assigned to measured $|F(\mathbf{k})|$, this will lead to arbitrary

φ_i which do not necessarily represent the real crystal. This is referred to as the phase problem in crystallography. There is no general solution to the phase problem, but since the 1950s various partial solutions and case-by-case solutions have been widely developed to phase diffraction data [155].

Inside a crystal, the smallest part of a unit cell that can generate the whole cell through a set of symmetry operations is referred to as the asymmetric unit. In order to characterize the contents of the unit cell, the asymmetric unit and the set of symmetry operations generating the rest of the unit cell should also be determined. These can involve rotations, reflections, translations or inversions. A crystal containing many symmetry operations facilitates structure determination since a smaller set of atomic positions can be determined to characterize the whole crystal. The set of symmetry operations characterizing a crystal can be represented by its space group, of which 230 unique groups exist. The space group can be determined through analysis of extinct reflections on diffraction patterns. This is due to the presence of symmetry operations inducing constraints on the structure factors, which leads to some reflections to be systematically extinct. The extinctions present in the measured data can be analyzed by looking at specific 2D sections of the 3D intensity distribution and comparing observed extinctions with tabulated information on the space groups in the International Tables for Crystallography [156].

In summary, in order to characterize the atomic structure of a crystal, the unit cell, the space group and the positions of the atoms inside the unit cell have to be determined. The unit cell and the space group can be determined through the presence, relative positions of the reflections and relative symmetries between them, while the positions of the atoms can be determined through phasing of reflection intensities.

Diffraction using electrons dates back to 1920s [157], which was initially to confirm Louis De Broglie's hypothesis of all matter particles being capable of behaving as waves. First structures using electron diffraction were published in the 1930s [158], and since then various structures have been published based on zone-axis electron diffraction [159], [160], with crystallographic phases being retrieved by TEM images in some cases [161]. However, X-ray and neutron diffraction have historically been the methods of choice in crystallography [162], [163]. This is essentially due to the small mean free path of electrons, which causes them to be diffracted multiple times inside a crystal thicker than a few nanometers. Multiple crystal planes can therefore contribute to a reflection intensity on an electron diffraction pattern. This is referred to as dynamical diffraction.

Figure 2.4 illustrates the difference between the kinematical approximation (electrons being diffracted a single time only) and dynamical diffraction. It can be seen that the direct relationship between measured intensities and the crystal planes are lost in the dynamical case.

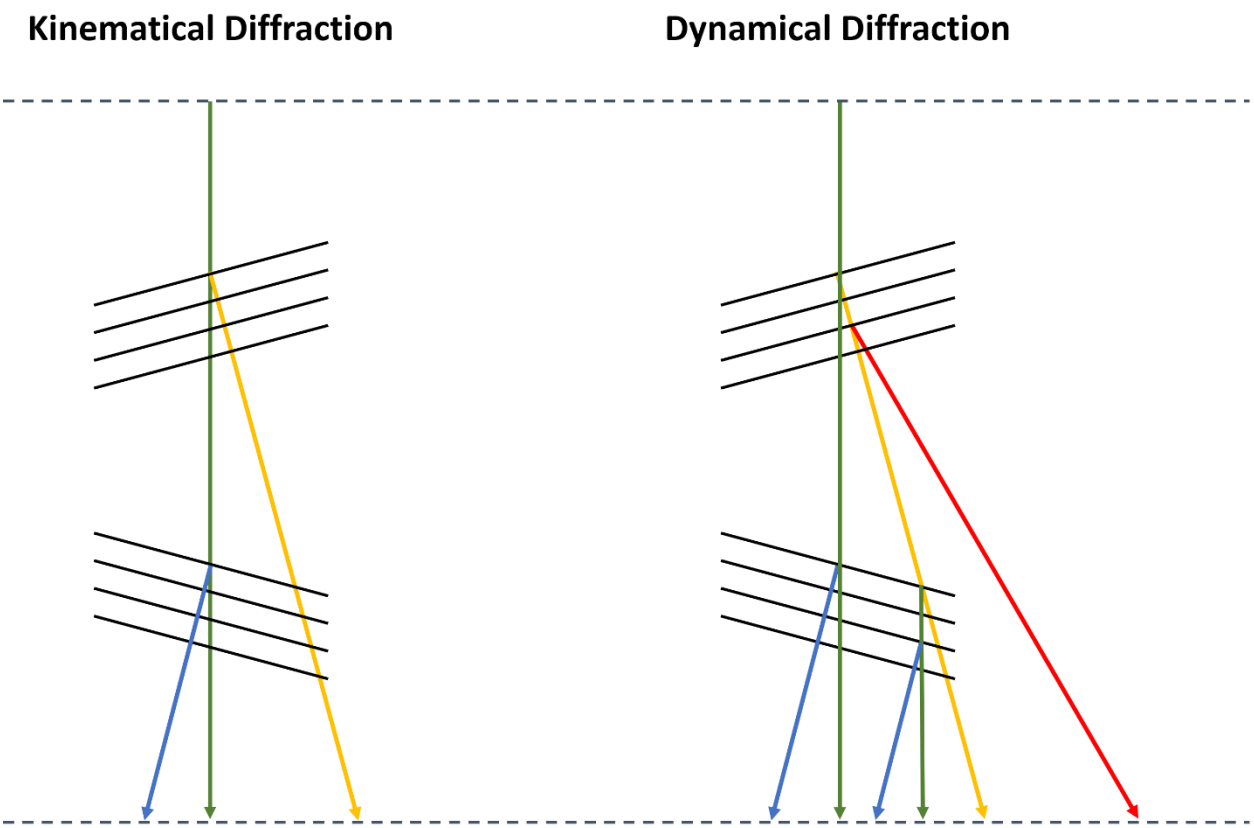

Figure 2.4: *Simplified comparison of kinematical and dynamical diffraction. In the kinematical approximation, the particles get diffracted only once and each recorded intensity is related to a single crystal plane family (yellow and blue beams on the left). In the dynamical case, the particles can get diffracted multiple times, breaking the direct relationship between the reflections and the crystal planes. This is shown here as additional beams being diffracted from already-diffracted beams on the right-hand side. This modifies the recorded intensities and can result in additional reflections (the red beam on the right-hand side). The illustration is simplified to two crystal plane rows with identical plane spacing but in different orientations. In reality, diffraction by multiple plane families often leads to a leveling of recorded intensities.*

Figure 2.5 shows how dynamical diffraction affects the measured intensities. Each diffracted beam can potentially act as a new direct beam due to dynamical diffraction, which leads eventually a levelling of the intensities as seen at the bottom of the figure. This causes significant difficulty in retrieving structural information from the measured intensities, since multiple structure factors are involved with a given reflection. The measured intensities then become unreliable for structure determination if processed with the kinematical approximation.

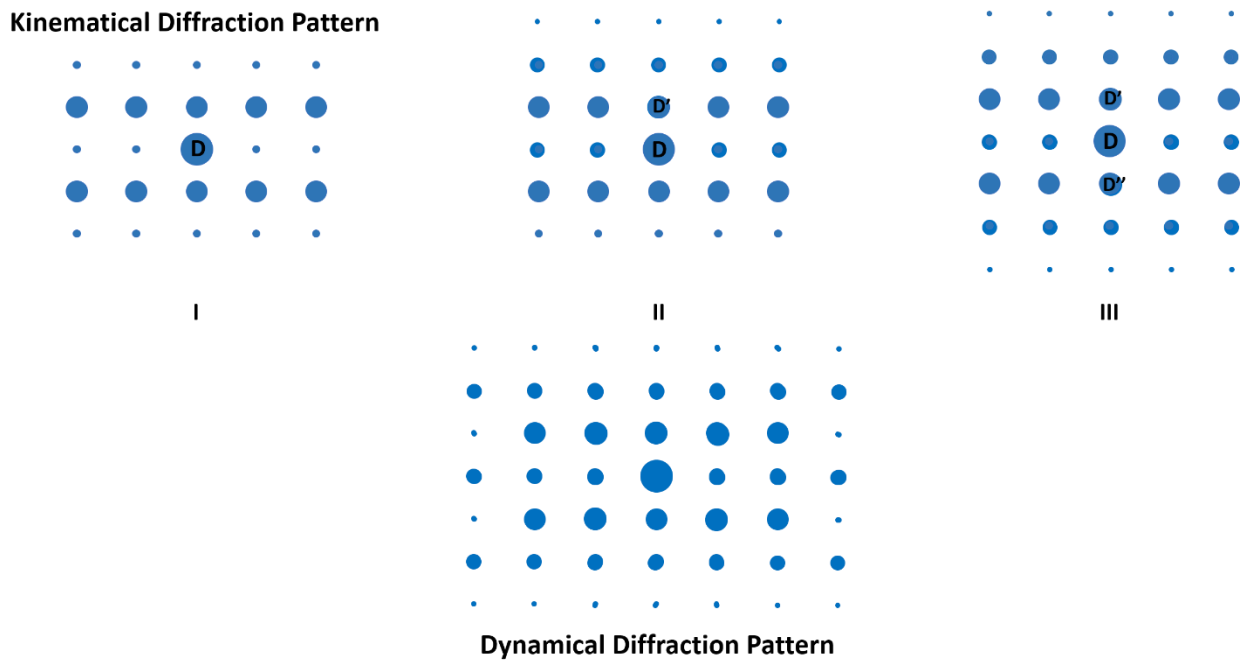

Figure 2.5: *Illustration of how relative intensities are modified due to dynamical diffraction. I) an example of a diffraction pattern with the direct beam in its center (D). II) and III) Due to dynamical diffraction, a diffracted beam can act as a new direct beam, denoted here as D' and D''. The generalized case shown at the bottom, where due to many diffracted beams acting as new direct beams, the intensities are significantly modified compared to I).*

3) Precession Electron Diffraction

As it was shown in Section 1, electron diffraction is a well-adapted tool for the study of nanometric size crystals, especially if they are beam-sensitive. Due to the strong interaction of electrons with matter and the resulting dynamical diffraction, however, for a long time they have been regarded as not suitable for the structure determination of unknown crystals. This has changed with the development of precession electron diffraction in 1994 [2], which allowed the reduction of dynamical effects on diffraction data. In precession electron diffraction (PED), the electron beam is tilted around its optical axis and precessed with a high frequency on a conical surface, with its vertex focused on the sample (**Figure 2.6**). As a result, the effects of dynamical diffraction on recorded data are reduced. In addition, the diffracted intensities are integrated over the entire relrod while the Ewald sphere moves through the relrod. PED was first performed on zone-axis oriented crystals where a large number of crystal planes diffract simultaneously. The resulting intensities are not totally free from dynamical effects, but it has been shown that they are often good enough to solve crystal structures [164], [165].

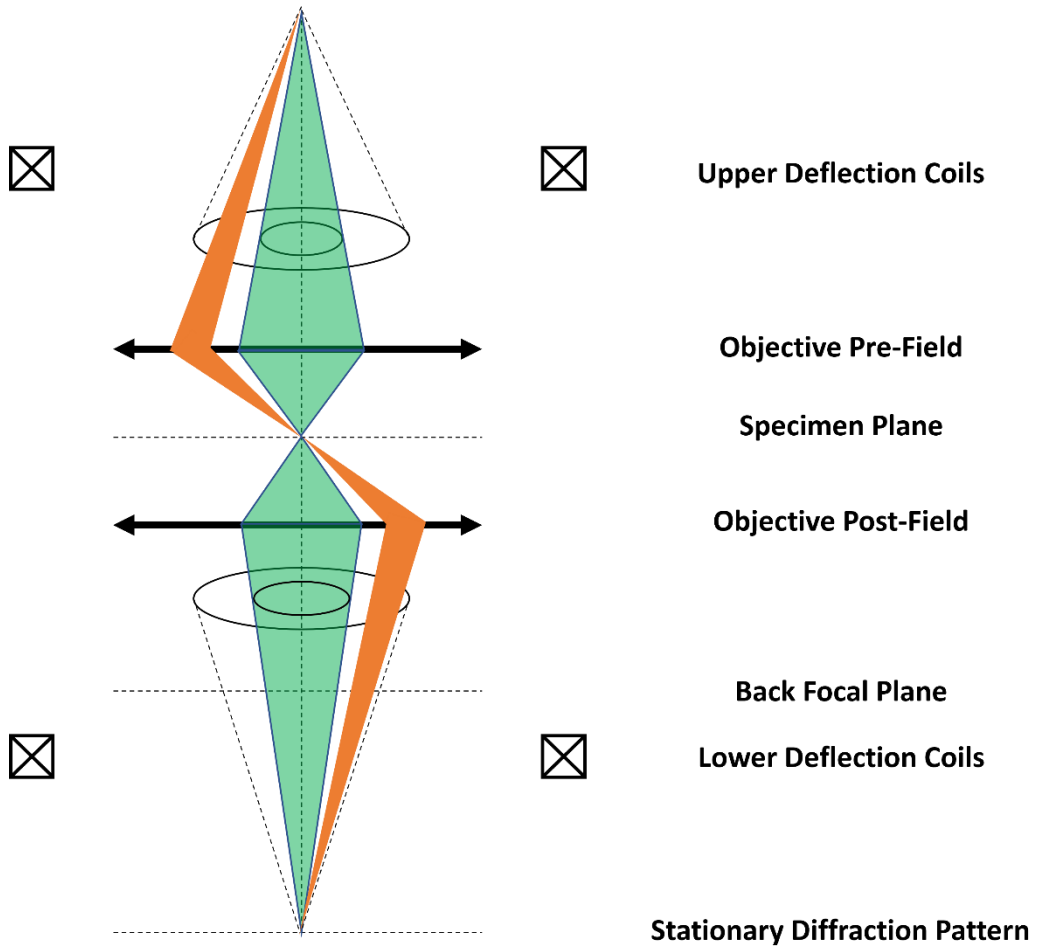

Figure 2.6: *Simplified illustration of electron beam trajectories in the case of a precessed (orange) vs. a non-precessed beam. A convergent beam geometry is used for this illustration. When the beam is precessed, the orange beam rotates around the larger circle at a given precession frequency while the small circle represents the diameter of the non-precessed beam at the same plane on the optical axis. After the beam traverses the specimen, the lower deflection coils refocus the beam into a stationary diffraction pattern.*

However, in the case of beam-sensitive crystals the zone-axis based method is not suitable, because the crystal has to be oriented to different zone axes by manually tilting the crystal while it is irradiated. The dose necessary for the data is therefore much too high for sensitive crystals. Methods that can be more easily automatized have subsequently been developed and are described in the next section.

4) 3D Electron Diffraction (3D ED)

4.1 Concept

The first 3D ED method was conceived in 2007 by Kolb and co-workers [166], [167], as it was realized that limitations of electron diffraction mainly due to dynamical diffraction could be addressed by changes in data acquisition strategy. In contrast to zone-axis data, in 3D ED no special orientation of the crystal with respect to the incident beam is required. 3D ED designates a growing number of electron diffraction data acquisition techniques that differ in details but have general properties in common. In all techniques the crystal is not oriented prior to the data acquisition. During the data acquisition the crystal is rotated around the goniometer axis and diffraction frames are recorded at equal intervals.

Figure 2.7 shows a schematic representation of the Ewald construction in the reciprocal space for the data acquisition in 3D ED. The green lines correspond to the traces of the Ewald sphere for different orientations of the crystal and the blue points represent the nodes of the reciprocal lattice. On this figure the rotation of the crystal around the goniometer axis is equivalent to an inclination of the Ewald sphere. Each green line corresponds therefore to one of the diffraction patterns recorded. Each intersection of the Ewald sphere with a node of the reciprocal lattice gives rise to a diffracted beam on the diffraction patterns. Examples of these diffraction frames corresponding to different orientations of the same crystal are given in **Figure 2.7**.

Even though reflections on each individual frame cannot be directly interpreted, if the relative orientation of each frame is known, the reflections can be merged into a single volume which then contains a 3D distribution of diffraction intensities. Spacing among the intensities in this distribution can then be used to determine the unit cell. The intensities can be indexed and integrated for subsequent structure determination. The extinction conditions can be determined from the systematic absences of reflections, allowing the determination of the space group or at least narrow down the number of possible space groups to a few which show the same extinctions.

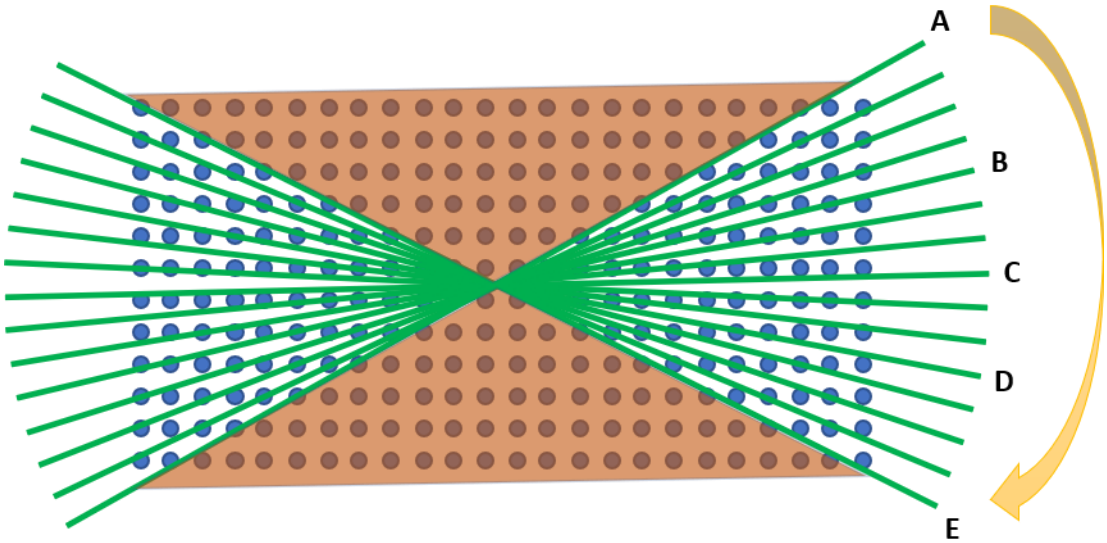
A
B
C
D
E

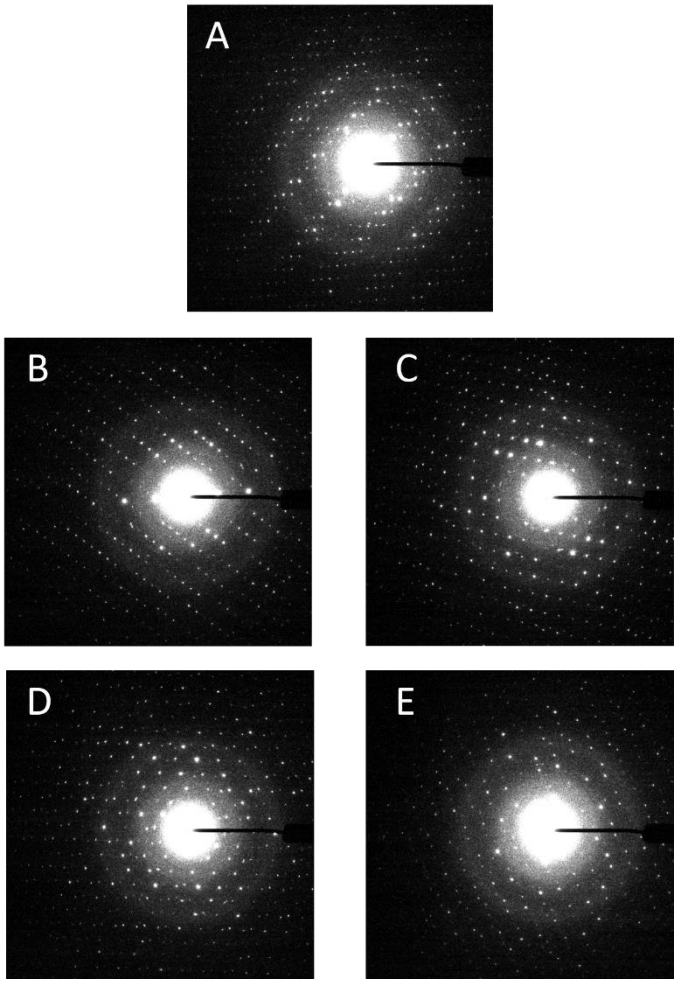
A
B
C
D
E

Figure 2.7: (previous page) *Illustration of how the reciprocal space is probed in 3D ED. The rows of blue circles represent nodes in reciprocal space for a crystal. The elongated shape of the nodes is omitted for simplicity. Each green line represents the Ewald sphere trace at a random crystal orientation with a fixed tilt step in-between. The traces can be approximated to linear cuts due to the small wavelength of electrons. The missing cone is colored in light brown as the area non-probed by the green lines. Examples of 3D ED diffraction patterns are given at the bottom for traces A to E. 2D information on each image can be extracted into a 3D volume if the image orientations are known.*

A complete rotation of the sample in TEM is not possible due to technical constraints as the beam eventually gets blocked by the sample holder at high tilt. Some reflections therefore fall into the so-called missing cone (represented in light brown on **Figure 2.7**) and cannot be retrieved. Although 3D ED is always incomplete, partially complete data is often sufficient for structure determination since the number of measured amplitudes often exceeds the number of variables to determine, represented by $\mathbf{r}_i$ in Eq. 3. Part of the missing cone can also be retrieved by exploiting the lattice symmetry and filling in the positions of symmetrically equivalent reflections.

The rotation of the sample during the data acquisition can be done in two ways, either step-wise with a fixed angle between subsequent positions of the crystal and a recording of the diffraction patterns while the crystal is immobile or a continuous rotation of the crystal. In the latter case, the crystal is rotated during the recording of the frames.

4.2 Step-wise 3D Electron Diffraction

Figure 2.7 corresponds to the situation where the sample is tilted in discrete steps and is immobile during the data acquisition. As can be seen from the figure, in this case some nodes may be missed, so some reflections may be lost in-between the steps or only partially recorded. This could be avoided by using a small tilt step, but in practice lowering the tilt step size might make the data acquisition less precise due to imperfections of the TEM goniometer. This could affect the correct merging of intensities from different frames if their relative orientations are less precisely known.

In order to overcome this problem, an initial alternative called rotation electron diffraction (RED) was developed [168]. Here, the relatively large goniometer tilt steps are complemented by smaller beam tilts performed by the TEM deflection coils. This allows to significantly reduce the missing wedge between the frames, but the number of frames per dataset is about 10 times higher than precession-based acquisition.

Instead of lowering the tilt step, the data missing in-between the frames can be retrieved by using a precessed beam [3], [169]. In the scheme of **Figure 2.8** the effect of the precession is a continuous movement of the Ewald sphere resulting in the green wedges represented in the figure. Compared to

static diffraction frames, precession enables integration of reflection intensities through a larger section proportional to the angle of precession. The precession angle can therefore be tuned to fill in the gaps in-between the tilt steps.

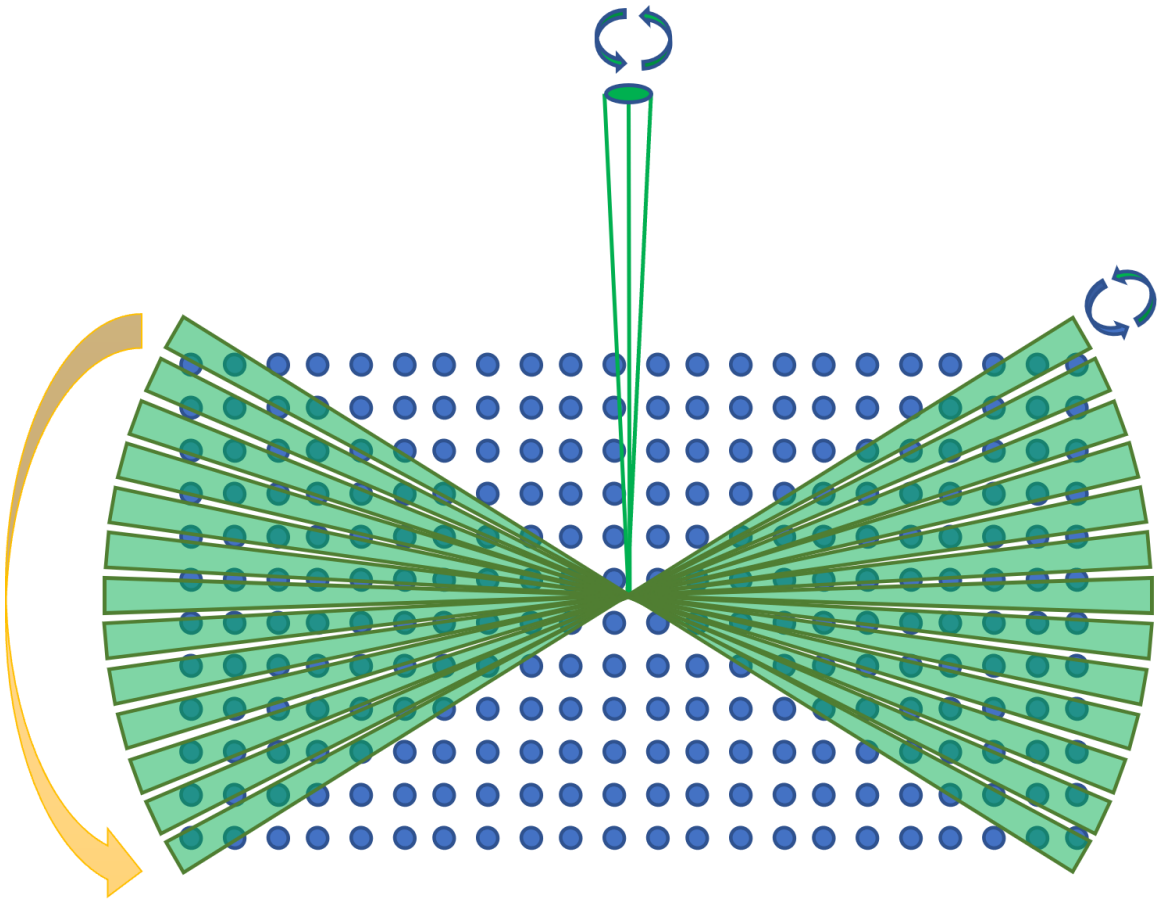

Figure 2.8: *Illustration of precession-assisted 3D ED. As a result of beam precession represented by the vertical cone, the Ewald sphere also precesses (blue arrows). This results in a better integration of the intensities represented by the larger green sections. In this figure, the green sections are separated for clarity. In reality, it is possible to set a tilt step and precession angle to assure a complete integration and overlaps among the green sections, with no blank sections in-between.*

Furthermore, as discussed in Section 2, intensity from diffracted beams can be present in the vicinity of the Bragg condition, even though the latter is not perfectly satisfied [8]. Some reflections may then be present in multiple consecutive frames each in the vicinity of the Bragg condition. Determination of the exact position of a reflection thus requires a full integration of its intensity profile through the relrods, which is not possible if there are gaps in-between the frames. It is therefore necessary to integrate the intensities through a larger section than the center of the Bragg condition, which can be achieved through tuning of the precession angle to induce overlaps among consecutive frames.

4.3 Continuous Rotation 3D Electron Diffraction

An alternative to step-wise data acquisition is the recording of the frames during a continuous rotation of the crystal. The data are continuously collected while the TEM goniometer rotates the sample. The rotation never stops during data acquisition to avoid mechanical instabilities, and the missing wedge is defined as the time the detector spends between each recording, in relation to the rotation speed (**Figure 2.9)**.

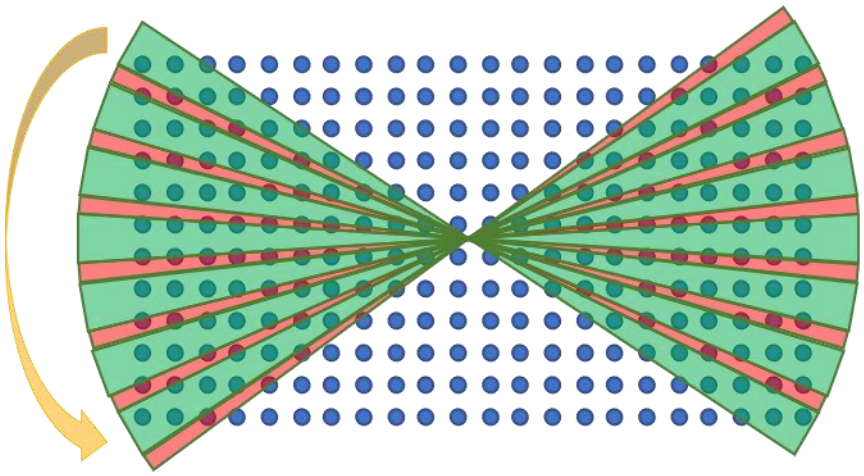

Figure 2.9: *Illustration of continuous rotation 3D ED. The crystal is continuously tilted while the detector records diffraction patterns. Since the crystal is continuously rotated, each image integrates a part of the reciprocal space (green sections). The size of each section is dependent on the specimen rotation speed and the exposure time per image. Due to a finite readout time between each pattern, there is a small gap between each section (red sections). The size of the red sections is exaggerated in this figure for a clarity. In reality, the readout time is short when fast detectors are used, and the integration can be approximated as continuous.*

3D ED in continuous rotation mode has been developed independently by different research groups in the 2010s [114], [170], [171]. It is often referred to as cRED or MicroED. Each frame corresponds to a wedge of crystal orientation as opposed to a static section, with the width of the section determined by the exposure time per frame and the rotation speed. This allows the intensities to be integrated, similar to acquisition with precession. Compared to step-based precession, continuous rotation allows to reduce the overall time the crystal stays under the beam, which is advantageous for beam-sensitive compounds. It however requires a fast camera with a low dead-time in-between each frame. Data acquisition is also typically 3-4 times faster than step-wise acquisition. Direct or hybrid detection cameras that are very fast in the data acquisition and read-out have been developed in the recent years, but they are still very costly and not available on most of the TEM already installed. One inconvenience of continuous rotation

compared to precession 3D ED is that reflections close to the rotation axis might not be as thoroughly integrated as in precession data due to the rotation movement covering less space than precession.

4.4 3D ED Applications and Beam Damage

Table 2.1 summarizes different types of 3D ED techniques. Despite their differences in data collection schemes, all these methods are based on the common goal of measuring electron diffraction data away from zone axes. Other variants of 3D ED exist [172], [173], but their description is beyond the scope of this thesis.

Table 2.1: *Chronologic summary of commonly used 3D ED techniques.*

3D ED Technique	Data Collection	Reference	Year
Automated Diffraction Tomography (**ADT**)	Step-Wise Static	[166], [167]	2007
Precession Electron Diffraction Tomography (**PEDT**)	Step-Wise Precession	[169]	2009
Rotational Electron Diffraction (**RED**)	Step-Wise combination of goniometer and beam tilts	[168]	2010
Continuous Rotational Electron Diffraction (**cRED**) / Micro-Electron Diffraction (**MicroED**) / Intregrated Electron Diffraction Tomography (**IEDT**)	Continuous Rotation	[114], [170], [171]	2014-2017

The ability of 3D ED to gather single-crystal data from nano-sized crystals has enabled it to be a technique of choice in cases where synthetizing crystals large enough for X-ray diffraction is impractical or impossible. This is often the case for nano-sized functional materials [174], [175], naturally nanocrystalline minerals [176], [177], porous materials [178], [179], as well as organic small-molecules [180] and proteins [181], [182]. The larger scattering cross-sections of electrons with matter allows to gather high-resolution diffraction data from nanocrystals, however it can also cause damage to crystals through inelastic scattering. This can lead to a loss of high-resolution data, or eventually to a complete loss of crystallinity.

Damage is often proportional to the electron dose, which in turn is proportional to how much time a crystal is exposed to the beam. In precession-based 3D ED, the crystal can be exposed to a beam for a long

duration since a tilt is performed between each frame. The inter-frame tilting can actually take longer than the actual data acquisition, which increases the electron dose on crystals, inflicting damage on those who are sensitive. The overall dose can be reduced in continuous rotation mode, but this requires a fast detector to be efficient and due to TEM goniometer instabilities, the crystal can move away from the beam during data acquisition. In both precession and continuous modes, crystal tracking is often necessary to keep the crystal under the beam. This can be done by repositioning of the crystal through imaging in-between tilts or using defocused diffraction patterns [172]. In both cases, the crystal is exposed to further electron dose while no diffraction data is being recorded. In the case of beam-sensitive crystals, it is important to use the applied dose in an efficient way, as shown in the following method.

5) Low-Dose Electron Diffraction Tomography

5.1 Concept

LD-EDT is a recently developed 3D ED technique specifically designed for beam-sensitive crystals [7]. This is achieved through minimization of the electron dose necessary to acquire datasets which allow structure determination. The critical aspect of this method is to eliminate all futile irradiation of crystals during data acquisition. LD-EDT is based on step-wise precession 3D ED, but without any scheme for crystal tracking. Without any tracking, crystals could potentially escape the zone of acquisition due to TEM goniometer instabilities. This is prevented by precisely positioning the sample holder at the eucentric height and using a large selected area electron diffraction (SAED) aperture. This reduces the amplitude of the crystal displacement below the diameter of the area selected by the SAED aperture. Crystal tracking and the additional electron dose affiliated with it can therefore be eliminated.

Using a large SAED aperture also makes sure that diffraction data is being collected from the same crystal volume throughout the measurement. This is in contrast to parallel nano-electron diffraction (NED) mode where a beam is used that is smaller than the sample. In this case the diffracting volume depends on the thickness of the crystal, which can change when the crystal displacement during the rotation brings a thinner or thicker part of the crystal into the beam. In addition, even for a crystal with constant thickness, the apparent thickness and so the analyzed crystal volume will change during the rotation, because the thickness will depend on the angle formed between the incident beam and the surface of the crystal.

Working in SAED mode also increases the overall crystal size from which diffraction data is recorded, compared to NED. This allows for a higher signal-to-noise ratio even when a lower dose rate is used, due to a higher number of diffracting unit cells. This makes SAED more favorable to gather data from beam-sensitive crystals.

The apparent diameter of the SAED aperture used in LD-EDT is 2 µm, which is sufficient to prevent crystals in the order of 500nm from escaping the selected area (**Figure 2.10**). Since a large diameter is used, increased blooming of the direct beam can prevent certain reflections close to it from being properly recorded. This is due to the increase in empty space inside the aperture allowing more electrons to pass without being diffracted. Therefore, a beam-stop is used to prevent the high intensity direct beam from damaging the detector.

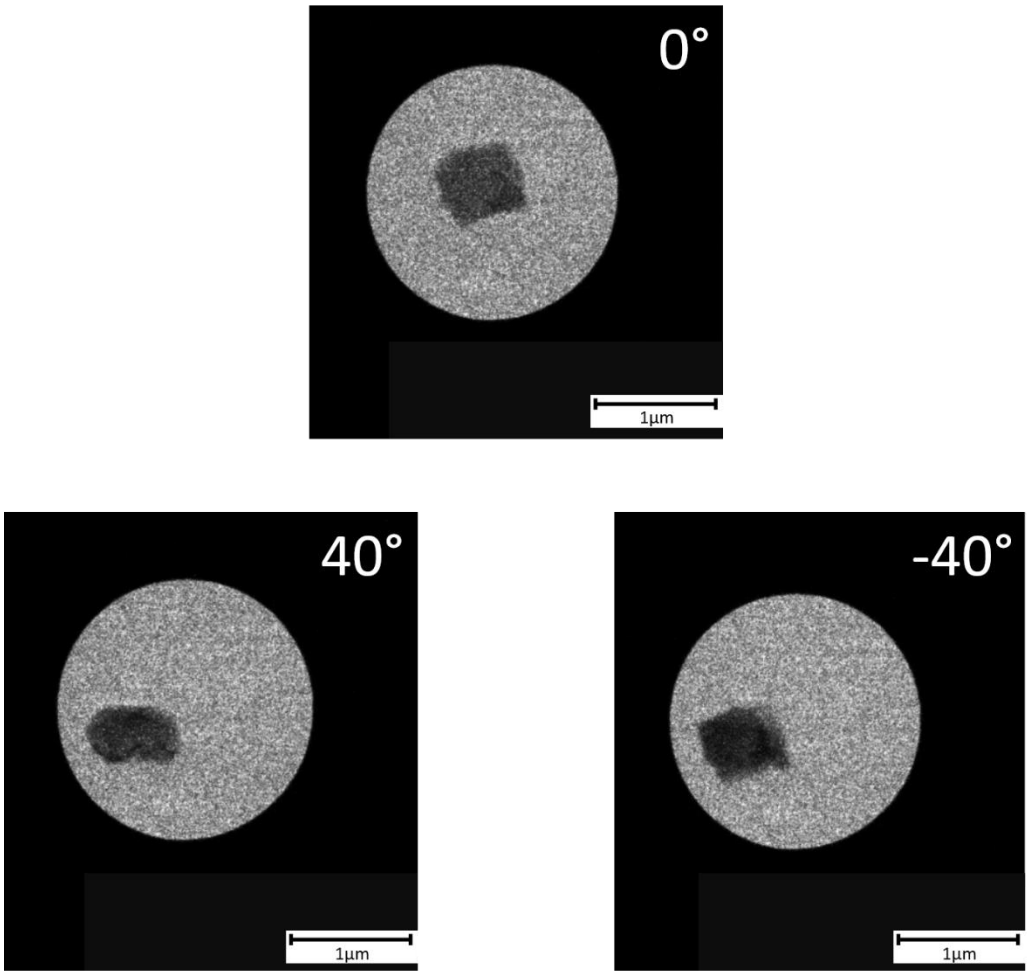

Figure 2.10: *TEM images of a crystal taken with a selected area aperture illustrating how the crystal stays inside the data acquisition zone throughout the tomography when the crystal is aligned close to the eucentric height, eliminating the need for crystal tracking.*

5.2 LD-EDT Data Acquisition

LD-EDT is the method used for the structure determinations presented in chapter 3. The following section will explain in more detail the application and exploitation of this method.

5.2.a Specimen Preparation

Most LD-EDT specimens are available in polycrystalline powder form. Standard specimen preparation consists of grinding a small quantity of powder in an agate mortar, suspended in ethanol to obtain small crystals. A few drops of the suspension are then deposited on a porous carbon-coated copper grid, in order to achieve an optimal concentration of particles for data acquisition. The particles adhere to the porous carbon-coated grid as ethanol rapidly evaporates in standard temperature and pressure. Some specimens can be sensitive to or dissolve in ethanol, in which case dispersion in distilled water can be performed. The dispersion process can be done in an ultrasound bath for more efficiency. For specimens sensitive to dispersion with any solution, a dry grinding can be performed inside an agate mortar onto which the grid can be introduced to gather crystals with direct contact. An overview of specimen preparation for electron diffraction is given in **Appendix A**.

5.2.b Experimental Setup

The grid is then mounted on a TEM sample holder. The sample holder used is specifically designed for tomographic data acquisition, by mechanical thinning of a standard single tilt sample holder, which increased maximum tilt range to 110°. An optical microscope is used to identify and remove any dust on the sample holder, which could interfere with the TEM vacuum.

Throughout this thesis, LD-EDT data acquisition was performed on a Philipps CM300 ST TEM with an accelerating voltage of 300 kV equipped with an EDX Bruker SDD detector (**Figure 2.11**). Precession of the electron beam was generated by a Nanomegas Spinning star device. The electron beam in the TEM as well as beam precession must also be aligned prior to data acquisition. In the LD-EDT method, this alignment is performed in a specific region of the sample grid which is subsequently discarded from data acquisition. It is especially important to align the eucentric height precisely, to reduce crystal movement. The sample holder is also tilted in positive and negative angle directions to determine the maximum possible tilt angle for the given specimen holder. which is usually between +/- 50-55°, the exact value being dependent on the position of the particle on the grid.

Frames are recorded with a TVIPS F416 CMOS camera, which is capable of fast acquisition with a large field of view, high-resolution (4kx4k) and dynamic range (16 bits).

Figure 2.11: *The Philips CM300 ST TEM used throughout this thesis is shown on the left. The TVIPS F416 CMOS camera used for recording diffraction patterns and images is shown on top right, and the Nanomegas Spinning star device used to generate a precessed beam is shown in bottom right.*

Before performing any measurements, a preliminary test is done to check the beam-sensitivity of crystals. This consists of irradiating crystals without any tilting and observing the loss of crystallinity through the fading of diffraction intensities as a function of the electron dose. A simple criterion is to assess at which dose the reflections corresponding to smallest lattice spacing start to fade. Fading of diffraction intensities under the beam is described in more detail in Chapter 1.

The dose rate is measured by locating an empty pore on the carbon grid and exposing the camera with the same irradiation rate to be used for data acquisition. Knowing that each electron that hits the camera generates in average 85 counts on the camera, the dose rate can be calculated from the number of counts, the exposure time and the surface of a sample area that is imaged in one pixel:

$$\text{Dose Rate}\left(\frac{\mathbf{e}^{-}}{\text{Å}^{2}\boldsymbol{s}}\right)=\frac{\mathbf{M}}{\boldsymbol{IPS}^{2}}\left(\frac{\mathbf{4}}{\mathbf{85}}\right)\mathbf{10}^{-2}$$

Eq. 2.5

where *M* represents the average number of counts per pixel during a 1s exposure, and *IPS* stands for image pixel size, in nm/pixel units. This is converted to $Å^2$ by multiplying with 10^{-2}. Its value depends on the choice of TEM camera length. The factor of 4 is due to binning of the images from 4k*4k to 2k*2k, which reduces their file size.

The electron dose is calculated by multiplying the dose rate with exposure time. This allowed to determine how much dose a crystal can withstand without going through significant damage. The dose during data measurement is then adjusted accordingly by carefully choosing the number of exposures and exposure time.

5.2.c Data acquisition

The search for crystals on the sample grid is performed on sections of the sample holder that weren't previously irradiated. The beam intensity has to be reduced as much as possible, to prevent crystals from being damaged prior to measurement. If the beam intensity is too low, it may be too difficult to actually see the crystals on the TEM fluorescent screen, so a compromise has to be found. Ideally, the crystals should not be too thick to reduce dynamical diffraction, but also not too small so that a decent signal is still measured.

When a particle with an appropriate size is found, it is centered inside the SAED aperture, and a diffraction pattern is recorded to check its crystallinity. The beam is immediately blanked afterwards. Although it is difficult to assess the quality of crystallinity at a random crystal orientation, the shapes of the reflections and the arrangement of reflection rows provide insight whether the particle contains one or multiple crystal phases, the former being necessary for successful structure determination.

Once a crystal is identified, the sample range is tilted to both extremes of the goniometer tilt range, where images are taken with an SAED aperture inserted to check whether the crystal stays inside the selected area or not. The beam is blanked at all times except for the image acquisition. If the crystal escapes the selected area at the extremes, it is re-centered or the eucentric height can be slightly adjusted for correction, which is again checked with static images instead of continuous irradiation.

To acquire LD-EDT data, the serial acquisition mode in TVIPS EMMENU software is used to automatize the tomographic recording. The sample holder is tilted to the starting angle, which is one of the extremes of the available tilt range. It is observed that for the Philipps CM300 ST TEM goniometer, going from positive to negative tilt is more stable compared to the contrary case. A fixed tilt step, the exposure time and the number of successive frames is defined in EMMENU. At each tilt position, the beam is automatically de-blanked, and a diffraction pattern recorded. After each recording, the beam is automatically blanked again until the sample is tilted to the next position, where another diffraction pattern is recorded. This operation is repeated until the other extremity of the tilt range is reached. Typically, data acquisition on a single-crystal lasts a few minutes, depending on the tomography range and the exposure time per frame.

5.3 LD-EDT Data Reduction & Integration

The raw image LD-EDT data containing the diffraction patterns is processed using the PETS2 software [183]. The data processing is done in several steps.

Important input information to start data processing include the orientation of the tilt axis, tilt angles of the frames and the camera length. The first step consists of locating the reflections on the frames. This can be optimized by manually selecting an intensity threshold to distinguish reflections from background noise, and the size of the reflections. The reflection sizes can change from one crystal to another and can be visually estimated on the frames. The precise position of the beam-stop is also measured to be input into PETS2. The next step involves the refinement of the tilt axis, by refining the angle between the projection of the tilt axis on the frames and the horizontal axis. It is necessary to determine the orientation of the rotation axis accurately in order to reconstruct the 3D reciprocal space precisely. This can be verified by inspecting the cylindrical projection of the reciprocal space, where reflections should follow sinusoidal lines and should be well clustered onto one another.

The second step is the determination of the crystal unit cell. Using the reconstructed 3D intensity distribution, PETS2 offers an automatic determination of the unit cell, but it is also possible (and

sometimes necessary) to do this manually. In the 3D representation of the observed reflections one can rotate the reciprocal space and define the basis vectors of the unit cell. In either case, the unit cell vectors are subsequently refined by the program and the reflections are indexed.

Prior to integration of the intensities, reflection profiles should be refined. These are plots of the intensities as a function of the excitation error, whose profile can differ in each individual dataset depending on the properties of the crystal as well as the electron beam. Frame geometry is also refined by correcting the tilt angles and distortions, to account for the imperfections of the TEM goniometer and optics [184].

The final step is the integration of the indexed intensities. During this process, positions of reflections on each frame are predicted using the unit cell and the orientation matrix of the crystal. The intensity at these positions is then measured according to the refined intensity profile. The intensities are measured in two different ways. First, for each reflection, the intensity is integrated over multiple frames. These intensities are approximated as kinematical intensities and used in the following to solve the structure and perform a first kinematical refinement. Then, the intensities are determined for the dynamical refinement. Here, for each reflection that appears on several subsequent frames the intensity on each frame is integrated independently.

5.4 Structure Determination

Prior to the interpretation of the intensities, the space group can be determined by analyzing extinctions present in the measured data through specific 2D sections of the 3D intensity distribution, and comparing observed extinctions with tabulated information on the space groups in the International Tables for Crystallography [156]. Determination of the space group is useful for the structure solution procedure, since it reduces the number of parameters to determine through the use of symmetry operations present in the space group. The 2D sections are also useful to assess overall data quality, such as identification of crystal twinning where multiple crystal domains in different orientations inside a same crystal can result in additional reflection rows. Even though off-axis data acquisition and precession reduce dynamical effects, the latter can still be present in 3D ED data. This can especially impact space group determination through violation of systematic extinctions. A detailed analysis of relative intensities of reflections rows in the 2D sections is therefore necessary to determine the extinction conditions. An example of 2D sections used for space group determination is presented on **Figure 2.12**

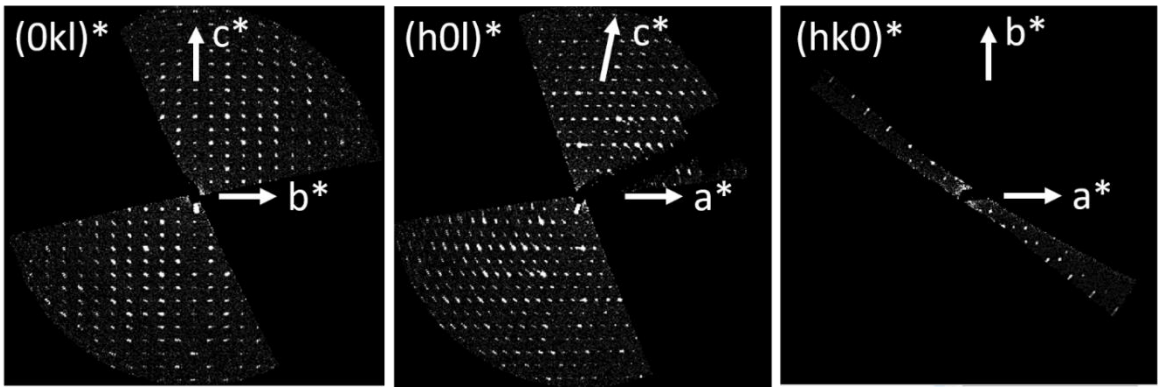

Figure 2.12: *Example of 2D sections of the intensity distribution in the reciprocal space used for space group determination. On the (h0l)* and (h0l)* sections, the 00l rows show drops in intensity for l = 2n+1, in addition to drops in intensity for all reflections with l = 2n+1 on (h0l)*. This indicates the P2/c space group. The extinctions are violated due to dynamical diffraction. There is very little information on the (hk0)* section due to corresponding reflections being in the missing cone.*

The kinematically integrated intensities, along with the unit cell and space group information are used for the structure determination process, implemented through Jana [185] software. The first step is the structure solution, where artificial phases are assigned to measured intensities from which an electrostatic potential map can be calculated by inverse Fourier transform. This map can then be interpreted to identify atomic positions. The phasing often involves applying prior crystallographic knowledge into the phase problem, such as the fact that crystals are made of discrete, fixed atoms and that the electrostatic potential should not contain negative values. In this case the number of variables to determine can be substantially reduced, and phases can be determined by exploiting relationships among the observed amplitudes. These are referred to as direct methods. These can be implemented in Jana2020 through the SIR2014 software package [186]. An alternative is the charge-flipping method [187]. Charge-flipping consists of assigning random phases to the measured amplitudes, applying Fourier transforms to obtain an electrostatic potential map, reversing the sign of potential values whose absolute values are below a given threshold, applying inverse Fourier transforms to get phased structure factors, then discarding the amplitudes and replacing them with the measured ones which are now assigned with the new phases, and repeating the process until an interpretable map can be obtained. Direct methods and charge-flipping often necessitate a high data resolution to be successfully implemented, which means recording reflections corresponding to crystal planes with small lattice spacing. If this is not possible, other approaches exist such as molecular replacement [188], which requires more prior knowledge of the structure contents. **Figure 2.13** summarizes the workflow of structure determination from 3D ED data.

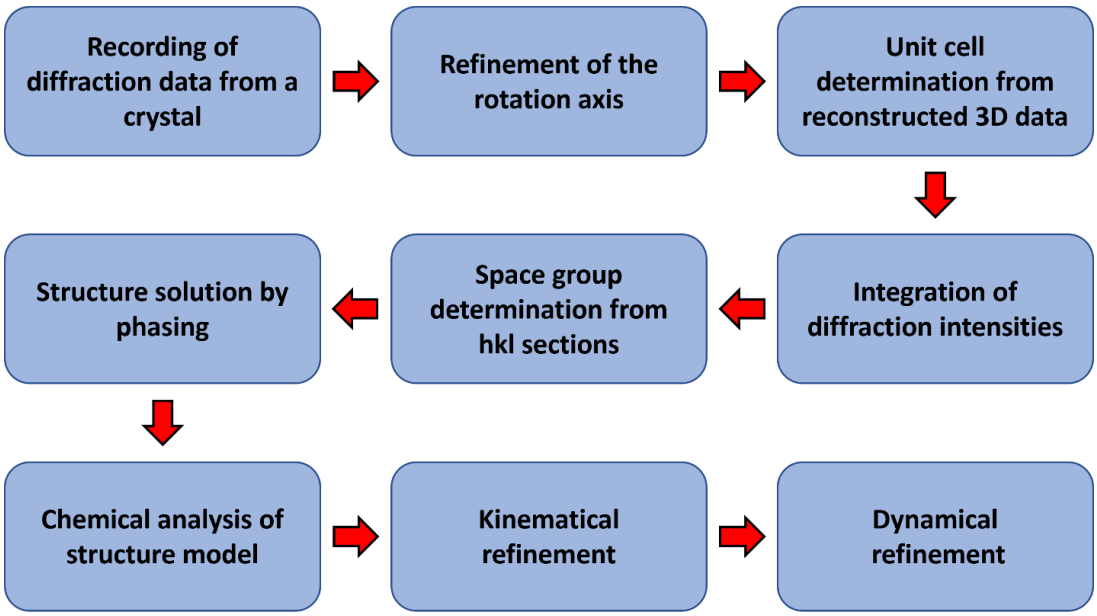

Figure 2.13: *Simplified flow chart of structure determination from 3D ED data. In order to improve the structure solution process, data from multiple particles with the same unit cell can be merged together.*

The result of the structure solution process is a structure model, where atoms are placed inside the unit cell through interpretation of the electrostatic potential map. The structure model can be manually interpreted using chemical knowledge about the crystal, which includes assessment of the stoichiometry, coordination and inter-atomic distances. The structure model can be incomplete in some cases or may contain additional ghost atoms through misinterpretation of noise in data. These can be corrected by manually editing the structure model guided by chemical knowledge.

The second step of structure determination is the refinement of the structure model. Once a model is obtained from the electrostatic potential map, its structure factor amplitudes can be calculated and compared to those experimentally measured. Kinematically integrated intensities related to a reflection in multiple frames are considered to assign a single intensity to each reflection. In order to validate a model, the calculated amplitudes must agree precisely with the measured intensities. This is not always the case, due to issues such as imprecise recording of the intensities, incomplete or erroneous structure models and dynamical diffraction. To minimize the difference between the calculated and measured intensities, the structure models can be finely adjusted to minimize an error function comparing the two intensities. This process is iterated until the error function is reduced to a minimal value. A commonly used standard indicator to compare refined models with the measured data is the crystallographic *R* factor, defined as;

$$\boldsymbol{R} = \frac{\sum_{\boldsymbol{k}} \left| |\boldsymbol{F_{meas}}(\boldsymbol{k})| - |\boldsymbol{F_{calc}}(\boldsymbol{k})| \right|}{\sum_{\boldsymbol{k}} |\boldsymbol{F_{meas}}(\boldsymbol{k})|}$$

Eq. 2.6

In **Eq. 2.6**, F_{meas} and F_{calc} are measured and calculated amplitudes for reflection **k**, respectively. *R* would be equal to zero for a perfect fit, while a random model typically has an R equal to or higher than 0.6 [189]. Overfitting during refinement could lead to low *R* values for arbitrary models, it is therefore useful to complement model validity with other indicators. A weighted *R* factor can also be used:

$$\boldsymbol{wR} = \sqrt{\frac{\sum_{\boldsymbol{k}} \boldsymbol{w_k} [|\boldsymbol{F_{meas}}(\boldsymbol{k})| - |\boldsymbol{F_{calc}}(\boldsymbol{k})|]^2}{\sum_{\boldsymbol{k}} \boldsymbol{w_k} \, |\boldsymbol{F_{meas}}|^2}}$$

Eq. 2.7

In **Eq. 2.7**, the weights w_k associated to each term of the sum are equal to the inverse of the standard deviation on the measured amplitude. Another alternative indicator is the goodness of fit (GoF), defined as:

$$\boldsymbol{GoF} = \sqrt{\frac{\sum_{\boldsymbol{k}} \boldsymbol{w_k} [|\boldsymbol{F_{meas}}(\boldsymbol{k})| - |\boldsymbol{F_{calc}}(\boldsymbol{k})|]^2}{\boldsymbol{n_{obs}} - \boldsymbol{n_{par}}}}$$

Eq. 2.8

n_{obs} and n_{par} are the number of observation and the number of refined parameters, respectively. GoF should ideally approach zero for an ideal structure model. For all 3 indicators mentioned here, the intensities (squares of the structure factors) may also be used for the calculation, instead of the structure factors. The reflections **k** used in the sum can either be all measured reflections in the data, or those reflections above a certain observation threshold defined by the ratio of their measured intensity over the standard deviation of the measurement (I/σ). Throughout this thesis, an observation threshold of $I/\sigma > 3$ was used. If an indicator is calculated only on reflections satisfying this threshold, this is specified with (obs) in its expression, while the calculation on all reflections is specified with (all). Calculations with all reflections will always be greater because the model is not refined to the reflections that contribute to

this calculation, but the two indicators (obs) and (all) should ideally be similar since a correct structure model should predict all the data with uniform accuracy.

In some cases, a better interpretation of the electrostatic potential map through structure refinement with a low *R* can reveal locations of missing atoms in the model. If calculations for the refinement process are performed in the kinematical approximation, the process is referred to as a kinematical refinement. Despite a considerable reduction of dynamical diffraction effects on diffraction data in 3D ED experiments, a purely kinematical refinement on 3D ED data often leads to higher figures of merit, compared to typical values obtained from XRD data. This can lead to inaccurate structure models with limited information on subtle structure features such as locations of small atoms and partial occupancies. An alternative is dynamical refinement [190], where intensities for the refinement process are calculated via the dynamical diffraction theory. In contrast to kinematical refinement, intensities are extracted and treated individually from each frame. In addition to the structure model, the crystal thickness and frame orientations are also refined to allow an accurate modelling of dynamical diffraction. Dynamically refined structures are typically 2-3 times more accurate compared to those kinematically refined [4]. **Figure 2.13** summarizes different steps of crystal structure determination using LD-EDT data.

6) Conclusion

Electron diffraction allows to gather structural information from very small crystals, down to tens of nanometers. 3D ED electron has recently emerged as a powerful technique to characterize nanocrystals by reducing dynamical diffraction effects on measured data and increasing data coverage. Data quality can still suffer from electron beam damage, as discussed in Chapter 1. LD-EDT is a 3D ED method optimized for sensitive specimens, by lowering the electron exposure as much as possible during data acquisition, without requiring any specialized hardware. Throughout this work, the structure determination of beam-sensitive compounds has been done using LD-EDT. The results are discussed in Chapter 3, while a further optimization of LD-EDT data acquisition is presented in Chapter 4.

Chapter III: Structure Determination using LD-EDT

This chapter describes how LD-EDT was used to determine the structures of two specimens during this thesis. These specimens, which include a hydrated mineral and a metal organic framework (MOF) are extremely beam-sensitive and require extremely low dose conditions to retain their crystallinity under the electron beam. They also crystallize in very small sizes below the micrometer scale, making LD-EDT a very adapted technique to characterize their crystal structure.

1) Bulachite

1.1 Background

Bulachite is a naturally occurring, hydrated mineral. It was identified in the Black Forest, Germany in 1963 and described by K. Walenta in 1983 [191]. The proposed chemical composition was $Al_2(AsO_4)(OH)_3(H_2O)_3$ via chemical analysis, and PXRD analysis showed an orthorhombic symmetry with unit cell parameters *a* = 15.53 Å, *b* = 17.78 Å and *c* = 7.03 Å. A second occurrence was reported from Sardinia, Italy by Frau & Da Pelo in 2001 [192]. Scanning Electron Microscope (SEM) images taken on these samples showed that Bulachite particles are in form of thin fibres 150 µm long with diameters typically smaller than 0.25 µm. PXRD patterns collected on the Sardinia samples were indexed using the unit cell proposed by Walenta. It was also suggested that this sample may have formed by hydration of mansfieldite [193] in the presence of aqueous aluminium.

The most recent Bulachite sample was identified in Cap Garonne (France) in 2020, which was the subject of the work described here. **Figure 3.1** shows an image of this sample, where Bulachite forms white patchy regions formed on bulk pharmacoalumite. This sample is composed of very thin lath-like crystals typically up to 50 µm long, 0.4 µm wide and 0.1 µm thick (**Figure 3.2**). Interestingly, PXRD data measured from this sample did not perfectly match the pattern measured by Walenta, with some peaks missing and other additional peaks being present. Synchrotron PXRD experiments revealed that this sample contained a hydrated derivative of Bulachite, with the original Bulachite phase being present only at the surface of the bulk samples.

Bulachite is part of a small but diverse group of hydrous aluminum arsenate minerals. Although crystal structures of these compounds may vary widely [194], they often contain aluminum-centered AlO_6 octahedra and arsenic-centered AsO_4 tetrahedra. Their structural flexibility is a consequence of the ability of the octahedra to rotate around their corner-linkage with AsO_4 tetrahedra. This also leads to large

negative thermal expansion coefficients. They often dehydrate in a step-wise manner at different temperatures, forming potentially new minerals at these steps.

Figure 3.1: *An image of the Cap Garonne sample. The patchy white regions on the surface are Bulachite, formed on a yellow bulk of pharmacoalumite. FOV is 15 mm.*

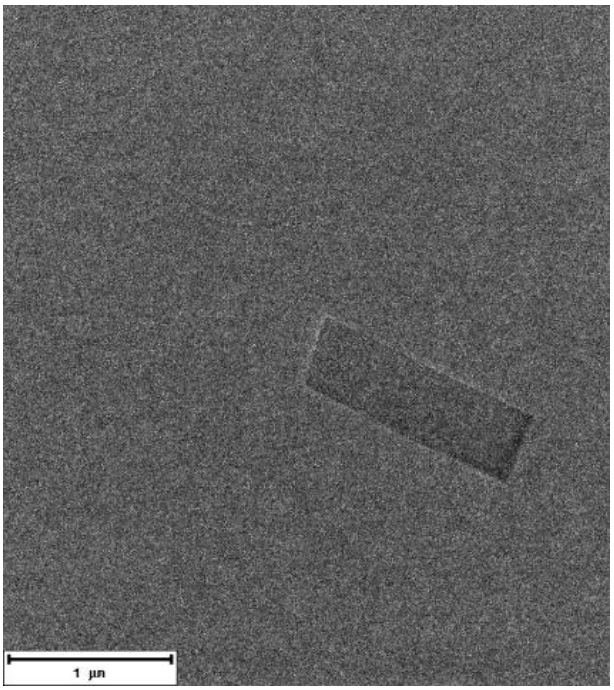

Figure 3.2: *A TEM image of a representative Bulachite particle. The image was taken in low dose conditions in order to preserve the crystal structure. The lath-like morphology can be seen, with the low thickness resulting in low contrast on the image. The scale bar corresponds to 1 µm.*

Despite its long past identification, the crystal structure of Bulachite remained unknown until this thesis. This was both due to the small size of the crystals not giving sufficient signal in SCXRD, and the specimens consisting of two phases with different degrees of hydration, which renders PXRD data very difficult to interpret. The presence of water molecules also makes Bulachite prone to beam damage due to possible radiolysis damage and subsequent diffusion (see Chapter 1).

1.2 Data Acquisition

The Cap Garonne sample was obtained in collaboration with Ian Grey, from CSIRO Melbourne, Australia. The crystals were pre-heated to 100°C in order to remove the hydrated phase. A preliminary PXRD analysis indeed matched the pattern provided by Walenta. Standard specimen preparation for LD-EDT was applied here, described previously in **Chapter 2**. Prior to LD-EDT data collection, beam resistance was assessed by qualitative diffraction fading. It was observed that crystals remained stable until 3.0 $e^-/Å^2$. Energy dispersive X-ray spectroscopy (EDS) was performed on crystals selected for data collection, which revealed an atomic composition of 65% Al and 35% As (oxygens excluded), which is in proximity to the ideal ratio provided by Walenta.

LD-EDT data was collected from selected well-crystallized particles. Once the electron beam was aligned, the search for crystals was performed in low dose conditions to avoid any prior beam damage. Due to their platy lath shape, most particles lie flat on the TEM grid via preferential orientation. **Figure 3.3** provides an illustration of the relevant experimental parameters used during data acquisition.

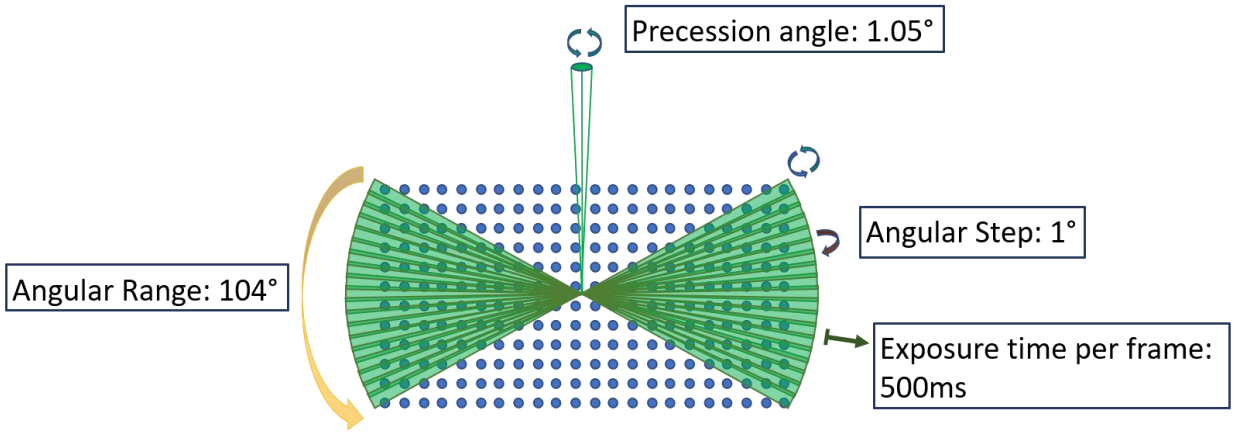

Figure 3.3: *A schematic representation of LD-EDT data acquisition on Bulachite crystals. The combination of a precession angle =1.05° and an angular step of 1° results in overlaps among the patterns, to integrate the intensities. The relatively large missing cone is reduced during data processing through exploitation of lattice symmetry.*

A precise alignment of the eucentric height allowed a high angular range of 104° on a number of particles. An angular step of 1° was set between each pattern and the precession angle was set to 1.05°. This induces overlaps among consecutive images, leading to a more accurate integration of intensities. A dose rate of 0.056 $e^-/Å^2.s$ was employed along with an exposure time per image of 500 ms, which limited the dose per dataset to 3.0 $e^-/Å^2$. This leads to an acquisition time of about 8 minutes per dataset, where the real exposure time of the crystal is 52.5 seconds but the data transfer from the TEM to the piloting computer takes about 4 seconds at each tilt step. Data was acquired from a total of 11 crystals.

1.3 Data Processing

The recorded data was processed with PETS2 and Jana2020, as described in Chapter 2. The cylindrical projection of the reciprocal space obtained after the refinement of the omega angle of the tilt axis (**Figure 3.4**) shows sharp spots on sinusoidal lines. This reveals a precise refinement of the omega angle, which is the angle between the projection of the tilt axis and the horizontal axis and already hints at a good quality of the diffraction data. The reflections from individual diffraction patterns were then processed into a 3D volume of the intensity distribution in reciprocal space. The data was indexed with an orthorhombic unit cell of a = 15.6 Å, b = 17.7 Å and c = 7.9 Å. These parameters agree with the cell proposed by Walenta, except for a 13% longer c axis. Indexing of PXRD data from our collaboration in Melbourne confirmed however the longer c axis. This unit cell allowed for a 100% indexation rate of the measured intensities. **Figure 3.5** shows the indexation of the intensities in the projection along the three principal axes of this unit cell. It can be seen that the reconstructed reciprocal lattice is well defined with clear spotty lattice points, which are indexed by the unit cell.

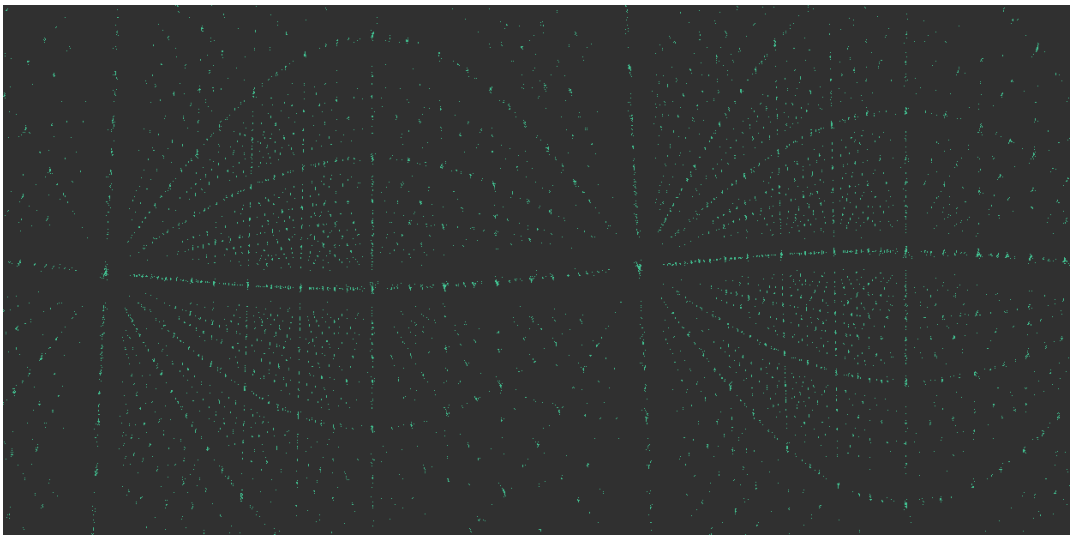

Figure 3.4: *Cylindrical projection of the intensity clusters used for refining the orientation of the tomography rotation axis. Appearance of sinusoidal lines with sharp reflections indicates a successful refinement of relative orientations of the frames.*

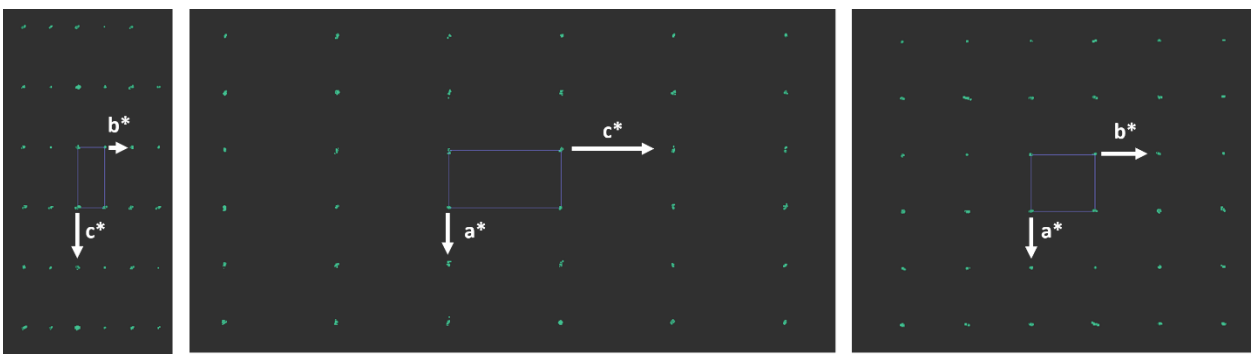

Figure 3.5: *Display of clustered intensities in reciprocal space with the unit cell superposed. The three sections are projections along the a*, b* and the c* axes in that order from left to right. Thanks to a precise refinement of frame orientations, reflections are well clustered into sharp peaks that are indexed by the unit cell. The 3 projections are not on the same scale.*

Figure 3.6 shows the 3D volume of intensities in the reciprocal space reconstructed from LD-EDT data, as well as principal *hkl* sections of it used for space group determination. Manual inspection of the sections showed that reflections were extinct for odd values of *h* on *hk0* and odd values of *k+l* on *0kl*. The corresponding extinction symbol is *Pn-a*, which leaves two choices for the space group: *Pnma* and $Pn2_1a$.

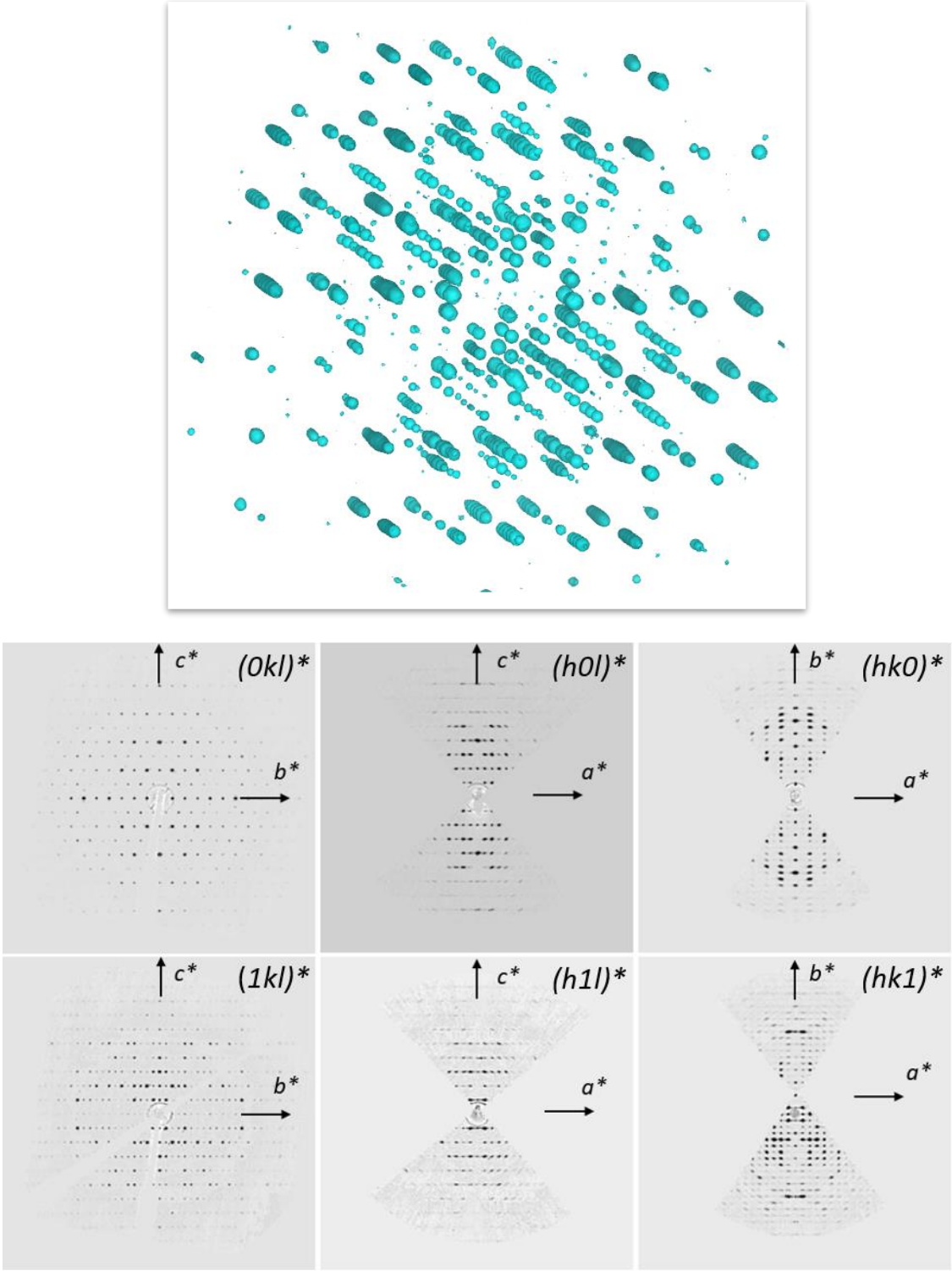

Figure 3.6: *At the top, 3D distribution of the measured intensities in reciprocal space from Bulachite is shown. At the bottom, 6 principle hkl sections from the 3D distribution. It can be seen that despite the preferential orientation, a tilt range of 104° was sufficient to gather information through all 3 axes. The extinctions observed here lead to the Pn-a extinction symbol.*

1.4 Structure Solution

Given the two possibilities for the space group, the strategy was to perform structure solutions for the two possible space groups and compare the quality of the resulting models. Data quality from different crystals was assessed primarily via the *hkl* sections, where clearly spotty reflections indicate a high degree of crystalline order. One dataset was chosen for structure determination using this criterion, which diffracted at a resolution of 0.8 Å. This dataset contained 2438 independent reflections and a data completeness of 75% for a resolution of 0.8 Å, the effective missing cone being reduced thanks to orthorhombic symmetry. Due to preferential orientation of the particles, data merging was not performed since the gain in completeness was estimated to be very limited. Inspection of the *hkl* sections from different crystals showed that the flat face of the crystals corresponded to the (**b,c**) plane, with the **c** axis presumably being parallel to the long dimension of the laths.

For the structure solution process, charge flipping via Superflip [187] and direct methods via SIR2014 [186] were used. The principles behind these algorithms are discussed in Chapter 2. Structure models with the two possible space groups were obtained from the chosen dataset. To assess the coherence of the structure models output by the algorithms, inter-atomic distances were compared to those from minerals with similar chemical composition. Two such minerals with the same Al/As ratio used to this end were Penberthycroftite [$Al_6(AsO_4)_3(OH)_9(H_2O)_5$].8$H_2O$ [195] and Bettertonite [$Al_6(AsO_4)_3(OH)_9(H_2O)_5$]. 11$H_2O$ [196]. In these compounds, Al-O and As-O bond distances are in the range of 1.90-2.00 Å and 1.60-1.70 Å, respectively. Considering these criteria, the most coherent model was obtained from SIR2014 using the *Pnma* space group. The list of atomic coordinates of the structure model is reported in **Table 3.1**. The structure is represented on **Figure 3.7**.

Table 3.1: *List of raw fractional atomic coordinates obtained via SIR2014 using Pnma as space group. The height represents the density attributed to the atom in the electrostatic potential map.*

Atom	Height	x	y	z	B(Å^2)
As1	5.54	0.325	0.01	0.117	0.81
As2	4.83	0.4	0.25	-0.074	0.69
Al1	2.83	0.134	0.07	0.258	1.39
Al2	2.73	0.162	-0.1	0.252	1.49
Al3	2.56	0.211	0.169	0.005	1.66
O1	2.17	0.208	0.158	0.25	0.73
O2	2.07	0.233	-0.002	0.216	1.00
O3	1.9	0.239	0.157	-0.235	1.49
O4	1.89	0.302	0.25	0.005	1.60
O5	1.84	0.419	0.021	-0.249	1.38
O6	1.82	0.315	0.092	0	1.73
O7	1.75	0.139	0.095	0.02	1.49
O8	1.7	0.146	0.25	-0.022	0.64
O9	1.68	0.346	-0.064	-0.003	2.43
O10	1.63	0.395	0.019	0.27	1.29
O11	1.62	0.348	0.116	0.509	2.31
O12	1.58	0.417	0.175	-0.201	1.00
O13	1.4	0.518	0.121	0.202	2.69
O14	1.22	0.484	0.25	0.081	2.60
H1	0.92	0.448	0.25	0.471	1.32
H2	0.52	0.137	0.25	0.563	1.32
H3	0.52	0.545	0.25	-0.172	1.32
H4	0.45	0.057	0.25	-0.148	1.32
H5	0.29	0.421	0.25	0.386	1.32

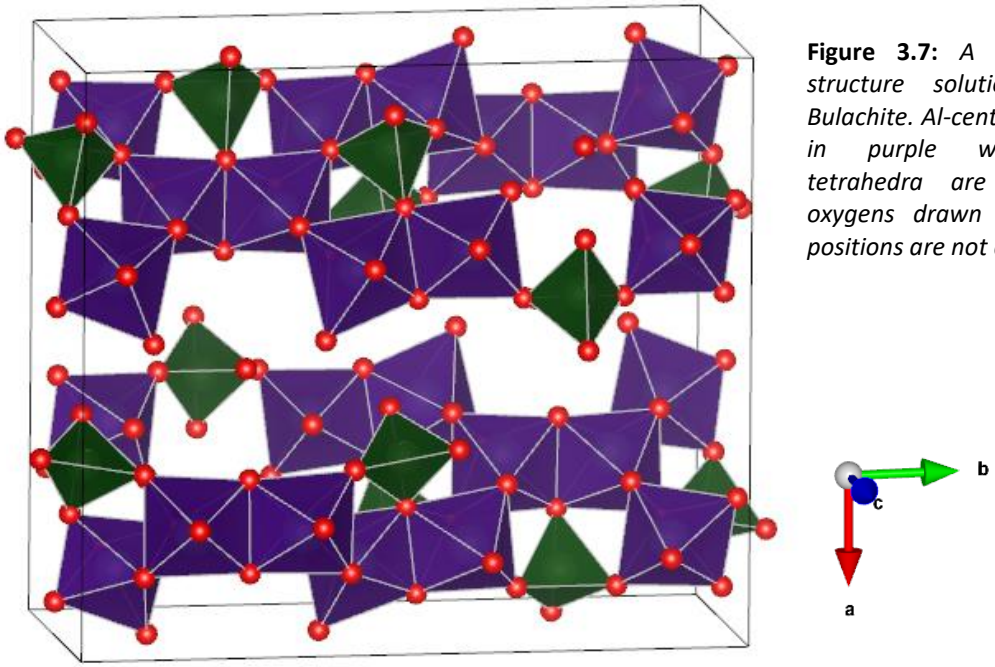

Figure 3.7: *A projection of the structure solution obtained for Bulachite. Al-centered octahedra are in purple while As-centered tetrahedra are in green, with oxygens drawn in red. Hydrogen positions are not drown.*

A hetero-polyhedral layered structure is obtained, composed of spiral columns of edge-sharing AlO_6 octahedra which are inter-connected by AsO_4 tetrahedra via corner-sharing. In addition to the coherence of the inter-atomic distances, this structure solution was also chemically coherent where all the cations and oxygens were correctly identified without manual intervention. This is evident when comparing values in the height column in **Table 3.1**. The amplitudes of peaks in the electrostatic potential map are related to the atomic weights, and in this model clear jumps are seen passing from one type of atom to another. The final *R* value of the model was 30.11%, calculated by SIR2014. Hydrogen positions proposed by SIR2014 were initially discarded since they could not be chemically interpreted. The hydrogen positions contained in the structure could not be directly determined from the structure solution but inferred during structure refinement discussed below.

1.5 Structure Refinement

As per our collaboration agreement, the structure model obtained from LD-EDT data was first refined on synchrotron PXRD data measured at the Australian Synchrotron by our collaborators. Data resolution was limited to 1.0 Å for this process, and data collection and refinement conditions are given in **Table 2**. The profile parameters of the PXRD pattern were established via a Le Bail structureless fit. The unit cell parameters were refined to be *a* = 15.3994(3) Å, *b* = 17.6598(3) Å and *c* = 7.8083(1) Å. If the Walenta unit

cell with a shorter *c* axis was used for the Le Bail fit, a deterioration of the fit parameters was observed. This could be a result of the higher resolution of the synchrotron PXRD data compared to the Debye-Scherrer camera with Fe *K*α radiation used by Walenta. The coordinates of the atoms were refined by imposing soft distance restraints for Al-O and As-O bond distances of 1.900(5) Å and 1.670(1) Å, respectively. These correspond to mean bond distances observed from other minerals with similar chemical composition. Angular restraints were also imposed on AsO_4 tetrahedra. Group isotropic displacement parameters for all atoms were also refined. Fit indices at the convergence of the refinement are given in **Table 3.2** and the refined PXRD pattern is presented in **Figure 3.8.** *Rp* and *Rwp* are respectively profile and weighted profile *R* factors comparing the calculated and measured PXRD intensity profiles. *GoF* is the goodness of fit, and *Rf* is the final *R* factor whose definition is given in **Chapter 2**.

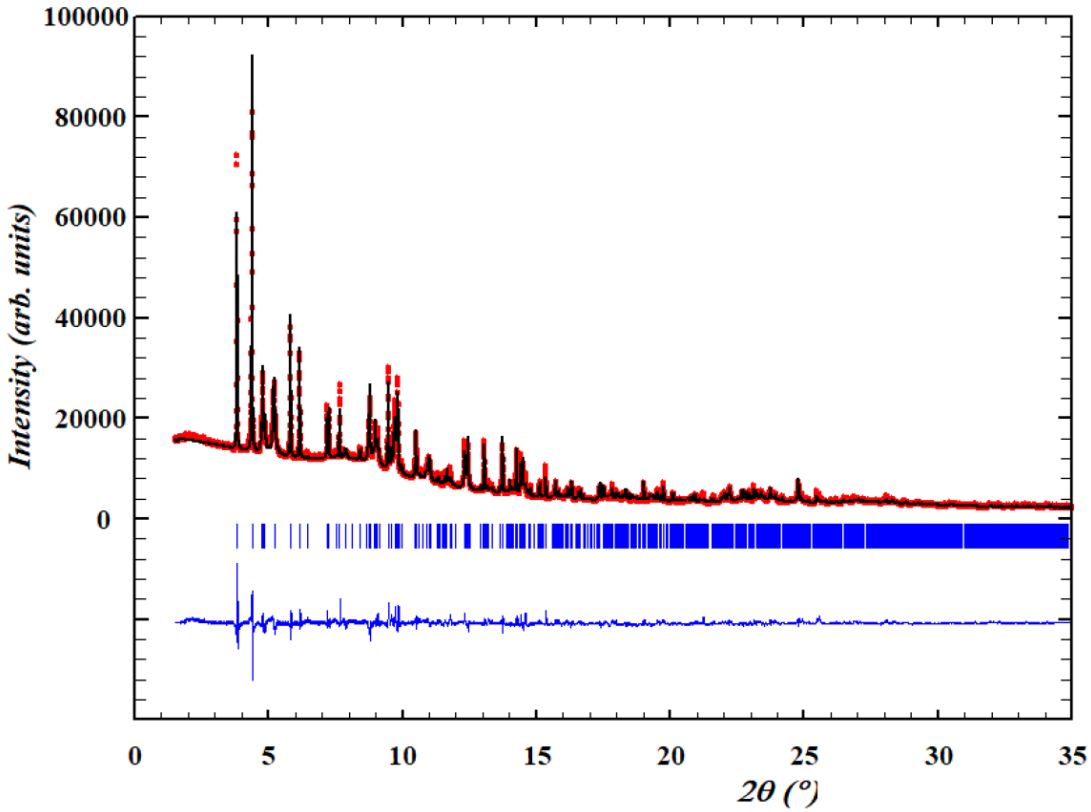

Figure 3.8: *Measured (red points) and calculated (black line) synchrotron PXRD pattern from Bulachite. The short bars indicate positions of the reflections, while the difference between the measurement and the fit is plotted in blue.*

Table 3.2: *Relevant parameters concerning synchrotron PXRD data collection and refinement for Bulachite.*

Formula	$[Al_6(AsO_4)_3(OH)_9(H_2O)_4]\cdot 2H_2O$
Unit-cell parameters (Å)	*a* = 15.3994(3), *b* = 17.6598(3), *c* = 7.8083(1)
Volume (Å3), Z	2123.46(7), 4
Space group	*Pnma*
X-ray radiation source, wavelength (Å)	Australian Synchrotron, 0.59028(6)
2θ range, step size (°)	1.50 to 104.82, 0.00375
Resolution for structure analysis (Å), number of contributing reflections	1.0, 1158
Number of profile parameters	8
Number of structural parameters/restraints	63/38
Profile function	Pseudo-Voigt
Background	Interpolation between 40 selected points
Rp*, *Rwp*, *GoF*, *Rf	3.73, 5.09, 4.29, 10.7

The list of refined atomic coordinates is given in **Table 3.3**. The bond valence sum calculations (BVS) done using parameters from Gagné and Hawthorne [197] revealed that some of the oxygens are O^{2-} ions, others carry only one negative charge and have to be interpreted as OH^- groups while others appear neutral and correspond to water molecules as part of the polyhedra surrounding the Al in the layers, and others in-between the layers. The positions initially proposed to be H1 and H2 by SIR2014, located in-between the layers were interpreted as oxygen positions making up the inter-layer water molecules. **Table 3.3** shows the BVS calculations for different atoms, and different types of oxygens are classified with different codenames. Counting of atoms in the resulting structure gave a chemical composition of $[Al_6(AsO_4)_3(OH)_9(H_2O)_4]\cdot 2H_2O$, where the number of water molecules per aluminum was adjusted compared to the initial composition proposed by Walenta.

On **Table 3.3**, It can be seen that the isotropic displacement parameters for cations are higher compared to those refined for the oxygen atoms. This can be considered unusual since typically heavier cation positions often showcase less displacement compared to smaller oxygens. More reasonable displacement parameters were obtained from refinement on electron diffraction data, as shown below.

Table 3.3: *List of atomic coordinates refined on PXRD data, for Bulachite. U is the isotropic displacement parameter while BVS stands for bond valence sum. For oxygens, O refers to oxygens without any H bonds, Oh refers to OH groups and Ow refers to oxygens of water molecules within the layers. W are also oxygens, corresponding to water molecules between the layers.*

Atom	Wyckoff	x	y	z	U (Å^2)	BVS
As1	8d	0.82245(2)	0.00921(2)	0.3827(4)	0.0368(6)	5.22
As2	4c	0.9057(3)	0.25	0.5824(6)	0.0368(6)	5.24
Al1	8d	0.6329(6)	0.0696(5)	0.2444(2)	0.0368(6)	3.11
Al2	8d	0.8397(6)	0.0964(5)	0.7535(2)	0.0368(6)	2.96
Al3	8d	0.7207(6)	0.1692(6)	0.4971(2)	0.0368(6)	2.7
O1	8d	0.7276(5)	0.0061(6)	0.2856(2)	0.0186(2)	2.19
O2	8d	0.9002(6)	0.0190(6)	0.2359(2)	0.0186(2)	1.32
O3	8d	0.8160(7)	0.0885(5)	0.5006(2)	0.0186(2)	2
O4	8d	0.8459(7)	0.0642(5)	0.5099(2)	0.0186(2)	1.86
O5	4c	0.8043(5)	0.25	0.5078(2)	0.0186(2)	2.28
O6	4c	0.9752(8)	0.25	0.4186(2)	0.0186(2)	1.32
O7	8d	0.9217(6)	0.17267(2)	0.7019(7)	0.0186(2)	1.82
Oh1	8d	0.7085(9)	0.1522(7)	0.250(2)	0.0186(2)	0.98
Oh2	8d	0.6300(10)	0.0952(9)	0.4819(2)	0.0186(2)	0.98
Oh3	8d	0.9259(8)	0.0208(7)	0.772(3)	0.0186(2)	1.1
Oh4	8d	0.7386(8)	0.1541(7)	0.740(2)	0.0186(2)	1.01
Oh5	4c	0.6390(2)	0.25	0.511(3)	0.0186(2)	1
Ow1	8d	0.5229(9)	0.1135(7)	0.226(3)	0.0186(2)	0.55
Ow2	8d	0.8415(2)	0.1119(9)	0.9944(2)	0.0186(2)	0.51
W1	4c	0.93	0.25	0.018	0.074(1)	
W2	4c	0.3652	0.75	0.0187	0.074(1)	

Following refinement on synchrotron PXRD data by our collaborators, the structure was also refined on electron diffraction data. This consisted of an initial kinematical refinement followed by dynamical refinement on the same LD-EDT crystal data used for structure solution. This was performed in Jana2006, where several parameters relevant to the refinement process can be adjusted. The maximal diffraction vector, which defines the resolution limit for the calculations, was set to 2.0 Å^{-1}. The maximal excitation errors for reflections to be included in dynamical calculations and for those to be included in the refinement process were set to 0.01 Å^{-1} and 0.1 Å^{-1} respectively. There is also a parameter called RSg, which represents to what extent the intensity of a reflection is integrated by the beam precession. An RSg

lower than 1 corresponds to the case of reflections which pass through the exact Bragg condition twice during the precession motion. The RSg was set to 0.4 during this refinement. The number of integration steps along the precession circuit for the integration of the intensities was set to 128. This parameterMore detailed information about these parameters can be found in [190]. The thickness of the crystal was refined to 507 Å. Similar to the PXRD refinement, the positions initially identified as H1 and H2 by SIR2014 and initially discarded were identified in the Fourier difference map as oxygen positions of inter-layer water molecules. Once these positions were added to the structure, the atomic coordinates and isotropic atomic displacement parameters of all atoms were dynamically refined, and the final *R* values presented in **Table 3.4** were obtained. The list of dynamically refined atomic coordinates is given in **Table 3.5.** It can be seen that the thermal displacement parameters of the oxygens are now higher than those of the cations, with inter-layer oxygens being in particular higher than for the other oxygens.

Table 3.4: *Final dynamical refinement parameters on LD-EDT data from Bulachite.*

R(obs)	Reflections/Parameters	wR(obs)	R(all)	wR(all)	GoF(all)	GoF(obs)
10.56	2792/184	11.15	24.68	13.37	2.24	1.24

Table 3.5: *List of atomic coordinates refined on LD-EDT data, for Bulachite. B is the isotropic displacement parameter while BVS stands for bond valence sum. For oxygens, O refers to oxygens without any H bonds, Oh refers to OH groups and Ow refers to oxygens of water molecules within the layers. W are also oxygens, corresponding to water molecules between the layers.*

Atom	Wyckoff	x	y	z	B (Å^2)	Dist (Å)
As1	8d	0.8242(2)	0.0097(1)	0.3832(2)	0.0086(4)	0.031
As2	4c	0.9034(3)	0.25	0.5773(3)	0.0074(6)	0.054
Al1	8d	0.6334(4)	0.0720(2)	0.2396(4)	0.0051(8)	0.055
Al2	8d	0.8393(4)	0.0966(2)	0.7480(4)	0.0063(7)	0.056
Al3	8d	0.7140(4)	0.1665(2)	0.4916(4)	0.0052(8)	0.091
O1	8d	0.7289(7)	0.9977(3)	0.2846(6)	0.0223(2)	0.071
O2	8d	0.9011(7)	0.0219(3)	0.2307(6)	0.0244(2)	0.067
O3	8d	0.8128(7)	0.0906(3)	0.4958(6)	0.0241(13)	0.073
O4	8d	0.8407(7)	0.9334(3)	0.5053(6)	0.0246(13)	0.099
O5	4c	0.8037(8)	0.25	0.4855(7)	0.0060(14)	0.178
O6	4c	0.9862(2)	0.25	0.4348(1)	0.0380(24)	0.191
O7	8d	0.9179(7)	0.1751(3)	0.7036(6)	0.0149(12)	0.075
Oh1	8d	0.7088(6)	0.1552(2)	0.2458(6)	0.0107(11)	0.062

Oh2	8d	0.6295(7)	0.0921(3)	0.4776(6)	0.0200(13)	0.050
Oh3	8d	0.9323(6)	0.0219(2)	0.7482(6)	0.0107(11)	0.215
Oh4	8d	0.7368(6)	0.1569(2)	0.7322(6)	0.0167(12)	0.084
Oh5	4c	0.6445(9)	0.25	0.5121(7)	0.0084(15)	0.064
Ow1	8d	0.5233(8)	0.1238(3)	0.2010(7)	0.0346(16)	0.270
Ow2	8d	0.8420(8)	0.1189(3)	0.9924(7)	0.0341(15)	0.125
W1	4c	0.9654(13)	0.25	0.0290(12)	0.0611(31)	0.560
W2	4c	0.3400(20)	0.75	0.0581(18)	0.1872(66)	0.503

1.6 Discussion

Figure 3.9 shows the refined crystal structure of Bulachite. In addition to the polyhedral layers identified in the structure solution, the inter-layer water molecules are now visible represented by isolated oxygen atoms. Compared to the raw structure solution, the separation of the layers due to water molecules is more visible. Bulachite can be derived from pharmacoalumite with whom it is closely associated through acidic dissolution and reprecipitation:

$$3\,[Al_4(AsO_4)_3(OH)_3]^- + 8.5H_2O + 5H^+ \rightarrow 2\,[\boldsymbol{Al_6(AsO_4)_3(OH)_9(H_2O)_4}] + 3AsO_{2.5}$$

As mentioned above, hydrogen positions were not considered during the structure determination process. This is due to the very weak scattering from hydrogen atoms leading to their real space density being difficult to determine in an accurate manner.

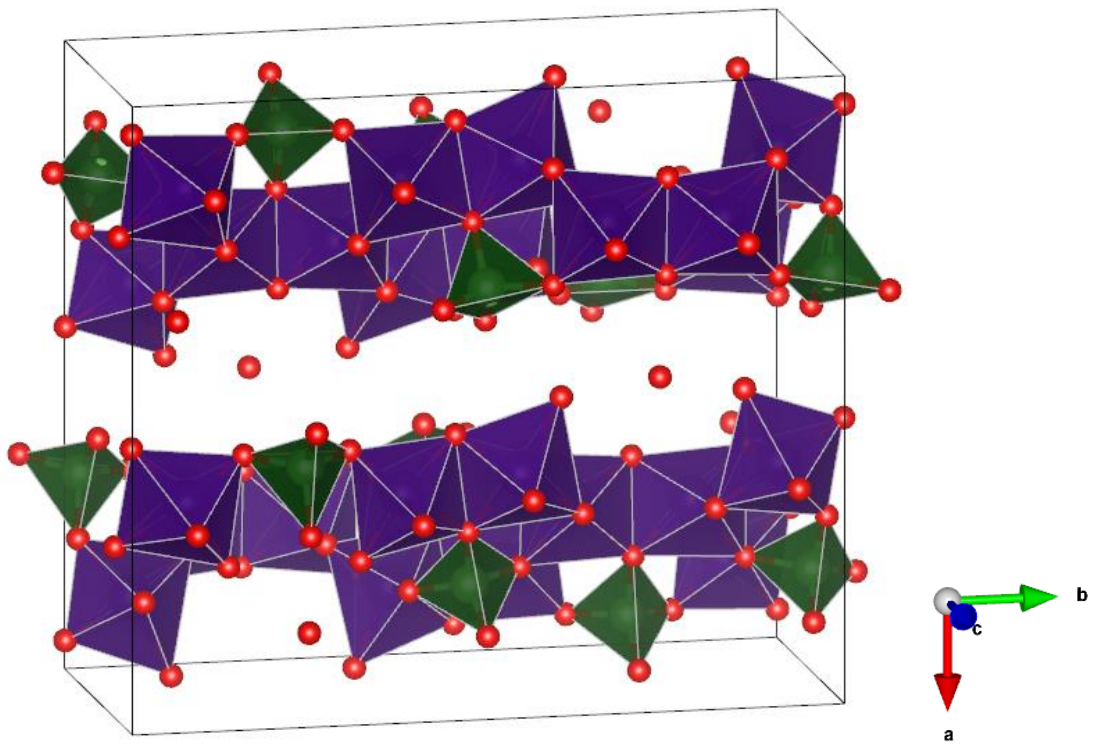

Figure 3.9: *A projection of the refined Bulachite structure. Al-centered octahedra are in purple while As-centered tetrahedra are in dark green, with oxygens drawn in red. Hydrogen positions are not drawn. The isolated oxygens between the layers correspond to inter-layer water molecules.*

As mentioned in Section 1.1, the Cap Garonne sample contained a hydrated phase in addition to Bulachite. This phase has the same aluminum to arsenate ratio but contains more water molecules in its unit cell. The resulting unit cell has the same *b* and *c* parameters but a large increase in *a* from 15.4 Å to 19.9 Å. This reflects an increase in the layer separation to incorporate an increased amount of water molecules. When the hydrated phase is heated, the unit cell starts to change above 50°C and transform completely into the Bulachite unit cell between 75°C and 100°C, as seen from synchrotron PXRD data. The transformation is not reversible [194].

During this thesis, non-pre-heated hydrated samples were also obtained for structure determination. Specimen preparation and data acquisition were performed in an identical manner as for Bulachite. Data processing however constantly yielded the Bulachite unit cell with the shorter *a* axis. This is presumably due to dehydration of the crystals inside the TEM. This could be either due to the escape of water molecules due to the TEM vacuum, or destruction of water molecules due to radiolysis. Structural collapse due to partial or complete dehydration of hydrated minerals in TEM vacuum has previously been reported [198], [199]. It is possible to prevent dehydration by working in cryogenic conditions to inhibit water diffusion [200], [201]. This however was not possible with the available hardware during this thesis. The

crystal structure of this phase was later characterized by our collaborators in Melbourne and named Galeaclolusite [202].

2) $\{[Mn^{II}_2[NIT(H, H)Im]_3(CF_3SO_3)\}_n$ (reference YI_OTf03)

2.1 Background

The next compound, referenced as YI_OTf03, is a metal organic framework (MOF). MOFs are porous coordination networks, typically consisting of a metal or a metal-containing cluster coordinated to an organic ligand, referred to as the linker molecule. Their structures are often permanently porous, whose characteristics can be tuned by modifying the metal and organic linker composition, as well as the synthesis conditions [203]. Their tunable porosity has shown promise in various fields such as catalysis [204], drug delivery [205] and chemical sensing [206].

The sample was obtained through collaboration with Dominique Luneau (LMI UCBL Lyon France). It is a 2D manganese-radical coordination polymer with an expected chemical composition of **$\{[Mn^{II}_2[NIT(H, H)Im]_3(CF_3SO_3)\}_n$**. where NIT and Im refer to nitronyl nitroxide and imidazole, respectively. This compound is a part of a family of manganese-nitronyl nitroxide ($C_7H_{13}N_2O_2$) radical 2D frameworks where the same Mn-radical layers are present but are separated by a different range of anions such as ClO_4^-, BF_4^- , PF_6^- [207]–[209] (**Figure 3.10**).

Figure 3.10: *Schematization of how 2D manganese-radical layers and the anions are stacked in compounds similar to YI_OTf03. Manganese-radicals form 2D layers which are separated by the anions, whose size influences the interlayer separation distance. The chemical content of the layer is the same for all compounds, but different anions are inserted among them.*

The size of the different anions has consequences on the crystal structure, especially on the size of the unit cell related to the inter-layer separation distance. The anion inserted in YI_OTf03 is triflate $CF_3SO_3^-$. These compounds showcase hysteretic valence tautomerism, where single and double bonds can be formed or ruptured without migration of atoms or molecules via a rapid reorganization of electrons making up the bonds. This manifests as a thermo-induced oxidation of manganese (II) ions to manganese (III) while some of the NIT-Im radicals are reduced. Different transition temperatures are obtained when different anions are present [208], and the transition temperatures are pressure-dependent [209]. This can be exploited into applications such as sensors, switches and signal processing.

Crystallographic characterization of members of the same 2D Mn-radical framework family with different anions have shown them to be isostructural [208], all of them crystallizing in the monoclinic space group $P2_1$ and having roughly the same unit cell dimensions (a ~ 10.3 Å, b ~ 17.5 Å, c ~ 11.0 Å, β ~ 94.0°) at room temperature. MOFs are often synthetized in powder form containing nano-sized crystals, from which it is difficult to obtain the crystal structure from XRD data. This is due to the difficulty of obtaining crystals large enough for X-ray diffraction. Although crystal structures of other compounds were determined via synchrotron XRD, the crystal structure of YI_OTf03 remained unknown. This could be due to it having a relatively more complex structure than other members of its family, which results in more overlaps in PXRD data due to larger unit cell parameters. 3D ED has had recent success in *ab initio* structure determination of MOFs [210] thanks to its capacity to extract high-resolution information from small crystals. However, as discussed in Chapter 1, MOFs are known for their beam-sensitivity [10], [210]. Organic linkers inside MOFs are prone to radiolysis damage, and smaller radicals produced by radiolytic bond breakage can easily diffuse inside the crystal due to the porous nature of the structure. This lowers the probability of recombination and amplifies the rate of secondary reactions resulting in a rapid loss of crystallinity. It is therefore necessary to collect high-resolution data from small crystals without damaging them, which can be achieved through low-dose electron diffraction.

2.2 Specimen Preparation

The sample was obtained in form of a polycrystalline powder. Initially, the powder was crushed in ethanol and a drop was deposited onto a TEM grid with a flat carbon support for TEM observation. The morphology of the crystals was seen to be that of very thin plates (**Figure 3.11**). Most particles had the same plate shape, and qualitative averaging from a number of different plates gave two planar dimensions of 400 nm and 4-5 µm. The perpendicular dimension could not be quantitatively determined in the same

manner. However, the plates were so thin that they were almost invisible under electrons in imaging mode without the objective aperture. This was especially the case in low dose conditions. An estimation of the third dimension was therefore in the order of tens of nm. The observed morphology is in accordance with an expected 2D structure, as the planar dimensions presumably made of the 2D Mn-radical layers were much larger than the perpendicular counterpart, along which the anions are intercalated.

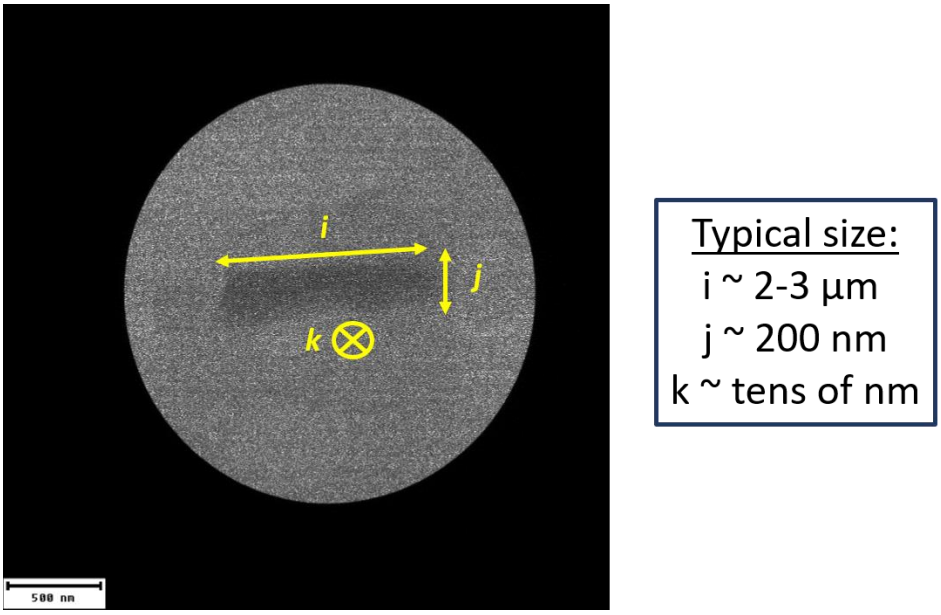

Figure 3.11: *TEM image of a representative YI_OTf03 particle, with the typical crystal dimensions indicated. Measurements from multiple crystals were averaged. The perpendicular dimension (i.e. thickness) could not be measured, but the small order of magnitude is estimated given that the crystals were almost invisible without contrast aperture in image mode.*

Prior to LD-EDT data acquisition, beam-sensitivity of the specimen was assessed to determine optimal exposure conditions. Qualitative diffraction fading was employed to this end (see Chapter 1). The criterion was to determine the electron dose at which high-resolution peaks disappear. Diffraction fading measurements were performed on multiple crystals, and the sensitivity was seen to be fairly consistent, with visual inspection showing that the high-resolution peaks faded at around 1.8 $e^-/Å^2$ (**Figure 3.12**). This critical dose criterion however tends to overestimate the amount of dose before the onset of damage, as data can already be affected before the disappearance of high-resolution reflections, in form of relative intensity changes and partial fading. It was therefore decided that a maximum dose of 1.0 $e^-/Å^2$ should be used to avoid beam damage as much as possible while keeping a reasonable signal-to-noise ratio.

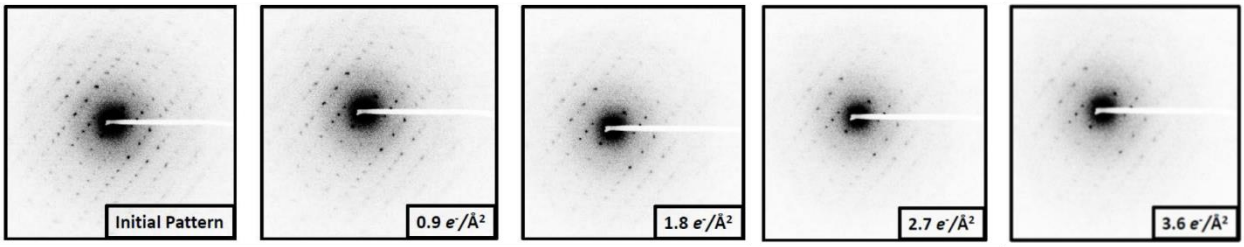

Figure 3.12: *Diffraction fading observed on YI_OTf03. It can be seen that the reflections fade progressively compared to the initial pattern, with the outermost higher-resolution reflections fading the fastest. Visible changes are especially apparent between 0.9 and 1.8 $e^-/Å^2$.*

Collection of 3D ED data from very thin crystals can render data processing more difficult, due to reflections being measured in shape of streaks, as opposed to spotty reflections in reciprocal space [8]. This makes the measurement of lattice spacing more difficult and intensity integration less precise, due to the difficulty of locating the exact position of reflections in the reciprocal space. In contrast, too thick crystals exhibit more dynamical diffraction which also affects the data quality in a negative manner. Ideally, an intermediary crystal thickness should be preferred to optimize the diffraction data quality. Considering the very thin YI_OTf03 crystals obtained by the standard preparation method with grinding, specimens for LD-EDT experiments were subsequently prepared by sonication in ethanol as opposed to grinding, with the intention of obtaining crystals as thick as possible. Small quantities of nanocrystalline powder were dissolved in ethanol and placed inside an ultrasound bath, where the crystals keep their initial size without being broken into smaller pieces by grinding but are still dispersed enough to be deposited onto the TEM carbon grid. After a few minutes of sonication, a few droplets were deposited on the carbon grid and the ethanol was removed by evaporation. Droplets were taken from the bottom of the container used for sonication, where the concentration of the heaviest crystals is expected to be higher. The concentration of crystals on the TEM grid could be adjusted by modifying the number of droplets introduced on the grid.

2.3 Data Acquisition

The search for suitable crystals was performed under low dose conditions, to avoid any prior damage to crystals. This was in practice difficult due to the thin nature of the crystals making them less visible under low illumination. Whenever it was possible to locate a particle, the TEM was quickly switched to diffraction mode to check for crystallinity. The dose was kept at the critical value determined via diffraction fading by choosing an adapted dose rate by varying the TEM spot size, limiting the tomography range to +/-40° and the exposure time per frame to 400 ms. This was an initial compromise to maintain a reasonable

signal-to-noise ratio as well as data completeness. The beam was precessed at 1.05° and the angular step size between two successive frames was 1°. It was seen that most particles were well crystallized, and LD-EDT datasets were collected from 20 different single crystals under these conditions. Due to the consistent thin plate morphology, all observed particles were preferentially oriented with their large section parallel to the grid.

2.4 Data Processing

The recorded data was processed with PETS2 and Jana2020, as described in **Chapter 2** and in an identical manner as Bulachite. As expected, due to the thin nature of the crystals, the data showed streaks in the reconstructed reciprocal space in the direction parallel to the beam. This made the measurement of the lattice spacing along this direction and as a consequence unit cell determination more difficult. The unit cells determined from various particles were monoclinic (*b*-setting) with consistent *a* and *b* axis lengths of ~9.8 Å and 19.0 Å respectively, whereas the *c* axis length and β angle (between the **a** and **c** axes) diverged among the particles. This was due to the aforementioned streaks being parallel to the **c** direction, which is systematically parallel to the missing cone of the tomography. The data obtained along the **c** axis here is purely dependent on a 3D reconstruction during data processing, as opposed to a direct measurement. This was the case for all measured datasets, due to the preferential orientation.

To determine a reliable unit cell, the strategy was to use the automatic unit cell search feature in PETS2 to determine the length of the *c* axis, and then use *hkl* sections obtained from the indexed data to assess data quality, with the crystal with the least streaks considered to be the most reliable for unit cell determination. Out of the 20 datasets, *hkl* sections of one dataset in particular showed a low density of streaks, and clearly defined lattice directions (**Figure 3.13**).

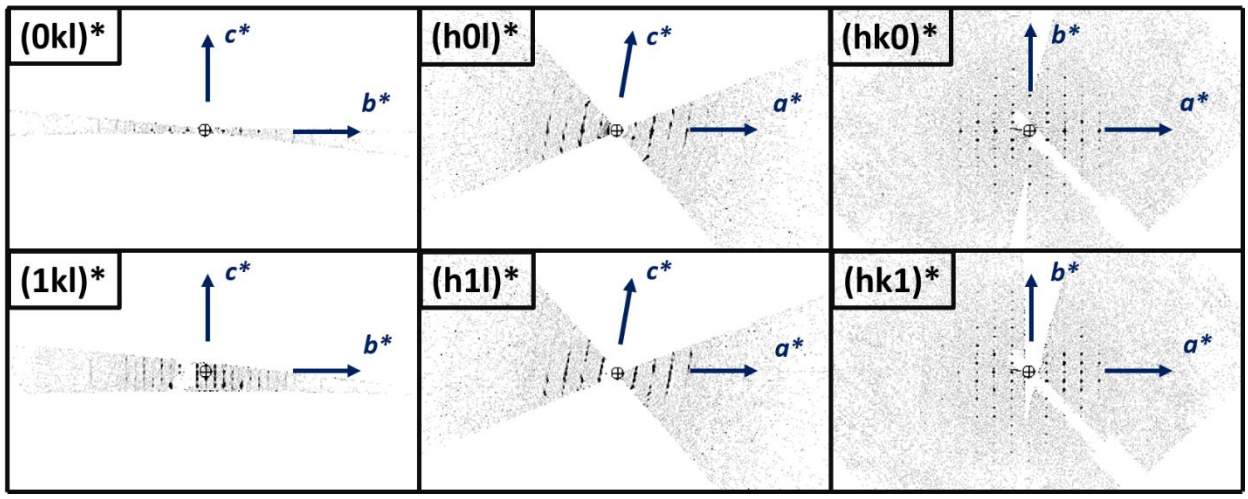

Figure 3.13: *6 principle hkl sections from a YI_OTf03 crystal with a low density of streaks. It can be seen that very little information is available along the* ***c*** *axis. The extinctions observed here lead to the* $P2_1/c$ *space group, but extinctions on h0l were not common to all datasets.*

Figure 3.14 shows the cylindrical projection of the reciprocal space obtained from this dataset. Despite the presence of sinusoidal lines, the remaining streaks blur the reciprocal space along a particular direction (vertical), which falls onto the missing cone during data acquisition.

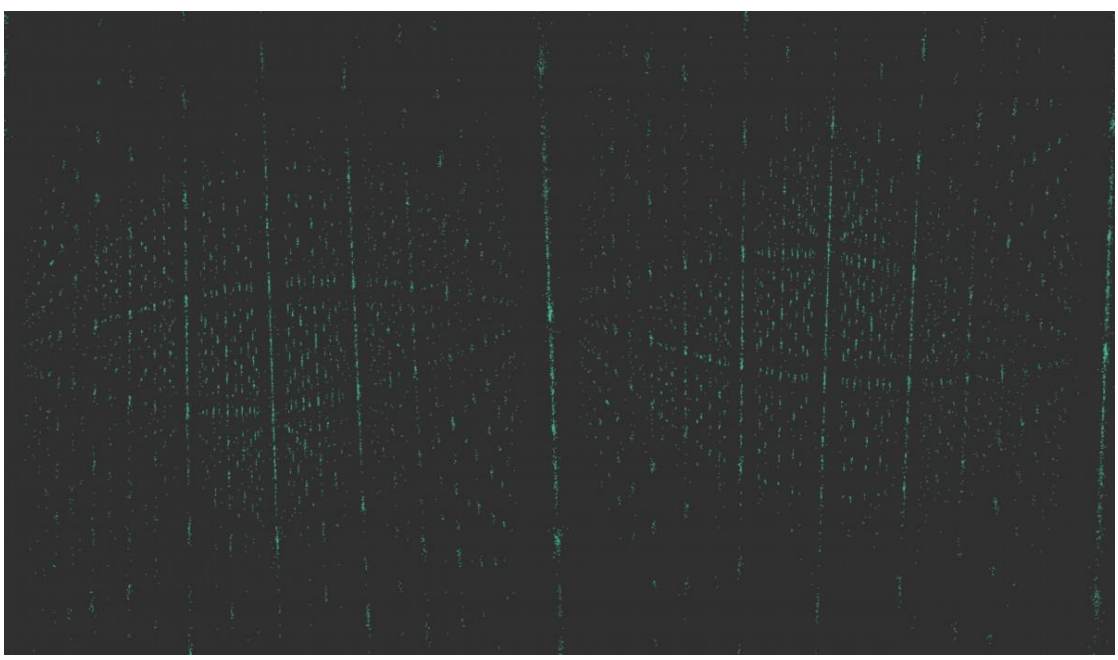

Figure 3.14: *Cylindrical projection of the intensity clusters used for refining the orientation of the tomography rotation axis, from a dataset with a low density of streaks in reciprocal space.*

The unit cell obtained was monoclinic with unit cell parameters *a* = 9.8 Å, *b* = 18.9 Å, *c* = 25.9 Å, and β= 99.7° (**Figure 3.15**). This monoclinic unit cell agrees with the systems of the other compounds of the family,

but the unit cell volume is more than doubled compared to other compounds. A comparison of unit cell parameters of compounds in the same family is given in (**Table 3.4**). The doubling is due to the substantial increase in *c* axis length, while *a* and *b* axis lengths are comparable to other compounds. The increase in *c* could be due to a larger space between the 2D layers and the triflate anions, with triflate anions possibly occupying a larger space compared to other anions. All datasets were consequently indexed with this unit cell.

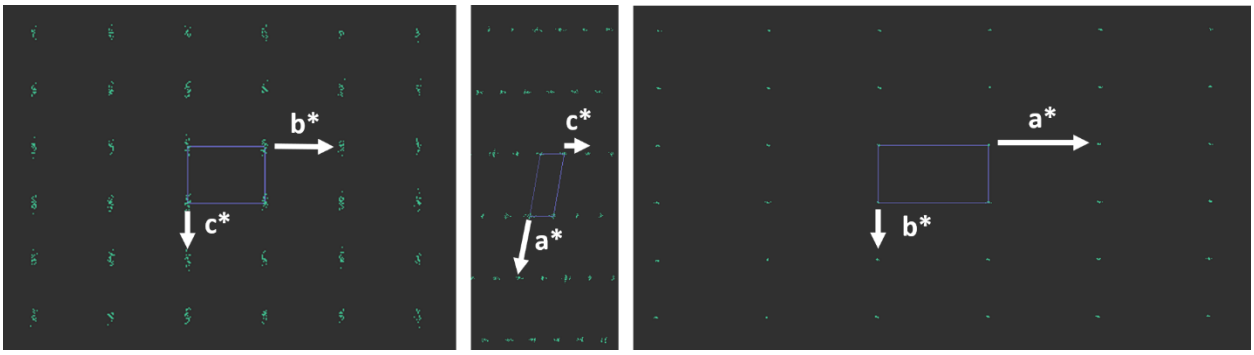

Figure 3.15: *Display of clustered intensities in reciprocal space with the unit cell superposed. The three sections are views along the a*, b* and the c* axes in that order from left to right. The steaks along the c* direction can be seen, which reduces the precision on its length. The 3 projections are not on the same scale.*

On **Figure 3.13**, the apparent systematic absences are $k = 2n$ for the *0k0* row and $l = 2n$ for *h0l*, which suggests the space group $P2_1/c$. The $k = 2n$ extinction for the *0k0* row was common in many datasets, where streaks in *hkl* sections were weak enough to distinguish systematic extinctions. The *h0l* extinctions however were not common to other datasets. In some cases, $P2_1/n$ ($h + l = 2n$) and $P2_1$ (no *h0l* extinctions) were observed. This is presumably due to a lack of reliable information along the ***c**** direction, which falls in the missing cone during data acquisition. Dynamical diffraction could also play a role in blurring extinctions, although given the thin nature of the crystals and the *0k0* extinctions being clear in many crystals, data should not be significantly affected by dynamical diffraction. The presence of a glide plane (*c* or *n*) was therefore unclear.

Table 3.4: *Unit cell parameters of compound with the same 2D manganese-radical layers separated with different anions. A clear jump in the length of c (perpendicular to the layers) axis for the triflate anions can be seen.*

Anion	*a* (Å)	*b* (Å)	*c* (Å)	β (°)
ClO_4^-	10.325(1)	17.870(1)	11.063(1)	93.430(4)
BF_4^-	10.308(3)	17.943(5)	11.085(3)	94.077(3)
PF_6^-	10.850(2)	17.085(4)	11.085(3)	94.362(16)
CF_3-SO_3^-	9.8	18.9	25.9	99.7

In an attempt to determine the space group more accurately, additional data was collected where the tilt range per dataset was increased from +/- 40 ° to +/- 50°, thereby increasing the data completeness which was typically in the 40-50% range in previous data. The total electron dose per particle was kept constant by subsequently reducing the exposure time per frame. This allowed to collect data with a completeness up to 70%, however the **c** axis still remained inside the missing cone despite the higher completeness.

2.5 Alternative Data Collection to Break Preferential Orientation

In order to obtain reliable information in the direction of the ***c**** axis, it was necessary to gather data from crystals in different orientations. Previous methods to break preferential orientation of crystals on TEM grids used in literature [211] include perturbing the flat TEM grid in order to induce a non-homogenous orientation distribution of particles upon deposition, or introducing obstacles on a flat grid which prevents crystals from lying flat. These two approaches were adapted here considering the available resources.

Perturbation of a TEM grid was deemed unpractical considering the need to constantly re-adjust the eucentric height prior to data acquisition. Instead, TEM grids were bent in half through a line close to their middle section so that the particles deposited at the edge of the bent grid would have rotated orientations. This approach was not fruitful however since the concentration of particles exactly at the edge of bending was too unpredictable. Standard deposition where particles were deposited before bending led to too few particles on the edge, while maintaining the grid vertically to force the migration of particles to the edge during ethanol evaporation led to a too high particle density, preventing single crystal data acquisition. Another difficulty was that the carbon film had a higher apparent thickness close to the edge due to bending, which made the localization of thin plates more difficult at low dose rates.

A more practical approach was to introduce obstacles on the flat TEM grid. The choice of obstacles to be deposited on the grid was spheres of polystyrene. This choice was coherent in this case since their

amorphous structure would not affect the diffraction data acquisition, and their morphology was unaffected by the electron beam or the TEM vacuum. Ideally, the size of the obstacles should be comparable to the particle size for an efficient orientation perturbation. Spheres of variable sizes were available to us varying from 50 to 500 nm, and the approach was to prepare a cocktail of different sphere sizes (50, 350 and 500 nm) to see which size was most efficient in perturbing the crystals. TEM observation showed that a high density of obstacles coupled with moderate particle density was optimal to locate a reasonable amount of perturbed crystals (**Figure 3.16**).

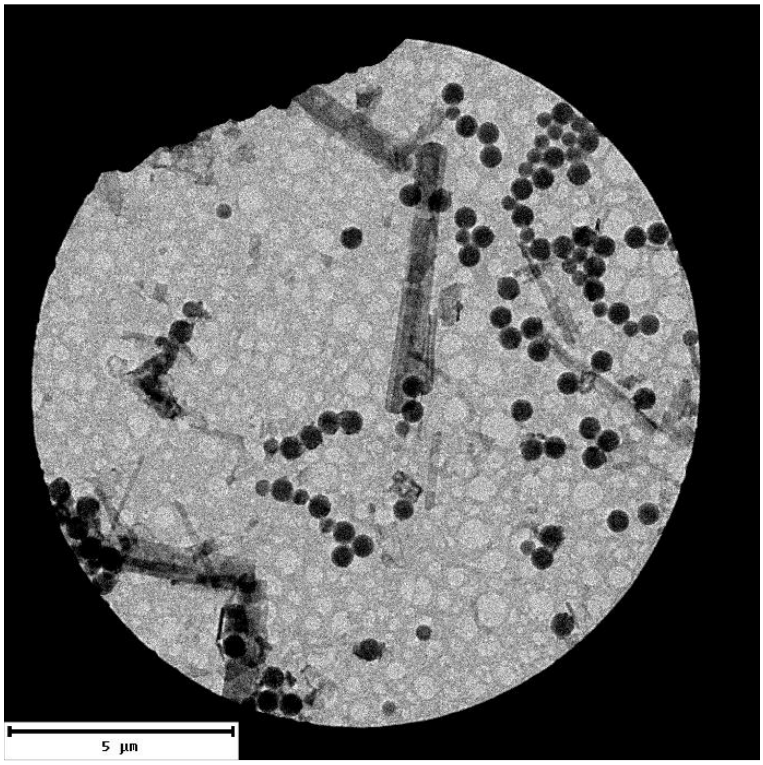

Figure 3.16: *TEM image of a grid where spherical particles of polystyrene were introduced to perturb the preferential orientation of YI_OTf03 crystals. The dark circles are the polystyrene spheres in different sizes, while YI_OTf03 crystals are seen as more transparent plates. As seen on this image, it was possible to position YI_OTf03 crystals on the spheres to change their orientation.*

LD-EDT data acquisition from such perturbed crystals showed that the missing cone was indeed rotated, although with the **c** axis still outside the tomography range. A perturbation of high amplitude is needed to record data along the x axis. However, the very thin nature of the crystals makes this setting statically improbable, the plates leaning on polystyrene spheres with a high angle tending to slip down.

2.6 Structure Determination

Attempts at *ab initio* structure solution with LD-EDT data were unsuccessful due to low data resolution. Most crystals diffracted up to 1.8 Å, with the best resolution available out of the datasets with spotty *hkl* sections being 1.5 Å. This is insufficient since direct methods typically require a data resolution of 1.1-1.2 Å to solve structures [212]. The reason behind the low resolution of this data might be either a low initial crystallinity of the crystals, or beam damage despite the low dose conditions. The low crystallinity might be a result of in-plane transitions in the 2D Mn-radical layers decreasing short-range order, which cannot be confirmed before structure determination. Considering beam damage, the analysis of the evolution of data resolution during data acquisition did not show a significant drop in resolution over time. During data processing, PETS2 can be used to measure the maximum resolution available on each individual frame. An example is plotted in **Figure 3.17**. The resolution fluctuates among the frames due to their evolving orientation and noise in data, but no significant drop is seen in later frames. This was observed on multiple crystals, meaning that they did not get damaged during data acquisition. It is however possible that they were pre-damaged during the search for crystals on the grid, despite the use of a low dose rate. As discussed in Chapter 1, it is always the high-resolution reflections who fade first, and they fade much more rapidly than lower resolution reflections.

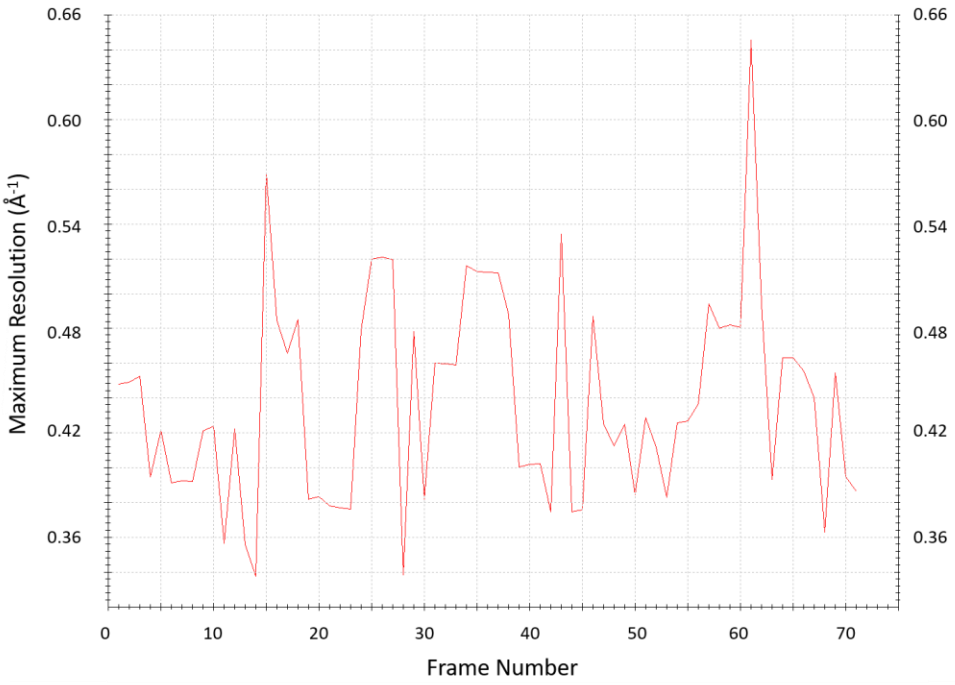

Figure 3.17: *Example of how data resolution evolves in consecutive frames of LD-EDT data on YI_OTf03. The absence of a significant drop over time suggests that the crystals are not noticeably damaged during data acquisition.*

When an *ab initio* determination is not possible, an alternative method to achieve structure solution is molecular replacement [188]. This method is based on the knowledge of which molecules and fragments are present inside the unit cell, without their exact locations and orientations being known. Atoms inside the molecules are fixed as rigid intramolecular bond lengths and angles, the variables for each molecule or fragment being their position and orientation. The goal is then to minimize the difference between measured and calculated structure factors for different positions and orientations of the molecules. Molecular replacement has previously been used on 3D ED data [213], [214] to solve protein structures, which also makes it suitable for 3D ED data on MOF structures with a large number of independent positions. In the case of YI_OTf03, the conformation of the molecules inside the layers as well as the structure of the triflate anions are known from compounds in the same family. With the unit cell and space group determined from LD-EDT data, they can therefore be defined as input for molecular replacement.

To implement structure determination through molecular replacement, we collaborated with Dominique Housset and Wai-Li Ling from the Institute of Structural Biology (IBS, Grenoble France). Additional diffraction datasets on YI_OTf03 were collected at IBS Grenoble with the goal of recording higher

resolution data. The new data was collected on a Tecnai F20 TEM operated at 200 kV, equipped with a Medipix hybrid pixel detector [215]. Hybrid pixel detectors are more sensitive than CMOS detectors as the pixels count electrons directly without readout noise. High-resolution reflections with weaker intensity can therefore be more easily recorded without increasing the electron dose. The specimen preparation was identical to previous experiments. As opposed to a manual search of particles on the Phillips CM300, particles were located digitally via low magnification images, which allows to reduce their pre-exposure. 3D ED data was collected in continuous rotation mode (see Chapter 2) where crystals are continuously rotated during data acquisition, without beam precession. The rotation speed was kept constant, and each image corresponded to a tilt range of 0.367°. The total tilt range varied between +/- 45° and +/- 60°, depending how long crystals could be kept under the beam. Data was acquired with a parallel beam in SAED mode. A total of 31 new datasets was obtained.

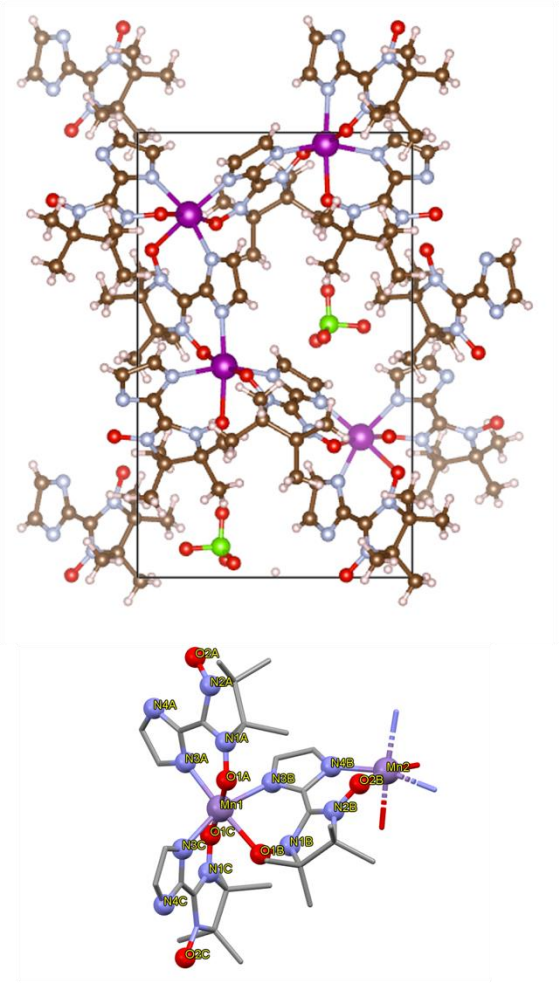

Figure X: *(top) The crystal structure of $\{[Mn^{II}_2[NIT(H, H)Im]_3(ClO_4)\}_n$ (bottom) The Mn-Radical input molecule used for molecular replacement*

The XDS software package [216] was used to process the new datasets. Out of the 31 measured datasets, 18 were indexed with the monoclinic unit cell previously determined from precession data, with slightly

different unit cell parameters. The new parameters were *a* = 10.0 Å (9.8 Å), *b* = 20.4 Å (18.9 Å), *c* = 28.1 Å (25.9 Å) and β= 98.1° (99.7°) with the previous parameters given in parentheses. The difference in unit cell parameters may be a consequence of uncertainties related to TEM calibration. The ratios of the parameters remain very similar, with the ratio of *c*/*b* being the same. The largest difference is for the *c* axis, which is 8.5 % longer in length. This is expected due to a reduced amount of information along this axis in both types of data. The space group $P2_1$ was retained, as suggested by *hkl* sections of LD-EDT data and considering the fact that all other compounds in the same family crystallize in this space group.

The data resolution obtained during the IBS experiment was higher than in previous experiments. Most indexed crystals diffracted up to 1.40 Å, with 3 crystals diffracting in the 1.2-1.3 Å range. This is most probably related to the absence of pre-exposure during the search for crystals, which rapidly affects high-resolution information. The higher sensitivity of the Medipix detector also makes it easier to record the higher resolution reflections, which are weaker in intensity.

Structure solution through molecular replacement was implemented in XDS. 8 datasets were merged leading to a data completeness of 73%. The lack of gain in completeness compared to a single dataset is expected due to the preferential orientation of the particles. The criterion used to choose which datasets to merge was the correlation coefficient $CC_{1/2}$ [189], which measures the correlation of intensities measured in different datasets for the same reflections. The molecules used as input were the asymmetrical unit of $\{[Mn^{II}_2[NIT(H, H)Im]_3(ClO_4)\}_n$, with the ClO_4^- anion replaced by the triflate anion. The crystal structure of $\{[Mn^{II}_2[NIT(H, H)Im]_3(ClO_4)\}_n$, and molecular representations of the input molecules are given in **Figure X**.

The structure model obtained is given in **Figure 3.18**, along with the list of atomic coordinates in **Table 3.5**. It can be noted that the thermal displacement factors are very high, since the structure is not refined. The initial R-factor without the addition of triflate anions was at 24%, which improves to 21.8% with the anions placed in-between the layers. The layers contain two types of Mn centers, both coordinated to three bidentate $NITIm^-$ radicals. Each Mn is coordinated to 3 oxygens from imidazole radicals and 3 nitrogens from nitronyl nitroxide radicals in deformed octehedra but differ in the stereochemistry (**Figure 3.19**). For one Mn site, the 3 Im nitrogen atoms are in the plane of the octahedron along with one NIT oxygen with two NIT oxygen atoms in the octahedral apexes in a meridional (*mer*) configuration. For the other Mn site, the octahedral plane is made of two NIT oxygen and two Im nitrogen atoms, the apexes shared by the two radicals in a facial (*fac*) configuration. The two sites are connected by both NIT and Im radicals.

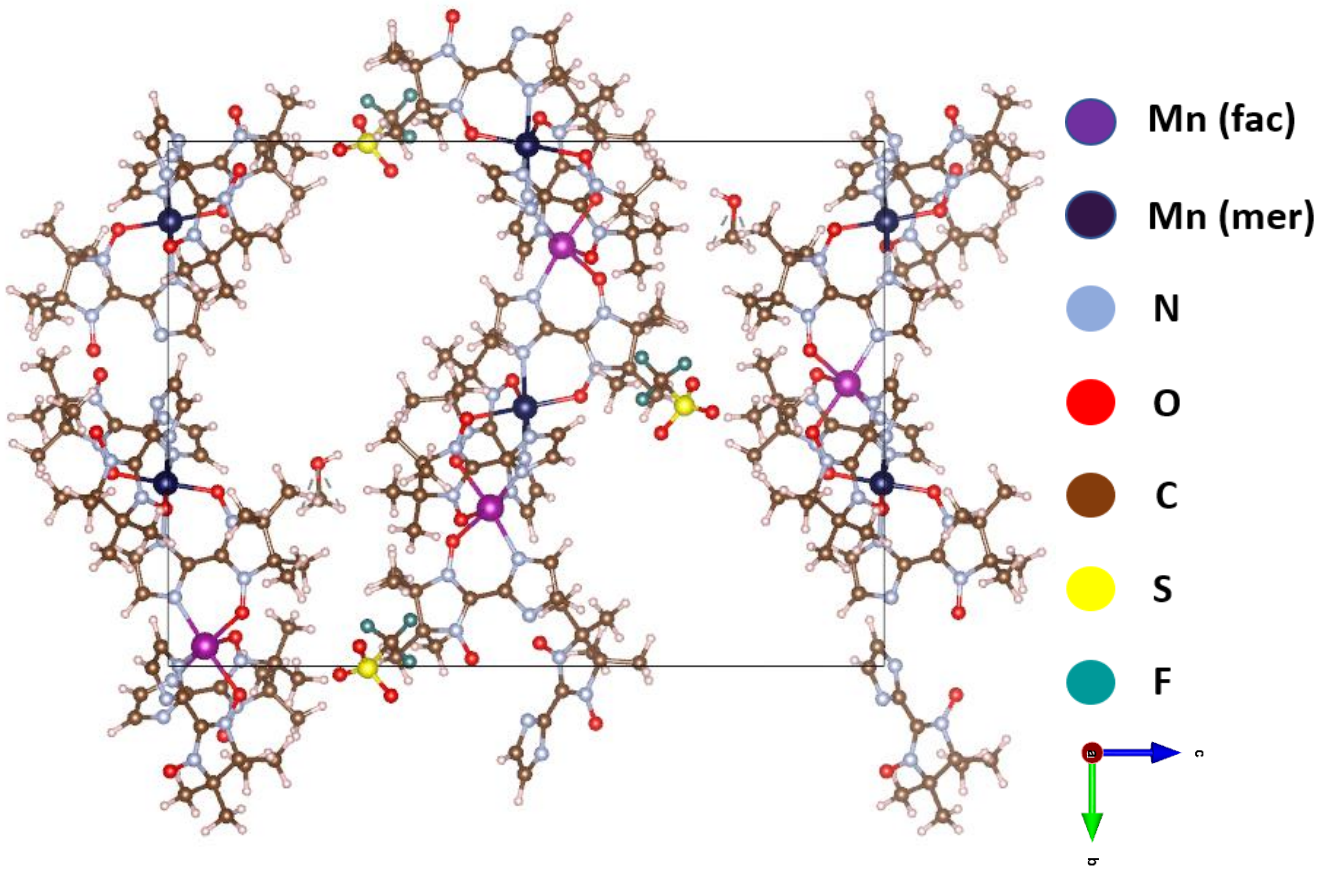

Figure 3.18: *Crystal structure of YI_OTf03 obtained by molecular replacement from 3D ED data. Two independent Mn sites are distinguished in purple (fac) and in dark purple (mer). Hydrogens are drawn in white.*

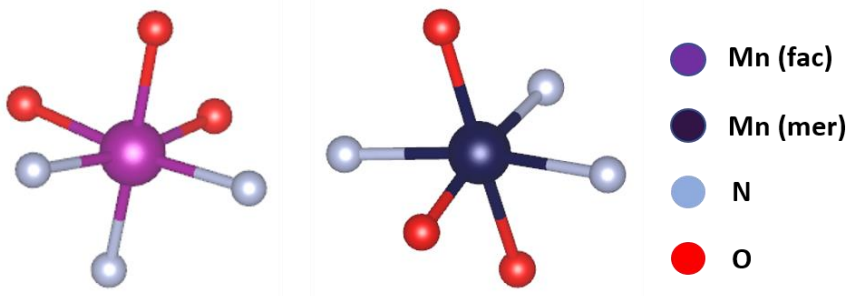

Figure 3.19: *View of the two Mn environments. The two octahedra are chemically identical but differ in the spatial distribution of Mn-radical bonds*

The $[Mn_2(NITIm)_3]^+$ 2D layers are in the ***ab*** plane, with the longer ***c*** axis perpendicular to the layers. In comparison to other compounds of the family, the ***a*** and ***c*** axes are interchanged, with the ***a*** axis being in the perpendicular direction to the layers in other compounds. The layers are arranged in a serpentine-like geometry, with the apexes on top of each other, where the triflate anions are located (**Figure 3.20**). This contributes to the longer unit cell dimension perpendicular to the layers, compared to other compounds. In-between the apexes, large pores along the ***a*** axis can be seen, commonly present in MOF structures. In

addition to the anions, a residue of electrostatic potential was observed between the apexes. These can be interpreted as methanol molecules being a residue of the solvent used during crystallization. The stoichiometry of this structure gives a chemical composition of $\{[Mn^{II}_4[NIT(H, H)Im]_6(CF_3SO_3)\}_n$, as opposed to $\{[Mn^{II}_2[NIT(H, H)Im]_3(CF_3SO_3)\}_n$ which was initially expected. This new composition still has the same Mn/radical ratio compared to the expected composition, but with a higher global multiplicity compared to the anions. This is due to two consecutive layers inside the structure being distinct, which can be easily seen on Figure 20. This is the main reason behind the longer unit cell dimension perpendicular to the layers.

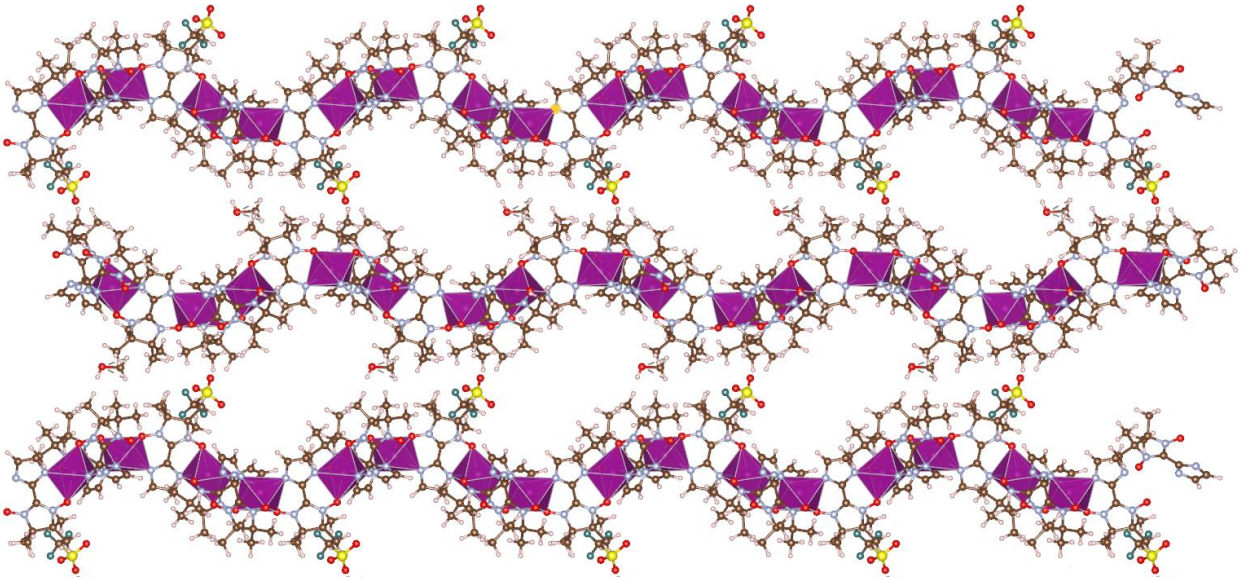

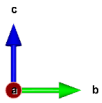

Figure 3.20: *The serpentine-like geometry of the 2D Mn-radical layers. It can be seen that the apexes of subsequent layers coincide, where they interact with the triflate anions. Large pores along the* ***a*** *axis are visible.*

Table 3.5: *List of atomic coordinates in the crystal structure of YI_OTf03, obtained via molecular replacement. Mn 1 and Mn3 correspond to (mer) positions while Mn2 and Mn4 are the (fac) positions. All positions are in the 2a Wyckoff site. The coordinates are not refined.*

Atom	x	y	z	B(Å^2)
Mn1	0.740	0.007	0.501	7.22
Mn2	0.740	0.301	0.450	7.59
Mn3	0.247	0.152	0.003	10.84
Mn4	0.238	-0.038	0.052	9.99
S1	0.090	0.004	0.279	11.4
F1	0.068	0.088	0.339	12.96

F2	0.092	0.076	0.278	12.45
F3	0.079	0.008	0.337	12.45
O1	0.409	0.385	0.209	12.45
O2	0.306	0.132	0.078	12.08
O3	0.038	0.200	0.003	11.86
O4	0.201	0.168	0.069	11.86
O5	0.564	0.044	0.519	11.88
O6	0.719	0.014	0.424	10.38
O7	0.825	0.029	0.583	10.53
O8	0.135	0.057	0.312	10.49
O9	0.601	0.055	0.094	10.49
O10	0.187	0.055	0.100	10.49
O11	0.112	0.398	0.104	12.38
O12	0.309	0.109	0.597	11.73
O13	0.608	0.237	0.398	11.73
O14	0.091	0.221	0.591	11.72
O15	0.020	0.016	0.240	9.61
O16	0.196	0.038	0.268	9.79
N1	0.372	0.077	0.095	9.69
N2	0.034	0.178	0.037	8.4
N3	0.153	0.225	0.090	10.11
N4	0.484	0.017	0.547	10.11
N5	0.665	0.068	0.402	10.08
N6	0.885	0.084	0.598	10.14
N7	0.515	0.010	0.102	9.93
N8	0.149	0.109	0.080	9.39
N9	0.113	0.333	0.106	7.32
N10	0.360	0.054	0.583	8.31
N11	0.611	0.174	0.391	9.01
N12	1.014	0.174	0.602	9.86
N13	0.432	0.097	0.006	9.6
N14	0.104	0.062	0.002	9.59
N15	0.307	0.261	0.006	9.6
N16	0.613	0.104	0.502	10.24
N17	0.804	0.097	0.505	9.85

N18	0.934	0.063	0.495	9.84
N19	0.609	0.027	0.006	9.84
N20	0.062	0.001	0.015	10.44
N21	0.281	0.369	0.010	10.81
N22	0.453	0.167	0.522	10.69
N23	0.790	0.205	0.489	10.7
N24	0.113	0.129	0.506	10.7
C1	0.447	0.318	0.212	10.62
C2	0.462	0.041	0.074	10.55
C3	0.060	0.115	0.046	10.56
C4	0.177	0.289	0.075	10.55
C5	0.447	0.047	0.550	8.62
C6	0.678	0.129	0.422	8.59
C7	0.969	0.122	0.575	8.51
C8	0.006	0.045	0.312	8.13
C9	0.609	0.054	0.038	7.95
C10	0.019	0.037	0.010	8.76
C11	0.351	0.362	0.036	8.48
C12	0.535	0.206	0.498	8.44
C13	0.861	0.197	0.534	8.45
C14	0.110	0.102	0.463	8.2
C15	0.350	0.046	0.142	11.88
C16	0.113	0.222	0.063	10.23
C17	0.046	0.225	0.133	11.42
C18	0.420	0.060	0.578	11.79
C19	0.575	0.068	0.356	11.68
C20	0.861	0.113	0.645	11.68
C21	0.465	0.006	0.149	11.68
C22	0.174	0.177	0.099	13.36
C23	0.041	0.299	0.148	12.73
C24	0.330	0.011	0.603	12.73
C25	0.559	0.143	0.345	12.73
C26	0.958	0.174	0.648	10.71
C27	0.348	0.099	0.181	11.59
C28	0.228	0.245	0.024	11.31

C29	0.049	0.168	0.168	11.31
C30	0.353	0.118	0.549	11.31
C31	0.610	0.017	0.318	11.02
C32	0.706	0.128	0.639	10.93
C33	0.206	0.014	0.132	10.92
C34	0.037	0.285	0.082	10.93
C35	0.091	0.213	0.109	9.68
C36	0.535	0.091	0.613	9.86
C37	0.451	0.038	0.373	9.77
C38	0.879	0.061	0.685	8.73
C39	0.445	0.074	0.168	8.85
C40	0.320	0.188	0.108	10.1
C41	0.097	0.329	0.167	9.68
C42	0.363	0.006	0.658	9.74
C43	0.675	0.161	0.315	9.53
C44	0.086	0.167	0.686	8.6
C45	0.597	0.023	0.181	13.27
C46	0.081	0.179	0.149	11.35
C47	0.133	0.304	0.187	17.82
C48	0.179	0.027	0.593	16.72
C49	0.431	0.173	0.318	19.32
C50	0.894	0.241	0.656	22.44
C51	0.501	0.053	0.026	21.43
C52	0.008	0.059	0.020	21.43
C53	0.259	0.306	0.028	21.42
C54	0.502	0.105	0.525	20.21
C55	0.755	0.143	0.471	19.93
C56	0.006	0.106	0.527	19.94
C57	0.501	0.098	0.046	19.93
C58	0.120	0.003	0.022	18.74
C59	0.364	0.293	0.045	21.76
C60	0.638	0.165	0.486	20.78
C61	0.869	0.130	0.543	20.76
C62	0.997	0.059	0.456	20.78
H1	0.429	0.299	0.242	18.54

H2	0.680	0.043	0.063	18.61
H3	0.002	0.088	0.020	18.61
H4	0.389	0.401	0.060	18.61
H5	0.519	0.257	0.489	16.04
H6	0.902	0.236	0.558	16.48
H7	0.181	0.110	0.438	16.72
H8	0.394	0.294	0.186	16.04
H9	0.542	0.313	0.209	15.25
H10	0.253	0.123	0.177	15.49
H11	0.288	0.204	0.011	15.58
H12	0.025	0.124	0.152	16.03
H13	0.427	0.146	0.534	15.92
H14	0.689	0.035	0.300	16.11
H15	0.651	0.084	0.632	15.03
H16	0.365	0.076	0.216	14.86
H17	0.289	0.280	0.039	15.91
H18	0.023	0.177	0.199	17.92
H19	0.304	0.149	0.571	17.26
H20	0.523	0.009	0.293	17.28
H21	0.683	0.150	0.671	17.26
H22	0.425	0.134	0.179	17.49
H23	0.186	0.266	0.005	16.99
H24	0.146	0.165	0.179	16.99
H25	0.282	0.100	0.520	16.99
H26	0.640	0.028	0.336	17.84
H27	0.681	0.161	0.610	19.12
H28	0.206	0.023	0.105	18.69
H29	0.019	0.314	0.052	18.72
H30	0.107	0.252	0.085	18.7
H31	0.493	0.120	0.639	19.34
H32	0.472	0.011	0.385	18.85
H33	0.866	0.083	0.718	18.84
H34	0.182	0.008	0.164	18.85
H35	0.096	0.312	0.104	14.66
H36	0.175	0.208	0.136	14.1

H37	0.594	0.122	0.594	14.38
H38	0.370	0.037	0.345	13.47
H39	0.807	0.023	0.677	16.25
H40	0.133	0.050	0.120	15.82
H41	0.057	0.273	0.102	15.79
H42	0.080	0.169	0.088	15.53
H43	0.597	0.054	0.630	15.36
H44	0.423	0.066	0.402	14.63
H45	0.977	0.041	0.688	16.37
H46	0.383	0.102	0.142	15.46
H47	0.387	0.167	0.079	18.15
H48	0.148	0.342	0.138	19.5
H49	0.296	0.027	0.671	19.08
H50	0.684	0.213	0.313	19.08
H51	0.150	0.208	0.684	19.07
H52	0.539	0.098	0.177	19.67
H53	0.336	0.165	0.140	19.19
H54	0.083	0.372	0.187	19.19
H55	0.352	0.053	0.674	19.18
H56	0.651	0.142	0.280	17.68
H57	0.057	0.165	0.721	20.18
H58	0.397	0.070	0.200	19.37
H59	0.340	0.239	0.110	19.36
H60	0.157	0.295	0.189	19.37
H61	0.463	0.011	0.668	19.31
H62	0.768	0.141	0.331	18.8
H63	0.138	0.124	0.679	18.8
H64	0.580	0.026	0.218	18.79
H65	0.093	0.224	0.166	14.77
H66	0.084	0.283	0.220	14.12
H67	0.160	0.074	0.607	15.01
H68	0.446	0.224	0.313	13.84
H69	0.971	0.278	0.661	15.07
H70	0.680	0.008	0.179	15.34
H71	0.108	0.140	0.170	15.06

H72	0.153	0.354	0.193	14.53
H73	0.124	0.008	0.611	14.74
H74	0.349	0.166	0.337	14.62
H75	0.824	0.253	0.626	34.36
H76	0.618	0.071	0.169	29.59
H77	0.021	0.173	0.143	30.41
H78	0.225	0.279	0.176	32.2
H79	0.146	0.025	0.556	32.07
H80	0.409	0.150	0.284	29.59
H81	0.845	0.239	0.687	28.56
H82	0.472	0.127	0.078	28.41
H83	0.200	0.011	0.042	19.44
H84	0.416	0.271	0.078	21.15
H85	0.718	0.179	0.466	19.95
H86	0.918	0.107	0.576	19.95
H87	0.965	0.030	0.424	19.95
H88	0.425	0.402	0.237	20.6

2.7 Discussion

The crystal structure of YI_OTf03 was solved using both LD-EDT and continuous rotation 3D ED data, in low dose conditions. The unit cell and the space group were determined using LD-EDT data, with adjustments to specimen preparation in order to get information along the ***c*** axis. However, *ab initio* structure determination was not possible due to insufficient data resolution. This could have been a result of beam damage to crystals inflicted prior to data acquisition, during the search for particles despite the use of very low dose rates. The relatively constant data resolution observed in subsequent frames in a tomography for many crystals is evidence to this point. Preliminary diffraction fading experiments had shown that crystals should be stable until 1.0 $e^-/Å^2$. However, it is possible that prior damage also affected these experiments. As discussed in Chapter 1, high-resolution reflections fade fastest due to beam damage. These are often sensitive to initial intermolecular bond breakage and consequent molecular repacking, leading to rapid short-range crystallinity loss prior to intramolecular bond breakage. YI_OTf03 is especially prone to crystallinity loss through molecular repacking due to the presence of large pores inside its structure, giving the molecules more freedom to repack. The pores also allow for an easier

diffusion of radicals formed due to intramolecular bond breakage later on, reducing the rate of recombination reactions and a faster loss of crystallinity overall.

Resolution was improved in the IBS data (collaboration Dominique Housset and Wai-Li Ling), where pre-exposure was significantly reduced by searching the particles digitally on low magnification TEM images. Although the resolution was still not enough for *ab initio* methods, it was sufficient for a structure solution using molecular replacement, aided by chemical knowledge on the expected structure contents. The obtained structure contains the 2D manganese-radical layers as expected from other similar compounds, although with a more distinctive difference in two independent manganese centers in *meridional* and *facial* configurations. The packing of the layers connected by triflate anions lead to a much larger layer separation compared to similar compounds.

Attempts at *ab initio* structure solution using the IBS data were not successful, due to the data resolution still being too low. Considering the model obtained with molecular replacement, further work is needed to refine the structure against 3D ED data. 3D ED data has previously been used to refine MOF structures [217] although no dynamical refinement has been made [218]. Dynamical refinement has only very recently been adapted for continuous rotation 3D ED data, through the use of overlapping virtual frames [219]. The complexity of the YI_OTf03 structure containing 198 independent positions (including hydrogens) and the relatively low data resolution might however make a dynamically refinement difficult to implement.

The difficulty in recording high-resolution data from YI_OTf03 provided an opportunity to investigate how data quality from beam-sensitive specimens could be improved. How beam damage affects data quality, and commonly used remedies for damage were discussed in detail in Chapter 1. Environmental remedies such as low temperature and high voltage require specific hardware which are not always available. The LD-EDT method is capable of significantly lowering the electron dose to reduce damage, but very low dose also leads to low SNR, which might also make it difficult to record weaker high-resolution data. It would therefore be desirable to avoid beam damage without sacrificing SNR. Given that high-resolution reflections fade the fastest, it would be essential to record them rapidly for a successful structure determination. This would be possible for instance if frames containing highest quality data could be recorded in priority above others. These are often low tilt frames where the apparent crystal thickness is smaller, and where the TEM goniometer stability is higher. This could be achieved with data collection in dose-symmetric mode, discussed in the next chapter.

Chapter IV: Implementation of a Dose-Symmetric Tomography Scheme in 3D Electron Diffraction

1) Introduction

As we have seen in the previous chapters, preventing beam damage is one of the essential factors for the success of the structure solution of unknown beam-sensitive crystals, because all the data have to be recorded before the structure of the crystal is too damaged. The extent of damage can also be reduced by working at cryogenic temperature or with a high accelerating voltage [12], but these conditions may not always be favorable due to phase transitions at low temperature or technical constraints. Minimizing the electron dose is therefore the most simple and efficient way to reduce damage as much as possible. The LD-EDT method employed in the previous chapter has been optimized for efficiency in the parsimonious use of electron dose, but there are structures that require even lower doses than those achievable with this method. In this chapter we propose to further improve this method to achieve data collection with even lower doses without sacrificing the SNR.

1.1 Effect of Apparent Crystal Thickness

In a standard electron diffraction tomography, the crystal is tilted around the goniometer axis of the TEM during data acquisition. Although the crystal volume stays constant during data acquisition, the apparent thickness of the crystal with respect to the beam changes as a function of the tilt angle. This is due to the anisotropic morphology observed for most crystals. Given that the crystals possess faces with different sizes, they are often deposited on the flat specimen grid with the face with the largest surface size being parallel to the grid surface. Considering that the beam arrives vertically on the crystal, the distance travelled by the beam electrons inside the crystal is shortest when the crystal is at zero tilt. As the tilt angle is increased towards any extremity, the electron beam ceases to be normal to the crystal face with the largest size, and beam electrons travel a longer distance inside the crystal (**Figure 4.1**).

In addition to dynamical scattering, crystals with higher thickness suffer from absorption due to an increased rate of non-elastic scattering events, resulting in less electrons being transmitted through the specimen [8]. This reduces the recorded intensity of the reflections, lowering the SNR. This makes reflections with low intensity more difficult to detect, which is often the case for high-resolution reflections. This has been well documented in literature, where the resolution is reduced at high tilt angles [113], and high tilt frames being excluded from dynamical refinement due to absorption effects [220]. It is therefore more favorable to acquire data from thin crystal sections to maintain data quality.

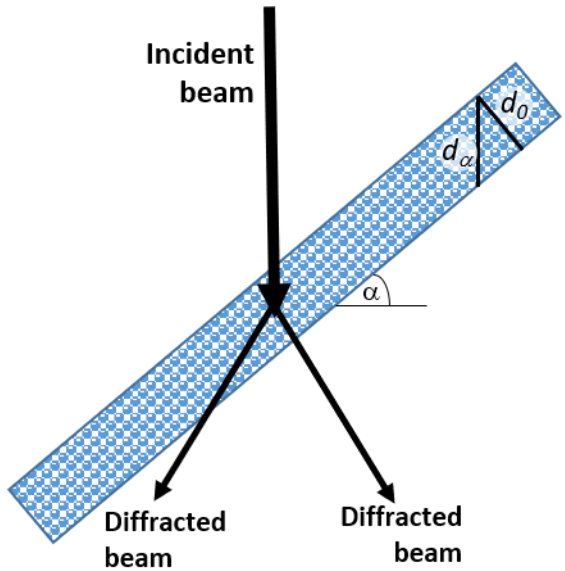

Figure 4.1: *Visualization of how the apparent crystal thickness changes when a crystal is tilted. Upon tilting, the thickness of the crystal in the direction of the transmitted beam increases from d_0 to d_α. Diffracted beams travel different distances inside the crystal depending on the diffraction direction.*

Since the apparent thickness is minimal at zero tilt, it is at zero tilt that diffraction data suffers less from absorption and dynamical scattering. However, for sensitive crystals beam damage can be so severe that high-resolution information is only available during the initial stages of data acquisition. In standard 3D ED where the sample is tilted from one extremity of the tilt range to the other, the initial frames correspond to the largest apparent thickness **(Figure 4.2**). In this case, high-resolution reflections which suffer from increased absorption and dynamical scattering at high tilt angles are already lost by the time these effects are reduced at zero tilt.

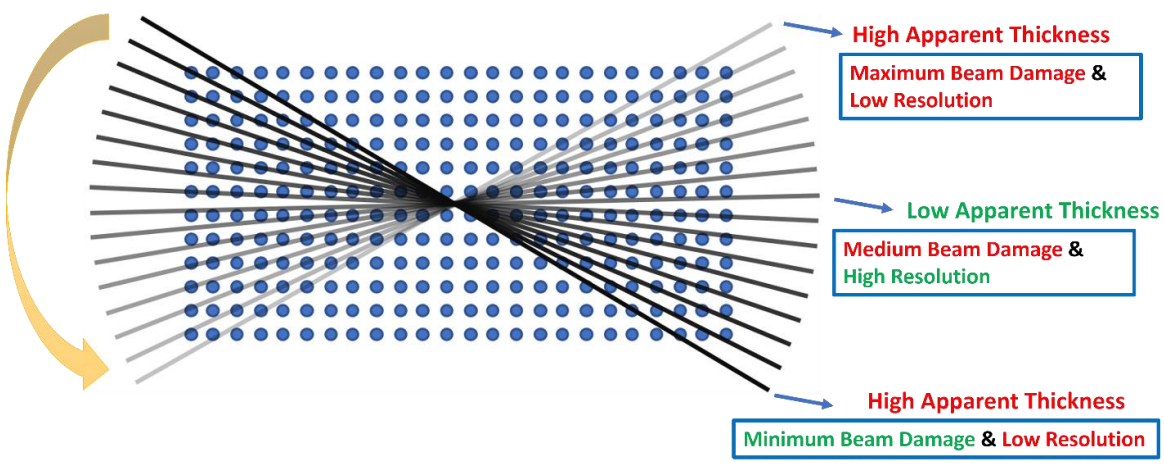

Figure 4.2: *Representation of a typical 3D ED tomography. The blue dots represent reciprocal lattice nodes while each line represents a diffraction image with its intensity corresponding to the signal strength affected by beam damage.*

1.2 Dose-Symmetric Tomography & Sub-Tomogram Averaging

An alternative tomographic tilt scheme has been developed in the cryo-electron tomography field (cryo-ET), called the dose-symmetric tilt scheme [221]. In this case the data acquisition begins at zero tilt, followed by progressively going to higher tilt angles while the tilt direction is oscillated (**Figure 4.3**). For example, for a 1° tilt step, the first frame would be taken at 0°, the second at +1°, the third at -1°, the fourth at +2°, and so on. This tilt scheme is referred to as dose-symmetric tomography (DST).

In cryo-ET [9], specimens are tilted while projection images are recorded in a step-wise manner. These are then aligned to reconstruct a 3D representation of the recorded area. The information inside the tomogram is limited by a low SNR, since the dose rate has to be kept low in order to reduce the accumulated dose during data acquisition. If data sets on multiple identical objects are recorded, the quality of the data can be improved by averaging the information from different objects and thus reducing the noise. Averaging of multiple sub-volumes improves the SNR and allows to discern high-resolution information. This is referred to as sub-tomogram averaging [222]. The efficiency of sub-tomogram averaging relies on recording a maximum amount of high-resolution information while maintaining sufficient low-resolution information, which is used to align the high-resolution sub-volumes.

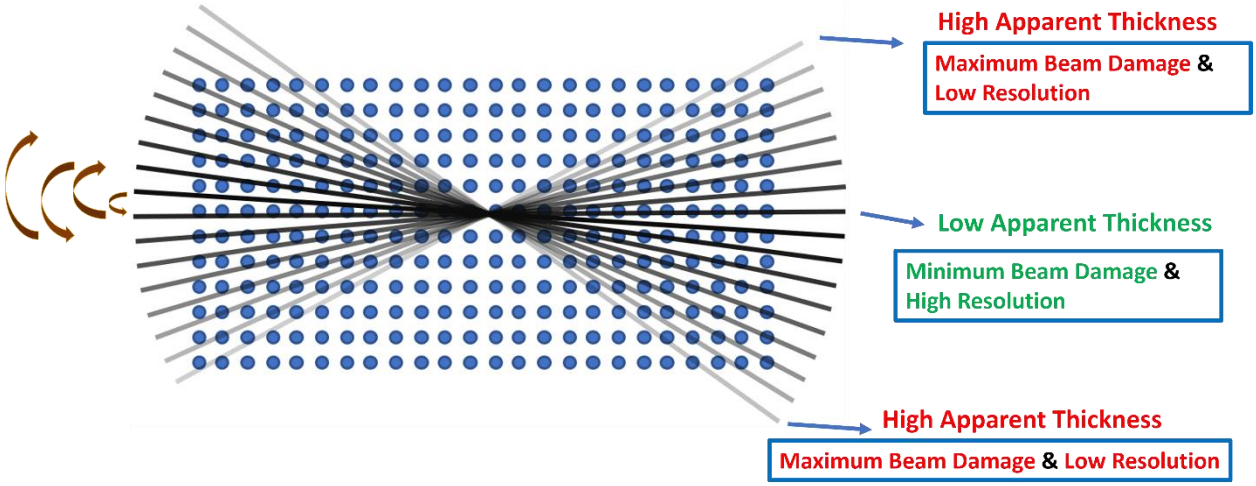

Figure 4.3: *Representation of a 3D ED dose-symmetric tomography in the reciprocal space. Each line represents a diffraction image with its intensity representing the signal strength affected by beam damage. It can be seen that the signal strength is better focused to probe the higher density of information around zero tilt.*

We decided to adapt the concept of DST and sub-tomogram averaging to 3D ED to improve data acquisition for beam-sensitive specimens. When a diffraction tomography is recorded with the DST scheme, the frames recorded close to zero tilt will contain more high-resolution reflections due to the

smaller apparent thickness and low amount of damage, as well as reduced dynamical effects. As the tilt angle is incrementally increased, beam damage will affect the frames which already suffer from increased absorption and dynamical scattering. Intensities in these frames will be unreliable for crystal structure solution and refinement. However, given that the positions of the reflections do not change, these frames can still be used to determine the unit cell, index the reflections and to determine the extinction conditions.

In this scheme, the dose rate for the experiment can be increased because only the cumulated dose of the first frames needs to be low enough not to damage the crystal. The total dose is allowed to inflict damage at higher tilt angles but without complete amorphization of the specimen at high tilt. The total range of the tomography does not have to be large, since according to the literature, a total range of 30° is typically sufficient to determine unit cells [223].

For each individual dataset, all the frames are used to refine the rotation axis and to determine the unit cell. Frames above a certain tilt threshold can then be discarded and intensities can be integrated from low tilt frames only (**Figure 4.4**).

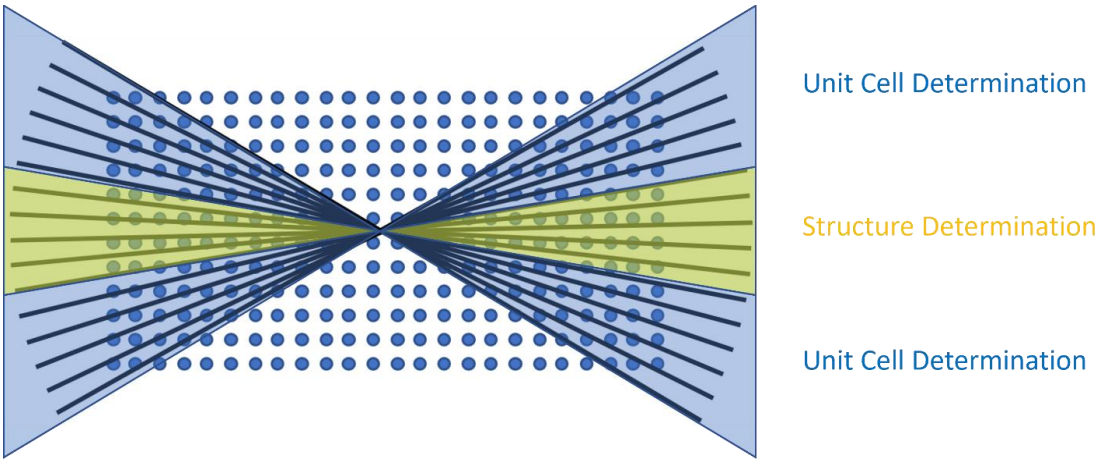

Figure 4.4: *Representation of the sub-tomogram averaging concept adapted to 3D ED data. All frames including lower quality high tilt frames in blue are used for unit cell determination, but only the low tilt frames in yellow are used for structure determination*

Although this will provide high-quality data in terms of damage prevention, resolution and dynamical effects, data completeness will be low. In order to achieve sufficient completeness for structure solution and refinement, low tilt data collected from various crystals via DST can be merged. Data merging is often employed in 3D ED to enhance completeness of data limited by the missing cone [224]–[226]. Lightowler *et al*. [227] and Clabbers *et al*. [228] employed a similar strategy on beam-sensitive crystals by collecting

diffraction data in small wedges over a larger tilt range to achieve high completeness. In these cases, each dataset covered a different section of the total possible tilt range, instead of being collected solely in the low tilt range. Lightowler et al. noted that despite a sufficient data resolution of 1.0 Å and a completeness of 70%, direct methods could not solve the structure. This was attributed to insufficient completeness and missing information along the ***b*** axis in particular. It was however possible to solve the structure via simulated annealing.

For structure solution and kinematical refinement, data merging from different crystals involves identification of common reflections in different datasets, which are used to establish a common scale. This work therefore aims to verify whether it is possible to use damaged high tilt frames to accurately determine the unit cell, and to assess if it is possible to solve and refine a crystal structure by only merging frames close to zero tilt. If there is no preferential orientation of the crystals a high data completeness can be achieved by merging a large number of sub-tomograms, but at the price of introducing potential errors in the scale factors of the different data sets. The combination of dose-symmetric tomography with LD-EDT is referred henceforth as DS-EDT.

2) Implementation in 3D Electron Diffraction

In order to distinguish the two challenges in DS-EDT of using only low tilt frames for structure determination and using damaged frames for indexation of reflections, this work was divided into two sections with one test structure each.

For the initial section, 3D ED data was collected on the complex oxide $Sr_5CuGe_9O_{24}$ [229], to find out the minimum number of frames around zero tilt necessary per dataset that allows structure determination by data merging. Since $Sr_5CuGe_9O_{24}$ is an inorganic compound not prone to ionization damage, this allows decoupling of data merging analysis from the concept of indexation of reflections using damaged frames.

Once the concept of using only low tilt frames to achieve structure determination is confirmed, the second section would then consist of collecting DS-EDT data from a beam-sensitive material, manganese formiate [230]. The dose rate would be tuned to make sure that high tilt frames would be damaged, but not completely amorphized. Following the unit cell determination, datasets can then be truncated to a certain tilt range around the zero tilt position, based on results obtained in the first section.

2.1 Proof of Concept with $Sr_5CuGe_9O_{24}$

2.1.a $Sr_5CuGe_9O_{24}$

The crystal structure of $Sr_5CuGe_9O_{24}$ was first solved with LD-EDT and is shown in **Figure 4.5**. It is a pyroxene derivative, synthetized in high pressure and high temperature conditions by the MRS team of the Néel Institute. $Sr_5CuGe_9O_{24}$ crystallizes in the monoclinic space group *P2/c*, with unit cell parameters refined by X-ray powder diffraction a = 11.8817(3) Å, b = 8.1928(2) Å, c = 10.3237(2) Å and β = 101.597(13)° [229]. The unit cell contains 9 independent strontium, copper and germanium cation positions, and 13 O positions (**Table 4.1**).

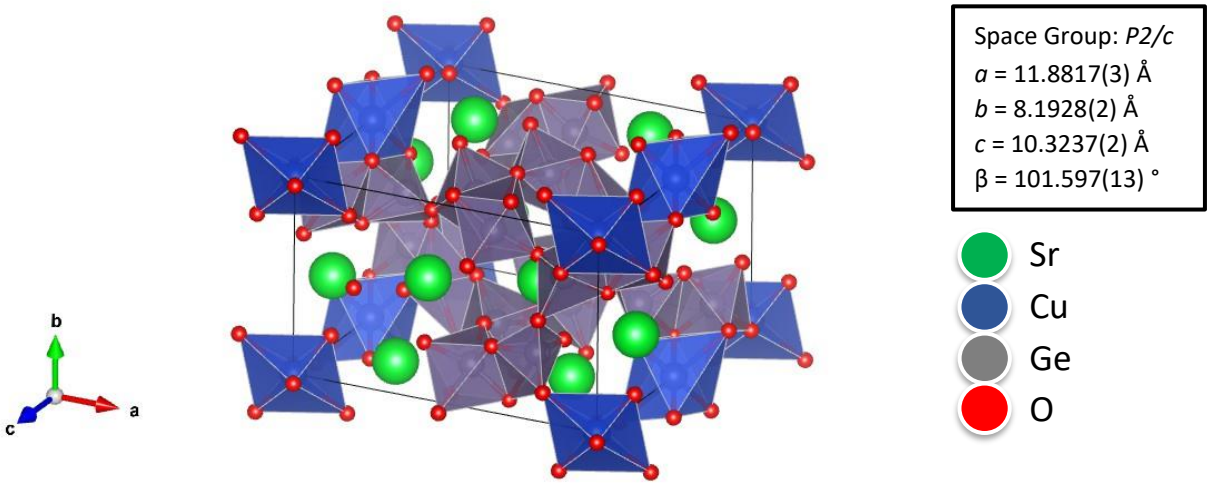

Figure 4.5: *Crystal structure of $Sr_5CuGe_9O_{24}$. Sr-centered oxygen polyhedra are not drawn for clarity*.

Table 4.1: *List of atomic coordinates of $Sr_5CuGe_9O_{24}$ [14]*

Atom	Wyck.	x	y	z	B (Å^2)
Sr1	2e	0	0.3531(8)	0.75	0.528
Sr2	4g	0.7559(4)	0.0316(5)	0.6837(4)	0.371
Sr3	4g	0.6505(4)	0.4849(5)	0.6817(5)	0.631
Ge1	4g	0.8529(5)	0.711(6)	0.9356(5)	0.426
Ge2	4g	0.5889(4)	0.175(7)	0.3708(6)	0.939
Ge3	4g	0.7896(5)	0.6712(7)	0.4766(5)	0.576
Ge4	4g	0.5412(4)	0.8401(7)	0.4122(6)	0.741
Ge5	2e	0	0.7801(9)	0.75	0.607
Cu1	2a	0	0	0	0.450
O1	4g	0.7965(2)	0.6948(3)	0.3147(3)	0.836
O2	4g	0.5443(2)	0.9636(3)	0.6298(3)	0.836
O3	4g	0.9437(2)	0.5934(3)	0.8274(3)	0.836
O4	4g	0.6465(2)	0.675(3)	0.4887(3)	0.836
O5	4g	0.4149(2)	0.7358(3)	0.4686(3)	0.836
O6	4g	0.6706(2)	0.9767(3)	0.4206(3)	0.836
O7	2f	0.5	0.3445(5)	0.25	0.836
O8	4g	0.9095(2)	0.8177(3)	0.065(3)	0.836
O9	4g	0.8692(2)	0.7837(3)	0.5955(3)	0.836
O10	4g	0.7165(2)	0.7236(3)	0.8356(3)	0.836
O11	4g	0.8166(2)	0.5265(3)	0.0261(2)	0.836
O12	2f	0.5	0.7399(4)	0.25	0.836
O13	4g	0.909(2)	0.9215(3)	0.8203(3)	0.836

The structure is formed of layers perpendicular to the **a** axis, composed of different sets of polyhedra running along the **c** axis. Three different types of coordination polyhedra around Ge atoms are observed. There are two independent Ge positions located inside O tetrahedra, two positions in a 5-fold coordination made of O pyramids, and one position inside an O octahedron. Even though it is not beam-sensitive, this shows that it has nevertheless a complex structure that serves as a reasonable test for the validity of the DS-EDT method.

2.1.b Data Acquisition

LD-EDT data acquisition was performed on a Philipps CM300 ST TEM with an accelerating voltage of 300 kV. Precession of the electron beam was generated by a Nanomegas Spinning star device. $Sr_5CuGe_9O_{24}$ was available in form of a fine powder. A small quantity of the powder was ground for a few minutes in an agate mortar, suspended in pure ethanol. A few drops of the suspension were deposited on a porous carbon-coated copper grid, in order to achieve an optimal concentration of particles for data acquisition. The grid was mounted on a home-made tomography TEM specimen holder. This single tilt holder has been mechanically thinned in order to increase the maximum tilt range to 110° (+/- 55°).

As this sample is not beam-sensitive, there is no difference in data quality between the acquisition in the standard tomography scheme and DS-EDT. However, the TVIPS EMMENU camera control software used to acquire diffraction data does not allow for automatic DS-EDT acquisition, the DS-EDT data acquisition scheme has to be applied manually. This takes much more time than the automated tomography acquisition with EMMENU. For practical reasons and since it doesn't matter for the data quality, the standard procedure of data acquisition was applied for this sample to demonstrate the initial proof of concept.

A total of 20 LD-EDT datasets with total tilt ranges between 90°-100° (+/- 45° -- +/- 50°) were collected from different crystals, with a tilt step of 1° between the frames and a precession angle of 1.05°. Before each data collection, the maximum tilt range at the particle position was verified by tilting the grid until the signal was blocked by the edges of the specimen holder. The available tilt range is maximum at the center of the grid, and progressively diminishes towards the extremities, due to increased shadow from the grid or sample holder. For one particle, the accessible range was only 20° (+/- 10°) due to shadow from the copper bars on the grid.

2.1.c Data Processing

The raw image data from EMMENU are processed using the PETS2 software [183] as described in Chapter 2. To determine the unit cells, the automatic unit cell search function in PETS2 was initially utilized followed by manual inspection and adjustment. The previously published unit cell for $Sr_5CuGe_9O_{24}$ was determined for 14 particles out of 21. 3D ED data can be relatively inaccurate in determining unit cell parameters compared to XRD data mainly due to errors in TEM camera length calibration. To account for this, unit cell parameters within a 5% error range were considered to be correct. The other 7 particles

suffered from low quality data hampering refinement of the rotation axis or peak analysis. Intensities were then integrated from the 14 datasets who yielded the correct unit cell. Manual analysis of data resolution using the resolution rings feature in PETS2 revealed that most particles diffracted up to a high-resolution of 0.7 Å. In addition to the default data processing protocol discussed in Chapter 2, a correction of optical distortions in the frames was implemented. This procedure, which became available in the PETS2 software in 2022 [184], allows to correct for optical distortions present on the frames due to imperfections of optics in TEMs. This allows for a more precise integration of intensities. Two examples of integrated intensity data are given in **Figure 4.6**.

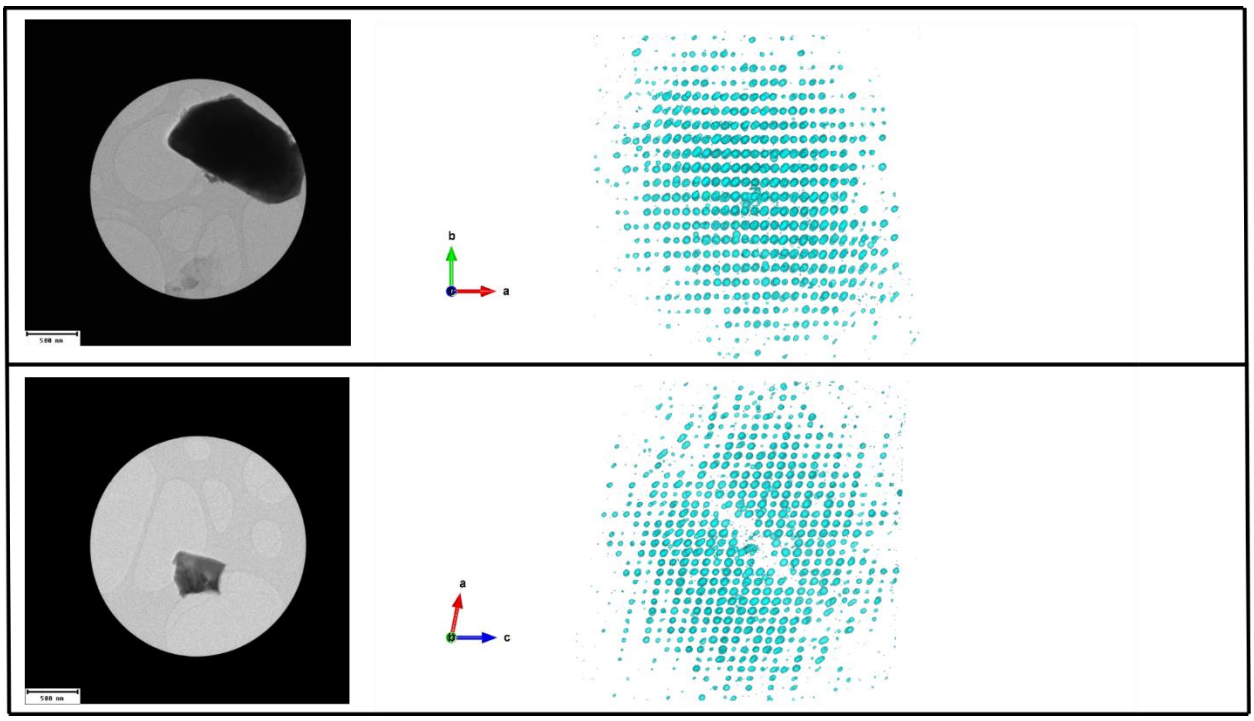

Figure 4.6: *On the left, TEM images of two $Sr_5CuGe_9O_{24}$ crystals taken with a selected area diffraction aperture are given. The totality of the crystals is kept inside the aperture during tilting. The scale bars correspond to 500 nm. On the right, are the corresponding reconstructed 3D intensity distributions in reciprocal space obtained by data processing in PETS2.*

The criterion for deciding which datasets could be used for the data merging process was the success of *ab initio* structure solution on each individual dataset. Given the high number of independent atom positions in the unit cell, only the cation structure was considered at this stage. This would assure that the data used for merging was reliable so that the proof of concept would not suffer from data quality, without eliminating too many particles due to a lack of correct oxygen structure. Structure solution was performed with the SIR2014 package [186] embedded into the Jana2020 [185] suite. SIR2014 employs direct methods to phase intensities measured from the diffraction frames. Phased intensities are then used to obtain an

electrostatic potential map through Fourier transforms, which can be interpreted for a structure model. For each dataset, the raw structure models obtained by SIR2014 were assessed by comparing the cation positions to those from the previously published structure. It was seen that the correct structure was obtained from 11 out of the 14 datasets. Particle B, whose tilt range was already limited to 20° (+/-10°) without truncation, yielded the correct cation structure along with 5 out of 13 oxygen positions. This showed that data truncated to +/- 10° around zero was already reliable for structure determination. Relevant data acquisition parameters for the 11 particles used for data processing are given in **Table 4.2**.

Table 4.2: *Data acquisition parameters on particles used for data merging*

Particle	Angular Range(°)	Dose Rate($e^-/Å^2.s$)	Exposure time per frame T_{exp} (ms)	Dose($e^-/Å^2$)
A	90 (+/- 45°)	0.082	1000	7.46
B	20 (+/- 10°)	0.082	1000	1.72
C	90 (+/- 45°)	0.082	1000	7.46
D	50 (+/- 25°)	0.082	1000	4.18
E	90 (+/- 45°)	0.200	500	9.10
F	100 (+/- 50°)	0.200	500	10.10
G	100 (+/- 50°)	0.200	500	10.10
H	100 (+/- 50°)	0.200	500	10.10
I	90 (+/- 45°)	0.200	500	9.10
J	90 (+/- 45°)	0.200	500	9.10
K	90 (+/- 45°)	0.200	500	9.10

After excluding datasets that lead to a wrong structure, the remaining 11 datasets were then individually truncated by symmetrically removing high tilt frames, into smaller tilt ranges of maximum +/-20°, +/-15°, +/- 10° and +/- 5°. This was achieved by editing the PETS2 configuration file to exclude the truncated frames, and re-processing each dataset through PETS2 using the rotation axis and unit cell previously refined using all the frames. Particle B was also included in the +/- 20°and +/- 15° range data despite its low angular range, since the essential goal is to set a maximum range in each case, even though not all particles attain this range.

Truncated data were merged in Jana2020. The merging process involves identification of common reflections among the datasets to determine a unique intensity scale by rescaling each dataset according to intensity differences measured for the common reflections. The efficiency of the scaling process

increases with increasing the number of common reflections, which can be limited for increased truncation. This can be quantified through the R_{merge} calculated by Jana2020, which is based on post-scaling differences in intensity for the common reflections:

$$\mathbf{R_{merge}} = \frac{\sum_k \sum_{i=1}^{n} |\boldsymbol{I_i(k)} - \boldsymbol{I_{mean}(k)}|}{\sum_k \sum_{i=1}^{n} \boldsymbol{I_i(k)}}$$

R_{merge} measures the spread of n independent measurements of the intensity of a reflection **k** (I_i(**k**)), around its average (I_{mean}(**k**)). It is therefore a useful indicator to assess the coherence of the merged datasets. The redundancy factor represents the frequency at which the reflections were measured among the different datasets. In order to distinguish the standard R factor from R_{merge}, the former is referred to as R_{model} throughout this chapter.

The goal at this stage was to determine the minimum number of frames per dataset necessary for structure determination, and to assess the effectiveness of merging low tilt data from multiple particles. To simplify the assessment, initially only the raw structures obtained from SIR2014 were considered for comparison, before subsequent refinement. The presence of various high-*Z* cations can result in an increased rate of dynamical effects which would render kinematical refinement ineffective, and the high number of independent positions in the structure would result in the dynamical refinement being very demanding in calculation time.

SIR2014 is often capable of identifying the correct atom positions from 3D ED data but not always the correct identity of the atom. This can easily be manually corrected in Jana2020 using preliminary chemical knowledge on the compound. In cases where an atom was located at an expected position, this was considered as correct even if the chemical identity was incorrect. The accuracy of the structure models was quantified by the mean distance of the atom positions in the models to their positions in the previously published structure refined on powder X-ray data. Multiplicity of the positions was taken into account in the mean distance calculation. The distance between two atom positions in a monoclinic unit cell is calculated with the following expression:

$$\textbf{Distance}\ (\text{Å}) = (\mathbf{x_o} - \mathbf{x_i})^2\mathbf{a^2} + (\mathbf{y_o} - \mathbf{y_i})^2\mathbf{b^2} + (\mathbf{z_o} - \mathbf{z_i})^2\mathbf{c^2} - \mathbf{2cos}\ (\boldsymbol{\beta})(\mathbf{x_o} - \mathbf{x_i})\mathbf{a}(\mathbf{z_o} - \mathbf{z_i})\mathbf{c}$$

Where x_o, y_o, z_o and x_i, y_i, z_i represent the atomic fractional coordinates in the previously published structure and in a given new structure from 3D ED data, respectively. *a*, *b*, *c* and β are the unit cell

parameters of $Sr_5CuGe_9O_{24}$ expressed in Å and in radians. For simplicity, this quantity is referred to as ''Dist'' throughout this chapter.

2.1.d Results

For each case, data from all available particles was merged into a single dataset. In case of truncation to +/- 20°, the data from 11 particles lead to a completeness of 100% and a redundancy of 5.79. In the +/- 15° range, 11 particles were merged to a completeness of 99% and a redundancy of 4.79. Completeness then fell for +/- 10° to 96% (redundancy: 3.85) but still remained at 84% for +/- 5° (redundancy: 2.82). Compared to data completeness, redundancy was reduced in a more continuous manner. This was due to truncated data covering the same reciprocal area as the remaining data, with the loss of information translated as a reduction in redundancy instead of completeness. Parameters relevant for different truncation cases are regrouped in **Table 4.3**.

Table 4.3: *Evolution of relevant parameters related to DS-EDT data merging. R_{merge} and Redundancy are calculated by Jana2020 while R_{model} and completeness are calculated by SIR2014.*

Data Range	Completeness (to 0.7 Å) (%)	R_{merge}(obs)	Redundancy
+/- 20°	100	20.38	5.79
+/- 15°	99	19.11	4.79
+/- 10°	96	17.61	3.85
+/- 5°	84	15.22	2.82

For the selection of common reflections to be used for scaling, Jana2020 considers by default only reflections with I/σ superior to 10. In all cases, this was lowered to 5 to compensate for the reduced number of common reflections in truncated data. It can be seen that R_{merge} was gets smaller as the data range is reduced. This is due to the smaller size of the data at lower ranges, although the higher quality of data in the low tilt range compared to higher tilt angles may also play a role.

At +/- 20°, the resulting structure model shows significant accuracy and is capable of identifying all positions. Going lower to the +/- 15° range, there is an improvement in both oxygen and cation positions accuracy compared to +/- 20°. When the range was lowered to +/- 10°, the complete structure was still solved, with again both oxygen and cation positions accuracy improving over the +/- 15° case. Going down to +/- 5°, it was still possible to solve the complete structure, despite a decrease in oxygen accuracy

compared to the +/- 10° and +/- 15 °structures (see **Table 4.4**). In all cases, the largest Dist was measured on the same O7 position.

Table 4.4: *Evolution of relevant parameters related to model accuracy following DS-EDT data merging. Dist values are calculated by comparison to the previously published structure refined on X-Ray data.*

Data range	R_{model} (obs)	Dist Cations (Å)	Dist Oxygens (Å)	Dist Overall (Å)	Largest Dist (Å)
+/- 20°	20.49	0.025	0.152	0.103	0.242
+/- 15°	22.83	0.023	0.144	0.097	0.274
+/- 10°	21.65	0.023	0.141	0.095	0.266
+/- 5°	23.03	0.023	0.147	0.099	0.242

Figure 4.7 showcases the evolution of the structure models obtained as a function of the total range per particle. The comparison of projections on this figure visually illustrates how accurate all the models are, compared to the X-ray refined structure. These results show that it is possible to go down to +/- 5° and still determine all atom positions by data merging.

The data was then investigated more thoroughly to find out how accuracy is related to completeness. The +/- 10° data was taken as an example. Instead of merging all 11 available datasets at once, datasets were merged one by one and structure solution was performed at each step to assess how accuracy progressively evolved when increasing the number of datasets. No criterion was employed to choose in which order the particles were merged. **Table 4.5** shows how different factors evolve as more datasets are merged. In cases of 1 and 2 datasets, the totality of oxygen positions could not yet be distinguished, for which 3 datasets were necessary along with a completeness of 59%. Dist on oxygens and on all positions was therefore calculated from 3 datasets and forward.

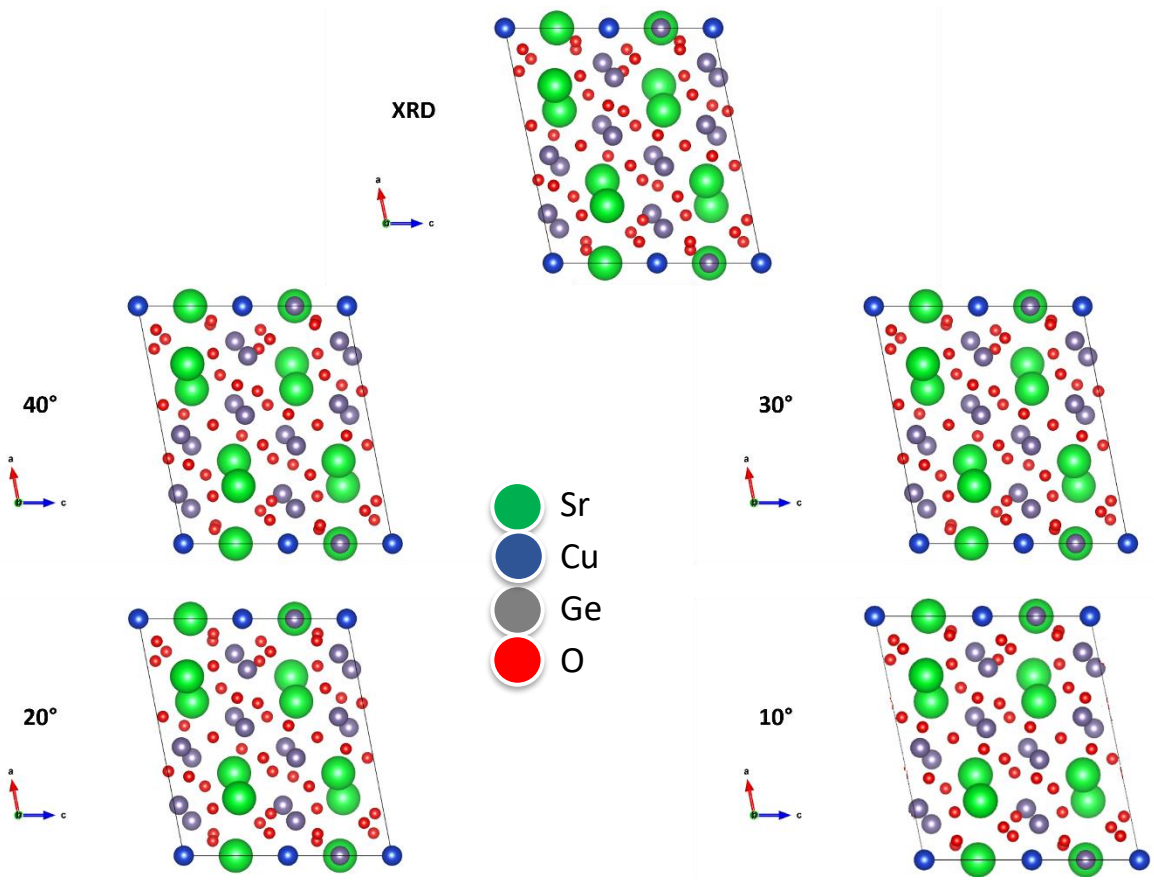

Figure 4.7: *Projections along the **b** axis of the four $Sr_5CuGe_9O_{24}$ structures obtained from DST data, with the previously published XRD-refined structure given at the top for comparison.*

It can be seen that the overall *Dist* usually improves as a function of completeness, except for the merging of two particles (particles C and E). This evolution is plotted in **Figure 4.8**.

Cation accuracy, which is higher than the accuracy of the oxygen positions, often improves as more particles are merged. This is also the case for the oxygen positions. Since there are more oxygens in the structure, the overall trend is dominated by the evolution of the oxygen accuracy.

However, in some cases the addition of more data does not improve the accuracy, despite an improvement in completeness. This could be due to some particles suffering more from dynamical effects, which can result in more incoherence in intensities. It can be seen that the best overall accuracy is actually obtained with 8 particles, instead of all 11.

Table 4.5: *Evolution of relevant parameters related to model accuracy as a function of data completeness. In cases of 1 and 2 particles, not all oxygen positions could be identified and only Dist for cations is calculated as a result. Comp. refers to data completeness and Red. refers to redundancy.*

N	Comp. (to 0.7 Å) (%)	R_{merge} (obs)	Red.	R_{model} (obs)	Dist Cations (Å)	Dist Oxygens (Å)	Dist Overall (Å)	Largest Dist (Å)
1	26	N/A	1.67	26.6	0.046	N/A	N/A	N/A
2	46	9.48	1.83	22.9	0.021	N/A	N/A	N/A
3	59	11.61	2.06	26.0	0.031	0.169	0.116	0.430
4	67	14.10	2.40	31.6	0.024	0.162	0.109	0.307
5	78	13.94	2.56	21.4	0.023	0.155	0.104	0.324
6	80	14.68	2.62	25.6	0.020	0.145	0.097	0.283
7	86	15.25	2.88	25.9	0.021	0.146	0.098	0.307
8	90	15.57	3.13	25.9	0.021	0.140	0.094	0.258
9	92	16.47	3.27	24.2	0.022	0.145	0.098	0.250
10	93	23.93	3.49	23.9	0.020	0.143	0.096	0.266
11	96	17.61	3.85	21.7	0.023	0.141	0.095	0.266

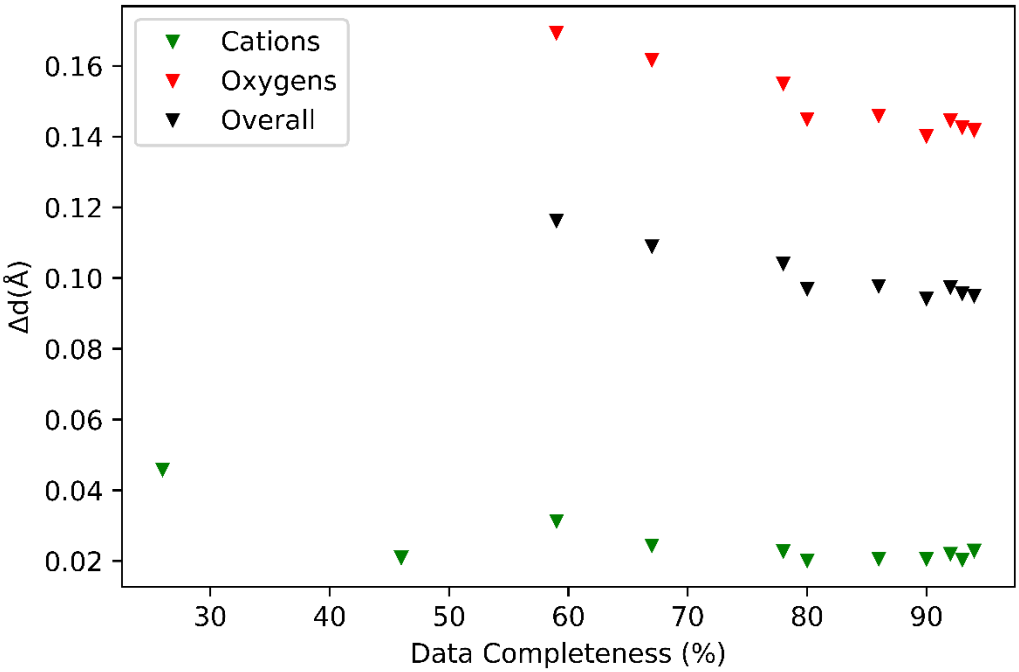

Figure 4.8: *The evolution of accuracy against data completeness. Accuracy tends to improve with completeness, but a visible decline is seen upon the merging of some particles.*

Following the analysis of structure solutions obtained from DS-EDT data, dynamical refinements were performed. Dynamical refinement [190] refers to modelling of measured intensities using the theory of dynamical diffraction, where incident electrons can be diffracted multiple times inside the crystal and as a result multiple crystal planes can contribute to a single reflection. This is especially adapted to interpret electron diffraction data which can contain dynamical effects. In the case of $Sr_5CuGe_9O_{24}$, the presence of heavy cations increases the chances of dynamical diffraction, which can be taken into account with dynamical refinement.

For dynamical refinement, unlike in the kinematical case, reflections on each image are treated separately and one distinct reflection file is generated for each frame of each dataset. Before dynamical refinement, an initial kinematical refinement is performed, which allows the dynamical refinement process to start closer to the point of convergence. In all cases, refinements were made on F^2(obs) with maximum data resolution set to 1.1 Å. All positions were freely refined with isotropic displacement parameters. The occupancies were not refined. For all dynamical refinements on DS-EDT data, the same parameters used during the refinement of Bulachite were kept (see Chapter III Section 1.5). Extinction corrections were implemented during kinematical refinement but not for dynamical refinement. The first step of dynamical refinement consists of optimizing the thickness of each particle to describe the observed intensities. This step is performed separarely for each dataset. Once the thicknesses are optimised, 10 cycles of dynamical refinement are performed. The second phase involved optimisation of frame orientations. This involves calculating the misalignment of each frame of each crystal from the orientation predicted by the corresponding orientation matrix. A small number of frames for which a considerable deviation of above 0.5° was calculated were removed from the refinement process. More cycles were then performed until the refinement converged. In all cases, dynamical refinement parameters RSg_{max}, DSg_{max} and g_{max} were set to 0.7, 0.0015 and 1.2, respectively. **Table 4.6a and 4.6b** summarize the results obtained.

Table 4.6a: *Summary of results obtained from dynamical refinement on $Sr_5CuGe_9O_{24}$ DS-EDT data, related to model accuracy.*

Data	Dist Cations (Å)	Dist Oxygens (Å)	Dist Overall (Å)	Largest Dist (Å)
40° (+/- 20°)	0.018	0.149	0.096	0.232
30° (+/- 15°)	0.019	0.136	0.091	0.225
20° (+/- 10°)	0.019	0.136	0.091	0.244
10° (+/- 5°)	0.016	0.131	0.087	0.268

Table 4.6b: *Summary of results obtained from dynamical refinement on $Sr_5CuGe_9O_{24}$ DS-EDT data, related to the final refinement values.*

Data	Reflections/ Parameters	R_{model}(obs) (%)	R_{model}(all) (%)	wR_{model} (obs) (%)	wR_{model} (all) (%)	GoF(obs) (%)	GoF(all) (%)
40° (+/- 20°)	14323/518	10.39	10.99	19.88	20.06	2.92	2.68
30° (+/- 15°)	11072/419	10.35	10.94	19.82	20.01	2.90	2.68
20° (+/- 10°)	7753/319	10.26	10.88	19.60	19.80	2.85	2.64
10° (+/- 5°)	4078/209	10.16	10.78	19.03	19.22	2.76	2.56

In all cases, the R_{model} was significantly lowered after dynamical refinement, indicating a better fit between the intensities calculated from the final structures and the measured intensities. R_{model} decreases as the tilt range is reduced since there was less data overall for calculation of error. Dynamical refinement also improves the accuracy of all the models. It is seen that accuracy improves at lower tilt range with the best accucary observed for the +/- 5° data.

The list of atomic coordinates obtained upon refinement on the +/- 5° data is presented in **Table 4.7**.

It can be seen that the higher accuracy measured on the cation positions is also accompanied by typically lower thermal displacement parameters, compared to oxygens. This is due to their larger scattering power making it easier to measure their positions more precisely.

To summarize, it was possible to achieve structure determination by using only low tilt frames from multiple particles. The lower limit was determined to be +/- 5°. The data was of sufficient quality to allow dynamical refinement of the structures, with the refined structures being accurate compared to the X-ray refined structure. This therefore validated the concept of DS-EDT as proof of concept. However, the specimen used in this section was obviously not actually beam-sensitive. In order to verify the true usefulness of the method, it was applied to a beam-sensitive specimen as described in the next section.

Table 4.7: *List of atomic coordinates obtained by dynamical refinement on 10° (+/-5°) data*

Atom	Wyckhoff position	x	y	z	Dist (Å)	B (Å^2)
Sr1	2f	0	0.3540(5)	0.75	0.0074	0.316(8)
Sr2	4g	0.7564(2)	0.0323(3)	0.6826(2)	0.01304	0.631(6)
Sr3	4g	0.6516(2)	0.4849(3)	0.6828(3)	0.0190	0.8124(6)
Ge1	4g	0.8530(3)	0.7102(4)	0.9343(3)	0.0148	0.7809(7)
Ge2	4g	0.5883(3)	0.1749(4)	0.3709(3)	0.0070	0.3549(7)
Ge3	4g	0.7903(3)	0.6703(4)	0.4788(3)	0.0267	0.5364(7)
Ge4	4g	0.5403(3)	0.8427(4)	0.414(3)	0.0289	0.473(8)
Ge5	2f	0	0.7777(6)	0.75	0.0197	0.394(8)
Cu1	2d	0	0	0	0	0.552(8)
O1	4g	0.8038(8)	0.699(1)	0.3142(8)	0.093	1.745(2)
O2	4g	0.5416(8)	0.956(1)	0.6248(8)	0.090	1.420(2)
O3	4g	0.9380(8)	0.610(1)	0.8395(8)	0.187	1.025(2)
O4	4g	0.6415(8)	0.678(1)	0.4915(8)	0.067	0.710(2)
O5	4g	0.4153(8)	0.748(1)	0.4683(9)	0.098	1.814(2)
O6	4g	0.6626(7)	0.982(1)	0.4014(7)	0.240	0.316(2)
O7	2e	0.5	0.312(2)	0.25	0.268	0.947(2)
O8	4g	0.9051(8)	0.832(1)	0.071(8)	0.137	0.552(2)
O9	4g	0.8714(7)	0.798(1)	0.5972(8)	0.124	0.237(2)
O10	4g	0.7145(7)	0.733(1)	0.8295(7)	0.106	0.237(2)
O11	4g	0.8167(8)	0.531(1)	0.0333(8)	0.084	1.58(2)
O12	4g	0.5	0.740(1)	0.25	0.00	0.394(2)
O13	2e	0.9183(8)	0.910(1)	0.8340(8)	0.217	1.104(2)

2.2 Application to Manganese Formiate

2.2.a Manganese Formiate

After validation of the proof of concept on $Sr_5CuGe_9O_{24}$, we intended to test the performance of the DS-EDT method on the beam-sensitive metal-organic framework (MOF) of manganese formiate. The powder sample of manganese formiate was provided by Dominique Luneau (LMI UCBL Lyon France). Its chemical composition was $Mn_2(COOH)_2(H_2O)_2$ crystallizing in the low symmetric monoclinic space group $P2_1/c$, with unit cell parameters a = 8.8263(1) Å, b = 7.2247(1) Å, c = 9.6305(1) Å and β = 97.689(1)° [230]. The structure of manganese formiate is represented in **Figure 4.9**.

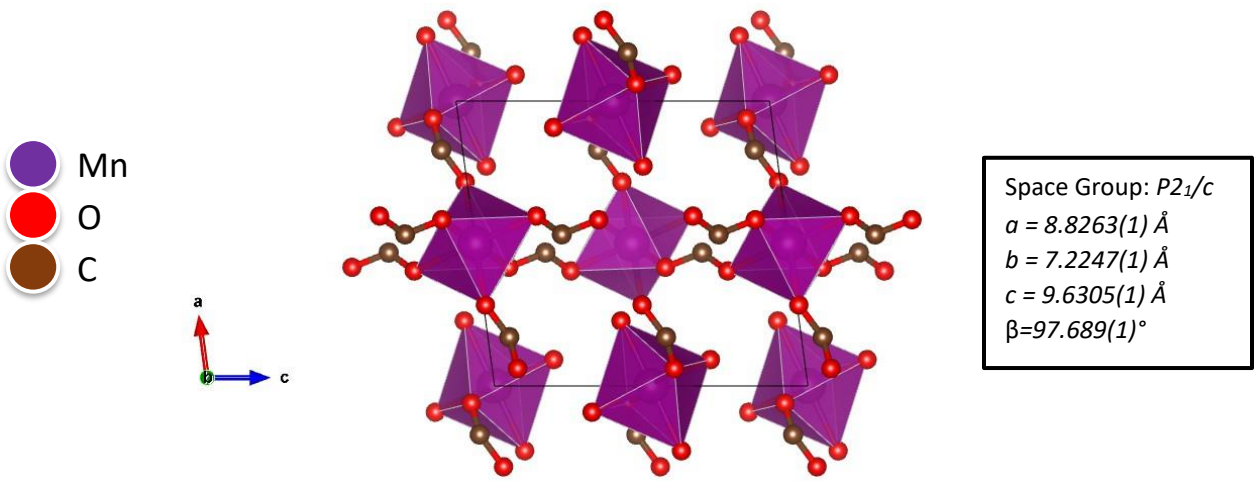

Figure 4.9: *Projection along the **b**-axis of the crystal structure of manganese formiate. Hydrogen positions are omitted.*

The structure consists of Mn ions connected to formiate and water molecules. Two distinct Mn sites can be distinguished. In one site Mn ions are octahedrally coordinated to 6 formiate oxygen atoms. They are interconnected by formiate bridges making up layers in the ***bc*** plane. In the second site the octahedra surrounding Mn ions consist of 4 water oxygens and 2 formiate oxygens. These sites are not interconnected unlike the first site and form separate layers in-between those formed by the other Mn site. Formiate bridges between Mn ions link the two layers.

2.2.b Data Acquisition

The sample preparation for TEM experiment was problematic: ethanol reacts with manganese formiate crystals leading to a loss of crystallinity visible on electron diffraction patterns. It was therefore necessary

to perform a dry preparation. Crystals were ground in an agate mortar without dispersion in a solution, and the carbon coated grid was dropped and gently pressed several times onto different locations on the ground power to collect a sufficient quantity of crystals. Furthermore, crystals turned out to be sensitive to grinding which appeared to induce amorphization. However, grinding is essential to break down the initially large crystals making up the powder into crystal sizes small enough for TEM analysis, which is generally in a sub-micrometer scale. Crystals were therefore ground extremely gently by using no more than gravity as grinding force, for a longer period of a few minutes until sufficiently small crystals were obtained without damage.

Prior to diffraction data acquisition, a preliminary analysis was made to assess the beam-sensitivity of the crystals. Crystals diffracting at high-resolution were irradiated with a known dose rate calculated via the method described in the first section: the fading of reflections under the beam was observed (see **Figure 4.10** as an example). Analysis on multiple particles showed that high-resolution reflections fade at around 2.0 $e^-/Å^2$. The dose per particle during DS-EDT data acquisition was adapted so that the dose inflicted in the +/- 10° range would not exceed this critical dose. The higher tilt frames would then get damaged but would be used for unit cell determination only. This would ensure that crystals were damaged enough to provoke diffraction fading but, in the meantime, to avoid complete amorphization. Diffraction data were then manually collected in DS-EDT mode. The total tilt range per particle was set to +/- 30°, which is a sufficient range for accurate unit cell determination [223]. Data acquisition parameters for 11 particles are given in **Table 4.8**.

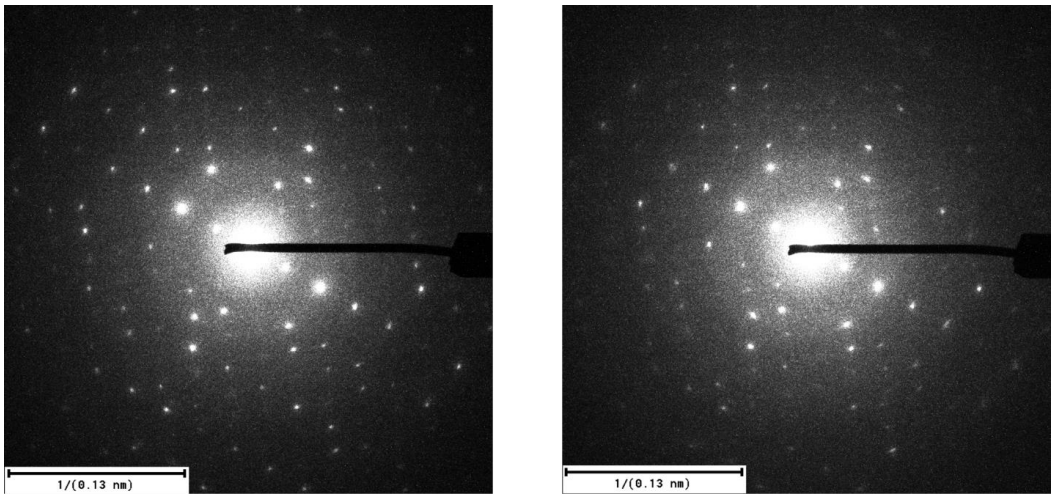

Initial Diffraction Pattern *Diffraction Pattern after 2.0 $e^-/Å^2$*

Figure 4.10: *Example of diffraction intensity loss under the beam from a manganese formiate crystal. High-resolution reflections fade first, lower-resolution reflections remain sharp but also lose part of their intensity*

Table 4.8: *Relevant experimental parameters for DS-EDT data acquisition from Mn Formiate. The dose rate was measured numerically and the exposure time per frame was adjusted to inflict the necessary amount of damage.*

Particle	Angular Range (°)	Dose Rate ($e^-/Å^2.s$)	T_{exp} per frame (ms)	Dose ($e^-/Å^2$)
A	60	0.020	5000	6.10
B	60	0.020	5000	6.10
C	60	0.020	5000	6.10
D	60	0.016	3000	2.93
E	60	0.016	4000	3.90
F	60	0.014	5000	4.27
G	60	0.014	5000	4.27
H	60	0.021	5000	6.40
I	60	0.021	5000	6.40
K	60	0.022	3000	4.03
L	44	0.022	4000	3.96

Once a suitable crystal was identified, a first diffraction image was taken at zero tilt. To ensure goniometer stability, each image was taken with prior tilt being in the same direction. As such, to take the second image at 1°, the crystal was first tilted to 2° and then to 1°. The third image was taken after tilting directly to -1°, followed by tilting to 3° and back to 2° for the fourth image, and so on until reaching -30°. High tilt frames showed clear signs of beam damage as patterns were reduced to only a few reflections in some cases.

In order to check for beam damage rigorously, an image at -30° was systematically taken before DS-EDT data acquisition for comparison. Examples are shown in **Figure 4.11**. Comparing pre- and post-tomography diffraction patterns, it can clearly be seen that a significant portion of reflections disappeared or lost their intensity, which is a clear sign of beam damage.

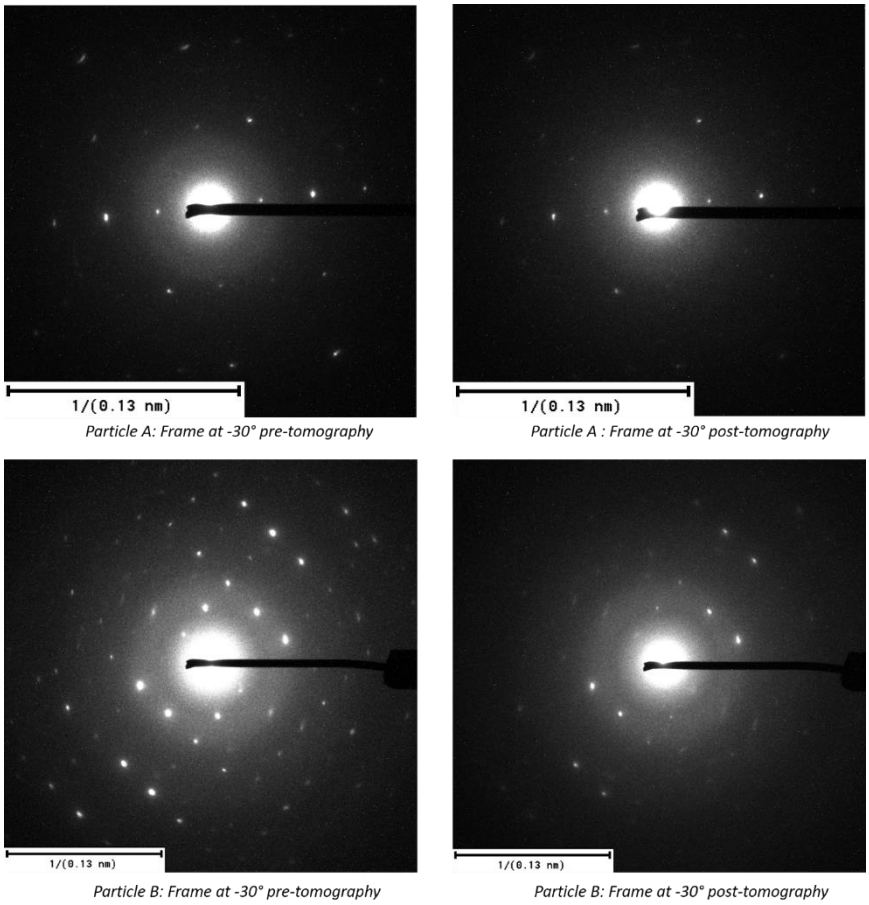

Figure 4.11: *Verification of beam damage to manganese formiate particles. Diffraction images from the same crystal in same orientation were taken before and after DS-EDT data acquisition. It can be seen that crystals undergo substantial damage but a limited number of reflections remain sharp to allow unit cell determination*

2.2.c Data Processing

Data processing with PETS2 was performed in the same manner as in the first section, with particles indexed with the previously known unit cell. **Figure 4.12** contains two examples of probed particles and the corresponding 3D intensity reconstructions. Even though the data shows good quality with clearly spotty reflections, compared to $Sr_5CuGe_9O_{24}$ there is more noise in the data due to lower electron dosage, visible on the figure as indiscriminate intensity around the reflections.

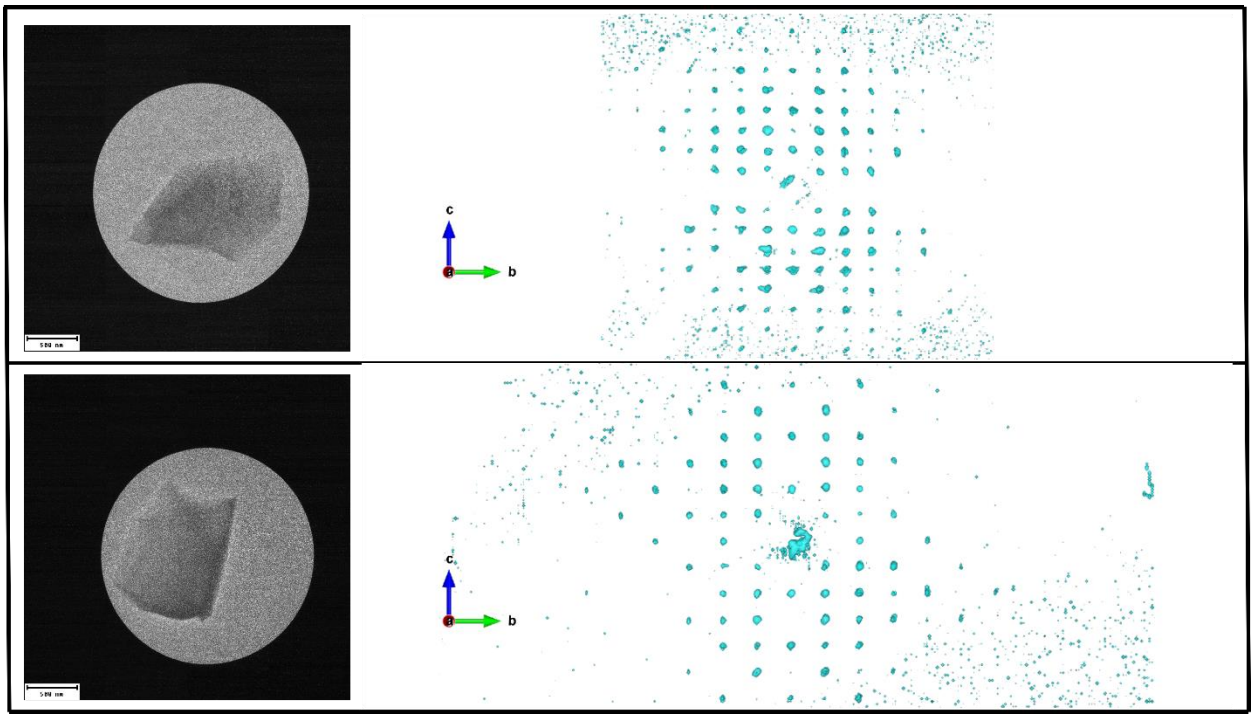

Figure 4.12: *On the left, TEM images of two manganese formiate crystals taken with a selected area diffraction aperture are given. All crystals are kept inside the aperture during tilting. The scale bars correspond to 500 nm. On the right are the corresponding reconstructed 3D intensity distributions in reciprocal space obtained by data processing in PETS2.*

Out of the 11 particles from which DS-EDT data was collected, the correct unit cell within a 5% error range was found for 9 of them. These were particles A to I (see **Table 4.8**). To demonstrate the advantage of the DS-EDT method in case of beam-sensitive particles, and in contrast to the first section, the datasets for which the structure solution using SIR2014 was successful were excluded from the data merging process. As a structure solution could be achieved for particles H and I, only the remaining 7 particles A to G, for which the structure solution using SIR2014 failed were used for truncation and data merging. For these datasets, considerable damage to high tilt frames hindered structure determination. During the structure determination process, hydrogen positions were not considered since they are often too difficult to locate. Most datasets diffracted in the 1.00 – 1.25 Å range, with the highest resolution observed being 0.83 Å.

2.2.d Results

Initially, data from these 7 particles was initially truncated to 20°(+/-10°) around zero tilt and merged in Jana2020. In all cases, common reflections with I/σ higher than 4 were used to scale the data. Despite the fact that the data used for merging was from particles for whom structure solution failed individually,

merging of 20° data from 7 particles led to a succesful structure solution with SIR2014. Data resolution was cut to 0.9 Å. **Table 4.9** contains relevant parameters concerning data merging. Data completeness is noticeably lower when compared to when +/-10° data from 11 particles of $Sr_5CuGe_9O_{24}$ were merged (96 %). This could be due to a higher degree of preferential orientation of manganese formiate crystals on the TEM grid, and the fact that not all datasets diffracted up to 0.9 Å.

Table 4.9*: Relevant parameters related to merging of DS-EDT data from 7 manganese formiate crystals in +/-10° range.* R_{merge} *and Redundancy are calculated by Jana2020 while* R_{model} *and completeness are calculated by SIR2014.*

Tilt range and number of particles	Completeness (%) (to 0.9 Å)	R_{merge}(obs)	Redundancy
+/-10°, 7 Particles	48	9.61	4.81

The raw model contained a total of 13 independent positions (**Table 4.10**). In this list, the height column is an indicator of the electron density amplitude assigned to a given atom position. SIR2014 is often capable of accurately determining the atom positions but the assignment of the chemical identity may be incorrect. In this case, the raw list from SIR2014 contains 2 manganese positions clearly distinguished in terms of height, followed by 6 oxygen and 5 carbon positions. Even though carbon and oxygen have similar contributions to the electrostatic potential, the data quality was sufficient to distinguish them correctly in 6 out of 8 positions. Looking at the carbon positions, it can be seen that there is a clear increase in the displacement parameter B after C2. Considering the chemical composition of manganese formiate, removing the 3 carbons after C2 indeed reveals all the correct positions. Chemical knowledge on the formiate molecules can then be used to distinguish among oxygens and carbons.

The manually corrected model was then used as starting model for dynamical refinement. Data resolution was set to 1.1 Å for both refinements. An initial run of kinematical refinement with default parameters in Jana2020 led to a R_{model} of 29.8 %. A dynamical refinement was performed with RS_g, DS_g and g_{max} set to 0.7, 0.0015 and 1.2, respectively. The thickness optimisation was succesful for all datasets with clear minima observed in thickness optimisation plots. Refinement was performed on F^2(obs) and led to a final R_{model} of 13.08 %.

Table 4.10: *List of atomic coordinates obtained by SIR2014 on manganese formiate 20° data. Atom (SIR2014) refers to the atom identity assigned by SIR2014 while Atom (DRX) refers to the actual identity of the atom based on DRX data.*

Atom (SIR)	Atom (DRX)	Height	x	y	z	Dist(Å)	B(Å^2)
Mn2	Mn1	3.30	0	0	0	0.000	1.63
Mn1	Mn2	3.29	0.5	0.5	0	0.000	1.56
O1	O1	1.35	0.783	0.154	0.004	0.032	0.91
O5	O2	1.24	0.916	0.735	0.104	0.181	2.33
O3	O3	1.22	0.594	0.609	0.202	0.054	3.56
O4	O4	1.21	0.594	0.22	0.087	0.304	4.54
O6	O5	1.05	0.915	0.611	0.298	0.135	4.61
C1	O6	1.05	0.266	0.475	0.059	0.132	2.23
O2	C1	1.00	0.683	0.109	0.062	0.111	2.70
C2	C2	0.97	0.976	0.716	0.223	0.086	0.85
C3	N/A	0.61	0.320	0.596	0.061	N/A	6.77
C4	N/A	0.50	0.021	0.839	0.204	N/A	6.70
C5	N/A	0.30	0.268	0.089	0.171	N/A	13.01

The refined atomic coordinates are given in **Table 4.11** and the refined structure is shown in **Figure 4.13**.

Table 4.11: *List of atomic coordinates obtained by DS-EDT on Mn Formiate in the case of dynamical refinement on +/- 10° data merged from 7 particles.*

Atom	Wyckhoff position	*x*	*y*	*z*	Dist(Å)	B(Å^2)
Mn1	2a	0.000	0.000	0.500	0.000	2.6(1)
Mn2	2d	0.500	0.500	0.500	0.000	0.8(1)
O1	4e	0.708(2)	0.349(1)	0.4973(8)	0.069	2.7(2)
O2	4e	0.416(3)	0.264(1)	0.6014(9)	0.059	4.1(2)
O3	4e	0.394(2)	0.105(1)	0.7986(8)	0.149	2.9(2)
O4	4e	0.931(3)	0.277(1)	0.4220(9)	0.081	4.7(3)
O5	4e	0.910(3)	0.108(1)	0.2889(9)	0.086	4.6(3)
O6	4e	0.219(3)	0.019(1)	0.4414(9)	0.118	5.0(3)
C1	4e	0.837(3)	0.391(1)	0.4414(1)	0.123	5.2(3)
C2	4e	0.473(3)	0.216(1)	0.7320(8)	0.128	2.4(2)

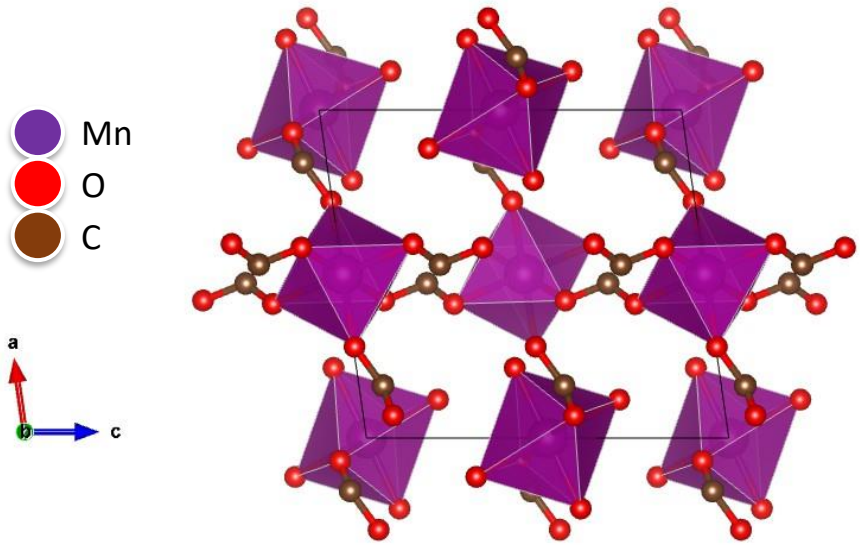

Figure 4.13: *Projection along the **b**-axis of crystal structure of manganese formiate dynamically refined on +/-10° DS-EDT data. Hydrogen positions were not determined*

Final refinement parameters are presented in **Table 4.12**.

Table 4.12: *Final refinement parameters on +/-10° DS-EDT data merged from 6 particles.*

Data	Reflections/ Parameters	R_{model} (obs)	wR_{model} (obs)	R_{model} (all)	wR_{model} (all)	GoF (all)	GoF (obs)
+/-10°, 7 Particles	1674/182	13.08	23.64	16.06	24.19	3.72	4.71

The dynamical refinement improved the accuracy of the oxygen positions, and R_{model} decreased drastically (see **Table 4.13**).

This study proved that DS-EDT made it possible to achieve structure determination including dynamical refinement, by merging low tilt DST data from 7 datasets from which it was impossible to get the structure individually due to accumulated beam damage.

Table 4.13: *Relevant parameters related to data merging and model accuracy for different models obtained on +/-10° DS-EDT data merged from 7 particles. Comp. refers to data completeness and Red. refers to redundancy.*

Data	Comp. (to 0.9 Å) (%)	R_{merge}(obs)	Red.	R_{model} (obs)	Dist Carbons (Å)	Dist Oxygens (Å)	Dist Overall (Å)	Largest Dist (Å)
+/-10°, 7 Particles Structure Solution	48	9.61	4.81	24.18	0.099	0.140	0.115	0.304
+/-10°, 7 Particles Dyn. Refinement	48	9.61	4.81	13.08	0.125	0.094	0.090	0.149

The next step an investigation to find out whether the same result could be obtained with fewer particles or with smaller tilt ranges, as observed in the first section. This was performed by progressively removing datasets from the merging process and checking if the structure solution was still correct. The minimum number of datasets necessary for structure solution was determined to be 4, which were particles A, B, E and F. Relevant parameters from the merging process are given in **Table 14**.

Table 4.14*: Relevant parameters related to merging of DS-EDT data from 4 manganese formiate crystals in +/-10° range. R_{merge} and Redundancy are calculated by Jana2020 while R_{model} and completeness are calculated by SIR2014.*

Tilt range and number of particles	Completeness (%) (to 0.9 Å)	R_{merge} (obs)	Redundancy
+/-10°, 4 Particles	42	10.08	3.12

The I/σ of common reflections to be used for scaling was set to 4 to calculate a common scale. Compared to the 7 particles dataset, completeness and redundancy decreased expectedly, while R_{merge} slightly increased despite the smaller size of the data. This could be due to less precise common scale calculation as a result of the smaller number of common reflections. The relatively small drop in completeness could be due to the removed datasets covering similar areas of the reciprocal space as the remaining 4 particles. Despite the lower completeness, the overall Dist of the raw structure solution was better than the 7 particles case..

The 4 particles structure was then dynamically refined. Final atomic coordinates after the refinement are presented in **Table 4.15**.

Table 4.15: *List of atomic coordinates obtained by DS-EDT on Mn Formiate after refinement on +/- 10° data merged from 4 particles.*

Atom	Wyckhoff position	*x*	*y*	*z*	Dist(Å)	B(Å^2)
Mn1	2a	0.000	0.000	0.500	0.000	2.2(1)
Mn2	2d	0.500	0.500	0.500	0.000	0.6(2)
O1	4e	0.293(3)	0.647(1)	0.505(1)	0.081	2.8(3)
O2	4e	0.585(3)	0.741(1)	0.397(1)	0.061	3.0(3)
O3	4e	0.608(2)	0.898(1)	0.198(1)	0.171	2.2(3)
O4	4e	0.067(3)	0.728(2)	0.580(1)	0.096	3.4(3)
O5	4e	0.092(3)	0.899(1)	0.292(1)	0.042	3.2(3)
O6	4e	0.219(3)	0.022(2)	0.441(1)	0.125	3.9(3)
C1	4e	0.151(4)	0.611(2)	0.561(2)	0.198	4.4(4)
C2	4e	0.530(3)	0.785(1)	0.269(1)	0.104	2.1(3)

The final refinement parameters are given in **Table 4.16**. The final R_{model} is lower than for the structure with 7 particles. This is presumably due to the smaller size of the data. Despite the lower R value, the overall *Dist* is slightly higher than for the 7 particles structure.

Table 4.16: *Final dynamical refinement parameters on +/-10° DS-EDT data merged from 4 particles.*

Tilt range and number of particles	Reflections/ Parameters	R_{model} (obs)	wR_{model} (obs)	R_{model} (all)	wR_{model} (all)	GoF (all)	GoF (obs)
+/-10°, 4 Particles	879/116	11.53	20.39	14.41	20.94	4.11	3.17

Dynamical refinement improved slightly the accuracy for both oxygen and carbon positions, and R_{model} (see **Table 4.17**).

Table 4.17: *Relevant parameters related to data merging and model accuracy for different models obtained on +/-10° DS-EDT data merged from 4 particles. Comp. refers to data completeness and Red. refers to redundancy.*

Tilt range and number of particles	Comp. (to 0.9 Å) (%)	R_{merge} (obs)	Red.	R_{model} (obs)	Dist Carbons (Å)	Dist Oxygens (Å)	Dist Overall (Å)	Largest Dist (Å)
+/-10°, 4 Particles Structure Solution	42	10.08	3.12	23.05	0.165	0.134	0.126	0.195
+/-10°, 4 Particles Dyn. Refinement	42	10.08	3.12	11.53	0.151	0.096	0.098	0.198

The similarity in accuracy between data from 7 particles and 4 particles suggests an absence of direct relationship between data completeness and model accuracy. Another alternative was to lower the tilt range per dataset to check if structure determination was possible with fewer frames. To this end, datasets were further truncated to a range of +/- 5°around zero. I/σ was kept at 4 for scaling. This led to a higher R_{merge} compared to the 7 particles case, as was the case for 4 particles. Completeness was also reduced more significantly compared to the other 2 cases (**Table 4.18**).

Table 4.18: *Relevant parameters related to merging of DS-EDT data from 7 manganese formiate crystals in +/-5° range. R_{merge} and Redundancy are calculated by Jana2020 while R_{model} and completeness are calculated by SIR2014.*

Tilt range and number of particles	Completeness (%) (to 0.9 Å)	R_{merge} (obs)	Redundancy
+/-5°, 7 Particles	38	14.30	3.73

A comparison of overall completeness and completeness above 1.0 Å is given in **Table 4.19**. Comparing the can be seen that the +/-5° case to the +/-10° case with the same number of particles, it can be seen that the loss of overall completeness and the loss of completeness at high resolution are at similar rates, with the loss of completeness at high resolution being relatively larger. This agrees with the fact that the +/-10° zone was in principle damage-free, so the frames removed in the +/- 5-10° region contain high resolution information untouched by beam damage.

Table 4.19: *Comparison of data completeness for different cases of manganese formiate DS-EDT data merging. Completeness is calculated by SIR2014.*

Data	Overall Completeness (%) (to 0.9 Å)	Completeness between 1.0-0.9 Å (%)
+/-10°, 7 Particles	48	26
+/-10°, 4 Particles	42	21
+/-5°, 7 Particles	38	17

Merging of +/- 5 ° data also led to a successful structure solution with SIR2014. Kinematical and dynamical refinements were performed with same parameters as the previous cases. Final refinement parameters are given in **Table 4.20**.

Table 4.20: *Final dynamical refinement parameters on +/- 5° DS-EDT data merged from 7 particles.*

Tilt range and number of particles	Reflections/ Parameters	R_{model} (obs)	wR_{model} (obs)	R_{model} (all)	wR_{model} (all)	GoF (all)	GoF (obs)
+/-5°, 7 Particles	991/114	12.66	22.43	15.44	23.06	4.45	3.68

The list of refined atomic coordinates is provided in **Table 4.21**. Comparing the accuracy to the 7 particles +/-10° cases, accuracy of both oxygen and carbon positions improves despite the lower data completeness. (see **Table 4.22**)

Table 4.21: *List of atomic coordinates obtained by DS-EDT on Mn Formiate in the case of dynamical refinement on +/- 5° data merged from 7 particles.*

Atom	Wyckhoff position	*x*	*y*	*z*	Dist(Å)	B(Å^2)
Mn1	2a	0.000	0.000	0.500	0.000	2.4(2)
Mn2	2d	0.500	0.500	0.500	0.000	0.6(1)
O1	4e	0.787(4)	0.354(2)	0.503(1)	0.049	3.1(3)
O2	4e	0.925(4)	0.734(1)	0.604(1)	0.127	2.6(3)
O3	4e	0.899(3)	0.893(1)	0.801(1)	0.103	2.6(3)
O4	4e	0.571(4)	0.269(2)	0.581(1)	0.136	4.1(3)
O5	4e	0.400(4)	0.108(2)	0.286(1)	0.100	3.9(3)
O6	4e	0.275(4)	0.011(2)	0.562(1)	0.065	4.3(3)
C1	4e	0.648(4)	0.389(2)	0.564(2)	0.006	4.3(4)
C2	4e	0.982(4)	0.785(1)	0.730(1)	0.169	1.1(3)

Table 4.22: *Relevant parameters related to data merging and model accuracy for different models obtained on +/-5° DS-EDT data merged from 7 particles.*

Tilt range and number of particles	Comp. (to 0.9 Å) (%)	R_{merge} (obs)	Red.	R_{model} (obs)	Dist Carbons (Å)	Dist Oxygens (Å)	Dist Overall (Å)	Largest Dist (Å)
+/-5°, 7 Particles Structure Solution	38	14.30	3.73	24.91	0.288	0.316	0.274	0.511
+/-5°, 7 Particles Dyn. Refinement	38	14.30	3.73	12.66	0.088	0.097	0.084	0.169

The results obtained in this section validate the utility of data acquisition in DS-EDT. It was possible to determine the crystal structure of manganese formiate by merging non-damaged frames from multiple particles. These datasets otherwise contained damaged high tilt frames which prevented them from achieving a structure solution. It was possible to lower the number of particles or the tilt range and still determine the structure, and dynamically refine the structures. Further on, the best accuracy was obtained on the lowest tilt range, which shows the advantage of using smaller tilt ranges with less beam damage and apparent thickness.

3) Analysis of Raw Data in case of Unknown Compounds

During the first section, the interpretation and assessment of $Sr_5CuGe_9O_{24}$ structure solutions obtained via direct methods was heavily guided by prior knowledge of the structure. This was to ensure a rapid flow of data comparison to assess the validity of the DST method. It is however worth to consider whether DS-EDT data could lead to a correct structure without making any prior assumptions on the expected structures other than their chemical composition. To show the power of DS-EDT, the raw structure solutions using +/-5° data from $Sr_5CuGe_9O_{24}$ was considered, obtained from merging of 7 particles. The list of atomic coordinates obtained from SIR2014 is given in (**Table 4.23**).

Table 4.23: *List of most accurate atomic coordinates obtained by SIR2014 on $Sr_5CuGe_9O_{24}$ 10° data. Atom (SIR2014) refers to the atom identity assigned by SIR while Atom (DRX) refers to the actual identity of the atom based on DRX data.*

Atom (SIR2014)	Atom (DRX)	Height	x	y	z	Dist(Å)
Sr1	Sr1	8.59	0	0.641	0.25	0.048
Sr2	Sr3	8.56	0.757	0.968	0.183	0.014
Sr3	Sr2	8.28	0.651	0.516	0.182	0.010
Ge1	Ge2	7.54	0.412	0.175	0.13	0.015
Ge2	Ge3	7.11	0.789	0.672	0.478	0.016
Ge3	Ge4	7.05	0.54	0.845	0.413	0.043
Ge4	Ge1	7.00	0.853	0.709	0.933	0.031
Ge5	Ge5	6.97	0	0.224	0.25	0.034
Cu1	Cu1	5.76	0	0	0	0.000
O1	O13	2.78	0.921	0.088	0.33	0.205
O2	O10	2.76	0.707	0.268	0.333	0.139
O3	O9	2.73	0.866	0.8	0.601	0.147
O4	O7	2.65	0.5	0.315	0.25	0.242
O5	O8	2.56	0.902	0.833	0.066	0.153
O6	O4	2.54	0.642	0.322	0.998	0.103
O7	O6	2.52	0.335	0.978	0.099	0.226
O8	O5	2.51	0.585	0.752	0.031	0.133
O9	O12	2.48	0.5	0.737	0.25	0.024
O10	O3	2.34	0.061	0.389	0.159	0.201
O11	O11	2.20	0.822	0.473	0.532	0.097
O12	O2	2.10	0.545	0.044	0.118	0.136
O13	O1	2.02	0.804	0.697	0.313	0.089
O14	N/A	1.03	0.935	0.808	0.790	N/A
O15	N/A	1.03	0.655	0.689	0.868	N/A

The height column is an indicator of the electron density amplitude assigned to a given atom position. In this case, the list contains a total of 24 positions with 9 cations and 15 oxygens. Since the height column is related to the electron density amplitude, it should ideally showcase discrete jumps between different chemical elements. This is the case for the cations, where clear jumps in the height column can be seen. Looking at the remaining 15 oxygens, a clear jump in height can be seen for the last two oxygens at the end of the list. These oxygens are indeed not in the known structure, so their removal results in all oxygen

positions being correctly identified. This removal can also be done by considering the chemical composition of the compound. This means that by analyzing the raw list from SIR2014, all the positions can be correctly identified.

This raw data analysis shows that it would be possible to solve the crystal structures without a priori knowledge of the expected positions, based on statistics derived during the structure solution process and chemical knowledge. The chemical knowledge can either be available from the crystal synthesis process or could be obtained in a TEM from EDX data.

4) Discussion

The aim of this work was to examine whether the technique of dose-symmetric tomography coupled with sub-tomogram averaging could be successfully adapted to 3D electron diffraction. Dose-symmetric tomography involves temporally prioritizing data acquisition from the low tilt range to gather higher resolution data before the onset of beam damage, in addition to less dynamical scattering due to lower apparent thickness. Implementation of sub-tomogram averaging then involves extracting low tilt frames from various particles and achieving structure determination by merging.

The first section involving $Sr_5CuGe_9O_{24}$ showed that structures could be obtained by merging a limited number of low tilt frames from various particles. Comparing accuracy of models obtained from merging of datasets truncated to different ranges, it can be seen that all atom positions with considerable accuracy can be identified down to 10° (+/-5°)-ranged datasets (**Table 4.11**). Given the low number of frames per dataset in this range, it was worthwhile to investigate how accuracy was related to parameters such as data completeness or R_{merge}. This revealed that although accuracy often improved with completeness, this was not always the case (**Figure 4.8**).

The question remains on which criterion to use for selecting which datasets to merge. Improvement of models as a function of completeness has previously been demonstrated [231], and one suggested parameter for merging is the cross-correlation of indexed intensities [227], [231]. This parameter compares the intensities of different measurements of the same reflections, and it has been shown that merging datasets with low correlation leads to higher R_{model} values. However, since accuracy does not correlate with R_{merge} a more thorough analysis to identify relevant factors for dataset selections is needed.

It was possible to perform dynamical refinement on DST data from $Sr_5CuGe_9O_{24}$. In all cases, R_{model} and model accuracy improved significantly. The best accuracy is obtained for the lowest tilt range of +/-5°. This would indicate that while the quantity of data and data completeness are significant for structure solution, they have less an effect on the refinement process, where the quality of data can supersede the importance of data completeness.

Measurements on manganese formiate showcase the ability of DST data collection to circumvent beam damage on 3D ED data. The 20° (+/-10°) range was kept below the critical dose while higher tilt damaged frames were used for rotation axis refinement and unit cell determination. 7 datasets were considered for which structure solution was not individually possible due to accumulation of damage. However, merging data truncated down to 10° (+/-5°) from each of them led to a succesful structure determination. With our data, the minimum number of datasets necessary to achieve a structure solution was 4, with comparable accuracy than the totality of 7 particles (**Table 4.24**).

Comparison of data completeness among the 7 and 4 particles cases revealed that the excluded particles did not contribute significantly to data completeness, due to presumably covering a similar area of reciprocal space. In all cases, data was of sufficient quality to allow for dynamical refinement which further improved the accuracy. Although it could be possible to get hydrogen positions from Fourier difference maps after dynamical refinement [232], this was not attempted here. Inspection of high tilt frames used in this section showed a considerable amount of accumulated damage (**Figure 4.10**, **Figure 4.11**). They, however, still allowed for an accurate indexation of the intensities in the lower tilt range which led to a structure solution.

3D ED data collection with DST allows a more efficient use of the electron dose on sensitive compounds. If the totality of a dataset is necessary for structure determination, the electron dose has to be employed in a conservative manner so that the critical dose is not exceeded until the end of acquisition. In DS-EDT on the contrary, since only the low tilt region is to be employed for structure determination, a higher dose rate can be used to concentrate the critical dose on this region, letting higher tilt regions to get damaged. As our results show here, damaged high tilt frames can still be used to index the reflections. The exact range to keep after truncation as well as the dose rate may be adjusted for different specimens depending on their sensitivity.

Table 4.24: *Relevant parameters related to model accuracy for different models obtained on Mn Formiate. For each model, the total tilt range per particle is indicated followed by the number of particles merged. Comp. refers to data completeness and Red. refers to redundancy.*

Tilt range and number of particles	Comp. (to 0.9 Å) (%)	R_{merge} (obs)	Red.	R_{model} (obs)	Dist Carbons (Å)	Dist Oxygens (Å)	Dist Overall (Å)	Largest Dist (Å)
+/-10°, 7 Particles Structure Solution	48	9.61	4.81	24.18	0.099	0.140	0.115	0.304
+/-10°, 7 Particles Dyn. Refinement	48	9.61	4.81	13.08	0.125	0.094	0.090	0.149
+/-10°, 4 Particles Structure Solution	42	10.08	3.12	23.05	0.165	0.134	0.126	0.195
+/-10°, 4 Particles Dyn. Refinement	42	10.08	3.12	11.53	0.151	0.096	0.098	0.198
+/-5°, 7 Particles Structure Solution	38	14.30	3.73	24.91	0.288	0.316	0.274	0.511
+/-5°, 7 Particles Dyn. Refinement	38	14.30	3.73	12.66	0.088	0.097	0.084	0.169

A high angular range per particle is often not needed to accurately determine the unit cell, so the individual tilt range for DST data does not have to be high. In this work, a total range of 60° was sufficient for manganese formiate. The completeness of DS-EDT data is not limited by the maximum tilt range of

the TEM goniometer, since high completeness can instead be achieved by merging low tilt data from various particles while beam damage is avoided and apparent crystal thickness is kept low.

One of the key steps of 3D ED data processing is the refinement of the rotation axis and the the determination of the frame orientations. Even though the eucentric height has been carefully adjusted, mechanical imperfections of the TEM goniometer can result in a movement of the sample during tilting, leading to a variation of the camera length. Our experience shows that this is especially noticeable at high tilt and highly dependent on the sample holder. Therefore, keeping the total tilt range per particle low and using low tilt data only improves data processing by allowing a more precise refinement of frame orientations. This is also important for dynamical refinement as the orientation of each frame must be precisely refined. A common convention in dynamical refinement is to exclude frames for which the calculated deviation of orientation from their expected orientation is superior to 0.5°. During dynamical refinement on DS-EDT data, the number of such frames was extremely low, which could be related to DS-EDT taking advantage of improved goniometer stability at low tilt.

Results obtained during this thesis shows that DS-EDT is able to circumvent beam damage to highly sensitive compounds without sacrificing the SNR. $Sr_5CuGe_9O_{24}$ and manganese formiate are two very different compounds on which DS-EDT was tested. $Sr_5CuGe_9O_{24}$ has a complex structure with a considerable number of atom positions to determine while manganese formiate is highly beam-sensitive with a molecular structure. The success of these tests therefore shows the potential of DS-EDT to be generalized to many more compounds, to improve 3D ED data quality.

It is worthwhile to compare the possible advantages and disadvantages of using DS-EDT to continuous rotation electron diffraction. The latter is also able to use the electron dose quite efficiently, thanks to rapid data acquisition. Thanks to its shorter acquisition time and ease of implementation for TEMs equipped with a fast detector, the continuous rotation method has currently a wider range of adoption compared to step-wise precession. On the other hand, when a TEM is not equipped with a fast detector, DS-EDT represents an important alternative for data acquisition from beam sensitive materials. It has previously been shown that LD-EDT can achieve the same efficiency in dosage as continuous rotation. Given that DS-EDT can reduce the electron dose up to an order of magnitude compared to LD-EDT, it can potentially allow for lower electron dosage than continuous rotation without compromising the SNR, whereas a lower dose in continuous rotation implies either a lower SNR, or lower data completeness. A comparison of data quality between DS-EDT and continuous rotation is not possible at this stage, but the

reduced requirements on hardware and software for the implementation of DS-EDT gives it potential for a wide adoption in the 3D ED community.

Conclusion and Perspectives

Conclusion

This thesis is placed in the context of the recent spectacular progress in the development of electron crystallography methods based on 3D electron diffraction, both from the point of view of data acquisition and that of their processing. 3D Electron Diffraction has become a widely adapted technique to solve crystal structures of nano-sized crystals. A significant amount of crystal structures in both materials and life sciences have been determined by 3D ED. This work focused on the application and optimization of the low-dose electron diffraction tomography method (LD-EDT), developed in the Néel Institute for the determination of structures of electron beam-sensitive materials.

Beam damage is a common issue which affects the quality of diffraction data. Electron beam-sensitive samples being at the heart of this thesis, a wide bibliographic study of the radiation damage caused by the electron beam was conducted to identify the damage mechanisms. Crystallinity loss is often dominated by a process called radiolysis, where energy absorption by inelastic scattering leads to chemical bond breakage. Most of the damage is inflicted by secondary electrons released upon bond breakage, and crystallinity loss rates differ among specimens due to differences in damage pathways in the crystals. Moreover, different crystals from a same phase can be affected differently, depending in particular on crystal thickness. Environmental factors such as temperature, accelerating voltage, dose rate and sample preparation play a role, but they don't affect all specimens in the same way. All of these phenomena impact the diffraction data. General trends could be extracted from literature and discussed.

In order to ensure the quality of our diffraction data, a reliable method to characterize the crystal degradation level according to the electron dose received is needed. The "diffraction fading" method, widely used in teams studying irradiation damage, particularly in organic materials, is the most sensitive technique to investigate beam damage to crystals. This method consists in analyzing the attenuation (fading) of diffracted beams under electron irradiation, in case of beam-sensitive materials. This gradual disappearance is mainly linked to the degradation of the crystal structure. A quantitative study of the diffracted intensities as a function of electron dose therefore provides information on the degradation level in the crystal. As high-resolution information necessary for structure determination could be lost due to the loss of crystallinity induced by the electron beam, preliminary diffraction fading studies were carried out for each material studied in this work, to characterize its resistance degree of under the electron beam.

LD-EDT was then applied to two sensitive materials, the mineral Bulachite $[Al_6(AsO_4)_3(OH)_9(H_2O)_4]\cdot 2H_2O$ provided by Ian Grey (CSIRO Melbourne Australia) and discovered in 1983 but whose structure could never be determined, and the MOF $\{[Mn^{II}_2[NIT(H, H)Im]_3(CF_3SO_3)\}_n$, referenced in our work as YI_OTf03.

We solved the structure of Bulachite with LD-EDT data. The total dose was kept below 3.0 $e^-/ Å^2$ and data was collected inside a tilt range of +/- 52°. The dataset chosen for structure determination contained 2438 independent reflections with a data completeness of 75% at 0.8 Å resolution. The unit cell was determined to be *a* = 15.6 Å, *b* = 17.7 Å and *c* = 7.9 Å with orthorhombic symmetry. The space group was determined from *hkl* sections to be either *Pnma* or $Pn2_1a$, with the former one confirmed during the structure solution process. The structure was revealed to contain layers made of Al and As-centered polyhedra, with water molecules both inside and in-between the layers. The structural model was first refined from PXRD data and published [233]. A dynamical refinement from the electron diffraction data was then performed, with a final result very close to that from X-ray data. The success of this study opens the way to the structural solution of other minerals, whose structure has not yet been determined by X-ray diffraction.

For the MOF YI_OTf03, experiments by LD-EDT were performed, leading to the determination of the unit cell and lattice symmetry. However, the hardware available at the Néel Institute did not allow data to be obtained with a resolution greater than 1.5 Å, which was insufficient for *ab initio* structure solution. A continuous rotation 3D ED experiment was then carried out in collaboration with Dominique Housset and Wai-Li Ling (IBS Grenoble) on a TEM equipped with a direct detection detector. This allowed record diffracted beams at a wider angle. Nevertheless, the structure solution attempt by *ab initio* methods from this new data remained unsuccessful. The data was then processed by molecular replacement, exploiting *a priori* knowledge of structure contents. The structural model was obtained by Dominique Housset. The crystal structure of YI_OTf03 contains 2D manganese-radical layers arranged in a serpentine-like geometry with layer apexes making contact, where they are bound to inter-layer triflate anions. Large pores are present in-between the apexes, typical of MOF structures. There are two distinct layers present in the asymmetrical unit, who differ in the number of independent Mn centers and their conformation. This and the large size of the triflate anions lead to the c axis being more than 2 times larger compared to other compounds of the same family, whereas unit cell axes parallel to the 2D layers have similar dimensions. The model has now to be refined in future work.

A modification to the LD-EDT acquisition method was proposed during this thesis, by implementing a dose-symmetric tomography (DST) scheme. This consists of collecting data starting from zero tilt and increasing the tilt angle progressively in a symmetrical manner. Dose symmetric electron diffraction

tomography (DS-EDT) could be the solution to record the undamaged crystal data in the best experimental conditions. This involves commencing data acquisition at low specimen tilt, where the highest-resolution reflections are available due to lower apparent thickness with minimal dynamical diffraction. These frames also have better angular precision due to better stability of the TEM goniometer at small angles.

The preliminary step was to determine the acceptability of a certain level of degradation by the material with as final goal the structure solution and refinement. The electron dose could be adjusted so that low tilt data containing high-resolution information remain undamaged with a reasonable SNR while high tilt frames with less crucial information are obtained after the accumulation of damage. The high tilt frames were used for rotation axis refinement and unit cell determination and discarded thereafter. The intensities were integrated only from low tilt frames and structure determination was achieved by merging low tilt data from various particles. This method was tested and verified on two compounds, the complex oxide $Sr_5CuGe_9O_{24}$, and the MOF manganese formiate. Experiments on $Sr_5CuGe_9O_{24}$ showed that it was possible to obtain and dynamically refine the structure by using only +/- 5° frames from 11 particles. The power of DS-EDT was then shown on manganese formiate: a merge of +/- 5° data taken from 7 datasets who individually failed to yield the structure due to beam damage was used to obtain and dynamically refine the structure. The quality of DS-EDT data was sufficient to dynamically refine the obtained structures, and the obtained atomic positions agreed well with those obtained from X-ray diffraction. For both compounds, the best accuracy was obtained by using the lowest tilt range possible.

Perspectives

This thesis focused on using electron diffraction to characterize beam-sensitive materials. Diffraction data can be affected by beam damage in a very complex manner. The question of how to select a critical dose for a given specimen remains difficult to answer. Criteria purely based on intensity measurements such as the 1/e criterion (D_e) or dose for complete fading (D_c) are often insufficient to account for non-monotonous and non-uniform fading. More relevant criteria could be defined based on how damage affects information in real space. This could be investigated by correlating diffraction fading measurements with progressive structure determination from damaged data, which could allow to quantitatively determine how intensity loss has an impact on specific structure features. Previous studies have been done to quantify damage in real space as a function of electron dose, but no direct connection to diffraction fading has been made. A better understanding of the relationship between diffraction fading and real-space information could also allow to correct damage effects on diffraction data, which could be one of the sources for the typically higher *R*-values obtained in the 3D ED field. As an alternative way, dose fractionation, which involves summing intensities from multiple short-exposure frames, could be implemented in 3D ED to remove damage effects on data by choosing the critical dose post-experiment.

While a complete description of beam damage to crystals and its effect on diffraction data remains to be proposed, prevention of damage through low-dose techniques such as DS-EDT remains essential. Implementation of dose-symmetric tomography in LD-EDT could further be improved with a better understanding of the data merging process. Even though higher data completeness is seen to be associated with a higher structure accuracy, this is not always the case. A simple and efficient criterion for selection of datasets for the merging process could be identified with a more thorough analysis of how the accuracy changes with relevant parameters, such as scaling factors and resolution of individual datasets. Pre- and post-refinement accuracy also do not evolve in the same manner as a function of the tilt range, where the effect of the latter is less profound post-refinement. Similar to how frames above a certain tilt threshold are discarded for the structure solution process, a second threshold could be defined for refinement, where data completeness may have less importance over the quality of the frames, which is better for the lower tilt frames.

Improvements in 3D ED data acquisition and processing are essential in strengthening its adoption in the field of crystallography, with one of the main remaining challenges being the reduction of *R* factors in refined structures. This is mostly related to dynamical diffraction, along with contributions from inelastic

scattering, and beam damage. Considerable effort has already been made to reduce dynamical diffraction, by averaging them out via integration or taking them into account via dynamical refinement. Inelastic scattering could be managed by using energy filtering. One remaining untapped potential in 3D ED would be the extraction of phases from TEM images. This has previously been done on 2D crystals and from zone-axis orientations but hasn't been incorporated into 3D ED where phases are determined artificially during data processing. Since most crystallographic information resides in phases rather than intensities, direct measurement of phases could improve structure determination accuracy, by circumventing the phase problem.

Appendix

Appendix A: Specimen Preparation in Electron Diffraction

In case of powder samples, crystals are deposited on TEM grids for observation. TEM grids are covered by amorphous carbon membranes supported by thin metal layers, with typical diameters of a few millimetres. The membranes can be either holey or continuous, which can support the deposited crystals. Holey carbon presents more visible features useful for beam alignment and produces less noise in the data. A typical TEM grid can be seen in **Figure S1**. In order to collect data from single crystals, the concentration of crystals deposited on the grid should be adjusted so that there is a sufficient number of crystals for observation but not too much that they agglomerate. In case of beam sensitive crystals, preparation as a powder is more ideal since processing the sample might cause damage. Powdered samples may also be the only available option in case of samples which are difficult to crystallize.

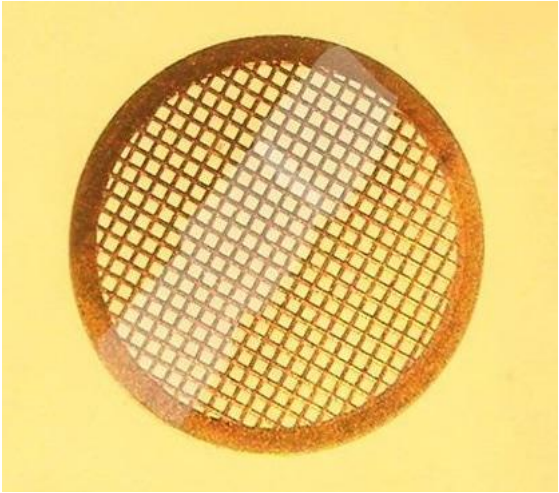

Figure S1: *An image of a typical TEM grid. The carbon membranes are located inside the square shaped holes in-between the metal support seen here in light brown. The diameter of the grid is typically a few millimeters.*

If the powder consists of sub-micrometre sized crystals, crystals can be deposited on the grid without any special preparation procedure. If the crystals is in micrometre size or larger, they can be ground in an agate mortar to obtain smaller crystals suitable for electron diffraction. Crystals can be deposited on the grid in a dry or wet manner. In a wet preparation, the crystals are dispersed inside a liquid medium. Drops

of this dispersion can be introduced onto the grid, which leads to deposition of the crystals through evaporation of the liquid. The concentration of crystals on the grid can be adjusted by adjusting the amount of crystals dispersed, or by adjusting the quantity of liquid deposited onto the grid. Dispersion of the crystals can be further optimised by ultrasonication. It is important to choose a dispersion medium which does not react with or dissolve the crystals. Ethanol is the most commonly used liquid medium for crystal dispersion, but other solvents can be used in case the crystals react to ethanol. If it is not possible to preserve the crystals inside a liquid medium, a dry preparation can be performed. In the dry case, the crystals are simply brought into contact with the grid where they stick to the carbon layer. This can be achieved for example by dropping the crystals using a small spatula, plunging the grid inside the powdered sample or dropping the grid onto an agate mortar where the sample was ground. Despite the advantage of simplicity, dry preparation can lead to agglomeration of crystals, along with a general difficulty in adjusting crystal concentration.

In the case of beam sensitive crystals, specialised preparation techniques can be implemented. These often consist of partially or completely encapsulating crystals with a solid layer, which helps to reduce diffusion rates associated with beam damage but also to protect crystals from the possibly negative impact of the TEM vacuum. This can be done for instance by embedding crystals in glucose, by washing the grid with a glucose solution after crystal deposition [106]. A more common technique is to embed crystals in amorphous ice. This consists of wet deposition onto a grid followed by rapid freezing by plunging the grid into liquid ethane [16]. This technique has been used mainly on hydrated protein crystals to maintain their structure under vacuum, although it has recently been adapted for hydrated mineral samples as well [234]. Crystals can also be encapsulated by thin films, such as amorphous carbon [88], Al or Au films [100]. This consists of depositing the crystallised sample as an epitaxial film on the grid, followed by covering of the film with an evaporated substance. An alternative technique is to stain the crystals with heavy metal salts, through deposition of a solution containing the latter onto the grid after crystal deposition [95]. Even though the main concern of staining is for contrast enhancement in TEM imaging, there is evidence to suggest that they have an effect on beam stability of the crystals [95], [110].

References

[1] R. J. D. Tilley, *Perovskites: structure-property relationships*, First edition. Chichester, West Sussex: Wiley, 2016.

[2] R. Vincent and P. A. Midgley, *Ultramicroscopy*, vol. 53, no. 3, pp. 271–282, Mar. 1994, doi: 10.1016/0304-3991(94)90039-6.

[3] U. Kolb, E. Mugnaioli, and T. E. Gorelik, "Automated electron diffraction tomography - a new tool for nano crystal structure analysis," *Cryst. Res. Technol.*, vol. 46, no. 6, pp. 542–554, Jun. 2011, doi: 10.1002/crat.201100036.

[4] M. Gemmi *et al.*, "3D Electron Diffraction: The Nanocrystallography Revolution," *ACS Cent. Sci.*, vol. 5, no. 8, pp. 1315–1329, Aug. 2019, doi: 10.1021/acscentsci.9b00394.

[5] R. Henderson, "The potential and limitations of neutrons, electrons and X-rays for atomic resolution microscopy of unstained biological molecules," *Q. Rev. Biophys.*, vol. 28, no. 2, pp. 171–193, May 1995, doi: 10.1017/S003358350000305X.

[6] A. Saha, S. S. Nia, and J. A. Rodríguez, "Electron Diffraction of 3D Molecular Crystals," *Chem. Rev.*, p. acs.chemrev.1c00879, Aug. 2022, doi: 10.1021/acs.chemrev.1c00879.

[7] S. Kodjikian and H. Klein, "Low-dose electron diffraction tomography (LD-EDT)," *Ultramicroscopy*, vol. 200, pp. 12–19, 2019.

[8] D. B. Williams and C. B. Carter, *Transmission Electron Microscopy*. Boston, MA: Springer US, 2009. doi: 10.1007/978-0-387-76501-3.

[9] R. Danev, H. Yanagisawa, and M. Kikkawa, "Cryo-Electron Microscopy Methodology: Current Aspects and Future Directions," *Trends Biochem. Sci.*, vol. 44, no. 10, pp. 837–848, Oct. 2019, doi: 10.1016/j.tibs.2019.04.008.

[10] Q. Chen *et al.*, "Imaging Beam-Sensitive Materials by Electron Microscopy," *Adv. Mater.*, vol. 32, no. 16, p. 1907619, Apr. 2020, doi: 10.1002/adma.201907619.

[11] D. T. Grubb, "Radiation damage and electron microscopy of organic polymers," *J. Mater. Sci.*, vol. 9, no. 10, pp. 1715–1736, Oct. 1974, doi: 10.1007/BF00540772.

[12] R. F. Egerton, "Radiation damage to organic and inorganic specimens in the TEM," *Micron*, vol. 119, pp. 72–87, Apr. 2019, doi: 10.1016/j.micron.2019.01.005.

[13] M. R. Stevens, Q. Chen, U. Weierstall, and J. C. H. Spence, "Transmission Electron Diffraction at 200 eV and Damage Thresholds below the Carbon K Edge," *Microsc. Microanal.*, vol. 6, no. 4, pp. 368–379, Jul. 2000, doi: 10.1007/s100050010041.

[14] R. M. Glaeser, "Specimen Behavior in the Electron Beam," *Methods Enzymol.*, vol. 579, no. The Resolution Revolution: Recent Advances In cryoEM, pp. 19–50, 2016.

[15] L. Reimer and H. Kohl, *Transmission electron microscopy: physics of image formation*, 5. ed. New York, NY: Springer, 2008.

[16] R. A. Steinbrecht and K. Zierold, Eds., *Cryotechniques in Biological Electron Microscopy*. Berlin, Heidelberg: Springer Berlin Heidelberg, 1987. doi: 10.1007/978-3-642-72815-0.

[17] R. F. Egerton, "Control of radiation damage in the TEM," *Ultramicroscopy*, vol. 127, pp. 100–108, Apr. 2013, doi: 10.1016/j.ultramic.2012.07.006.

[18] R. F. Egerton, "Mechanisms of radiation damage in beam-sensitive specimens, for TEM accelerating voltages between 10 and 300 kV," *Microsc. Res. Tech.*, vol. 75, no. 11, pp. 1550–1556, Nov. 2012, doi: 10.1002/jemt.22099.

[19] G. R. Freeman, "Basics of radiation chemistry," in *The Study of Fast Pbocesses and Transient Species by Electron Pulse Radiolysis*, D. Reidel Pub. Co., 1982, pp. 19–33.

[20] M. S'ari *et al.*, "Towards developing a predictive approach to assessing electron beam instability during Transmission Electron Microscopy of drug molecules," *Mol Pharm*, vol. 13, p. 13, 2018.
[21] K. A. Taylor and R. M. Glaeser, "Electron microscopy of frozen hydrated biological specimens," *J. Ultrastruct. Res.*, vol. 55, no. 3, pp. 448–456, Jun. 1976, doi: 10.1016/S0022-5320(76)80099-8.
[22] J. R. Fryer, "The effect of dose rate on imaging aromatic organic crystals," *Ultramicroscopy*, vol. 23, no. 3–4, pp. 321–327, Jan. 1987, doi: 10.1016/0304-3991(87)90242-7.
[23] E. J. VandenBussche and D. J. Flannigan, "Reducing Radiation Damage in Soft Matter with Femtosecond-Timed Single-Electron Packets," *Nano Lett.*, vol. 19, no. 9, pp. 6687–6694, Sep. 2019, doi: 10.1021/acs.nanolett.9b03074.
[24] K. Stenn and G. F. Bahr, "Specimen damage caused by the beam of the transmission electron microscope, a correlative reconsideration," *J. Ultrastruct. Res.*, vol. 31, no. 5–6, pp. 526–550, Jun. 1970, doi: 10.1016/S0022-5320(70)90167-X.
[25] G. Földiák, "Radiolysis of liquid hydrocarbons," *Radiat. Phys. Chem. 1977*, vol. 16, no. 6, pp. 451–463, Jan. 1980, doi: 10.1016/0146-5724(80)90191-0.
[26] E. S. Copeland, T. Sanner, and A. Pihl, "Transfer of Radiation Energy between Macromolecules at 77°K," *Int. J. Radiat. Biol. Relat. Stud. Phys. Chem. Med.*, vol. 18, no. 1, pp. 85–89, Jan. 1970, doi: 10.1080/09553007014550851.
[27] W. R. K. Clark, J. N. Chapman, A. M. MacLeod, and R. P. Ferrier, "Radiation damage mechanisms in copper phthalocyanine and its chlorinated derivatives," *Ultramicroscopy*, vol. 5, no. 1–3, pp. 195–208, Jan. 1980, doi: 10.1016/0304-3991(80)90024-8.
[28] J. R. Fryer, "High-resolution imaging of organic crystals," *J. Electron Microsc. Tech.*, vol. 11, no. 4, pp. 310–325, Apr. 1989, doi: 10.1002/jemt.1060110410.
[29] R. F. Egerton, P. Li, and M. Malac, "Radiation damage in the TEM and SEM," *Micron*, vol. 35, no. 6, pp. 399–409, Aug. 2004, doi: 10.1016/j.micron.2004.02.003.
[30] T. Grant and N. Grigorieff, "Measuring the optimal exposure for single particle cryo-EM using a 2.6 Å reconstruction of rotavirus VP6," *eLife*, vol. 4, p. e06980, May 2015, doi: 10.7554/eLife.06980.
[31] R. M. Glaeser and K. A. Taylor, "Radiation damage relative to transmission electron microscopy of biological specimens at low temperature: a review," *J. Microsc.*, vol. 112, no. 1, pp. 127–138, Jan. 1978, doi: 10.1111/j.1365-2818.1978.tb01160.x.
[32] V. E. Cosslett, "Radiation damage in the high resolution electron microscopy of biological materials: A review*," *J. Microsc.*, vol. 113, no. 2, pp. 113–129, Jul. 1978, doi: 10.1111/j.1365-2818.1978.tb02454.x.
[33] M. J. Peet, R. Henderson, and C. J. Russo, "The energy dependence of contrast and damage in electron cryomicroscopy of biological molecules," *Ultramicroscopy*, vol. 203, pp. 125–131, Aug. 2019, doi: 10.1016/j.ultramic.2019.02.007.
[34] M. Nord, P. E. Vullum, I. Hallsteinsen, T. Tybell, and R. Holmestad, "Assessing electron beam sensitivity for SrTiO3 and La0.7Sr0.3MnO3 using electron energy loss spectroscopy," *Ultramicroscopy*, vol. 169, pp. 98–106, Oct. 2016, doi: 10.1016/j.ultramic.2016.07.004.
[35] S. D. Lin, "Electron Radiation Damage of Thin Films of Glycine, Diglycine, and Aromatic Amino Acids," *Radiat. Res.*, vol. 59, no. 3, p. 521, Sep. 1974, doi: 10.2307/3574071.
[36] T. A. Hall and B. L. Gupta, "Beam-induced loss of organic mass under electron-microprobe conditions," *J. Microsc.*, vol. 100, no. 2, pp. 177–188, Mar. 1974, doi: 10.1111/j.1365-2818.1974.tb03927.x.
[37] M. Isaacson, "Electron beam induced damage of organic solids: Implications for analytical electron microscopy," *Ultramicroscopy*, vol. 4, no. 2, pp. 193–199, Jan. 1979, doi: 10.1016/S0304-3991(79)90193-1.

[38] W. Chiu and T. W. Jeng, “Electron radiation sensitivity of protein crystals,” *Ultramicroscopy*, vol. 10, no. 1–2, pp. 63–69, Jan. 1982, doi: 10.1016/0304-3991(82)90188-7.

[39] L. Reimer, “IRRADIATION CHANGES IN ORGANIC AND INORGANIC OBJECTS,” *Lab. Investig. J. Tech. Methods Pathol.*, vol. 14, pp. 1082–1096, Jun. 1965.

[40] L. Reimer and J. Spruth, “Interpretation of the fading of diffraction patterns from organic substances irradiated with 100 keV electrons at 10-300 K,” *Ultramicroscopy*, vol. 10, no. 3, pp. 199–210, Jan. 1982, doi: 10.1016/0304-3991(82)90039-0.

[41] M. F. Schmid, J. Jakana, P. Matsudaira, and W. Chiu, “Effects of radiation damage with 400-kV electrons on frozen, hydrated actin bundles,” *J. Struct. Biol.*, vol. 108, no. 1, pp. 62–68, Jan. 1992, doi: 10.1016/1047-8477(92)90007-W.

[42] T.-W. Jeng and W. Chiu, “Quantitative assessment of radiation damage in a thin protein crystal,” *J. Microsc.*, vol. 136, no. 1, pp. 35–44, Oct. 1984, doi: 10.1111/j.1365-2818.1984.tb02544.x.

[43] P. Li and R. F. Egerton, “Radiation damage in coronene, rubrene and p-terphenyl, measured for incident electrons of kinetic energy between 100 and 200kev,” *Ultramicroscopy*, vol. 101, no. 2–4, pp. 161–172, Nov. 2004, doi: 10.1016/j.ultramic.2004.05.010.

[44] D. Zhang *et al.*, “Atomic-resolution transmission electron microscopy of electron beam–sensitive crystalline materials,” *Science*, vol. 359, no. 6376, pp. 675–679, Feb. 2018, doi: 10.1126/science.aao0865.

[45] H. Qi *et al.*, “Near–atomic-scale observation of grain boundaries in a layer-stacked two-dimensional polymer,” *Sci. Adv.*, vol. 6, no. 33, p. eabb5976, Aug. 2020, doi: 10.1126/sciadv.abb5976.

[46] M. Isaacson, D. Johnson, and A. V. Crewe, “Electron Beam Excitation and Damage of Biological Molecules; Its Implications for Specimen Damage in Electron Microscopy,” *Radiat. Res.*, vol. 55, no. 2, p. 205, Aug. 1973, doi: 10.2307/3573678.

[47] L. Reimer, “Methods of detection of radiation damage in electron microscopy,” *Ultramicroscopy*, vol. 14, no. 3, pp. 291–303, Jan. 1984, doi: 10.1016/0304-3991(84)90097-4.

[48] W. Chiu, K. H. Downing, J. Dubochet, H. G. Heide, E. Knapek, and F. Zemlin, “Cryoprotection in electron microscopy,” *J. Microsc.*, vol. 141, no. 3, pp. 385–391, Mar. 1986, doi: 10.1111/j.1365-2818.1986.tb02731.x.

[49] A. Boudet and C. Roucau, “Dégradation des monocristaux de polyéthylène en microscopie électronique entre 1 et 2,5 MV. I. Etude à température ambiante,” *J. Phys.*, vol. 46, no. 9, pp. 1571–1579, 1985, doi: 10.1051/jphys:019850046090157100.

[50] R. F. Egerton, “Choice of operating voltage for a transmission electron microscope,” *Ultramicroscopy*, vol. 145, pp. 85–93, Oct. 2014, doi: 10.1016/j.ultramic.2013.10.019.

[51] R. H. Wade and J. Pelissier, “The temperature dependence of the electron irradiation resistance of crystalline paraffin,” *Ultramicroscopy*, vol. 10, no. 3, pp. 285–290, Jan. 1982, doi: 10.1016/0304-3991(82)90049-3.

[52] J. Cattle, M. S’ari, N. Hondow, P. Abellán, A. P. Brown, and R. M. D. Brydson, “Transmission electron microscopy of a model crystalline organic, theophylline,” *J. Phys. Conf. Ser.*, vol. 644, p. 012030, Oct. 2015, doi: 10.1088/1742-6596/644/1/012030.

[53] E. Knapek, G. Lefranc, H. G. Heide, and I. Dietrich, “Electron microscopical results on cryoprotection of organic materials obtained with cold stages,” *Ultramicroscopy*, vol. 10, no. 1–2, pp. 105–110, Jan. 1982, doi: 10.1016/0304-3991(82)90192-9.

[54] M. K. Lamvik, “Radiation damage in dry and frozen hydrated organic material,” *J. Microsc.*, vol. 161, no. 1, pp. 171–181, Jan. 1991, doi: 10.1111/j.1365-2818.1991.tb03081.x.

[55] Z. J. W. A. Leijten, A. D. A. Keizer, G. de With, and H. Friedrich, “Quantitative Analysis of Electron Beam Damage in Organic Thin Films,” *J. Phys. Chem. C*, vol. 121, no. 19, pp. 10552–10561, May 2017, doi: 10.1021/acs.jpcc.7b01749.

[56] M. Ilett *et al.*, “Analysis of complex, beam-sensitive materials by transmission electron microscopy and associated techniques,” *Philos. Trans. R. Soc. Math. Phys. Eng. Sci.*, vol. 378, no. 2186, p. 20190601, Dec. 2020, doi: 10.1098/rsta.2019.0601.

[57] U. Kolb, T. E. Gorelik, E. Mugnaioli, and A. Stewart, “Structural Characterization of Organics Using Manual and Automated Electron Diffraction,” *Polym. Rev.*, vol. 50, no. 3, pp. 385–409, Jul. 2010, doi: 10.1080/15583724.2010.494238.

[58] J. Hattne, “Analysis of Global and Site-Specific Radiation Damage in Cryo-EM,” *Structure*, vol. 26, pp. 759–766, 2018.

[59] E. F. Garman and M. Weik, “Radiation Damage in Macromolecular Crystallography,” *Synchrotron Radiat. News*, vol. 28, no. 6, p. 6, 2015.

[60] G. Siegel, “Der Einfluß tiefer Temperaturen auf die Strahlenschädigung von organischen Kristallen durch 100 keV-Elektronen,” *Z Naturforsch*, no. 27 a, pp. 325–332, 1972.

[61] R. H. Wade, “The temperature dependence of radiation damage in organic and biological materials,” *Ultramicroscopy*, vol. 14, no. 3, pp. 265–270, Jan. 1984, doi: 10.1016/0304-3991(84)90094-9.

[62] B. E. Bammes, J. Jakana, M. F. Schmid, and W. Chiu, “Radiation damage effects at four specimen temperatures from 4 to 100K,” *J. Struct. Biol.*, vol. 169, no. 3, pp. 331–341, Mar. 2010, doi: 10.1016/j.jsb.2009.11.001.

[63] M. K. Lamvik, D. A. Kopf, and J. D. Robertson, “Radiation damage in l-valine at liquid helium temperature,” *Nature*, vol. 301, no. 5898, pp. 332–334, Jan. 1983, doi: 10.1038/301332a0.

[64] J. Pawley, “An HVEM for high resolution low-dose studies of biomacromolecules,” *Ultramicroscopy*, vol. 13, no. 4, pp. 387–405, Jan. 1984, doi: 10.1016/0304-3991(84)90005-6.

[65] T. Ohno, “**Fading and broadening of electron diffraction spot from beam-damaged multiple monolayer films**,” *J. Microsc.*, vol. 184, no. 1, pp. 17–21, Oct. 1996, doi: 10.1046/j.1365-2818.1996.1170674.x.

[66] J. R. Fryer and D. L. Dorset, Eds., *Electron Crystallography of Organic Molecules*. Dordrecht: Springer Netherlands, 1991. doi: 10.1007/978-94-011-3278-7.

[67] T. Ohno, “Intensity changes induced by beam damage in electron diffraction from behenic acid multiple monolayers,” *Ultramicroscopy*, vol. 48, no. 3, pp. 359–363, Mar. 1993, doi: 10.1016/0304-3991(93)90111-A.

[68] P. W. Teare, “The crystal structure of orthorhombic hexatriacontane, $C_{36}H_{74}$,” *Acta Crystallogr.*, vol. 12, no. 4, pp. 294–300, Apr. 1959, doi: 10.1107/S0365110X59000901.

[69] S. R. Craig, G. P. Hastie, K. J. Roberts, and J. N. Sherwood, “Investigation into the structures of some normal alkanes within the homologous series C13H28 to C60H122 using high-resolution synchrotron X-ray powder diffraction,” *J. Mater. Chem.*, vol. 4, no. 6, p. 977, 1994, doi: 10.1039/jm9940400977.

[70] A. V. Bailey, D. Mitcham, A. D. French, and G. Sumrell, “Unit cell dimensions of some long chain fatty acid polymorphs,” *J. Am. Oil Chem. Soc.*, vol. 52, no. 6, pp. 196–197, Jun. 1975, doi: 10.1007/BF02672169.

[71] K. H. Downing, “Temperature dependence of the critical electron exposure for hydrocarbon monolayers,” *Ultramicroscopy*, vol. 11, no. 4, pp. 229–237, Jan. 1983, doi: 10.1016/0304-3991(83)90003-7.

[72] D. L. Dorset, F. M. Holland, and J. R. Fryer, “The ‘quasi-thermal’ mechanism for electron beam damage of n-Paraffins,” *Ultramicroscopy*, vol. 13, no. 3, pp. 305–310, 1984, doi: 10.1016/0304-3991(84)90208-0.

[73] H. Kiho and P. Ingram, “Phase changes in polyethylene single crystals. The effects of thermal stress and electron irradiation,” *Makromol. Chem.*, vol. 118, no. 1, pp. 45–59, Nov. 1968, doi: 10.1002/macp.1968.021180104.

[74] D. L. Dorset and F. Zemlin, “Structural changes in electron-irradiated paraffin crystals at < 15K and their relevance to lattice imaging experiments,” *Ultramicroscopy*, vol. 17, no. 3, pp. 229–235, Jan. 1985, doi: 10.1016/0304-3991(85)90089-0.

[75] D. L. Dorset and F. Zemlin, “Specimen movement in electron-irradiated paraffin crystals — A model for initial beam damage,” *Ultramicroscopy*, vol. 21, no. 3, pp. 263–270, Jan. 1987, doi: 10.1016/0304-3991(87)90151-3.

[76] D. L. Dorset and J. N. Turner, “Thermal effects in electron-beam damage of organic crystals,” *Naturwissenschaften*, vol. 63, no. 3, pp. 145–146, Mar. 1976, doi: 10.1007/BF00600491.

[77] G. Valdrè and U. Muscatello, “Organization Modes and Electron Radiation Damage of Cardiolipin Crystals,” *J. Appl. Crystallogr.*, vol. 31, no. 6, pp. 869–873, Dec. 1998, doi: 10.1107/S0021889898007031.

[78] T. Ohno, “Electron beam damage of behenic acid films,” *Ultramicroscopy*, vol. 15, no. 4, pp. 319–324, Jan. 1984, doi: 10.1016/0304-3991(84)90126-8.

[79] C. J. Brown, “Crystal structure of β-copper phthalocyanine,” *J Chem Soc A*, vol. 0, no. 0, pp. 2488–2493, 1968, doi: 10.1039/J19680002488.

[80] T. Kobayashi and L. Reimer, “Limits in the High Resolution Electron Microscopy of Halogen Substituted Organic Molecule Single Crystals Caused by Radiation Damage,” *Bull. Inst. Chem. Res. Kyoto Univ.*, vol. 53, no. 2, pp. 105–116, 1975.

[81] D. G. Howitt and G. Thomas, “Electron damage in organic crystals,” *Radiat. Eff.*, vol. 34, no. 4, pp. 209–215, Jan. 1977, doi: 10.1080/00337577708233149.

[82] J. R. Fryer and F. Holland, “High resolution electron microscopy of molecular crystals III. Radiation processes at room temperature,” *Proc. R. Soc. Lond. Math. Phys. Sci.*, vol. 393, no. 1805, pp. 353–369, Jun. 1984, doi: 10.1098/rspa.1984.0062.

[83] M. Misra and R. F. Egerton, “Assessment of electron irradiation damage to biomolecules by electron diffraction and electron energy-loss spectroscopy,” *Ultramicroscopy*, vol. 15, no. 4, pp. 337–344, Jan. 1984, doi: 10.1016/0304-3991(84)90128-1.

[84] M. Koshino, Y. H. Masunaga, T. Nemoto, H. Kurata, and S. Isoda, “Radiation damage analysis of 7,7,8,8,-tetracyanoquinodimethane (TCNQ) and 2,3,5,6,-tetrafluoro-7,7,8,8,-tetracyanoquinodimethane (F4TCNQ) by electron diffraction and electron energy loss spectroscopy,” *Micron*, vol. 36, no. 3, pp. 271–279, Apr. 2005, doi: 10.1016/j.micron.2004.12.007.

[85] M. Koshino, H. Kurata, and S. Isoda, “Stability Due to Peripheral Halogenation in Phthalocyanine Complexes,” *Microsc. Microanal.*, vol. 13, no. 2, pp. 96–107, Apr. 2007, doi: 10.1017/S1431927607070201.

[86] M. Hayashida, T. Kawasaki, Y. Kimura, and Y. Takai, “Estimation of suitable condition for observing copper–phthalocyanine crystalline film by transmission electron microscopy,” *Nucl. Instrum. Methods Phys. Res. Sect. B Beam Interact. Mater. At.*, vol. 248, no. 2, pp. 273–278, Aug. 2006, doi: 10.1016/j.nimb.2006.04.168.

[87] J. R. Fryer, “Radiation damage in organic crystalline films,” *Ultramicroscopy*, vol. 14, no. 3, pp. 227–236, Jan. 1984, doi: 10.1016/0304-3991(84)90091-3.

[88] J. R. Fryer and F. Holland, “The reduction of radiation damage in the electron microscope,” *Ultramicroscopy*, vol. 11, no. 1, pp. 67–70, Jan. 1983, doi: 10.1016/0304-3991(83)90055-4.

[89] W. J. Claffey and D. F. Parsons, “Electron diffraction study of radiation damage in coronene,” *Philos. Mag.*, vol. 25, no. 3, pp. 637–643, Mar. 1972, doi: 10.1080/14786437208228896.

[90] K. Torii and Y. Iitaka, “The crystal structure of L -valine,” *Acta Crystallogr. B*, vol. 26, no. 9, pp. 1317–1326, Sep. 1970, doi: 10.1107/S0567740870004065.

[91] D. G. Howitt, R. M. Glaeser, and G. Thomas, “The energy dependence of electron radiation damage in l-valine,” *J. Ultrastruct. Res.*, vol. 55, no. 3, pp. 457–461, Jun. 1976, doi: 10.1016/S0022-5320(76)80100-1.

[92] J. R. Fryer, C. H. McConnell, F. Zemlin, and D. L. Dorset, “Effect of temperature on radiation damage to aromatic organic molecules,” *Ultramicroscopy*, vol. 40, no. 2, pp. 163–169, Feb. 1992, doi: 10.1016/0304-3991(92)90057-Q.

[93] S. M. Salih and V. E. Cosslett, “Radiation damage in electron microscopy of organic materials: effect of low temperatures,” *J. Microsc.*, vol. 105, no. 3, pp. 269–276, Dec. 1975, doi: 10.1111/j.1365-2818.1975.tb04059.x.

[94] E. Knapek, H. Formanek, G. Lefranc, and I. Dietrich, “The interpretation of radiation damage measurements with electron diffraction of organic materials at very low temperatures,” *Ultramicroscopy*, vol. 14, no. 3, pp. 253–263, Jan. 1984, doi: 10.1016/0304-3991(84)90093-7.

[95] R. M. Glaeser, “Limitations to significant information in biological electron microscopy as a result of radiation damage,” *J. Ultrastruct. Res.*, vol. 36, no. 3–4, pp. 466–482, Aug. 1971, doi: 10.1016/S0022-5320(71)80118-1.

[96] J. Brink and W. Chiu, “Contrast analysis of cryo-images of n-paraffin recorded at 400***kV out to 2·1 Å resolution,” *J. Microsc.*, vol. 161, no. 2, pp. 279–295, Feb. 1991, doi: 10.1111/j.1365-2818.1991.tb03090.x.

[97] T. Ohno, M. Sengoku, and T. Arii, “Measurements of electron beam damage for organic crystals in a high voltage electron microscope with image plates,” *Micron*, vol. 33, no. 4, pp. 403–406, Jan. 2002, doi: 10.1016/S0968-4328(01)00023-3.

[98] H. Choe *et al.*, “Mitigation of radiation damage in biological macromolecules via tunable picosecond pulsed transmission electron microscopy,” Biophysics, preprint, May 2020. doi: 10.1101/2020.05.15.099036.

[99] J. R. Fryer, C. McNee, and F. M. Holland, “The further reduction of radiation damage in the electron microscope,” *Ultramicroscopy*, vol. 14, no. 4, pp. 357–358, Jan. 1984, doi: 10.1016/0304-3991(84)90221-3.

[100] S. M. Salih and V. E. Cosslett, “Reduction in electron irradiation damage to organic compounds by conducting coatings,” *Philos. Mag.*, vol. 30, no. 1, pp. 225–228, Jul. 1974, doi: 10.1080/14786439808206550.

[101] J. R. Fryer, “Molecular arrays and molecular structure in organic thin films observed by electron microscopy,” *J. Phys. Appl. Phys.*, vol. 26, no. 8B, pp. B137–B144, Aug. 1993, doi: 10.1088/0022-3727/26/8B/022.

[102] M. Warkentin, J. B. Hopkins, R. Badeau, A. M. Mulichak, L. J. Keefe, and R. E. Thorne, “Global radiation damage: temperature dependence, time dependence and how to outrun it,” *J. Synchrotron Radiat.*, vol. 20, no. 1, pp. 7–13, Jan. 2013, doi: 10.1107/S0909049512048303.

[103] J. Z. Chen, C. Sachse, C. Xu, T. Mielke, C. M. T. Spahn, and N. Grigorieff, “A dose-rate effect in single-particle electron microscopy,” *J. Struct. Biol.*, vol. 161, no. 1, pp. 92–100, Jan. 2008, doi: 10.1016/j.jsb.2007.09.017.

[104] S. B. Hayward and R. M. Glaeser, “Radiation damage of purple membrane at low temperature,” *Ultramicroscopy*, vol. 4, no. 2, pp. 201–210, Jan. 1979, doi: 10.1016/S0304-3991(79)90211-0.

[105] V. R. Matricardi, R. C. Moretz, and D. F. Parsons, “Electron Diffraction of Wet Proteins: Catalase,” *Science*, vol. 177, no. 4045, pp. 268–270, Jul. 1972, doi: 10.1126/science.177.4045.268.

[106] P. N. T. Unwin and R. Henderson, “Molecular structure determination by electron microscopy of unstained crystalline specimens,” *J. Mol. Biol.*, vol. 94, no. 3, pp. 425–440, May 1975, doi: 10.1016/0022-2836(75)90212-0.

[107] S. W. Hui, “RADIATION DAMAGE OF PHOSPHATIDYLCHOLINE BILAYERS: EFFECTS OF TEMPERATURE AND HYDRATION,” *Ultramicroscopy*, vol. 5, pp. 505–512, 1980.

[108] W. Chiu, E. Knapek, T. W. Jeng, and I. Dietrich, “Electron radiation damage of a thin protein crystal at 4 K,” *Ultramicroscopy*, vol. 6, no. 3, pp. 291–295, Jan. 1981, doi: 10.1016/S0304-3991(81)80165-9.

[109] Y. Fujiyoshi, N. Uyeda, K. Morikawa, and H. Yamagishi, “Electron microscopy of tRNA crystals,” *J. Mol. Biol.*, vol. 172, no. 3, pp. 347–354, Jan. 1984, doi: 10.1016/S0022-2836(84)80031-5.
[110] R. M. Glaeser and L. W. Hobbs, “Radiation damage in stained catalase at low temperature,” *J. Microsc.*, vol. 103, no. 2, pp. 209–214, Mar. 1975, doi: 10.1111/j.1365-2818.1975.tb03896.x.
[111] H. Stark, F. Zemlin, and C. Boettcher, “Electron radiation damage to protein crystals of bacteriorhodopsin at different temperatures,” *Ultramicroscopy*, vol. 63, no. 2, pp. 75–79, Jun. 1996, doi: 10.1016/0304-3991(96)00045-9.
[112] D. Studer, H. Gross, K.-H. Müller, and A. Stemmer, “Electron microscopy of the orthorhombic purple membrane at 4.2 K,” *Ultramicroscopy*, vol. 11, no. 1, pp. 75–79, Jan. 1983, doi: 10.1016/0304-3991(83)90057-8.
[113] D. Shi, B. L. Nannenga, M. G. Iadanza, and T. Gonen, “Three-dimensional electron crystallography of protein microcrystals,” *eLife*, vol. 2, p. e01345, Nov. 2013, doi: 10.7554/eLife.01345.
[114] B. L. Nannenga, D. Shi, A. G. W. Leslie, and T. Gonen, “High-resolution structure determination by continuous-rotation data collection in MicroED,” *Nat. Methods*, vol. 11, no. 9, pp. 927–930, 2014.
[115] R. Bücker *et al.*, “Serial protein crystallography in an electron microscope,” *Nat. Commun.*, vol. 11, no. 1, p. 996, Dec. 2020, doi: 10.1038/s41467-020-14793-0.
[116] K. Kobayashi and K. Sakaoku, “The Changes of Polymer Crystals due to Irradiation with Electrons Accelerated at Various Voltages,” *Bull. Inst. Chem. Res. Kyoto Univ.*, vol. 42, no. 6, pp. 473–493, 1965.
[117] D. T. Grubb and G. W. Groves, “Rate of damage of polymer crystals in the electron microscope: Dependence on temperature and beam voltage,” *Philos. Mag.*, vol. 24, no. 190, pp. 815–828, Oct. 1971, doi: 10.1080/14786437108217051.
[118] S. Kumar and W. W. Adams, “Electron beam damage in high temperature polymers,” *Polymer*, vol. 31, no. 1, pp. 15–19, Jan. 1990, doi: 10.1016/0032-3861(90)90341-U.
[119] R. T. Read and R. J. Young, “Radiation damage and high resolution electron microscopy of polydiacetylene crystals,” *J. Mater. Sci.*, vol. 19, no. 1, pp. 327–338, Jan. 1984, doi: 10.1007/BF02403142.
[120] L. E. Thomas, C. J. Humphreys, W. R. Duff, and D. T. Grubb, “Radiation damage of polymers in the million volt electron microscope,” *Radiat. Eff.*, vol. 3, no. 1, pp. 89–91, Jan. 1970, doi: 10.1080/00337577008235620.
[121] B. Kuei and E. D. Gomez, “Elucidating Mechanisms for Electron Beam Damage in Conjugated Polymers,” *Microsc. Microanal.*, vol. 24, no. S1, pp. 1988–1989, Aug. 2018, doi: 10.1017/S1431927618010425.
[122] B. Kuei, C. Bator, and E. D. Gomez, “Imaging 0.36 nm Lattice Planes in Conjugated Polymers by Minimizing Beam Damage,” *Macromolecules*, vol. 53, no. 19, pp. 8296–8302, Oct. 2020, doi: 10.1021/acs.macromol.0c01082.
[123] H. Janik, “Electron-Beam Irradiation in TEM of Hard-Segment Homopolymers and Polyurethanes with Different Hard-Segment Content,” *Macromol. Rapid Commun.*, vol. 25, no. 12, pp. 1167–1170, Jun. 2004, doi: 10.1002/marc.200400061.
[124] A. E. Dray *et al.*, “Beam damage in a transition-metal-containing poly-yne,” *Ultramicroscopy*, vol. 41, no. 1–3, pp. 83–88, Apr. 1992, doi: 10.1016/0304-3991(92)90097-4.
[125] B. Kuei and E. D. Gomez, “Pushing the limits of high-resolution polymer microscopy using antioxidants,” *Nat. Commun.*, vol. 12, no. 1, p. 153, Dec. 2021, doi: 10.1038/s41467-020-20363-1.
[126] R. Hooley, A. Brown, and R. Brydson, “Factors affecting electron beam damage in calcite nanoparticles,” *Micron*, vol. 120, pp. 25–34, May 2019, doi: 10.1016/j.micron.2019.01.011.
[127] S. A. Moggach, T. D. Bennett, and A. K. Cheetham, “The Effect of Pressure on ZIF-8: Increasing Pore Size with Pressure and the Formation of a High-Pressure Phase at 1.47 GPa,” *Angew. Chem. Int. Ed.*, vol. 48, no. 38, pp. 7087–7089, Sep. 2009, doi: 10.1002/anie.200902643.

[128] Y. Li *et al.*, “Unravelling Degradation Mechanisms and Atomic Structure of Organic-Inorganic Halide Perovskites by Cryo-EM,” *Joule*, vol. 3, no. 11, pp. 2854–2866, Nov. 2019, doi: 10.1016/j.joule.2019.08.016.
[129] Y. Zhu *et al.*, “Unravelling surface and interfacial structures of a metal–organic framework by transmission electron microscopy,” *Nat. Mater.*, vol. 16, no. 5, pp. 532–536, May 2017, doi: 10.1038/nmat4852.
[130] V. E. Anikeeva, O. I. Semenova, and O. E. Tereshchenko, “$CH_3NH_3PbI_3$ crystal growth, structure and composition,” *J. Phys. Conf. Ser.*, vol. 1124, p. 041008, Dec. 2018, doi: 10.1088/1742-6596/1124/4/041008.
[131] S. Chen *et al.*, “Transmission electron microscopy of organic-inorganic hybrid perovskites: myths and truths,” *Sci. Bull.*, vol. 65, no. 19, pp. 1643–1649, Oct. 2020, doi: 10.1016/j.scib.2020.05.020.
[132] M. U. Rothmann *et al.*, “Structural and Chemical Changes to $CH_3NH_3PbI_3$ Induced by Electron and Gallium Ion Beams,” *Adv. Mater.*, vol. 30, no. 25, p. 1800629, Jun. 2018, doi: 10.1002/adma.201800629.
[133] J. Reyes-Gasga, G. R. Garcia, and M. Jose-Yacaman, “Electron-beam-induced structure transformation of the quasicrystalline phases of the Al62Cu20Co15Si3 alloy,” *Radiat. Phys. Chem.*, vol. 45, no. 2, pp. 283–291, Feb. 1995, doi: 10.1016/0969-806X(94)E0029-I.
[134] M. Mitome, Y. Bando, K. Kurashima, and Y. Kitami, “Temperature dependency of radiation damage in inorganic materials by 300 keV electrons,” *Microscopy*, vol. 50, no. 3, pp. 245–249, May 2001, doi: 10.1093/jmicro/50.3.245.
[135] S. Seraphin, D. Zhou, and J. Jiao, “Electron-beam-induced structural changes in crystalline C_{60} and C_{70},” *J. Mater. Res.*, vol. 8, no. 8, pp. 1895–1899, Aug. 1993, doi: 10.1557/JMR.1993.1895.
[136] E. E. Lachowski, S. J. Barnett, and D. E. Macphee, “Transmission electron optical study of ettringite and thaumasite,” p. 4, 2003.
[137] C. Rossler, J. Stark, F. Steiniger, and W. Tichelaar, “Limited-Dose Electron Microscopy Reveals the Crystallinity of Fibrous C-S-H Phases,” *J. Am. Ceram. Soc.*, vol. 89, no. 2, pp. 627–632, Feb. 2006, doi: 10.1111/j.1551-2916.2005.00714.x.
[138] Y. Yokota, H. Hashimoto, and T. Yamaguchi, “Electron beam irradiation of natural zeolites at low and room temperatures,” *Ultramicroscopy*, vol. 54, no. 2–4, pp. 207–214, Jun. 1994, doi: 10.1016/0304-3991(94)90119-8.
[139] H. Inui, H. Mori, A. Suzuki, and H. Fujita, “Electron-irradiation-induced crystalline-to-amorphous transition in β-SiC single crystals,” *Philos. Mag. B*, vol. 65, no. 1, pp. 1–14, Jan. 1992, doi: 10.1080/13642819208223042.
[140] R. W. M. Hooley, A. P. Brown, A. N. Kulak, F. C. Meldrum, and R. M. D. Brydson, “A Quantitative Evaluation of Electron Beam Sensitivity in Calcite Nanoparticles,” *J. Phys. Conf. Ser.*, vol. 902, p. 012005, Sep. 2017, doi: 10.1088/1742-6596/902/1/012005.
[141] S. Ghosh, H. Yun, P. Kumar, S. Conrad, M. Tsapatsis, and K. A. Mkhoyan, “Two Distinct Stages of Structural Modification of ZIF-L MOF under Electron-Beam Irradiation,” *Chem. Mater.*, p. acs.chemmater.1c01332, Jun. 2021, doi: 10.1021/acs.chemmater.1c01332.
[142] E. J. VandenBussche, C. P. Clark, R. J. Holmes, and D. J. Flannigan, “Mitigating Damage to Hybrid Perovskites Using Pulsed-Beam TEM,” *ACS Omega*, vol. 5, no. 49, pp. 31867–31871, Dec. 2020, doi: 10.1021/acsomega.0c04711.
[143] C. Kisielowski *et al.*, “Modulating Electron Beam–Sample Interactions in Imaging and Diffraction Modes by Dose Fractionation with Low Dose Rates,” *Microsc. Microanal.*, pp. 1–11, Sep. 2021, doi: 10.1017/S143192762101268X.
[144] A. F. G. Leontowich, A. P. Hitchcock, and R. F. Egerton, “Radiation damage yields across the carbon 1s excitation edge,” *J. Electron Spectrosc. Relat. Phenom.*, vol. 206, pp. 58–64, Jan. 2016, doi: 10.1016/j.elspec.2015.11.010.

[145] J. Lepault, F. P. Booy, and J. Dubochet, “Electron microscopy of frozen biological suspensions,” *J. Microsc.*, vol. 129, no. 1, pp. 89–102, Jan. 1983, doi: 10.1111/j.1365-2818.1983.tb04163.x.
[146] C. J. Russo and R. F. Egerton, “Damage in electron cryomicroscopy: Lessons from biology for materials science,” *MRS Bull.*, vol. 44, no. 12, pp. 935–941, Dec. 2019, doi: 10.1557/mrs.2019.284.
[147] S. H. Scheres, “Beam-induced motion correction for sub-megadalton cryo-EM particles,” *eLife*, vol. 3, p. e03665, Aug. 2014, doi: 10.7554/eLife.03665.
[148] R. M. Glaeser, “Images of paraffin monolayer crystals with perfect contrast Minimization of beam-induced specimen motion,” p. 11, 2011.
[149] D. Van Dyck and M. Wilkens, “Aspects of electron diffraction from radiation-damaged crystals,” *Ultramicroscopy*, vol. 14, no. 3, pp. 237–251, Jan. 1984, doi: 10.1016/0304-3991(84)90092-5.
[150] Z. Fisher, A. Jackson, A. Kovalevsky, E. Oksanen, and H. Wacklin, “Biological Structures,” in *Experimental Methods in the Physical Sciences*, vol. 49, Elsevier, 2017, pp. 1–75. doi: 10.1016/B978-0-12-805324-9.00001-7.
[151] G. Guo *et al.*, “Sample manipulation and data assembly for robust microcrystal synchrotron crystallography,” *IUCrJ*, vol. 5, no. 3, pp. 238–246, May 2018, doi: 10.1107/S2052252518005389.
[152] X. Zou, S. Hovmöller, and P. Oleynikov, *Electron crystallography: electron microscopy and electron diffraction*. Oxford New York: Oxford university press, 2011.
[153] W. H. Bragg and W. L. Bragg, “The reflection of X-rays by crystals,” *Proc. R. Soc. Lond. Ser. Contain. Pap. Math. Phys. Character*, vol. 88, no. 605, pp. 428–438, 1913, doi: 10.1098/rspa.1913.0040.
[154] P. P. Ewald, “Die Berechnung optischer und elektrostatischer Gitterpotentiale,” *Ann. Phys.*, vol. 369, no. 3, pp. 253–287, 1921.
[155] G. Taylor, “The phase problem,” *Acta Crystallogr. D Biol. Crystallogr.*, vol. D59, pp. 1881–1890, 2003.
[156] T. Hahn, *International Tables for Crystallography*, vol. Volume A: Space-Group Symmetry. New York: Springer, 2005.
[157] G. P. Thomson and A. Reid, “Diffraction of Cathode Rays by a Thin Film,” *Nature*, vol. 119, no. 3007, pp. 890–890, Jun. 1927, doi: 10.1038/119890a0.
[158] F. Haguenau, P. W. Hawkes, J. L. Hutchison, B. Satiat–Jeunemaître, G. T. Simon, and D. B. Williams, “Key Events in the History of Electron Microscopy,” *Microsc. Microanal.*, vol. 9, no. 2, pp. 96–138, Apr. 2003, doi: 10.1017/S1431927603030113.
[159] D. L. Dorset, “Electron Crystallography – Accomplishments and Challenges,” *Acta Crystallogr. A*, vol. 54, no. 6, pp. 750–757, Nov. 1998, doi: 10.1107/S0108767398006722.
[160] X. Zou and S. Hovmöller, “Electron crystallography: imaging and single-crystal diffraction from powders,” *Acta Crystallogr. A*, vol. 64, no. 1, pp. 149–160, Jan. 2008, doi: 10.1107/S0108767307060084.
[161] G. Wisedchaisri and T. Gonen, “Fragment-Based Phase Extension for Three-Dimensional Structure Determination of Membrane Proteins by Electron Crystallography,” *Structure*, vol. 19, no. 7, pp. 976–987, Jul. 2011, doi: 10.1016/j.str.2011.04.008.
[162] C. R. Groom, I. J. Bruno, M. P. Lightfoot, and S. C. Ward, “The Cambridge Structural Database,” *Acta Crystallogr. Sect. B Struct. Sci. Cryst. Eng. Mater.*, vol. 72, no. 2, pp. 171–179, Apr. 2016, doi: 10.1107/S2052520616003954.
[163] S. K. Burley *et al.*, “RCSB Protein Data Bank: biological macromolecular structures enabling research and education in fundamental biology, biomedicine, biotechnology and energy,” *Nucleic Acids Res.*, vol. 47, no. D1, pp. D464–D474, Jan. 2019, doi: 10.1093/nar/gky1004.

[164] M. Gemmi, H. Klein, A. Rageau, P. Strobel, and F. Le Cras, “Structure solution of the new titanate $Li_4Ti_8Ni_3O_{21}$ using precession electron diffraction,” *Acta Crystallogr. B*, vol. 66, no. 1, pp. 60–68, Feb. 2010, doi: 10.1107/S010876810904631X.
[165] H. Klein and J. David, “The quality of precession electron diffraction data is higher than necessary for structure solution of unknown crystalline phases,” *Acta Crystallogr. A*, vol. 67, no. 3, pp. 297–302, May 2011, doi: 10.1107/S0108767311006581.
[166] U. Kolb, T. Gorelik, C. Kübel, M. T. Otten, and D. Hubert, “Towards automated diffraction tomography: Part I—Data acquisition,” *Ultramicroscopy*, vol. 107, no. 6–7, pp. 507–513, Jun. 2007, doi: 10.1016/j.ultramic.2006.10.007.
[167] U. Kolb, T. Gorelik, and M. T. Otten, “Towards automated diffraction tomography. Part II—Cell parameter determination,” *Ultramicroscopy*, vol. 108, no. 8, pp. 763–772, Jul. 2008, doi: 10.1016/j.ultramic.2007.12.002.
[168] D. Zhang, P. Oleynikov, S. Hovmöller, and X. Zou, “Collecting 3D electron diffraction data by the rotation method,” *Z. Für Krist.*, vol. 225, no. 2–3, Jan. 2010, doi: 10.1524/zkri.2010.1202.
[169] E. Mugnaioli, T. Gorelik, and U. Kolb, “‘Ab initio’ structure solution from electron diffraction data obtained by a combination of automated diffraction tomography and precession technique,” *Ultramicroscopy*, vol. 109, no. 6, pp. 758–765, May 2009, doi: 10.1016/j.ultramic.2009.01.011.
[170] M. Gemmi, M. G. I. La Placa, A. S. Galanis, E. F. Rauch, and S. Nicolopoulos, “Fast electron diffraction tomography,” *J. Appl. Crystallogr.*, vol. 48, pp. 718–727, 2015.
[171] Y. Wang *et al.*, “Elucidation of the elusive structure and formula of the active pharmaceutical ingredient bismuth subgallate by continuous rotation electron diffraction,” *Chem. Commun.*, vol. 53, no. 52, pp. 7018–7021, 2017, doi: 10.1039/C7CC03180G.
[172] B. Wang, X. Zou, and S. Smeets, “Automated serial rotation electron diffraction combined with cluster analysis: an efficient multi-crystal workflow for structure determination,” *IUCrJ*, vol. 6, no. 5, pp. 854–867, Sep. 2019, doi: 10.1107/S2052252519007681.
[173] S. Plana-Ruiz *et al.*, “Fast-ADT: A fast and automated electron diffraction tomography setup for structure determination and refinement,” *Ultramicroscopy*, vol. 211, p. 112951, Apr. 2020, doi: 10.1016/j.ultramic.2020.112951.
[174] O. M. Karakulina, A. Demortière, W. Dachraoui, A. M. Abakumov, and J. Hadermann, “In Situ Electron Diffraction Tomography Using a Liquid-Electrochemical Transmission Electron Microscopy Cell for Crystal Structure Determination of Cathode Materials for Li-Ion batteries,” *Nano Lett.*, vol. 18, no. 10, pp. 6286–6291, Oct. 2018, doi: 10.1021/acs.nanolett.8b02436.
[175] T. Willhammar *et al.*, “Structure and vacancy distribution in copper telluride nanoparticles influence plasmonic activity in the near-infrared,” *Nat. Commun.*, vol. 8, no. 1, p. 14925, Apr. 2017, doi: 10.1038/ncomms14925.
[176] I. Rozhdestvenskaya *et al.*, “The structure of charoite, $(K,Sr,Ba,Mn)_{15–16}(Ca,Na)_{32}[(Si_{70}(O,OH)_{180})](OH,F)_{4.0} \cdot n H_2O$, solved by conventional and automated electron diffraction,” *Mineral. Mag.*, vol. 74, no. 1, pp. 159–177, Feb. 2010, doi: 10.1180/minmag.2010.074.1.159.
[177] I. V. Rozhdestvenskaya *et al.*, “The structure of denisovite, a fibrous nanocrystalline polytypic disordered `very complex’ silicate, studied by a synergistic multi-disciplinary approach employing methods of electron crystallography and X-ray powder diffraction,” *IUCrJ*, vol. 4, no. 3, pp. 223–242, May 2017, doi: 10.1107/S2052252517002585.
[178] Y.-B. Zhang *et al.*, “Single-Crystal Structure of a Covalent Organic Framework,” *J. Am. Chem. Soc.*, vol. 135, no. 44, pp. 16336–16339, Nov. 2013, doi: 10.1021/ja409033p.
[179] M. Feyand *et al.*, “Automated Diffraction Tomography for the Structure Elucidation of Twinned, Sub-micrometer Crystals of a Highly Porous, Catalytically Active Bismuth Metal-Organic Framework,” *Angew. Chem. Int. Ed.*, vol. 51, no. 41, pp. 10373–10376, Oct. 2012, doi: 10.1002/anie.201204963.

[180] C. G. Jones *et al.*, “The CryoEM Method MicroED as a Powerful Tool for Small Molecule Structure Determination,” *ACS Cent. Sci.*, vol. 4, no. 11, pp. 1587–1592, Nov. 2018, doi: 10.1021/acscentsci.8b00760.

[181] M. J. de la Cruz *et al.*, “Atomic-resolution structures from fragmented protein crystals with the cryoEM method MicroED,” *Nat. Methods*, vol. 14, no. 4, pp. 399–402, Apr. 2017, doi: 10.1038/nmeth.4178.

[182] M. D. Purdy, D. Shi, J. Chrustowicz, J. Hattne, T. Gonen, and M. Yeager, “MicroED structures of HIV-1 Gag CTD-SP1 reveal binding interactions with the maturation inhibitor bevirimat,” *Proc. Natl. Acad. Sci.*, vol. 115, no. 52, pp. 13258–13263, Dec. 2018, doi: 10.1073/pnas.1806806115.

[183] L. Palatinus, P. Brázda, M. Jelínek, J. Hrdá, G. Steciuk, and M. Klementová, “Specifics of the data processing of precession electron diffraction tomography data and their implementation in the program *PETS2.0*,” *Acta Crystallogr. Sect. B Struct. Sci. Cryst. Eng. Mater.*, vol. 75, no. 4, pp. 512–522, Aug. 2019, doi: 10.1107/S2052520619007534.

[184] P. Brázda, M. Klementová, Y. Krysiak, and L. Palatinus, “Accurate lattice parameters from 3D electron diffraction data. I. Optical distortions,” *IUCrJ*, vol. 9, no. 6, Nov. 2022, doi: 10.1107/S2052252522007904.

[185] V. Petříček, M. Dušek, and L. Palatinus, “Crystallographic Computing System JANA2006: General features,” *Z. Für Krist. - Cryst. Mater.*, vol. 229, no. 5, pp. 345–352, May 2014, doi: 10.1515/zkri-2014-1737.

[186] M. C. Burla *et al.*, “Crystal structure determination and refinement *via SIR2014*,” *J. Appl. Crystallogr.*, vol. 48, no. 1, pp. 306–309, Feb. 2015, doi: 10.1107/S1600576715001132.

[187] L. Palatinus, “SUPERFLIP– a computer program for the solution of crystal structures by charge flipping in arbitrary dimensions,” *J. Appl. Crystallogr.*, vol. 40, pp. 786–790, 2007.

[188] M. G. Rossmann, “The molecular replacement method,” *Acta Crystallogr. A*, vol. 46, no. 2, pp. 73–82, Feb. 1990, doi: 10.1107/S0108767389009815.

[189] P. A. Karplus and K. Diederichs, “Linking Crystallographic Model and Data Quality,” *Science*, vol. 336, no. 6084, pp. 1030–1033, May 2012, doi: 10.1126/science.1218231.

[190] L. Palatinus, V. Petříček, and C. A. Corrêa, “Structure refinement using precession electron diffraction tomography and dynamical diffraction: theory and implementation,” *Acta Crystallogr. Sect. Found. Adv.*, vol. 71, no. 2, pp. 235–244, Mar. 2015, doi: 10.1107/S2053273315001266.

[191] K. Walenta, “Bulachit: ein neues Aluminiumarsenatmineral von Neubulach im nördlichen Schwarzwald,” *Aufschluss*, vol. 34, pp. 445–451, 1983.

[192] F. Frau and S. Da Pelo, “Bulachite, a rare aluminium arsenate from Sardinia, Italy: the second world occurrence,” *NEUES Jahrb. Mineral. MONATSHEFTE*, vol. 1, pp. 18–26, 2001.

[193] V. T. Allen, J. J. Fahey, and J. M. Axelrod, “Mansfieldite, a new arsenate, the aluminum analogue of scorodite, and the mansfieldite-scorodite series,” *Am. Mineral.*, vol. 33, no. 3–4, pp. 122–134, 1948.

[194] I. E. Grey, “Crystal Chemistry of Hydrous Aluminium Arsenate Minerals,” *Crystallogr. Rep.*, vol. 66, no. 1, pp. 33–42, Jan. 2021, doi: 10.1134/S1063774521010065.

[195] I. E. Grey, J. Betterton, A. R. Kampf, C. M. Macrae, F. L. Shanks, and J. R. Price, “Penberthycroftite, $[Al_6(AsO_4)_3(OH)_9(H_2O)_5]\cdot 8H_2O$, a second new hydrated aluminium arsenate mineral from the Penberthy Croft mine, St. Hilary, Cornwall, UK,” *Mineral. Mag.*, vol. 80, no. 7, pp. 1149–1160, Dec. 2016, doi: 10.1180/minmag.2016.080.069.

[196] I. E. Grey, A. R. Kampf, J. R. Price, and C. M. Macrae, “Bettertonite, $[Al_6(AsO_4)_3(OH)_9(H_2O)_5]\cdot 11H_2O$, a new mineral from the Penberthy Croft mine, St. Hilary, Cornwall, UK, with a structure based on polyoxometalate clusters,” *Mineral. Mag.*, vol. 79, no. 7, pp. 1849–1858, Dec. 2015, doi: 10.1180/minmag.2015.079.7.16.

[197] O. C. Gagné and F. C. Hawthorne, “Comprehensive derivation of bond-valence parameters for ion pairs involving oxygen,” *Acta Crystallogr. Sect. B Struct. Sci. Cryst. Eng. Mater.*, vol. 71, no. 5, pp. 562–578, Oct. 2015, doi: 10.1107/S2052520615016297.

[198] J. Majzlan, L. Palatinus, and J. Plášil, “Crystal structure of Fe2(AsO4)(HAsO4)(OH)(H2O)3, a dehydration product of kaňkite,” *Eur. J. Mineral.*, vol. 28, no. 1, pp. 63–70, Mar. 2016, doi: 10.1127/ejm/2015/0027-2495.

[199] Y. Krysiak *et al.*, “The Elusive Structure of Magadiite, Solved by 3D Electron Diffraction and Model Building,” *Chem. Mater.*, p. acs.chemmater.1c00107, Apr. 2021, doi: 10.1021/acs.chemmater.1c00107.

[200] E. Mugnaioli *et al.*, “Electron Diffraction on Flash-Frozen Cowlesite Reveals the Structure of the First Two-Dimensional Natural Zeolite,” *ACS Cent. Sci.*, p. 9, 2020.

[201] G. Steciuk, J. Sejkora, J. Čejka, J. Plášil, and J. Hloušek, “Krupičkaite, Cu6[AsO3(OH)]6·8H2O, a new copper arsenate mineral from Jáchymov (Czech Republic),” *J. Geosci.*, pp. 37–50, Apr. 2021, doi: 10.3190/jgeosci.318.

[202] I. E. Grey *et al.*, “Galeaclolusite, $[Al_6(AsO_4)_3(OH)_9(H_2O)_4]\cdot 8H_2O$, a new bulachite-related mineral from Cap Garonne, France,” *Mineral. Mag.*, vol. 85, no. 2, pp. 142–148, Apr. 2021, doi: 10.1180/mgm.2020.98.

[203] X.-H. Bu, M. J. Zaworotko, and Z. Zhang, Eds., *Metal-organic framework: from design to applications*. Cham: Springer, 2020.

[204] C. J. Doonan and C. J. Sumby, “Metal–organic framework catalysis,” *CrystEngComm*, vol. 19, no. 29, pp. 4044–4048, 2017, doi: 10.1039/C7CE90106B.

[205] Y. Sun *et al.*, “Metal–Organic Framework Nanocarriers for Drug Delivery in Biomedical Applications,” *Nano-Micro Lett.*, vol. 12, no. 1, p. 103, Dec. 2020, doi: 10.1007/s40820-020-00423-3.

[206] L. E. Kreno, K. Leong, O. K. Farha, M. Allendorf, R. P. Van Duyne, and J. T. Hupp, “Metal–Organic Framework Materials as Chemical Sensors,” *Chem. Rev.*, vol. 112, no. 2, pp. 1105–1125, Feb. 2012, doi: 10.1021/cr200324t.

[207] K. Fegy, D. Luneau, T. Ohm, C. Paulsen, and P. Rey, “Two-Dimensional Nitroxide-Based Molecular Magnetic Materials,” *Angew Chem Int Ed*, vol. 37, p. 1270, 1998.

[208] C. Lecourt *et al.*, “Thermally-induced hysteretic valence tautomeric conversions in the solid state *via* two-step labile electron transfers in manganese-nitronyl nitroxide 2D-frameworks,” *Dalton Trans.*, vol. 49, no. 44, pp. 15646–15662, 2020, doi: 10.1039/D0DT03243C.

[209] C. Lecourt *et al.*, “Hypersensitive pressure-dependence of the conversion temperature of hysteretic valence tautomeric manganese–nitronyl nitroxide radical 2D-frameworks,” *Chem. Commun.*, vol. 57, no. 19, pp. 2376–2379, 2021, doi: 10.1039/D0CC08144B.

[210] Z. Huang, T. Willhammar, and X. Zou, “Three-dimensional electron diffraction for porous crystalline materials: structural determination and beyond,” *Chem. Sci.*, p. 10.1039.D0SC05731B, 2021, doi: 10.1039/D0SC05731B.

[211] J. T. C. Wennmacher *et al.*, “3D-structured supports create complete data sets for electron crystallography,” *Nat. Commun.*, vol. 10, no. 1, p. 3316, Dec. 2019, doi: 10.1038/s41467-019-11326-2.

[212] G. M. Sheldrick, “Phase annealing in SHELX-90: direct methods for larger structures,” *Acta Crystallogr. A*, vol. 46, no. 6, pp. 467–473, Jun. 1990, doi: 10.1107/S0108767390000277.

[213] M. T. B. Clabbers *et al.*, “MyD88 TIR domain higher-order assembly interactions revealed by microcrystal electron diffraction and serial femtosecond crystallography,” *Nat. Commun.*, vol. 12, no. 1, p. 2578, Dec. 2021, doi: 10.1038/s41467-021-22590-6.

[214] S. Ito *et al.*, “Structure determination of small molecule compounds by an electron diffractometer Synergy-ED,” Chemistry, preprint, Aug. 2021. doi: 10.33774/chemrxiv-2021-t9vkz-v2.

[215] I. Nederlof, E. van Genderen, Y.-W. Li, and J. P. Abrahams, “A Medipix quantum area detector allows rotation electron diffraction data collection from submicrometre three-dimensional protein crystals,” *Acta Crystallogr. D Biol. Crystallogr.*, vol. 69, no. 7, pp. 1223–1230, Jul. 2013, doi: 10.1107/S0907444913009700.

[216] W. Kabsch, “*XDS*,” *Acta Crystallogr. D Biol. Crystallogr.*, vol. 66, no. 2, pp. 125–132, Feb. 2010, doi: 10.1107/S0907444909047337.

[217] M. Ge, X. Zou, and Z. Huang, “Three-Dimensional Electron Diffraction for Structural Analysis of Beam-Sensitive Metal-Organic Frameworks,” *Crystals*, vol. 11, no. 3, p. 263, Mar. 2021, doi: 10.3390/cryst11030263.

[218] Z. Huang, E. S. Grape, J. Li, A. K. Inge, and X. Zou, “3D electron diffraction as an important technique for structure elucidation of metal-organic frameworks and covalent organic frameworks,” *Coord. Chem. Rev.*, vol. 427, p. 213583, Jan. 2021, doi: 10.1016/j.ccr.2020.213583.

[219] P. Klar *et al.*, “Chirality and accurate structure models by exploiting dynamical effects in continuous-rotation 3D ED data,” Chemistry, preprint, Nov. 2021. doi: 10.26434/chemrxiv-2021-4jh14.

[220] “Jingsuiite, TiB2, a new mineral from the Cr-11 podiform chromitite orebody, Luobusa ophiolite, Tibet, China: Implications for recycling of boron,” *Am. Mineral.*, Mar. 2021, doi: 10.2138/am-2021-7647.

[221] W. J. H. Hagen, W. Wan, and J. A. G. Briggs, “Implementation of a cryo-electron tomography tilt-scheme optimized for high resolution subtomogram averaging,” *J. Struct. Biol.*, vol. 197, no. 2, pp. 191–198, Feb. 2017, doi: 10.1016/j.jsb.2016.06.007.

[222] W. Wan and J. A. G. Briggs, “Cryo-Electron Tomography and Subtomogram Averaging,” in *Methods in Enzymology*, vol. 579, Elsevier, 2016, pp. 329–367. doi: 10.1016/bs.mie.2016.04.014.

[223] M. Gemmi *et al.*, “Structure determination of nano- crystals with precession 3D electron diffraction tomography in the transmission electron microscope,” p. 5, 2013.

[224] E. T. Broadhurst, H. Xu, S. Parsons, and F. Nudelman, “Revealing the early stages of carbamazepine crystallization by cryoTEM and 3D electron diffraction,” *IUCrJ*, vol. 8, no. 6, Nov. 2021, doi: 10.1107/S2052252521010101.

[225] F. Papi, J. Potticary, A. E. Lanza, S. R. Hall, and M. Gemmi, “Crystal Structure of a Peculiar Polycyclic Aromatic Hydrocarbon Determined by 3D Electron Diffraction,” *Cryst. Growth Des.*, vol. 21, no. 11, pp. 6341–6348, Nov. 2021, doi: 10.1021/acs.cgd.1c00820.

[226] G. Steciuk, B. Kiefer, W. Hornfeck, A. V. Kasatkin, and J. Plášil, “Molybdenum Disorder in Hydrated Sedovite, Ideally $U(MoO_4)_2 \cdot n H_2O$, a Microporous Nanocrystalline Mineral Characterized by Three-Dimensional Electron Diffraction, Density Functional Theory Computations, and Complexity Analysis,” *Inorg. Chem.*, p. acs.inorgchem.1c01506, Sep. 2021, doi: 10.1021/acs.inorgchem.1c01506.

[227] M. Lightowler, S. Li, X. Ou, X. Zou, M. Lu, and H. Xu, “Indomethacin Polymorph δ Revealed To Be Two Plastically Bendable Crystal Forms by 3D Electron Diffraction: Correcting a 47-Year-Old Misunderstanding**,” *Angew. Chem. Int. Ed.*, Jan. 2022, doi: 10.1002/anie.202114985.

[228] M. T. B. Clabbers, S. Z. Fisher, M. Coinçon, X. Zou, and H. Xu, “Visualizing drug binding interactions using microcrystal electron diffraction,” *Commun. Biol.*, vol. 3, no. 1, p. 417, Dec. 2020, doi: 10.1038/s42003-020-01155-1.

[229] H. Klein *et al.*, “Three different Ge environments in a new $Sr_5CuGe_9O_{24}$ phase synthesized at high pressure and high temperature,” *Acta Crystallogr. Sect. B Struct. Sci. Cryst. Eng. Mater.*, vol. 76, no. 5, pp. 727–732, Oct. 2020, doi: 10.1107/S2052520620008914.

[230] R. D. Poulsen *et al.*, “Synchrotron X-Ray Charge-Density Study of Coordination Polymer [Mn(HCOO)2(H2O)2]∞,” *Chem. - Eur. J.*, vol. 13, no. 35, pp. 9775–9790, Nov. 2007, doi: 10.1002/chem.200700756.

[231] M. Ge *et al.*, “On the completeness of three-dimensional electron diffraction data for structural analysis of metal–organic frameworks,” *Faraday Discuss.*, vol. 231, pp. 66–80, 2021, doi: 10.1039/D1FD00020A.
[232] L. Palatinus *et al.*, “Hydrogen positions in single nanocrystals revealed by electron diffraction,” *Science*, vol. 355, no. 6321, pp. 166–169, Jan. 2017, doi: 10.1126/science.aak9652.
[233] I. E. Grey *et al.*, “Bulachite, $[Al_6(AsO_4)_3(OH)_9(H_2O)_4]\cdot 2H_2O$ from Cap Garonne, France: Crystal structure and formation from a higher hydrate,” *Mineral. Mag.*, vol. 84, no. 4, pp. 608–615, Aug. 2020, doi: 10.1180/mgm.2020.52.
[234] J. Plášil *et al.*, “3D Electron Diffraction as a Powerful Tool to Study the Earliest Nanocrystalline Weathering Products: A Case Study of Uraninite Weathering,” *ACS Earth Space Chem.*, p. acsearthspacechem.1c00386, May 2022, doi: 10.1021/acsearthspacechem.1c00386.

Abstract

Recent progress in the development of electron crystallography methods has made 3D electron diffraction (3D ED) a widely adapted technique to investigate structures of nano-sized crystals. This thesis is based on low-dose electron diffraction tomography (LD-EDT) developed to characterize beam sensitive compounds. One of the remaining challenges in the 3D ED field is beam damage to crystals during experiments. The first chapter of the thesis therefore consists of an extensive literature review on the complex mechanisms involved in radiation damage in crystals and the complex involved mechanisms, and on the monitoring of crystallinity loss kinetics by measuring intensity loss of Bragg reflections, referred to as diffraction fading. Chapter 2 follows with an overview of 3D ED methodology with a specific focus on LD-EDT. In Chapter 3, LD-EDT has been applied to two beam sensitive compounds, a hydrated aluminum arsenate mineral called Bulachite and a 2D manganese-radical layered metal organic framework (MOF), referenced as YI_OTf03. The crystal structure of Bulachite was solved with LD-EDT data and refined with both X-rays and LD-EDT data. The structure has orthorhombic symmetry and contains layers composed of aluminum centered octahedra connected to arsenate tetrahedra. There are water molecules present both in and in-between the layers. In the case of YI_OTf03, the lattice symmetry was characterized by LD-EDT data and the structure was obtained by molecular replacement using continuous rotation 3D ED data. The structure has monoclinic symmetry and contains 2D layers with two chemically distinct manganese centers, surrounded by imidazole and nitronyl nitroxide radicals. The layers are in a serpentine-like conformation making contact at the apexes, which results in large pores in the structure. The fourth chapter of the thesis involves an improvement to LD-EDT data acquisition via implementation of a dose-symmetric tomography scheme. This consists of starting data collection at zero tilt and increasing the tilt angle progressively in a symmetric manner. The electron dose can be adjusted so that damage only accumulates at high tilt. All frames are used for indexing the data while only damage-free low tilt frames are used for structure determination. Beam damage is therefore bypassed without sacrificing the signal to noise ratio. Low tilt data from multiple crystals is merged to improve data completeness. This technique, referred to as dose-symmetric electron diffraction tomography (DS-EDT) was tested and verified on two compounds, the complex oxide $Sr_5CuGe_9O_{24}$, and the beam sensitive MOF manganese formiate. Our results show that structure determination is possible by merging data only +/- 10° frames from multiple particles. The effect of data completeness on the results obtained and limits concerning the number of minimum necessary datasets are discussed in this section.

Résumé

Les progrès récents dans le développement des méthodes de cristallographie électronique ont fait de la diffraction électronique 3D (3D ED) une technique largement adaptée à l'étude des structures des cristaux de taille nanométrique. Cette thèse est basée sur la diffraction d'électrons à faible dose en mode tomographie (LD-EDT) développée pour caractériser les composés sensibles au faisceau. L'un des défis dans le domaine de la 3D ED concerne l'endommagement des cristaux par le faisceau pendant les expériences. Le premier chapitre de la thèse consiste donc en une revue de littérature sur les dégâts d'irradiation dans les cristaux et les mécanismes complexes impliqués et sur le suivi de la cinétique de perte de cristallinité en mesurant la perte d'intensité des réflexions de Bragg (diffraction fading). Cette présentation est suivie du chapitre 2 décrivant la méthodologie de la 3D ED, avec un accent particulier sur la LD-EDT, puis du chapitre 3, dans lequel la LD-EDT a été appliquée à deux composés sensibles au faisceau, un minéral d'arséniate d'aluminium hydraté appelé Bulachite et un réseau métallo-organique (MOF) 2D manganèse-radical, référencé comme YI_OTf03. La structure cristalline de la Bulachite a été résolue à l'aide de données LD-EDT et affinée à l'aide de données de rayons X et LD-EDT. La structure présente une symétrie orthorhombique et contient des couches composées d'octaèdres centrés sur l'aluminium et reliés à des tétraèdres d'arséniate. Des molécules d'eau sont présentes à la fois dans et entre les couches. Dans le cas de YI_OTf03, la symétrie du réseau a été caractérisée par des données LD-EDT et la structure a été obtenue par remplacement moléculaire en utilisant des données ED 3D à rotation continue. La structure a une symétrie monoclinique et contient des couches 2D avec deux centres de manganèse chimiquement distincts, entourés de radicaux imidazole et nitronyl nitroxyde. Les couches ont une conformation en serpentin et entrent en contact au niveau des apex, ce qui entraîne de larges pores dans la structure. La dernière partie de la thèse implique une amélioration de l'acquisition de données LD-EDT via l'implémentation d'une technique de tomographie à dose symétrique. Cela consiste à collecter d'abord les données à l'inclinaison zéro et à augmenter progressivement l'angle d'inclinaison de manière symétrique. La dose d'électrons peut être ajustée de sorte que les dommages ne s'accumulent qu'à partir d'une inclinaison élevée. Toutes les images sont utilisées pour l'indexation des réflexions, tandis que seules les images sans dommages à faible inclinaison sont utilisées pour la détermination de la structure. Les dommages causés par le faisceau sont donc contournés sans sacrifier le rapport signal/bruit. Les données de faible inclinaison de plusieurs cristaux sont ensuite fusionnées pour améliorer la complétude des données. Cette technique, appelée tomographie par diffraction électronique à dose symétrique (DS-EDT), a été testée et vérifiée sur deux composés, l'oxyde complexe $Sr_5CuGe_9O_{24}$ et le formiate de manganèse, un MOF sensible au faisceau. Nos résultats montrent que la détermination de la structure est possible en fusionnant les données dans une gamme de +/- 10° provenant de plusieurs particules. L'effet de la complétude des données sur les résultats obtenus et les limites concernant le nombre de particules minimum nécessaires sont discutés dans cette section.